

ROBUST MULTIVARIABLE CONTROL OF HELICOPTERS: FROM MATHEMATICAL MODELS TO FLIGHT TESTS

Thesis submitted for the degree of
Doctor of Philosophy
at the University of Leicester

by

Alex Smerlas BSc (Kiev)
Department of Engineering
University of Leicester



March 1999

UMI Number: U532525

All rights reserved

INFORMATION TO ALL USERS

The quality of this reproduction is dependent upon the quality of the copy submitted.

In the unlikely event that the author did not send a complete manuscript and there are missing pages, these will be noted. Also, if material had to be removed, a note will indicate the deletion.



UMI U532525

Published by ProQuest LLC 2013. Copyright in the Dissertation held by the Author.
Microform Edition © ProQuest LLC.

All rights reserved. This work is protected against
unauthorized copying under Title 17, United States Code.



ProQuest LLC
789 East Eisenhower Parkway
P.O. Box 1346
Ann Arbor, MI 48106-1346

Copyright © by Alex J. Smerlas
Department of Engineering
University of Leicester
Leicester, LE1 7RH
United Kingdom

Ἐκδιδάσκει πάνθ' ὁ γηράσκων χρόνος.
(The time that makes us old teaches us everything)

Aisxilos (525-456 BC)
(The father of ancient Greek tragedy)

Στην οικογένειά μου με αγάπη
To my family with love

Abstract

This thesis describes the design and flight testing of advanced robust multivariable control laws for high performance fly-by-wire helicopters. The control laws are synthesised using H_∞ optimisation, which provides robust stability against a wide class of systems with unmodelled dynamics and parametric uncertainty. This is the first time that an H_∞ -based control system has been designed and successfully tested in both ground-based simulators and in real flight, on a fly-by-wire, variable stability helicopter.

The helicopter is a multivariable and highly nonlinear system. The dynamics vary significantly with the aircraft's orientation in the three-dimensional inertial space, the magnitude and direction of the velocity vector and different loading configurations. This implies a high pilot workload during operational tasks. The developed control laws, provide the pilot with a means to fly the aircraft safely and effectively throughout its flight envelope.

Special attention is paid to the effects of high order rotor dynamics on the control law robustness and performance, to controller implementation issues and to the effects of aircraft configuration to the perceived handling qualities of the helicopter.

For systems that undergo large parameter variations, a novel gain scheduled methodology is proposed, which not only stabilises the linearised plants within the scheduling variable region, but also achieves H_∞ performance control objectives. This method exploits the attractive observer-based structure of the H_∞ loop shaping feedback compensators.

Acknowledgements

I would like to thank my supervisor Professor Ian Postlethwaite and co-supervisor Dr. Daniel Walker for the encouragement and support they gave me during the last four years as well as the constructive criticism and reading of early drafts of this thesis. I would also like to thank Dr. Yiannis K. Konstantopoulos, Dr. Da-Wei Gu, Dr. Christopher Edwards, Professor Petko Petkov, Professor Michail Konstantinov and Professor Michail Goman for their precious advice ranging from complex mathematical topics to advanced aerodynamic phenomena.

The flight tests on the experimental Bell 205 Fly-By-Wire helicopter would not be possible without the facilities and the expertise of the Flight Research Laboratory (FRL) of the Canadian National Research Council. I would like to express my gratitude to the Flight Test Engineer Mr. Bill Gubbels and the test pilots who flew the Bell 205 experimental helicopter: Stephan Carignan and Robert Erdos from the FRL, Robert Horton from the UK Test Squadron of the Defence Evaluation and Research Agency (DERA) and Michael Haider from the US Army / National Aeronautics and Space Administration. I would also like to thank the FRL team for allowing me fly the Bell 205 helicopter - the flight was most enjoyable and hopefully there are more to come.

Dr. Michael Strange, Mr. Jeremy Howitt from DERA and Mr. Adrian Alford from Westland Helicopters deserve special thanks for arranging piloted simulations at the Motion Simulators at Bedford and Yeovil respectively.

Life in Leicester would not have been as enjoyable without my close friends and colleagues from the university; especially Frances Condron, Karim Benchaib, Emmanuel Prempain, Aamer Bhatti, Vassilios Tsachouridis, Matthew Turner and many others who created a friendly and fun environment at the university.

I feel necessary to thank my advisors and close friends from the Kiev Aviation Institute and the Ukrainian Academy of Sciences for introducing me to the fields of flight dynamics and control. I have greatly benefited from discussions with Professor Anatolyi Azarievich Tunik, Professor Evgenyi Pavlovich Udartsev, Professor Bladimir Ivanovich Kasianov, Professor Leonid Ivanovich Blochin, Professor Bladimir Ilich Zemlianskyi and Professor Bladimir Borisovich Larin. Whether to discuss scientific issues, or to practice the aerodynamics of sailing in the river Dnepr their company was most enjoyable.

I would also like to thank my school physics and maths mentors, Evaggelos Fotinopoulos and Yiannis Kerasaridis, who guided me throughout the educational years of my life. Our early weekend meetings were very beneficial to my understanding of physics and science.

Finally, I would like to thank my parents Yannis and Kathrin for tolerating me for the last twenty seven years and my brothers George and Pericles for their continuing encouragement and support.

During this research financial support came from the University of Leicester, the De-

fence Evaluation and Research Agency and the Engineering and Physical Sciences Research Council to whom I am grateful.

Contents

1	Introduction	1
1.1	Background and previous work	1
1.2	Summary of contents	7
1.3	Notation	9
1.3.1	Mathematical notation	9
1.3.2	Abbreviations	10
1.3.3	List of variable names	11
2	H_∞ loop shaping for helicopter flight control systems	13
2.1	H_∞ loop shaping	13
2.1.1	H_∞ loop shaping guarantees	16
2.2	Scaling	18
2.3	Weight selection	18
2.4	Incorporating time domain specifications	19
2.5	Design example	23
3	Design and piloted simulation of an H_∞ loop shaping compensator for the Bell 205 airborne simulator	32
3.1	Introduction	32
3.2	Description of the NRC Bell 205 flight dynamics model	33
3.2.1	Feedback signals	33
3.2.2	Mode description	34
3.2.3	The stabiliser bar	35
3.3	Model validation	37
3.4	The controller architecture	43
3.5	Controller design for the NRC Bell 205 FBW helicopter	46
3.6	Piloted simulation results	53

3.7	Discussion	55
4	Flight testing an H_∞ controller on the Bell 205 fly-by-wire helicopter	61
4.1	The Bell 205 fly-by-wire helicopter	62
4.2	Flight test	63
4.2.1	Coding and software requirements	63
4.2.2	Inceptor configuration	64
4.2.3	Instrument Configuration	64
4.2.4	Pilot experience	64
4.2.5	Test manoeuvres	64
4.3	Handling qualities evaluation	65
4.3.1	Forward flight - pilot observations	66
4.3.2	Mission task elements - pilot Observations	66
4.4	Quantitative analysis of the flight test data	67
4.5	Force-feel system "transparency"	75
5	Helicopter handling qualities improvement using rotor dynamics and H_∞ optimisation. Design, analysis and flight test results	80
5.1	Introduction	80
5.2	A High order model for the NRC Bell 205 helicopter	81
5.2.1	Rotor	82
5.2.2	Fuselage, tailplane and fin	83
5.3	Comparisons with flight test data	84
5.3.1	Feedback Signals	87
5.4	Controller design	88
5.4.1	Mode description	89
5.4.2	One degree-of-freedom synthesis	90
5.4.3	Two degrees-of-freedom synthesis	96
5.4.4	Implementation and testing	101
5.5	Flight test	101
5.5.1	Inceptor configuration	101
5.5.2	Instrument configuration	102
5.5.3	Pilot experience	102
5.5.4	Handling qualities evaluation	102
5.5.5	Mission task elements - pilot observations	103
5.6	Discussion	105
5.7	Multivariable compensators and stability of euler-type integration algorithms	107
5.8	Concluding remarks	109
6	Optimal design of multivariable, observer-based, gain-scheduled compen-	

sators	111
6.1 Introduction	111
6.2 An interpolation and robust control framework	112
6.2.1 Stability preserving interpolation	112
6.2.2 Right coprime factorisation	114
6.2.3 Gap metric	117
6.3 Gain-scheduling	118
6.3.1 Justification of blending region	118
6.3.2 Controller structure	119
6.3.3 An optimisation approach to gain-scheduling	120
6.4 Gain scheduling optimisation results	123
6.4.1 Optimisation results	124
6.4.2 Gap metric analysis	125
6.4.3 Gain-scheduled controller in simulation	127
6.5 Summary	130
7 Conclusions and suggestions for future research	131
7.1 Summary	131
7.1.1 The main contributions	131
7.2 Suggestions for future research	133
A Controller Code	141
B Flight test manoeuvres - ADS-33 tasks	145
C Recorded Flight Test Data - Time Histories of spot turn manoeuvre	148

Introduction

1.1 Background and previous work

This thesis is about the development and flight testing of robust multivariable *feedback compensators* for Fly-By-Wire (FBW) helicopters. The compensators are designed using advanced control theory (namely H_∞ optimisation) and evaluated on the unique 205 Fly-By-Wire helicopter at the Flight Research Laboratory of the National Research Council of Canada. This is the first time that an H_∞ control law has been successfully flight tested on a FBW rotorcraft.

The main reason for investigating the effects of feedback on rotary wing vehicles is to improve their poor flying qualities which are due to cross-axis coupling, dynamic uncertainty and open-loop instability. It is widely accepted that the provision of optimum handling qualities is best achieved through low cost improvements in aerodynamics and/or flight control laws, rather than fundamental changes to the vehicle. Designing a feedback compensator to alleviate the pilot's workload can also be useful in allowing more actuating surfaces to be used than the pilot's inceptors. The overall helicopter performance and pilot comfort during dynamic manoeuvring can be characterised by handling qualities ratings (HQRs), given by test pilots for specified tasks. The key question we shall be addressing is "how do we synthesise and evaluate a feedback compensator for rotary wing vehicles to ensure improved flying qualities in the face of high dynamic uncertainty and inherent cross-axes couplings?"

To eliminate the effects of cross-couplings and to compensate for uncertain dynamics is essential - yet both these problems are inherent to the rotorcraft configuration. In particular, the primary source of the vehicle handling deficiencies are the asymmetric forces and moments, produced by the rotor system. A rotating blade from the main helicopter rotor produces a distributed lift force causing velocity perturbations in all directions. For every rotation of 360 deg, the blade is aligned twice with the longitudinal and lateral axes, initiating perturbations in both pitch and roll loops of the helicopter. A pilot would feel

these perturbations as sharp rate responses of the fuselage (typically within 1 – 1.5 sec), but insufficient aerodynamic damping alters the initial rate responses by giving rise to incidence and sideslip variations. Unfortunately, these variations are mostly unpredictable as the strong main rotor wake creates unsteady aerodynamic effects around the aircraft's body¹. Similar phenomena occur due to the wake effects of the tail rotor. The closeness of the vertical fin to the rotor disk can have a significant impact on the helicopter's ability to achieve right or left rotations about its normal axis. Although not very useful at hover, the fin adds directional damping in forward flight and with the horizontal stabiliser provides important "stiffness" to neutralise the unstable effects of the rotor-fuselage system.

These dynamic characteristics of the helicopter require complicated multivariable control inputs, which imply high pilot workload and the possibility of poor handling qualities. For example, let us look at a typical helicopter manoeuvre - a sidestep task, where the pilot has to laterally translate the rotorcraft mainly using rolling commands. Roll inputs will dominate the response, but at the same time longitudinal and heading excursions will be caused by the vertical offset of the tail rotor thrust and the vertical fin side-force from the centre of mass. Also, a significant amount of off-axis motion will be exerted by the inclination of the lift vectors on individual blade sections. Height does not remain constant as the main rotor thrust is not perpendicular to the local horizon and lift no longer counter-balances the vertically directed rotorcraft's weight. Therefore, the pilot needs to simultaneously coordinate heading angle (with the pedals), height (with the collective lever) and keep track over the ground (using longitudinal inputs). The level of cross coupling depends on the aircraft cross inertias and the particular characteristics of the rotor disk (teetering, hingeless etc.). Furthermore, at high speeds the piloting strategy may be different. The pilot can use the left or right hand inceptors to initiate pitch motion - it all depends on the total airspeed, aerodynamic damping and the dihedral effects of the fuselage. From the above, it is not hard to see that unaugmented helicopters have poor handling qualities which are compensated for only at the expense of high pilot workload.

Over the years, much research has gone into the development of appropriate feedback compensation schemes to reduce pilot workload. Mechanical augmentation systems, such as the Bell stabiliser bar or the Hiller servo mechanism [25], were introduced to the rotor head as a means of enhancing the stability properties of the helicopter. With the introduction of very unstable airframes, the first feedback control concepts were developed. The electric signals from the gyros were compared with signals derived from the pilot stick and the resulting difference was used to drive the hydraulic actuators. This logic was implemented with analogue electronics and developed into the now widely used Stability and Control Augmentation Systems (SCAS).

Although SCAS offered significant weight savings over previous purely mechanical sys-

¹The term "aircraft" refers to any type of flight vehicle. The distinction between fixed and rotary wing configurations should be clear from the text.

tems, they were constrained to only 10% of the maximum actuator authority, which gave little assistance to the pilot in manoeuvring flight. There were two basic reasons for this limited control configuration. The first was the low reliability of the overall system hardware that needed triple or quadruple back-ups to satisfy safety criteria. The second was the difficulty of synthesising analogue feedback compensators to meet the handling quality requirements. Inherent dynamic uncertainty and cross-axis coupling were hard problems to tackle with the existing control law design techniques. However, the advancement of computer technology has now made it possible to augment the pilot demands with appropriately modified sensor outputs within the Flight Control Computer (FCC). In physical terms, the FCC receives inputs in the form of electrical or optical signals, and then it uses the actuators to alter the aircraft mass centre coordinates and the magnitude and direction of the associated velocity vector. Such systems make possible the implementation of complex nonlinear control laws, mode changing and gain scheduling, all of which improve the rotorcraft handling qualities. They also allow the detection of failures in sensors, actuators or other aircraft systems.

The first examples of such high-gain, multiply-redundant control laws appeared in fixed wing aircraft such as the F-16, F-18 and the Space Shuttle [1, 29]. On rotary wing vehicles, the first full-authority fiber-optic control system was the Advanced Digital/Optical Control System (ADOCS) program at NASA, tested on the UH-60 Black Hawk Helicopter [43]. The ADOCS program exposed some unknown, at that time, aspects of helicopter control laws, such as the importance of high frequency dynamics to high bandwidth controllers, the significance of total time delay to piloted handling qualities, and the difficulties of implementing digital feedback compensators. Since the ADOCS program, experimental work has been conducted on the Bo-105 of the German Aerospace Establishment (DLR), using model following concepts similar to ADOCS [68], and on the NRC Bell 205 helicopter, primarily using feedforward and feedback gain scheduled matrices [8]. Most of these research efforts concentrated on flight testing feedback compensators synthesised using Single-Input-Single-Output (SISO) control design techniques with the exception of some early LQR/LQG-based systems reported in [8] and [37].

While the above experiments demonstrated the improvement of helicopter handling qualities (HQs) due to feedback compensation, they failed to address adequately the flight control system tolerance to uncertainty. Designed using a mathematical description of the helicopter, feedback compensators modify the dynamic response of the unaugmented system to the degree that the mathematical model represents the real aircraft. A mathematical model, however, is just a set of differential equations describing only the salient features of a real system. The formulation of such equations, using analytical or identification methods from wind tunnel or flight test data, is in itself a very difficult task. Every model consists of mechanical parts (rigid or flexible body), dynamic loads (forces and moments), the power plant (engines and inertial interference) and other exogenous factors. The states

describing the above subsystems are essential to build an “accurate” representation of the real system, yet we use finite-dimensional time-invariant mathematical models to synthesise the majority of flight control laws. This can be partly² justified by the simplicity of ordinary differential equations, and the mathematically appealing form of the synthesised feedback compensator. The important point here is that with any mathematical description of a real process, model uncertainty will always be present. So, it is left to the compensator to ensure that the closed loop system remains insensitive to variations due to disturbances and noise.

In classical SISO feedback theory, this type of compensator is calculated to achieve good gain and phase margins and in this way robust stabilisation is achieved indirectly. However, for multi-input multi-output (MIMO) systems, as shown by Doyle and Stein [21], there are classes of systems (typically highly coupled with bad condition number), where loop by loop phase and gain margins can be misleading when addressing the system tolerance to uncertainties - and helicopter models often belong to this class of plants. Consider, for example, a typical quasi-static representation of a helicopter model G taken from [34], the singular values of which have been scaled to reflect output decoupling requirements (see Figure 1.1). The condition number $k(G(j\omega))$ (shown in Figure 1.2 as a function of frequency

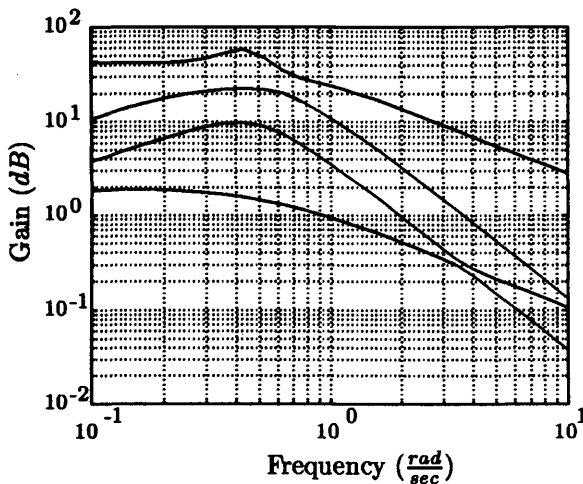


Figure 1.1 *Singular values of the model G*

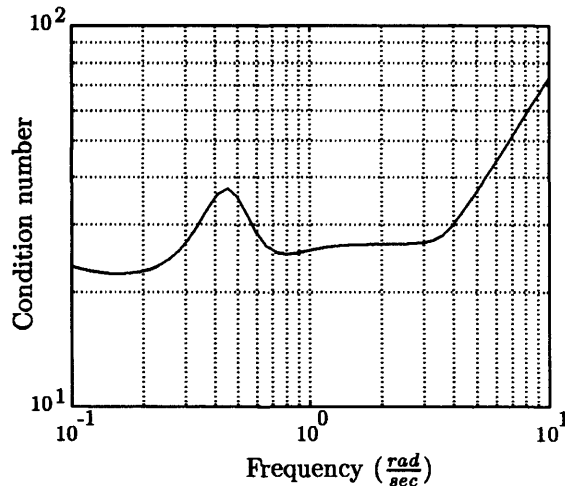


Figure 1.2 *Condition number of the model G*

ω) is relatively large, which indicates that the closed loop system may be sensitive to multi-input uncertainty³. That is, a small change in the input signal u can have a significant effect on the performance of the closed loop system. Thus, if the controller does not reject disturbances and noise, we may end up with a closed loop system that is either sensitive to perturbations or requires an unrealistic amount of control effort to achieve the desired performance. This is certainly the case with inverse or SVD-based controllers and there

²Higher order dynamics such as flexible modes and non-stationary aerodynamics are difficult to model, as well as too expensive to estimate using wind tunnels or flight tests.

³Admittedly, this uncertainty may not occur in practice, however, it is the probability of small disturbances entering at the input of G that makes the argument valid.

are several examples in the literature supporting this argument [63, ch3]. The ADOCS program mentioned earlier, is a good example of the system sensitivity to perturbations. The control law used inverse dynamics to cancel out the high order rotor states and PI feedback loops to compensate for the rigid body motion. One of the key-findings of that work was that accurate modelling of the rotor dynamics was critical to the success of these designs. The same argument is also valid for controllers designed with optimal methods. Despite the ability of the latter to handle multivariable plants in a more systematic way than their PID counterparts, they do not always guarantee tight bounds on internal and exogenous disturbances.

One of the most successful controller synthesis methods which addresses the robustness problems mentioned above is the Loop Shaping Design Procedure (LSDP) of McFarlane and Glover [45]. The method provides a stabilising controller while minimising the worst energy gain (H_∞ -norm) of the transfer functions from the disturbances d to the plant inputs and outputs (u and y in Figure 1.3 respectively). In this H_∞ framework, the perturbed

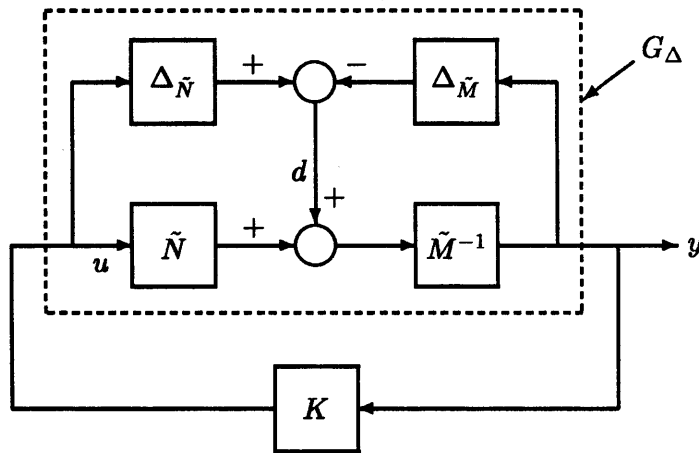


Figure 1.3 One degree of freedom configuration

plant model is represented by a normalised left coprime factorisation

$$G_\Delta(s) := (\tilde{M}(s) + \Delta_{\tilde{M}}(s))^{-1}(\tilde{N}(s) + \Delta_{\tilde{N}}(s)) \quad (1.1)$$

where $\tilde{M}^{-1}(s)\tilde{N}(s) = G(s)$ is the nominal plant, $\Delta_{\tilde{M}}(s), \Delta_{\tilde{N}}(s)$ are bounded, stable unknown transfer functions representing uncertainty, which satisfy $\|\Delta_{\tilde{N}}(s), \Delta_{\tilde{M}}(s)\|_\infty < \epsilon, \epsilon > 0$. We shall see later, in chapter 2, how this set-up enables disturbance and noise rejection to be achieved. For the moment, we just point out that the system in Figure 1.3 represents a broad range of plants and the controller K provides *guaranteed* robust stability against the perturbations $\Delta_{\tilde{M}}(s), \Delta_{\tilde{N}}(s)$. This property of the LSDP controller is of central importance in this thesis. It allows us, in chapter 3, to synthesise a robust controller for a highly uncertain model of the Bell 205 helicopter. In fact, the model we will use is just a set of body equations, derived with the Bell stabiliser bar on, with no knowledge of any rotor dynamics.

In [46], McFarlane and Glover introduce performance requirements are using two weighting functions, namely the pre- and post- compensators $W_1(s)$, $W_2(s)$, in order to modify the open loop singular values of the model $G(s)$. Guidelines for the choice of the pre- and post- compensator parameters are given by Freudenberg in [28] and Hyde in [56]. In this way, a controller can be designed using classical loop shaping ideas, while the robust stabilisation solution ensures that robust properties against the perturbations $\Delta_{\tilde{M}}(s)$, $\Delta_{\tilde{N}}(s)$ are achieved - subject to an $\|\cdot\|_\infty$ -norm being small. Furthermore, it was shown by Sefton [60] that the controller can be written as an exact observer and a state feedback, the form of which is appealing for real time implementation. This idea was very successfully used by Hyde in [56, 39] to implement a set of gain scheduled H_∞ controllers on the VAAC Harrier aircraft [42].

The VAAC Harrier experience was important in demonstrating the application of multivariable control to fixed-wing aircraft. The controller tackled successfully the nonlinear behaviour of the Harrier from hover to wing-borne flight. However, it did not exploit the full potential of the H_∞ methodology. By “potential” we mean the ability of the LSDP controller to “handle” a poorly modelled, highly coupled plant. This is because the control law was designed around the longitudinal motion of the aircraft stabilising pitch rate/flight path and airspeed. These variables are largely independent in forward flight and the frequencies around which pilots “close the loop” are far apart. This means that the workload associated with the left and right hand inceptors is largely independent and therefore “tolerable” by the human operator. Of course, in the hover regime the cross-axis coupling is significant, but pilots do not fly in this flight condition for extended periods anyway. In addition, the Harrier aircraft is a low angle-of-attack airplane, which makes unsteady aerodynamic effects easier to predict. Thus, the overall aircraft nonlinear behaviour can be modelled “reasonably well” and the robustness of the H_∞ controller is less of an issue.

In the rotary wing area, a number of H_∞ methods have been used to design control laws for helicopters, namely mixed sensitivity [69, 77] and two degrees-of-freedom (DOF) loop shaping [78, 73, 27]. The two DOF methodology, has emerged as the most suitable method, to-date, for the helicopter control problem. With the resulting controller it is possible to guarantee robustness, to use the implementation of an exact observer, and to incorporate handling qualities requirements as required by the Aeronautical Design Standard ADS-33 [2, 3]. In real flight, however, these nice properties may not be valid. The guidelines for the choice of the weighting function W_1 and W_2 are provided in terms of gain requirements around the frequencies of the model right-half-plane zeros and poles. Thus, these guidelines are most effective on plant models that are “reasonably accurate”. This is particularly relevant to rotary wing vehicles, where the uncertainty in the aerodynamic parameters of the linear time-invariant representations, can lead to poor models and possibly inappropriate performance weights. In addition, apart from the Harrier flight tests discussed earlier, there is no other indication that the unstructured uncertainty model of the normalised coprime

factors is a useful representation of unmodelled dynamics in hovering flight.

The experiments presented in chapters 4 and 5 address these questions in both qualitative and quantitative ways, using pilot opinion and data analysis, respectively. One of the findings, for example, suggests that we can use different linear time-invariant models to synthesise two controllers, which achieve similar HQRs in flight, however, the weighting functions in the H_∞ syntheses can be different. In addition, when the design model includes detailed information about high order rotor dynamics, the resulting compensator is more robust to noisy feedback signals and more sensitive to gain variations, than a controller designed only with rigid body measurements, during the design process.

Considerable attention will also be paid in analysing the effects of the other aircraft systems to the perceived handling qualities. The pilot has to assess the control law under the influence of inceptor functionality, environmental conditions, visual cues, instrument readings, etc. All these factors may mask the actual controller performance and it can be difficult, even during the post flight analysis, to identify the flying qualities due to the H_∞ controller alone. For example, depending on how much acceleration is achieved during a manoeuvre, test pilots can return different HQRs when evaluating the same controller with different right hand inceptors. Despite these practical difficulties, the control law behaviour is “transparent” to the pilot and the returned HQRs allow us to significantly improve both the controller robustness and performance.

1.2 Summary of contents

Details of the mathematical notation used, are given at the end of the introductory chapter. This contents of this thesis are outlined below:

Chapter 2: In the first part of this chapter, we collect together some useful properties of H_∞ loop shaping, which demonstrate how robustness and disturbance rejection are achieved with this method. Sections 2.2 and 2.3, highlight some important aspects of the original Loop Shaping Design Procedure, such as the guaranteed stability margin and the weighting function selection. Section 2.4 introduces the two DOF methodology, which allows us to include time domain requirements in the controller design process. This allows us to design a two DOF H_∞ controller in section 2.5, the architecture of which accommodates different response types required in rotary wing flight control systems.

Chapter 3: The chapter begins with a presentation of the dynamics of the Bell 205 helicopter. Section 3.2, describes the quasi-static linear time-invariant mathematical model, alongside possible feedback strategies, modes of motion, and the Bell 205 stabiliser bar effects on the aircraft responses. This allows us to achieve two goals in section 3.3. Firstly, it is possible to explain the differences between the quasi-static models and flight test data,

in both time and frequency domains. Secondly, it allows us to show, that enhancing the quasi-static models with *Padé* approximations to the time delay can benefit a great deal the control law design. Section 3.4 describes controller structure for real time implementation. In section 3.5, we develop a two DOF H_∞ loop shaping controller for the Bell 205 helicopter, and in section 3.6 we present the preliminary findings from investigating the controller functionality on the Large Motion Simulator at DERA, Bedford. The chapter concludes with section 3.7, which discusses the results and gives useful guidelines for designing prototype flight control laws.

Chapter 4 This chapter concentrates on the in-flight evaluation of the H_∞ controller designed in the previous chapter. Section 4.1, gives a general overview of the characteristics of the Bell 205 experimental aircraft, and section 4.2 describes the real time implementation of the controller and the conditions at the time of the flight test. Then, in section 4.3, we present the pilot comments after a full controller evaluation according to the ADS-33 standard manoeuvres, which are analysed quantitatively in section 4.4 using the recorded flight test data. The chapter concludes with 4.5, which discusses the flight test and proposes several modifications to the overall flight control system to enhance the observed performance.

Chapter 5 Building on the proposed modifications from the previous chapter, we use in-flight evaluation of three newly designed controllers to: assess the effect of the rotor dynamics on the controller performance; compare the original LSDP methodology with the two DOF loop shaping and improve the handling qualities ratings (i.e. the perceived controller performance). Section 5.3, compares the new high order models with the flight test data, and section 5.4 describes the design of the new control laws for the Bell 205 aircraft. In section 5.5, the flight test results are presented and in section 5.7, it is shown that successful controller implementation, (at least in the continuous time case), requires the ratio of the largest to the smallest controller eigenvalues to be “reasonably small”. The chapter is summarised in section 5.6, and motivates “intelligent” gain scheduling algorithms, as a means of extending the operation of linear multivariable controllers.

Chapter 6 In chapter 6, a general interpolation and robust control framework is formulated. The chapter discusses, stability interpolation methods, right coprime factorisation, and gap metric results in section 6.2. In section 6.3, the proposed performance based gain-scheduling methodology is presented; the observer based controller structure is discussed, and a three-step optimisation approach to gain-scheduling is presented. In section 6.4, we apply the results of the proposed design methodology to the Lynx Mk7 high performance helicopter; the justification of the selected blending region and a robustness/gap metric analysis of the results are also discussed. Finally, in section 6.5, concluding remarks are briefly discussed.

Chapter 7 draws together the main conclusions and contributions of this thesis. Suggestions for further work are also given.

1.3 Notation

All systems considered are linear, time-invariant and finite-dimensional. A (proper) transfer function (matrix) is represented in terms of state-space data as:

$$\left[\begin{array}{c|c} A & B \\ \hline C & D \end{array} \right] := C(sI - A)^{-1}B + D,$$

alternatively written as (A, B, C, D) , where A, B, C and D are real valued matrices, and I is the identity matrix of appropriate dimension. If $D = 0$, the zero matrix, then the system is strictly proper, and we shall write (A, B, C) . The system is *asymptotically stable* if and only if each of the eigenvalues of the matrix A has a strictly negative real part.

1.3.1 Mathematical notation

\Re	the field of real numbers
dB	decibels: x dB represents a gain of $10^{x/20}$
$ a $	the absolute value of the real number a
A^T	the transpose of the matrix A
A^H	the transpose of the complex conjugate of matrix A
$\det(A)$	the determinant of the square matrix A
$[A]_{ij}$ or a_{ij}	the (i, j) element of the matrix A
A^{-1}	the inverse of the square matrix A
$\lambda_{max}(A)$	the largest eigenvalue of the square matrix A
$\lambda_{min}(A)$	the smallest eigenvalue of the square matrix A
ρ	model matching parameter
$\sigma_i(A)$	the i th singular value of the matrix A
$\bar{\sigma}(A)$	the largest singular value of the matrix A
$\underline{\sigma}(A)$	the smallest singular value of the matrix A
$\kappa(A)$	the condition number of A , $\bar{\sigma}(A)/\underline{\sigma}(A)$
$diag\{A\}$	a diagonal matrix A
I	identity matrix of unspecified dimension
I_n	the $n \times n$ identity matrix
j	$\sqrt{-1}$; sometimes an index, as in a_{ij}
log or \log_{10}	logarithm to base 10
A_{cl}	closed loop matrix

M_o	reference model
\tilde{M}, \tilde{N}	normalised left coprime factors
M, N	normalised right coprime factors
$\Delta(\cdot)$	Full block perturbation matrix function
ζ	scheduling variable
ζ_1, ζ_2	plant envelope
α_1, β_1	scheduling range
α, β	angles of attack and sideslip respectively
θ, ϕ, ψ	Euler angles - earth referenced
δ_{long}	longitudinal cyclic
δ_{lat}	lateral cyclic
δ_{tr}	tail rotor collective
δ_{mr}	main rotor collective
p, q, r	Angular rates - body referenced
F, H	control and filter Riccati gains
$F_l(\cdot)$	Lower linear fractional transformation
J	optimal cost function
$\lambda(\cdot), \mu(\cdot)$	scheduling functions for F and H
δ_ν	ν gap metric
γ	stability margin
γ_{uy}	coherence function relating signal u to signal y
$G(s)$	a continuous time transfer function (matrix)
$\ G\ _\infty$	$\sup_\omega \bar{\sigma}(G(j\omega))$, if G is a continuous time transfer function (matrix)
RH_∞	set of asymptotically stable transfer functions G , with $\ G\ _\infty < \infty$
T_{zw}	transfer function from signal w to signal z
\exists	'there exists'
\in	'an element of'
\forall	'for all'
\neq	'not equal to'

1.3.2 Abbreviations

AC	Attitude Command
ACAH	Attitude Command Attitude Hold
ADOCS	Advanced Digital Optical Control System
ADS	Aeronautical Design Standard
CAD	Computer Aided Design
CARE	control algebraic riccati equation
DOF	Degrees-of-Freedom

DERA	Defence Evaluation and Research Agency
FARE	filter algebraic riccati equation
FCC	flight control computer
FRL	flight research laboratory
GCARE	generalised CARE
GFARE	generalised FARE
HELISIM	helicopter simulation model
HQR	handling quality rating
LFT	linear fractional transformation
LHP	left half-plane
LQG	linear quadratic Gaussian
LSDP	loop-shaping design procedure
LTI	linear time-invariant
MIMO	multi-input multi-output
NASA	National Aeronautics Space Administration
NRC	National Research Council
PI	proportional plus integral
PID	proportional-integral-derivative
RC	Rate Command
RCAH	Rate Command Attitude Hold
RHP	right half-plane
SCAS	stability control augmentation system
SISO	single-input single-output
SVD	singular value decomposition

1.3.3 List of variable names

ALPHA	angle of attack (<i>deg</i>)
AX	acceleration in x direction (ft/sec^2)
AY	acceleration in y direction (ft/sec^2)
AZ	acceleration in z direction (ft/sec^2)
BETA	sideslip angle (<i>deg</i>)
COLACT	collective actuator position (<i>in</i>)
CPA	lateral stick sensitivity (non dimensional)
CPC	pedal stick sensitivity (non dimensional)
CPB	longitudinal stick sensitivity (non dimensional)
DANET	lateral filtered stick inputs (<i>in</i>)
DENET	longitudinal filtered stick input (<i>in</i>)
DPNET	collective stick filtered input (<i>in</i>)

DRNET	pedal stick filtered input (<i>in</i>)
FDA	lateral actuator deflection (<i>in</i>)
FDE	longitudinal actuator deflection (<i>in</i>)
FDP	collective actuator deflection (<i>in</i>)
FDR	pedal actuator deflection (<i>in</i>)
HMIX	indicated height (<i>ft</i>)
HRA	radar altitude (<i>ft</i>)
LHACT	left hand actuator position (<i>in</i>)
P	roll rate (<i>deg/sec</i>)
PDYN	dynamic pressure (<i>psf</i>)
PHI	roll attitude (<i>deg</i>)
PMIX	mixed roll rate (<i>deg/sec</i>)
PSI	heading angle (<i>deg</i> from North)
PSTAT	static pressure (<i>psf</i>)
Q	pitch rate (<i>deg/sec</i>)
QMIX	mixed pitch rate (<i>deg/sec</i>)
R	yaw rate (<i>deg/sec</i>)
RHACT	right hand actuator positions (<i>in</i>)
RMIX	mixed yaw rate (<i>deg/sec</i>)
SACLA	lateral stick input (<i>in</i>)
SACLE	longitudinal stick input (<i>in</i>)
SACR	pedal stick input (<i>in</i>)
SACP	collective stick input (<i>in</i>)
TAS	true airspeed (<i>knots</i>)
THETA	pitch attitude (<i>deg</i>)
TRACT	pedal positions (<i>in</i>)
TTOT	Total temperature (<i>deg K</i>)
UMIX	mixed airflow forward velocity (<i>ft/sec</i>)
UDOT	forward velocity derivative (<i>ft/sec²</i>)
UDMIX	mixed airflow longitudinal velocity derivative (<i>ft/sec²</i>)
VMIX	mixed airflow lateral velocity (<i>ft/sec</i>)
VDOT	lateral velocity derivative (<i>ft/sec²</i>)
VDMIX	mixed airflow lateral velocity derivative (<i>ft/sec²</i>)
WMIX	mixed airflow vertical velocity (<i>ft/sec</i>)
WDOT	vertical velocity derivative (<i>ft/sec²</i>)
WDMIX	mixed airflow vertical velocity derivative (<i>ft/sec²</i>)

2.1 H_∞ loop shaping

In the previous chapter, we motivated the use of normalised coprime factors as a means of representing modelling uncertainty. In this chapter we will see how this uncertainty model leads to disturbance rejection in real systems. Of course, disturbances will always be present in the form of exogenous perturbations (wind gusts, atmospheric variations, etc.), or as parametric uncertainty (mechanical defects, sensor accuracy, etc.). In practice, these disturbances need to be bounded by some realistic value. To illustrate this idea in control terms, consider the configuration of Figure 2.1. In this Figure, d_u and d_n represent parametric uncertainties at the actuators and measurements, whilst d_y is a vector of exogenous disturbances. If the disturbance d_y is bounded, the total energy $\int_0^\infty d_y(t)^\tau d_y(t) dt$, injected

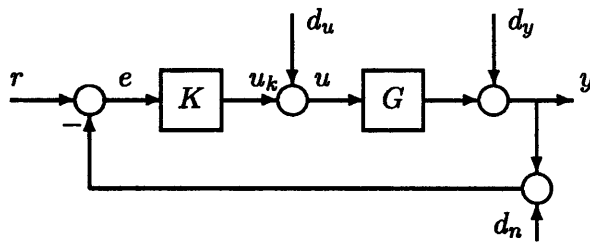


Figure 2.1 *Feedback control configuration with disturbances*

into the system by the signal d_y , is finite. Thus, the energy gain from d_y to the y can be written as $\frac{\int_0^\infty y(t)^\tau y(t) dt}{\int_0^\infty d_y(t)^\tau d_y(t) dt} \Big|_{d_y(t) \neq 0}$, and it is a measure of the disturbance effects on the system. Taking the square root of the maximum energy gain from d_y to y , it is possible to write that

$$\sup_{d_y(t) \neq 0} \left(\frac{\int_0^\infty y(t)^\tau y(t) dt}{\int_0^\infty d_y(t)^\tau d_y(t) dt} \right)^{0.5} = \sup_{\omega \in \mathbb{R}} \bar{\sigma}(S_o(j\omega)) := \|S_o(j\omega)\|_\infty \quad (2.1)$$

That is, we can express the effect of the exogenous disturbances d_y to y via a bound on the infinity norm of the corresponding transfer function $S_o(s) = (I + G(s)K(s))^{-1}$. In

equation (2.1), $\bar{\sigma}(S_o(j\omega))$ denotes the maximum singular value of the transfer function S_o ¹. If the feedback configuration of Figure 2.1 is internally stable², the equations describing the system can be written as:

$$y = T_o(r - d_n) + S_o G d_u + S_o d_y \quad (2.2)$$

$$u_k = K S_o(r - d_n) - K S_o d_y - T_i d_u \quad (2.3)$$

$$r - y = S_o(r - d_y) + T_o d_n - S_o G d_u \quad (2.4)$$

$$u = K S_o(r - d_n) - K S_o d_y + S_i d_u. \quad (2.5)$$

Here, $S_i = (I + KG)^{-1}$, $S_o = (I + GK)^{-1}$, $T_i = KG(I + KG)^{-1}$ and $T_o = GK(I + GK)^{-1}$ are the input, output, complementary input and complementary output sensitivities respectively. These transfer functions relate the disturbances to the internal signals u , u_k , y and $r - y$. Thus, by minimising the energy gains, as expressed by the $\|\cdot\|_\infty$ norms of S_i , S_o , T_i and T_o , we minimise the effects of the disturbances on the system. We can see from equation (2.3) for example, that to achieve high tolerance against the perturbation d_u , it is necessary to minimise the maximum energy gains $\sup_{d_u(t) \neq 0} \left(\frac{\int_0^\infty u_k(t)^T u_k(t) dt}{\int_0^\infty d_u(t)^T d_u(t) dt} \right)^{0.5}$ and $\sup_{d_u(t) \neq 0} \left(\frac{\int_0^\infty u(t)^T u(t) dt}{\int_0^\infty d_u(t)^T d_u(t) dt} \right)^{0.5}$, which is equivalent to minimising the infinity norms of both the input and the complementary input sensitivity functions $\|S_i\|_\infty$ and $\|T_i\|_\infty$.

The solution of such an energy gain minimisation problem, however, is not a straightforward task. Disturbance rejection requirements conflict at some frequencies since the disturbance signals contribute energy over the whole frequency spectrum. A popular paradigm for handling conflicting requirements is to minimise both the output and complementary output sensitivities. Their complementary nature, ($S_o = I - T_o$), shows that it is impossible to make S_o and T_o small at the same frequency. However, from the physics of a control system it is possible to discriminate between low and high frequency energy gains at the input, output and sensor points of Figure 2.1. For flight control systems, for example, the disturbances at the sensors are most critical at high frequencies. This motivates the use of weighting functions to impose frequency dependent constraints on the minimised energy gains. Consider, for example, two low-pass filters W_s and W_t . Then,

$$\|W_s S_o\|_\infty \quad (2.6)$$

enforces tracking and disturbance attenuation at low frequencies, whereas

$$\|W_t^{-1} T_o\|_\infty \quad (2.7)$$

ensures that high frequency sensor noise will be rejected.

The disturbance rejection requirements at the model input, output and measurements can also be stated in terms of singular value gains of the loop transfer functions $L_o = GK$

¹In the sequel the dependence on the Laplace operator "s" is dropped for brevity.

²For a definition of internal stability see [80, ch1, ch5]

and $L_i = KG$. The minimisation of $\|(I + GK)^{-1}\|_\infty$ for example, requires that $\sigma(GK)$ is large at frequencies where disturbance d_y is significant. Similarly, to reduce the effects of the perturbations d_u on the plant output y , it is necessary to achieve large $\sigma(K)$ in the frequencies where d_u is important. The conflicting requirements can also be expressed via the transfer functions L_o and L_i . Examining equation (2.2) it is possible to deduce that achieving large $\sigma(GK)$ can amplify the sensor disturbances d_n , if the frequencies over which $\sigma(GK) \gg 1$ exceed (or are close to) the sensor bandwidth. This is because $\sigma(GK) \gg 1 \Leftrightarrow \bar{\sigma}(S_o) \ll 1$, which implies that $y = T_o(r - d_n) + S_o G d_u + S_o d_y \approx (r - d_n)$. Similarly, equation (2.5) shows that if $\sigma(GK)$ is larger than the achievable aircraft bandwidth, the controller K will amplify any disturbances and sensor noise since $u = K S_o(r - d_n - d_y) - T_i d_u = S_i K(r - d_n - d_y) - T_i d_u \approx G^{-1}(r - d_n - d_y) - d_u$.

In summary, to meet the performance and robustness requirements for Figure 2.1, a controller K should be designed such that it minimises

$$\bar{\sigma}(K(I + GK)^{-1}), \bar{\sigma}((I + GK)^{-1}), \bar{\sigma}((I + GK)^{-1}G), \bar{\sigma}((I + KG)^{-1}) \quad (2.8)$$

at low frequencies and

$$\bar{\sigma}(GK(I + GK)^{-1}), \bar{\sigma}(KG(I + KG)^{-1}) \quad (2.9)$$

at high frequencies. In terms of the loop gain functions this is equivalent to maximising $\sigma(GK), \sigma(KG), \sigma(K)$ at low frequencies and minimising $\bar{\sigma}(GK), \bar{\sigma}(KG)$ at high frequencies, while keeping $\bar{\sigma}(K)$ "reasonably small". These requirements are illustrated graphically in Figure 2.2, where the singular values of the loop gain function GK must avoid the shaded regions. That is, for good performance, $\sigma(GK)$ must have high gain for all frequencies below ω_l , and for good robust stability $\bar{\sigma}(GK)$ should roll-off before the shaded boundary at $\omega > \omega_h$.

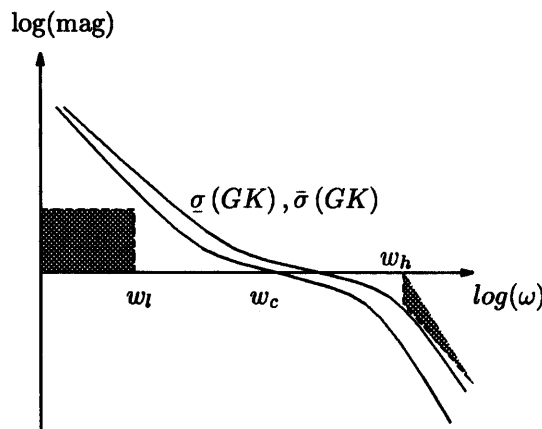


Figure 2.2 Design requirements in terms of the loop gain function GK

2.1.1 H_∞ loop shaping guarantees

The above requirements are precisely what the *Loop Shaping Design Procedure* (LSDP) of McFarlane and Glover [45, 54] tackles. Minimising³

$$\left\| \begin{bmatrix} K_\infty \\ I \end{bmatrix} (I - G_s K_\infty)^{-1} \tilde{M}_s^{-1} \right\|_\infty \leq \gamma \quad (2.10)$$

i.e. the $\|\cdot\|_\infty$ -norm of the transfer function from the input disturbances d to the signals u and y in Figure 1.3, for the weighted plant model

$$G_s = W_2 G W_1 = \tilde{M}_s^{-1} \tilde{N}_s = N_s M_s^{-1} \quad (2.11)$$

provides a stabilising controller $K = W_1 K_\infty W_2$, which guarantees that

$$\bar{\sigma} \left(K_\infty (I - G_s K_\infty)^{-1} \right) \leq \gamma \bar{\sigma} \left(\tilde{M}_s \right) \bar{\sigma} (W_1) \bar{\sigma} (W_2) \quad (2.12)$$

$$\bar{\sigma} \left((I - G_s K_\infty)^{-1} \right) \leq \min \left\{ \gamma \bar{\sigma} \left(\tilde{M}_s \right) k(W_2), 1 + \gamma \bar{\sigma} (N_s) k(W_2) \right\} \quad (2.13)$$

$$\bar{\sigma} \left(K_\infty (I - G_s K_\infty)^{-1} \right) \leq \min \left\{ \gamma \bar{\sigma} \left(\tilde{N}_s \right) k(W_1), 1 + \gamma \bar{\sigma} (M_s) k(W_1) \right\} \quad (2.14)$$

$$\bar{\sigma} \left((I - G_s K_\infty)^{-1} G_s \right) \leq \frac{\gamma \bar{\sigma} \left(\tilde{N}_s \right)}{\underline{\sigma} (W_1) \underline{\sigma} (W_2)} \quad (2.15)$$

$$\bar{\sigma} \left((I - K_\infty G_s)^{-1} \right) \leq \min \left\{ 1 + \gamma \bar{\sigma} \left(\tilde{N}_s \right) k(W_1), \gamma \bar{\sigma} (M_s) k(W_1) \right\} \quad (2.16)$$

$$\bar{\sigma} \left(G_s (I - K_\infty G_s)^{-1} K \right) \leq \min \left\{ 1 + \gamma \bar{\sigma} \left(\tilde{M}_s \right) k(W_2), \gamma \bar{\sigma} (N_s) k(W_2) \right\} \quad (2.17)$$

In equation (2.11) the nominal plant model G is cascaded with two weighting functions W_1, W_2 and expressed via its left and right normalised coprime factorisations. By “normalised” we mean that

$$\tilde{M}_s \tilde{M}_s^* + \tilde{N}_s \tilde{N}_s^* = I \quad (2.18)$$

for the left coprime factors, and

$$M_s^* M_s + N_s^* N_s = I \quad (2.19)$$

for the right coprime factorisation⁴. In the case of a strictly proper weighted plant $G_s = [A_s, B_s, C_s, 0]$, it is a well known fact that the left coprime factors $[\tilde{N}_s, \tilde{M}_s]$ can be obtained as

$$[\tilde{N}_s, \tilde{M}_s] = \left[\begin{array}{c|cc} A_s + H C_s & B_s & H \\ \hline C_s & 0 & I \end{array} \right]. \quad (2.20)$$

Here, $H = -Z C_s^*$, where Z is the solution to the *Generalised Filtering Algebraic Riccati Equation* (GFARE)

$$A_s Z + Z A_s^T - Z C_s^T C_s Z + B_s B_s^T = 0 \quad (2.21)$$

³Positive feedback arrangement is used in Figure 1.3.

⁴Note that the additive uncertainty, against which the model is stabilised, is different for the left and the right coprime factorisations. However, the minimum of the left hand side of equation (2.10) is the same in both formulations. “*” denotes the complex conjugate transpose operator.

Note that the maximum singular values of the normalised coprime factors $\bar{\sigma}(N_s)$, $\bar{\sigma}(M_s)$, $\bar{\sigma}(\tilde{N}_s)$, $\bar{\sigma}(\tilde{M}_s)$ can be expressed via the weighted plant model [75, ch18], [80, ch16]:

$$\bar{\sigma}(N_s) = \bar{\sigma}(\tilde{N}_s) = \left(\frac{\bar{\sigma}(G_s)^2}{1 + \bar{\sigma}(G_s)^2} \right)^{\frac{1}{2}} \quad (2.22)$$

$$\bar{\sigma}(M_s) = \bar{\sigma}(\tilde{M}_s) = \left(\frac{1}{1 + \underline{\sigma}(G_s)^2} \right)^{\frac{1}{2}} \quad (2.23)$$

Thus, equations (2.12) - (2.23) show that all the disturbances in Figure 2.1 are bounded in magnitude; and the tightness of these bounds depends on the weighting functions W_1 and W_2 , the nominal plant G and the achievable γ in equation (2.10). In terms of the loop gain functions $\bar{\sigma}(GK)$ and $\underline{\sigma}(KG)$, Glover and McFarlane show that the controller $K = W_1 K_\infty W_2$ bounds the degradation of the specified loop shape $G_s = W_2 G W_1$ both at the plant input and output. This degradation is no more than

$$\underline{\sigma}(KG) = \underline{\sigma}(W_1 K_\infty W_2 G) = \underline{\sigma}(W_1 K_\infty W_2 G W_1 W_1^{-1}) \geq \frac{\underline{\sigma}(W_2 G W_1) \underline{\sigma}(K_\infty)}{k(W_1)} \quad (2.24)$$

at the plant input u and

$$\underline{\sigma}(GK) = \underline{\sigma}(G W_1 K_\infty W_2) = \underline{\sigma}(W_2^{-1} W_2 G W_1 K_\infty W_2) \geq \frac{\underline{\sigma}(W_2 G W_1) \underline{\sigma}(K_\infty)}{k(W_2)}. \quad (2.25)$$

at the plant output y . Of course, one can argue that these bounds may not be tight because they depend on the condition numbers of the weights W_1 and W_2 . Experience has shown, however, that high order weighting functions give very little advantage in terms of desired loop shapes GK and KG , while they significantly increase the order of the resulting dynamic compensator $K = W_1 K_\infty W_2$. Thus, low order weights with small condition numbers $k(W_1)$ and $k(W_2)$ are very common in loop shaping and this will be evident in all the controller designs in this thesis. Finally, in equations (2.24) and (2.25), the minimum singular values $\underline{\sigma}(K_\infty)$, are bounded by functions of $\underline{\sigma}(G_s)$ and γ . This is a central result in [46, ch6] and it is formally stated below:

Theorem 1 Any controller, K_∞ , minimising $\left\| \begin{bmatrix} K_\infty \\ I \end{bmatrix} (I - G_s K_\infty)^{-1} \tilde{M}_s^{-1} \right\|_\infty$, also satisfies

$$\underline{\sigma}(K_\infty(j\omega)) \geq \frac{\underline{\sigma}(G_s(j\omega)) - \sqrt{\gamma^2 - 1}}{\sqrt{\gamma^2 - 1} \underline{\sigma}(G_s(j\omega)) + 1} \quad (2.26)$$

$\forall \omega$ such that $\underline{\sigma}(G_s(j\omega)) > \sqrt{\gamma^2 - 1}$.

Note that the plant G_s in the above theorem is assumed to be square for the bound to be strictly valid.

We are now ready to summarise the Loop Shaping Design Procedure as developed by McFarlane and Glover:

1. Utilising the weighting functions W_1 and W_2 give a desirable shape to the shaped plant given by $G_s = W_2GW_1$, where G is the nominal plant model. W_1, W_2 must be chosen such that G_s does not contain any unstable hidden modes.
2. Synthesise the stabilising controller K_∞ by minimising

$$\left\| \begin{bmatrix} K_\infty \\ I \end{bmatrix} (I - G_s K_\infty)^{-1} \tilde{M}_s^{-1} \right\|_\infty \quad (2.27)$$

3. Calculate the final feedback controller as $K = W_1 K_\infty W_2$.

Despite the simplicity of the above algorithm steps there are important practical aspects of multivariable loop shaping that the designer should take into account in order to arrive at a successful design. The following sections summarise the most important design considerations.

2.2 Scaling

The open loop model inputs and outputs are scaled so that they reflect the desired (or achievable) actuator usage and output decoupling. A popular form of input-output scaling is to normalise all the signals with respect to unity. A well-scaled system will have singular values closer to each other compared to the original plant. However, the designer must ensure that scaling does not change significantly the directionality of the model G . This is particularly important for ill-conditioned plants as it can result in large gains being injected in the wrong directions, which makes robust stabilisation even more difficult to achieve.

2.3 Weight selection

The philosophy of choosing a pre-compensator is to maximise as much as possible the feedback loop bandwidth, within the actuator constraints. Specifying a “desirable” weighting function W_1 involves the introduction of integral action at low frequencies of the plant G , to reduce steady-state error, and to ensure good output tracking performance. In the case of a rate command system double integrators are commonly used to boost the low frequency gain of the rate signal. The pre-compensator is also utilised to introduce robust stability considerations in to the design procedure. This is achieved by introducing zeros around the frequency of any right half plane (RHP) zeros, large gain around the frequency of any RHP poles, and lead compensation to improve the phase response of the system.

This choice is easily justifiable in the classical feedback theory since the magnitude of a stable SISO transfer function L , around the cross-over ω_o , is directly related to the phase margin (and therefore robust stability) of the system, via⁵ $\pi + \angle L(j\omega_o)$. Thus, for a stable

⁵This property carries through to the MIMO case to the degree that the system is diagonally dominant.

system L , the angle $\angle L(j\omega_0)$ can be written as the sum of the phase contributed by the minimum and non-minimum phase components [12, 22]:

$$\angle L(j\omega_0) = \underbrace{\frac{1}{\pi} \int_{-\infty}^{\infty} \frac{\overbrace{\frac{d \ln |L|}{d\nu}}^{\text{Slope of } |L(j\omega)|}}{d\nu} \operatorname{Incoth} \frac{|\nu|}{2} d\nu}_{\angle L_{\min.\text{phase}}(j\omega_0)} + \underbrace{\sum_{i=1}^n \angle \frac{-j\omega_0 + z_i}{j\omega_0 + z_i}}_{\angle L_{\text{non-min.}\text{phase}}(j\omega_0)} \quad (2.28)$$

In the above generalised version of Bode's integral formula, the attenuation rate $\frac{d \ln |L|}{d\nu}$, around the cross over ω_0 , should be no more than 20 db/decade if robust stability/performance are to be maximised. If the zero in the pre-compensator is much higher than the frequency of the loop bandwidth, there is a strong possibility of large control effort being exerted. To avoid this situation, it is necessary either to lower the loop bandwidth, and therefore to compromise performance, or to improve the model around the cross-over region ω_0 . If the first choice is taken and the nominal plant is unstable, it is important not to reduce the gain in the feedback loop too much as the system may be destabilised. Further analysis about the limitations imposed by RHP poles and/or zeros can be found in [63, ch5] and the references therein.

It is important to note here that the RHP zeros z_1, z_2, \dots, z_n impose severe limitations on the robustness properties of the closed loop system. This is due to the phase lag they introduce, which reduces the achievable phase margin. For example, a first order Padé approximation of a time delay e^{-sT} within a model, introduces a RHP zero at $Tz - 2 = 0 \Leftrightarrow z = 2/T$, and therefore, a phase lag of

$$\phi = \angle \frac{-j\omega_0 + z_i}{j\omega_0 + z_i} \bigg|_{\omega_0 = \frac{(2/T)}{4}} = 28^\circ \quad (2.29)$$

at $\omega_0 = \frac{(2/T)}{4} \text{ rad/sec}$.

As with the weight W_1 , the post-compensator W_2 can contain dynamic elements. One can argue that high gain at low frequencies via integrators can be implemented within the post-compensator; it also appears that in this way the designer avoids the difficulties associated with the input directionality of the plant. In practice, however, this can result in high frequency sensor noise being amplified. Choosing the W_2 as first order low pass filters ensures that noisy measurements, above a desirable cut-off frequency, will not enter the feedback loop. In most design examples we will use an identity matrix for W_2 weighting function. This may appear to be a limitation, but for many applications the singular value roll-off rates are adequate to provide the required disturbance rejection at high frequencies.

2.4 Incorporating time domain specifications

Incorporating time domain requirements into the Loop Shaping Design Procedure is not a straightforward task. Although the position of the zeros in the weighting functions governs

the rise time and damping of the output response, there is no explicit relationship that uniquely determines the required gain guaranteeing desirable closed loop response characteristics. To alleviate this problem one can introduce time domain specifications via an appropriately designed prefilter K_1 so that the closed loop system tracks an ideal step response model M_o . To find such a prefilter, one can use the standard Doyle and Glover algorithm in H_∞ theory [20], to minimise a weighted cost of the form

$$\|W(T_{r \rightarrow y}K_1 - M_o)\|_\infty \leq \gamma \quad (2.30)$$

where $T_{r \rightarrow y}$ is the closed loop transfer function in Figure 2.1, M_o is defined according to some time domain specifications, and W a weighting function used to penalise the difference $T_{r \rightarrow y}K_1 - M_o$ at frequencies where tracking requirements are important. This generic⁶ method provides the designer with the freedom to tackle disturbance rejection and tracking requirements independently. However, it can lead to controllers of large dimensions since the prefilter requires extra weights to enforce the model matching cost of equation (2.30).

The two degrees-of-freedom (DOF) design procedure as introduced in [38, 18] guarantees robust stability in the face of an ideal step response model and it does not significantly increase the controller dimension. This is because both feedback controller and prefilter are designed within a single design procedure, while the designer retains the freedom to specify disturbance rejection and tracking requirements separately. Figure 2.3 illustrates the block diagram of the two DOF setup. The closed loop response from the reference signals to the plant outputs follows that of a specified model M_o . The controller K is partitioned as $K = [K_1 \ K_2]$, where K_1 is the prefilter and K_2 is the feedback controller. The inner feedback controller K_2 is used to meet the robust stability requirements while the prefilter K_1 optimises the overall system to the command input. The use of the step response model is to ensure that

$$\|(I - G_s K_2)^{-1} G_s K_1 - M_o\|_\infty \leq \gamma \rho^{-2}, \quad (2.31)$$

where ρ is the model-matching parameter. From equation (2.31) it is obvious that as ρ increases $(I - G_s K_2)^{-1} G_s K_1 \rightarrow M_o$. By setting ρ equal to zero the two DOF setup reduces to the one DOF problem described earlier. The design cycle, given a plant with no direct feed-through term, can be described as follows⁷:

1. Select a pre-compensator W_1 according to the guidelines given in section 2.3. Note that in this two DOF setup W_2 must be a constant matrix. If we use dynamic W_2 , equation (2.31) implies that H_∞ optimisation forces the weighted output response to track the ideal model M_o .

⁶In the sense that it can readily accommodate unstable models.

⁷In [38] the algorithm iterates on two Riccati equation solutions, although one of those solutions should be zero. For more details see [72].

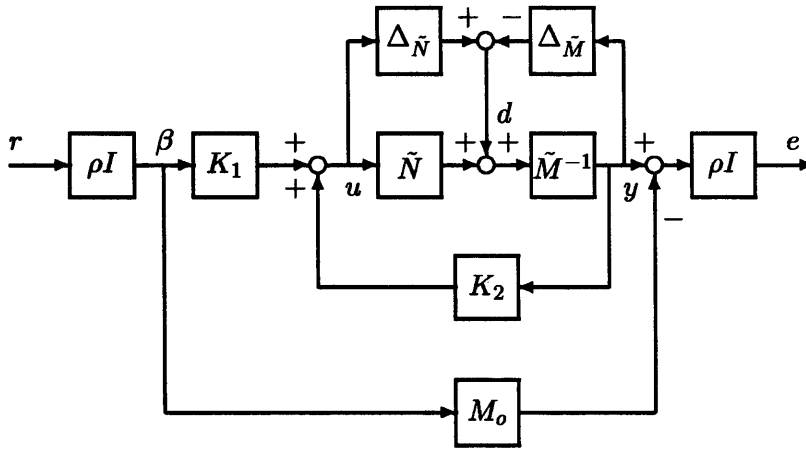


Figure 2.3 Two degrees-of-freedom configuration

2. Select a desired closed-loop transfer function M_o between the commands and controlled outputs.
3. Set the scalar parameter ρ to a small value greater than 1; in practice something in the range 1 to 3 will usually suffice. Very high values of ρ can lead to high γ values and therefore less tight bounds on the loop disturbances as shown in equations (2.12)-(2.17).
4. Using the state space representations of the plant coprime factors (see equation (2.20)) and the ideal model $M_0 = [A_0, B_0, C_0, 0]$, form the generalised plant P in the standard control configuration of Figure 2.4. In this Figure, P relates the control and the exogenous

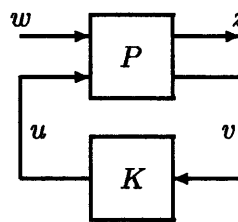


Figure 2.4 General control configuration

signals (u and r, d) to the the measured and the error variables ($\rho r, y$ and u, y, e). The equations governing the plant P can be written as

$$\begin{bmatrix} z \\ v \end{bmatrix} = \begin{bmatrix} P_{11} & P_{12} \\ P_{21} & P_{22} \end{bmatrix} \begin{bmatrix} w \\ u \end{bmatrix} \quad (2.32)$$

in transfer function form, or as

$$\begin{bmatrix} \dot{x} \\ x_0 \\ u \\ y \\ z \\ \rho r \\ y \end{bmatrix} = \underbrace{\begin{bmatrix} A_s & 0 & 0 & -H & B_s \\ 0 & A_o & B_o & 0 & 0 \\ 0 & 0 & 0 & 0 & I \\ C_s & 0 & 0 & I & 0 \\ \rho I & -\rho^2 C_o & 0 & \rho I & 0 \\ 0 & 0 & \rho I & 0 & 0 \\ C & 0 & 0 & I & 0 \end{bmatrix}}_P \begin{bmatrix} x \\ x_0 \\ r \\ d \\ u \end{bmatrix} \quad (2.33)$$

with state space elements.

5. Solve the standard H_∞ optimisation problem for the plant P using standard H_∞ optimisation routines [9]. The resulting controller equations may be written as an exact plant observer and a state feedback

$$\begin{bmatrix} \dot{\hat{x}} \\ \hat{x}_0 \end{bmatrix} = \begin{bmatrix} A_s + HC_s - B_s B_s^T X_{\infty 11} & -B_s B_s^T X_{\infty 12} \\ 0 & A_o \end{bmatrix} \begin{bmatrix} \hat{x} \\ x_0 \end{bmatrix} + \begin{bmatrix} 0 & -H \\ \rho B_o & 0 \end{bmatrix} \begin{bmatrix} r \\ y \end{bmatrix} \quad (2.34)$$

and

$$u = -B_s^T [X_{\infty 11} \quad X_{\infty 12}] \begin{bmatrix} \hat{x} \\ x_0 \end{bmatrix} \quad (2.35)$$

where $X_\infty = [X_{\infty 11} \quad X_{\infty 12}]$ is the partitioned generalised (according to the generalised plant P) control Riccati equation solution. The reader can refer to [45], [63, ch9] for more information on the algebraic Riccati equations in H_∞ control and loop shaping synthesis.

6. Partition the controller to a prefilter K_1 and a feedback controller K_2 . The prefilter K_1 is also scaled with a gain matrix $S_f = K_1^{-1}(0) \cdot K_2(0)$. This has been found to increase the speed of the system's response and to force the closed loop transfer function $(I - G_s K_2)^{-1} G_s K_1$ to match the unit matrix at steady-state.

Remark 2.4.0.1 *The achieved minimum cost function in equation (2.30), in practice, is chosen slightly suboptimal. This is for two reasons. Firstly, (and most importantly), only a suboptimal controller can be written in an observer-based form (see [60]). Secondly, often the H_∞ cost minimisation provides compensators with high frequency dynamics (i.e. very fast stable poles), which impose severe limitations on numerical realisation of the controller⁸. An intuitive explanation of this is that, since the closed loop transfer function $T_{w \rightarrow z}$ (from exogenous signals w to the error z in Figure 2.4) tends to be all-pass, ($T_{w \rightarrow z} T_{w \rightarrow z}^* = I$ see [16]), the controller tries to compensate for the plant dynamics at a wide range of frequencies. Therefore, to "cancel out" the low gain of the plant at high frequencies, the*

⁸Of course, it is possible to residualise the controller to eliminate these high frequency dynamics, but for the simulations and flight tests presented in this thesis a suboptimal solution is satisfactory.

resulting controller will contain high frequency poles. The experience reported in [56] is that a suboptimal controller does not suffer from this drawback.

The robust stability properties claimed above will be demonstrated through designs and flight tests in chapters 3, 4 and 5. For the remainder of this chapter we will concentrate on a more generic control system architecture using a Westland Lynx Mk7 helicopter model. This architecture provides an attitude command (AC) response type at low speed and can be readily extended to a rate command (RC) at high speed flight. This response type is a basic requirement in the Aeronautical Design Standard [3], but to this date there is no straightforward mechanism for blending between low and high speed control law modes. So, in addition to its pedagogical value, the next section shows that H_∞ loop shaping methods, can accommodate different control law architectures.

2.5 Design example

The Westland Lynx Mk7 is an agile, highly coupled, rotary wing vehicle. The model used for the control law design is given in a state space form and has been trimmed and linearised at 6 *knots* forward speed.

$$\begin{aligned}\dot{x} &= Ax + Bu \\ y &= Cx\end{aligned}\tag{2.36}$$

where

$$\begin{aligned}x &= (p \ q \ r \ \theta \ \phi \ \psi \ u \ v \ w \ \Theta_{lat} \ \Theta_{long} \ \Theta_{pedal})^T \\ u &= (\delta_{lat} \ \delta_{long} \ \delta_{pedal})^T\end{aligned}$$

Note that p , q , r are the body roll, pitch, and yaw angular velocities, respectively; θ , ϕ , ψ the body pitch, roll, and yaw angles respectively; u , v , w the translational velocities in body-fixed coordinates; Θ_{lat} , Θ_{long} , Θ_{pedal} represent 1-st order actuator positions; and δ_{lat} , δ_{long} , δ_{pedal} are the lateral cyclic, longitudinal cyclic, and pedal control inputs. Five of the above states comprise the output vector, namely ϕ , θ , r , p , q .

To enable attitude and rate tracking at different flight modes, a mixed rate/attitude signal was used as a primary feedback variable. For pitch and roll loops these signals have the form

$$c_1\theta + c_3q\tag{2.37}$$

$$c_2\phi + c_4p\tag{2.38}$$

Note that this is equivalent to feeding back proportional plus derivative signals, but with the additional benefit that these signals are available over the whole flight envelope. The

proportion of required rate to attitude, and vice versa, can be derived using different arguments. For the AC system, for example, the rates contribute significant damping, and therefore the constants c_3 and c_4 must be chosen with that in mind. To see this, consider a simplified helicopter model $G(s) = N_g/s^2$ of the pitch dynamics, where N_g is the plant open loop gain (see Figure 2.5). Assuming negative feedback with a control law of the form

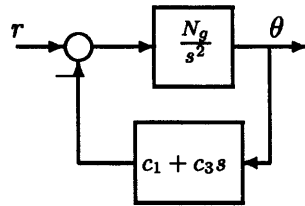


Figure 2.5 *Simplified pitch loop dynamics*

$c_1 + c_3s$, the closed loop transfer function from r to θ becomes $T_{r \rightarrow y} = \frac{N_g}{s^2 + N_g c_3 s + N_g c_1}$. Thus, rate feedback contributes directly to the damping of the AC system through the parameter c_3 . In addition, this feedback scheme allows for blending between low and high speed flight modes in a smooth manner. Thus, if the designer uses gain scheduling between two controllers the response type of the aircraft can be tailored to the mission task. Furthermore, the mixed attitude-rate signal is particularly important for a rate command system. This is for two reasons: firstly, an attitude hold facility can be enabled within a single controller structure; secondly, it allows the elimination of the attitude effect on the rate so that rate tracking is easily achievable. In mathematical terms, this effect manifests itself via an imaginary axis zero in the plant model G . Using a mixed attitude-rate feedback signal the limiting transmission zeros on the pitch and roll loops can be slightly shifted such that the controller will not place any poles very close to the origin (see remark 2.4.0.1 in section 2.4). The two following MATLAB⁹ scripts show a straightforward way to implement this scheme (c_1 and c_2 define the proportion of attitude added to the rate signal).

```
>> c1=0; c2=0;
>> c3=1; c4=1;
>> P2 = [c3 0 0 c1 0;
         0 c4 0 0 c2;
         0 0 1 0 0];
>> g=mmult(P2,g);
>> szeros(g)
ans =
-8.2724e-01
-7.5328e-02
-2.4163e-02
```

⁹MATLAB is a registered trademark of Mathworks Inc.

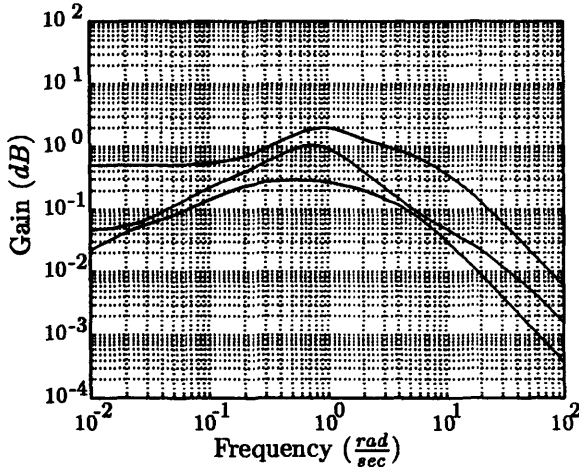
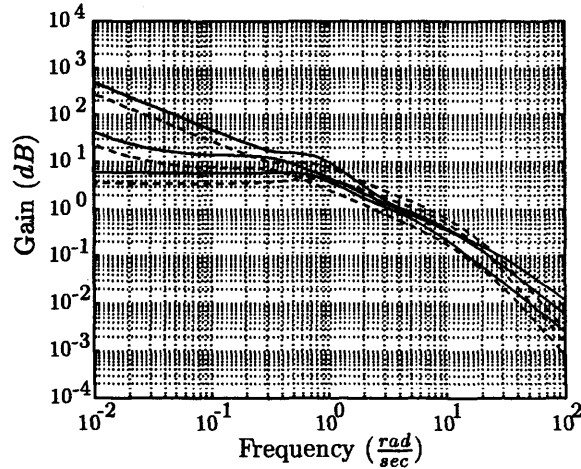
```
-1.1043e-14
-4.6197e-16
```

With a mixed rate-attitude signal the two zeros at $-1.1043e-14$ and $-4.6197e-16$ can be shifted to more desired locations. The magnitude of the new RHP zeros is exactly equal to the proportion of the secondary signal being added to the primary loop. In the following MATLAB script the two zeros have been shifted to $-4.0000e-01$ and $-3.9967e-01$.

```
>> c1=0.4; c2=0.4;
>> c3=1; c4=1;
>> P2 = [c3 0 0 c1 0;
         0 c4 0 0 c2;
         0 0 1 0 0];
>> g1=mmult(P2,g);
>> szeros(g1)
ans =
-8.2724e-01
-7.5328e-02
-2.4163e-02
-4.0000e-01
-3.9967e-01
```

For both low and high speed controllers, however, the proportion of the secondary signal must not change the gain and phase characteristics of the controlled loop at the cross-over. Should that happen, the stability (let alone the robustness) of the system can be jeopardised. In the Westland Lynx Mk7 control design presented in this section the constants c_1 , c_2 , c_3 and c_4 are determined initially for the linear controller synthesis and then they are modified appropriately during nonlinear simulations. The example describes the low speed Attitude-Command system. The Rate-Command can be designed in the same way, with the only difference being the higher order weighting function used to reduce the effects of the attitudes on the rates.

According to the procedure outlined in section 2.2, the designer must ensure all inputs and outputs are in compatible units. The design model contains all the inputs in *rads* of swashplate angular deflections. So, normalising them with respect to unity, $\frac{1}{\max(u_i)}$ unit of deflection in each input direction will be equally important for the controller. Similarly, it is possible to scale the output vector. Note that these normalisations assume that the linear controller will be capable of providing the same tracking over the whole range of helicopter state variation. Although this is not entirely true, (especially for state variations much larger than the equilibrium conditions where the linearisation was performed), it provides a simple and straightforward method to scale an open loop plant (see Figure 2.6).

Figure 2.6 Singular values of the model G_{sc} Figure 2.7 $W_2G_{sc}W_1K_a$ (solid) and $GW_2K_{\infty}W_1$ (dashed)

Alternatively, scaling can also be performed with respect to dynamic pressure around the aircraft's body. Although this method is not widely used, it allows the linear controller to be used over a very large range of altitudes and speeds. To see how this is done, recall the basic equations of aerodynamic forces and moments acting on the different helicopter components¹⁰. Fuselage forces and moments:

$$\left. \begin{aligned} X_f &= \frac{1}{2}\rho(\Omega R)^2 S_p U^2 c_{xf}(\alpha_f, \beta_f), & M_f &= \frac{1}{2}\rho(\Omega R)^2 S_p l_f V_f^2 c_{mf}(\alpha_f, \beta_f) \\ Y_f &= \frac{1}{2}\rho(\Omega R)^2 S_s U^2 c_{yf}(\alpha_f, \beta_f), & N_f &= \frac{1}{2}\rho(\Omega R)^2 S_s l_f V_f^2 c_{nf}(\alpha_f, \beta_f) \\ Z_f &= \frac{1}{2}\rho(\Omega R)^2 S_p U^2 c_{zf}(\alpha_f, \beta_f), & L_f &= \frac{1}{2}\rho(\Omega R)^2 S_s l_f U^2 c_{lf}(\alpha_f, \beta_f) \end{aligned} \right\} \quad (2.39)$$

Empennage forces and moments:

$$\left. \begin{aligned} Z_{tp} &= \frac{1}{2}\rho(\Omega R)^2 S_{tp} U^2 c_{ztp}(\alpha_{tp}, \beta_{tp}) & M_{tp} &= (l_{tp} + x_{cg})Z_{tp} \\ Y_{fn} &= \frac{1}{2}\rho(\Omega R)^2 U^2 S_{fn} c_{yfn}(\alpha_{fn}, \beta_{fn}) & N_{fn} &= -(l_{fn} + x_{cg})Y_{fn} \end{aligned} \right\} \quad (2.40)$$

where S_p and S_s are the plan and side areas of the fuselage, $c_{(\cdot)}$ are lifting coefficients (dependent on the incidence (α) and sideslip (β) angles¹¹), X, Y, Z, M, N, L are the main fuselage forces and moments, l_f represents the distance of the moments to the fuselage reference point, Ω is the rotorspeed and R is the blade radius. Note that the dynamic pressure $\bar{q} = (1/2)\rho U^2$ is present as a direct proportion in each of the main fuselage and empennage equations. Therefore, the linear control law can be altered so that it compensates for the $(1/2)\rho U^2$ effects.

Remark 2.5.0.1 The main reason for using \bar{q} and not airspeed (U) for normalisation is that lift forces (and therefore blade stall) are functions of \bar{q} rather than U alone. In addition, at higher altitudes air density ρ can be approximated using barometric altitude as $\rho = \frac{p}{R_b(T_0 - T_{grad}h)}$. Here, p is the static pressure as a function of temperature $p =$

¹⁰We will describe in more detail these equations in chapter 5 for the Bell 205 helicopter.

¹¹Subscripts f, fn, tp denote fuselage, fin and tailplane respectively.

$p_0 \left(\frac{T}{T_0}\right)^{\frac{g}{R_b T_{grad}}}$, with $p_0 = 101325.0$ Pa, $T_{grad} = 0.0065$ K/m, $T_0 = 288.15^\circ$ K (for height $h < 11.000$ m), $R_b = 287.05$ m²/s²/°K Boltzman's gas constant, and $g = 9.806$ m/s² the vertical gravity acceleration at $h = 0$ m.

According to the procedure of section 2.3, inspection of the open loop model, reveals that it has a pair of unstable poles at 0.7 rad/sec.

```
>> rofd(spoles(g))
```

real	imaginary	frequency	damping
4.8995e-01	-5.2465e-01	7.1785e-01	-6.8252e-01
4.8995e-01	5.2465e-01	7.1785e-01	-6.8252e-01
-5.0000e-01	-7.5753e-01	9.0767e-01	5.5086e-01
-5.0000e-01	7.5753e-01	9.0767e-01	5.5086e-01
-1.6227e+00	0.0000e+00	1.6227e+00	1.0000e+00
-1.7227e+00	0.0000e+00	1.7227e+00	1.0000e+00
-6.8610e+00	0.0000e+00	6.8610e+00	1.0000e+00
-6.8610e+00	0.0000e+00	6.8610e+00	1.0000e+00
-6.8610e+00	0.0000e+00	6.8610e+00	1.0000e+00
-8.8450e+00	0.0000e+00	8.8450e+00	1.0000e+00
-3.2650e+01	0.0000e+00	3.2650e+01	1.0000e+00

```
>>
```

This means that, in at least two loops, the open loop gain around this frequency must be large enough to compensate for the unstable plant dynamics. Of course, it is difficult to relate explicitly, unstable poles to particular loops in a multivariable system. However, it is possible to characterise the “dominant” aircraft dynamics in terms of phugoid, short period, dutch roll, and spiral modes of motion. These modes appear in different frequencies and therefore can be used to give the designer a “feel” for the weight selection procedure. We will do that in the next chapter for the H_∞ control law of the Bell 205 helicopter. For the moment, we note from Figure 2.6, that we need a constant gain (K_a) to set the cross over frequencies of the plant at 3 – 4 rad/sec. This constant gain depends on the actuator capabilities and the vibrational characteristics of the aircraft and will be analysed in detail in the next chapter. For good tracking performance and an attenuation rate of 20 dB/decade at the cross over, we use a weight of the form $\frac{s+1.5}{s}$

```
>> W1a = nd2sys([1 1.5],[1 0]);
>> W1b = nd2sys([1 1.5],[1 0]);
>> W1c = nd2sys([1 1.5],[1 0]);
>> W1 = daug(W1a,W1b,W1c);
```

```
>> W2 = daug(1,1,1);
>> W2GscW1=mmult(W2,Gsc,W1,Ka);
```

The shaped plant $W_2G_{sc}W_1K_a$ is shown in Figure 2.7 with solid lines. The cost function minimisation, in equation (2.10), ensures that the desired open loop cross gains are bounded from both sides, when an H_∞ controller is calculated (see equations (2.24) over (2.25)). The achieved loop gains $GW_2K_\infty W_1$ are also shown on Figure 2.7, with dashed lines. The H_∞ controller has reduced the attenuation of the singular values and has “robustified” the loop against the normalised coprime perturbation model. In this example, the scalings and the constant gain K_a have been absorbed into the dynamic weights W_1 and W_2 .

Having designed a weighting function W_1 that provides good disturbance rejection, time domain specifications can be included directly in the design procedure using the two DOF approach described earlier. The user-defined step response model, M_o in Figure 2.3, is usually diagonal, emphasising maximum output decoupling and exhibiting ideal handling qualities.

```
>> roll_model = nd2sys(2.38^2,[1 2*0.8*2.38 2.38^2]);
>> pitch_model = nd2sys(2.38^2,[1 2*0.8*2.38 2.38^2]);
>> yaw_model = nd2sys(4.90^2,[1 2*0.6*4.90 4.90^2]);
>> M_o = daug(roll_model,pitch_model,yaw_model);
```

Robust performance with respect to this ideal model is imposed with the model-matching parameter ρ according to equation (2.31). For our example $\rho = 1.4$. Finally, a slightly suboptimal controller was obtained using standard H_∞ optimisation routines [9].

```
Test bounds:      2.3665 < gamma <=      5.0000
-----
gamma   hamx_eig  xinf_eig  p/f
-----
5.000   1.0e-03    3.3e-10   p
.....
.....
3.187   1.0e-03   -9.7e+03   f
3.188   1.0e-03    3.5e-10   p
3.188   1.0e-03    3.5e-10   p
-----
Gamma value achieved:      3.1875
-----
```

Typically, a few iterations are carried to ensure that the stability margin γ is not too high for the chosen value of ρ . Typically, the parameter ρ is used by the designer to trade off

performance and robustness requirements. As ρ increases the stability margin γ degrades; an example of such degradation for our helicopter example is shown in table 2.1. It is evident that the better the model-matching the less robust is the design we can achieve. Note the controller poles are $-1.0269 \cdot 10^{-3}$ and $-3.1049 \cdot 10^{-2}$. According to remark 2.4.0.1

ρ	1.1	1.2	1.3	1.4	1.5	1.6	1.7	1.8
γ_{opt}	2.92	3.00	3.09	3.18	3.28	3.37	3.47	3.57
γ_{subopt}	3.21	3.30	3.40	3.50	3.60	3.71	3.81	3.92

Table 2.1 Stability margin as a function of ρ

the controller contains these poles in order to compensate for the effects of the open loop zeros. The magnitudes of the corresponding controller poles for this attitude command system are $-1.0269 \cdot 10^{-3}$ and $-3.1049 \cdot 10^{-2}$. Note, however, that this *is not* an exact pole-zero cancellation like in other H_∞ design methods. In fact, one of the advantages of the H_∞ LSDP method that the resulting controller does not enforce such cancellations between the plant and the controller.

>> ridf(spoles(Ksub))

real	imaginary	frequency	damping
-1.0269e-03	0.0000e+00	1.0269e-03	1.0000e+00
-3.1049e-02	0.0000e+00	3.1049e-02	1.0000e+00
-1.8223e+00	0.0000e+00	1.8223e+00	1.0000e+00
-1.9982e+00	0.0000e+00	1.9982e+00	1.0000e+00
-2.0041e+00	0.0000e+00	2.0041e+00	1.0000e+00
-2.2012e+00	0.0000e+00	2.2012e+00	1.0000e+00
-1.9040e+00	-1.4280e+00	2.3800e+00	8.0000e-01
-1.9040e+00	-1.4280e+00	2.3800e+00	8.0000e-01
-1.9040e+00	1.4280e+00	2.3800e+00	8.0000e-01
-1.9040e+00	1.4280e+00	2.3800e+00	8.0000e-01
-3.2640e+00	0.0000e+00	3.2640e+00	1.0000e+00
-2.9452e+00	-3.9270e+00	4.9087e+00	6.0000e-01
-2.9452e+00	3.9270e+00	4.9087e+00	6.0000e-01
-6.8610e+00	0.0000e+00	6.8610e+00	1.0000e+00
-1.3642e+01	-1.0714e+01	1.7347e+01	7.8646e-01
-1.3642e+01	1.0714e+01	1.7347e+01	7.8646e-01
-1.9523e+01	0.0000e+00	1.9523e+01	1.0000e+00
-2.0703e+01	-6.3535e+00	2.1656e+01	9.5600e-01

-2.0703e+01	6.3535e+00	2.1656e+01	9.5600e-01
-2.6509e+01	0.0000e+00	2.6509e+01	1.0000e+00

The controller was implemented as in Figure 2.8. Note that the robust stability properties in equations (2.12) over (2.17) are associated only with the feedback controller K_2 in Figure 2.8. To illustrate this, Figures 2.9 and 2.10 show the output and complementary sensitivity

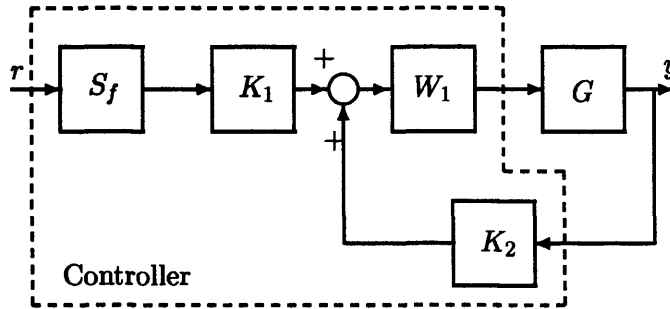


Figure 2.8 Implementation of the two DOF H_∞ controller

functions, S_o and T_o , respectively. It is clear that the disturbances at the output and sensor point of the diagram 2.1 will be rejected above 6 rad/sec. As noted earlier, these bounds

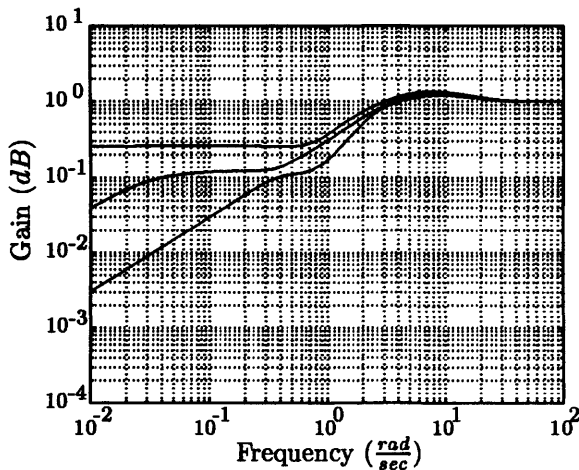


Figure 2.9 Sensitivity function $(I - G_s K_2)^{-1}$

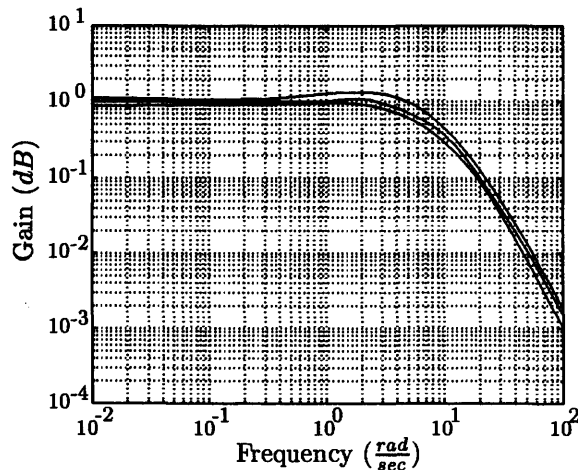


Figure 2.10 Complementary sensitivity function $(I - G_s K_2)^{-1} G_s K_2$

can also be expressed via the achieved loop gain function $G_s K_2$. Figure 2.11 shows the specified versus the achieved loop gains in the two DOF design procedure. Note that, due to the model matching part of the optimisation, the roll-off of the loop gains above 10 rad/sec is higher than 20 dB/decade.

Figure 2.12 shows the output responses of the ideal model and the closed loop system to a unit step input on lateral cyclic. The H_∞ controller provides excellent decoupling between the controlled outputs and the primary output response tracks satisfactorily the ideal model.

There are two aspects of the two degrees-of-freedom H_∞ loop shaping controller that

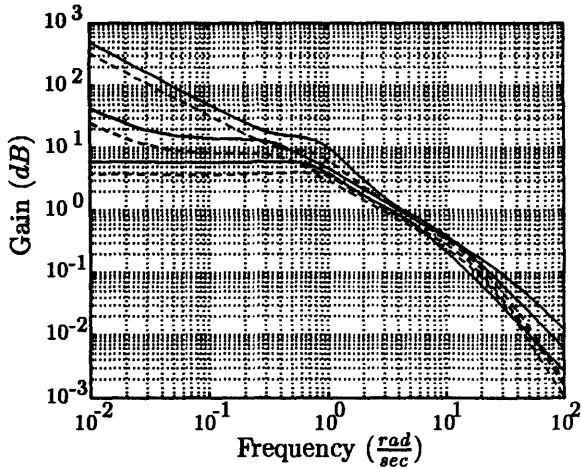


Figure 2.11 Specified vs achieved loop gains: two DOF formulation

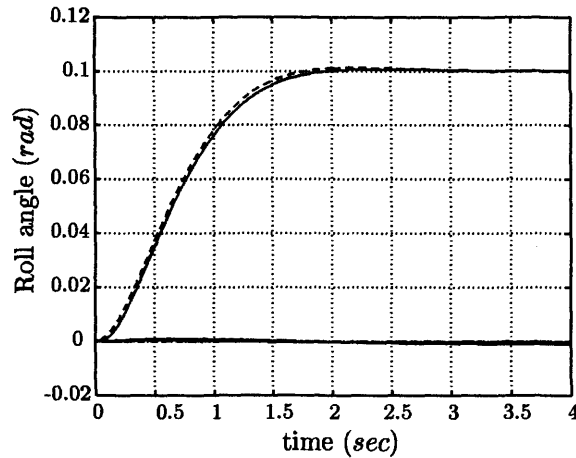


Figure 2.12 Output step responses of roll angle (solid) and the ideal model (dashed)

make it particularly attractive for helicopter applications. Firstly, the controller can be written as an exact observer plus a state feedback (see equations (2.34) - (2.35)). This property allows the feedback gains to be interpolated in a gain scheduling framework to capture known plant nonlinearities. Secondly, the controller can handle multivariable plants in a natural way, which allows for high levels of decoupling to be achieved. Experience shows that time responses, like those in Figure 2.12, are typical for helicopter control laws designed with two DOF H_∞ loop shaping. Unlike loop-by-loop approaches, where the compensator cross terms are designed implicitly, H_∞ controllers account for all the cross-couplings in a single synthesis procedure, while the off-axis responses are bounded in magnitude. This is very important for real time applications as the off-axis model uncertainty can be quite significant. This decoupling potential, however, does not imply that a helicopter control problem can be treated as a "black box" by the designer. Most of real time applications require the designer to know not only the achievable performance of the vehicle, but also the possible deficiencies of the helicopter mathematical models. Only then it is possible to arrive at a successful controller design and implementation on a Fly-By-Wire helicopter.

Design and piloted simulation of an H_∞ loop shaping compensator for the Bell 205 airborne simulator

3.1 Introduction

We start this chapter by giving further motivation for the use of two degrees-of-freedom H_∞ loop shaping as an attractive design method for highly coupled systems. In the previous chapter, we concentrated on the disturbance rejection capabilities of loop shaping controllers. It was also shown how it is possible to introduce time domain requirements using model matching, while preserving the robust properties of the initial configuration. In this chapter we elaborate on this methodology and design a loop shaping controller for an actual Fly-By-Wire (FBW) helicopter: the National Research Council of Canada (NRC) Bell 205 Airborne Simulator. Firstly, we show the basic dynamic characteristics of the model used for controller design and compare them with experimental data. Next, we design the feedback compensator according to the example of the previous chapter, but relying heavily on flight mechanics knowledge about the actual vehicle. The synthesised controller was tested on the Large Motion System (LMS) within the Advanced Flight Simulator complex at the Defence Evaluation & Research Agency (DERA), Bedford. Pilot comment and Cooper-Harper handling qualities ratings were recorded. Based on these assessments, the chapter concludes by giving a number of guidelines for synthesising prototype flight control laws using H_∞ -related methods. These guidelines form the basis of the subsequent controller flight test which is presented in chapter 4.

The response type of a helicopter, e.g. ACAH, can be easily accommodated through the two-degrees-of-freedom controller synthesis as discussed in the previous chapter. In addition, ground-based design experience [74, 65, 64], shows that adequate output decoupling is best achieved through two DOF schemes (see Figure 2.8 in chapter 2). Recall that in the original one DOF design procedure of Glover and McFarlane, we essentially translate time domain requirements into frequency dependent weights and for a coupled multivariable system this can be a difficult task. The weighting function selection, described in section 2.3, is most effective when either the desired loop bandwidths have similar crossovers, or

when the controlled outputs are largely decoupled in frequencies. In the case of the Bell 205 helicopter, the open loop plant is severely coupled, and bandwidth specifications are different. The rotor and fuselage are dynamically coupled in the frequency range of the desired closed-loop crossover and the rotor system is a dominant source of inter-axis coupling and dynamic uncertainty. The Bell 205 is “reasonably” agile in roll and yaw loops, but in pitch the achievable bandwidth is restricted by the mast-rocking mode of the teetering rotor system. The frequency of this mode is around 13.5 *rad/sec* and it appears as a strong flapping motion of the whole teetering rotor system which, if excited by the control system, can seriously damage the aircraft.

3.2 Description of the NRC Bell 205 flight dynamics model

The helicopter mathematical model used for control law design can be found in [34]. It comprises the standard six-degrees-of-freedom (DOF) stability and control derivatives. Only 6 states were available in the original state space description of the aircraft: three rotational rates and three translational velocities. Thus, to enable ACAH controller design, the model was augmented with the pitch and roll attitudes and their gravity-dependent couplings to force equations. Thus, the resulting six DOF state equations for the fuselage forces (X, Y, Z) and their corresponding moments (M, N, L) are given by

$$\left. \begin{aligned}
 X: \quad \dot{u} &= X_u u + X_w w + X_q q + X_v v + X_p p + X_r r + g \cos(\theta_0) \sin(\phi_0) \\
 Y: \quad \dot{v} &= Y_u u + Y_w w + Y_q q + Y_v v + Y_p p + Y_r r + g \cos(\phi_0) \sin(\theta_0) \\
 Z: \quad \dot{w} &= Z_u u + Z_w w + Z_q q + Z_v v + Z_p p + Z_r r + g \cos(\theta_0) \cos(\phi_0) \\
 M: \quad \dot{q} &= M_u u + M_w w + M_q q + M_v v + M_p p + M_r r \\
 N: \quad \dot{r} &= N_u u + N_w w + N_q q + N_v v + N_p p + N_r r \\
 L: \quad \dot{p} &= L_u u + L_w w + L_q q + L_v v + L_p p + L_r r \\
 \dot{\theta} &= q \\
 \dot{\phi} &= p
 \end{aligned} \right\} \quad (3.1)$$

where θ_0, ϕ_0 define the earth-measured equilibrium position of the helicopter. Heading is usually omitted from the description of the linear time invariant approximation of the model. This is because the heading angle appears only in the kinematic equation relating the rate of change of heading to the fuselage rates p, q and r .

3.2.1 Feedback signals

The feedback signals, derived from the sensors, include the primary controlled variables θ, ϕ in pitch and roll axes and yaw rate r in the heading loop. Pitch and roll rates (q and p respectively) were also fed back to the controller to improve the closed loop damping (see the example corresponding to Figure 2.5). This choice can be further justified by noting that for low flap hinge offset and teetering rotor helicopters, such as the Bell 205, the

changes in rotor hub forward (X) and lateral (Y) forces are the primary contribution to the pitch and roll moments about the aircraft's centre of mass. Hence, when pitch and roll rate information is being used for feedback, the stability derivatives X_q and Y_p contribute directly to the aircraft damping.

The possibility of using heading rate $\dot{\psi}$ instead of yaw rate r as a primary feedback variable in the directional loop was also considered on the grounds that $\dot{\psi}$ is an earth-based measurement perpendicular to the pitch and roll attitudes. However, design experience has shown that H_∞ controllers handle the inter-axis coupling successfully with either of these measurements. An important point here is that the helicopter has essentially "rate-command" response characteristics particularly at high frequencies, where pilots are subjected to high workload. Thus, the decoupling of body-axis rates p , q and r (as a means of decoupling the attitudes and the directional axis) has been taken to be of higher priority than the interaction of p , q and $\dot{\psi}$.

3.2.2 Mode description

It can be argued that the six degrees-of-freedom model, described by the system of equations (3.1), is adequate for low-moderate frequency, handling qualities analysis. The rationale behind the neglected dynamics is that the higher rotor and inflow phenomena behave in a quasi-steady manner, i.e. they are much faster than the fuselage motions and have enough time to reach their steady state within the typical time constants of the whole aircraft response modes. We will revisit these assumptions later in chapter 5. More detailed on these assumptions, alongside the necessary conditions of weakly coupled systems, are discussed in detail in Padfield [53, appendix4].

Mode	Real	Imaginary	Frequency	Damping	
1	8.0752e-02	-5.3177e-01	5.3787e-01	-1.5013e-01	Dutch roll
	8.0752e-02	5.3177e-01	5.3787e-01	-1.5013e-01	
2	8.7130e-02	3.2458e-01	3.3607e-01	-2.5926e-01	Phugoid
	8.7130e-02	-3.2458e-01	3.3607e-01	-2.5926e-01	
3	-1.0112e+00	0.0000e+00	1.0112e+00	1.0000e+00	Roll subsidence
4	-7.2787e-01	0.0000e+00	7.2787e-01	1.0000e+00	Heave subsidence
5	-5.4437e-01	3.0673e-01	6.2483e-01	8.7122e-01	Roll/pitch
	-5.4437e-01	-3.0673e-01	6.2483e-01	8.7122e-01	

Table 3.1 *Dynamic modes of the Bell 205 helicopter at hover*

Similar frequency separation arguments can be used when examining the basic modes of motion for a given linearisation. The resulting eigenvalues can be separated into slow and fast modes, the latter behaving in a quasi-steady manner. At hover, the basic modes of the Bell 205 helicopter are shown in table 3.1. The first two modes at low speed manifest

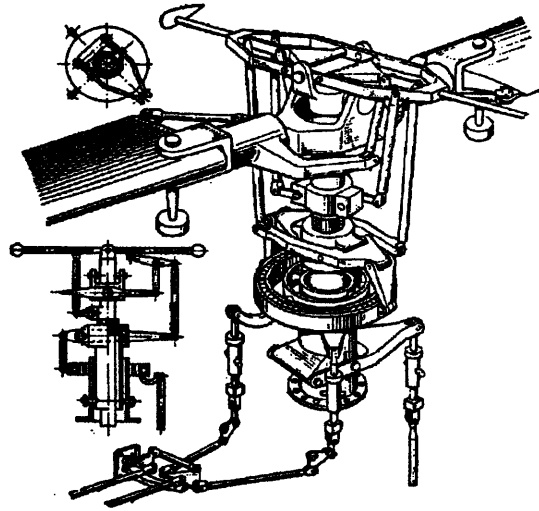


Figure 3.1 *The Bell 205 stabiliser bar*

themselves as coupled longitudinal/lateral oscillations. As the forward speed increases, the first oscillation develops into the known dutch roll motion and the second into the phugoid mode. The roll/pitch coupling, shown as mode number 5, is essentially what we call short period in the fixed wing aircrafts, and the other modes are subsidences, having distinct meaning at hover, but develop into more coupled motions at high speeds. Roll subsidence, for example, becomes the roll/yaw coupling, while heave appears to be heavily coupled with pitch motion.

3.2.3 The stabiliser bar

Ignoring the high order rotor dynamics for the moment, the main characteristic of the model that can affect the control law design is that the derivatives in the equations (3.1), have been obtained assuming a Bell stabiliser bar active on the main rotor-head (see Figure 3.1). The purpose of the bar is to provide a time-lagged feedback of rotor-mast angular rates in longitudinal and lateral directions; the time lag being a result of the bar inertia and damping mechanism. The operation of the bar is based on its gyroscopic properties initiating pitch and roll damping moments proportional to the difference between the gyroscope and the swashplate deflection. These damping moments act in the pitch and roll directions of fuselage motion by constraining the motion of the rotor disk and therefore stabilising the aircraft. The bar, however, has been removed from the actual aircraft and therefore it is a primary source of uncertainty when designing feedback compensators using this linearised model. A detailed description of the bar equations can be found in [13]. Ignoring the high

frequency motion of the bar, the resulting equations of motion become

$$\left. \begin{aligned} \frac{d(\delta_{long})}{dt} &= -\frac{1}{T_b} \delta_{long} + c_s q \\ \frac{d(\delta_{lat})}{dt} &= -\frac{1}{T_b} \delta_{lat} - c_s (p \cos(i_m)) \end{aligned} \right\} \quad (3.2)$$

where T_b is the time constant of the bar response, c_s is the non-dimensional bar to blade linkage factor and i_m is the longitudinal shaft tilt. For the Bell 205 $T_f \simeq 3$ sec and $c_s = 0.16$. The stabilising effect of the bar can also be seen from the schematic block diagram in Figure 3.2. For both pitch and roll loops the effect of the stabiliser bar dynamics is subtracted

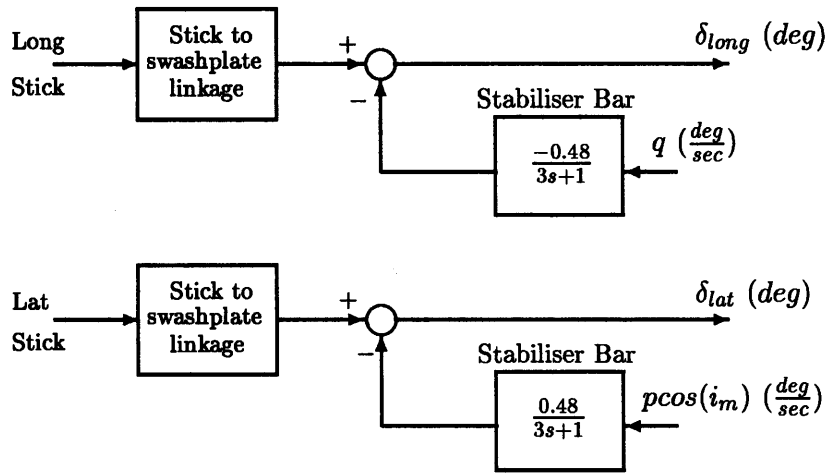


Figure 3.2 *Stabiliser bar block diagram*

from the longitudinal and lateral cyclic deflection respectively. Note the negative sign in the longitudinal stabiliser bar transfer function. It accounts for the sign difference between pilot induced commands (long stick in Figure 3.2) and pitch rate response in helicopters. Bearing in mind that the aerodynamic derivatives in equation (3.1) represent the helicopter dynamics for small perturbations, the initial model response can show how the stabiliser bar affects the initial rate responses in both the pitch and roll loops. The swashplate deflection in pitch (δ_{long} in Figure 3.2) equals the sum of the feedforward and feedback loops and therefore, the initial pitch helicopter response (as predicted by the model) should be overestimated when compared to the actual response of the vehicle.

The bar has the opposite effect in the roll loop. In this case the overall feedback signal is subtracted from the pilot-induced demand. Thus, with the bar on, the model should underestimate the initial roll rate dynamic response when compared to the same rate response of the Bell 205. We shall see in the next section that the experimental results from the comparisons between the NASA model responses and the actual helicopter behaviour seem to confirm the above arguments.

3.3 Model validation

Validation of the NASA model against flight test data in both time and frequency domains revealed that the classical 6 DOF model roughly captures the salient rigid body modes. However, the omission of the stabiliser bar and other higher rotor dynamics introduce significant uncertainty.

Figures 3.4, 3.6, and 3.8 show a comparison of the NASA model and helicopter on-axis time responses to doublet inputs at 60 *knots* Indicated Air Speed (IAS) in lateral, longitudinal and directional axes respectively. The actuator signals used to obtain the flight test data as well as to drive the NASA model are shown in Figures 3.3, 3.5 and 3.7. Note that the comparisons are performed at 60 *knots* for two reasons. Firstly, the helicopter at high speeds is more stable than it is at hover so pulse inputs do not cause extreme attitude excursions from the linear perturbation approximation assumptions. Secondly, due to the cross-axis coupling at hover, it is more difficult for the pilot to perform pure inputs in one axis alone without contaminating the primary aircraft response with off-axis pilot induced perturbations. For both longitudinal and lateral loops the experimental data confirm the

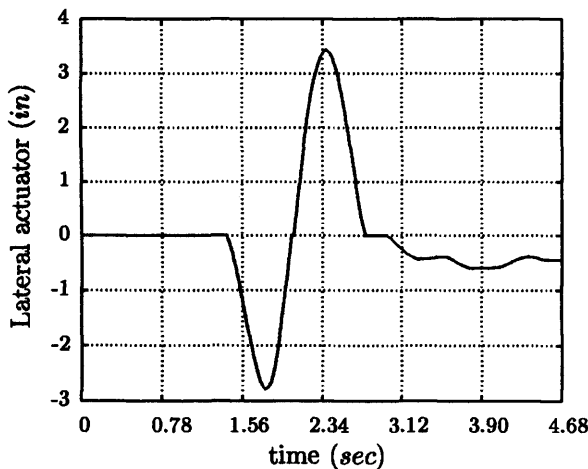


Figure 3.3 Time history of doublet input in lateral axis

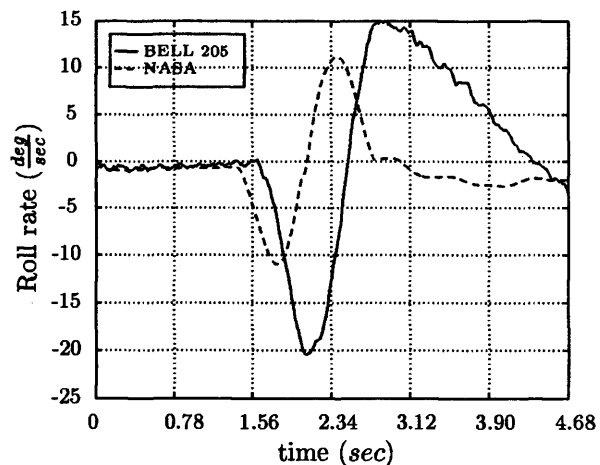


Figure 3.4 Comparison of flight test data and NASA 6DOF model responses to a doublet input in lateral axis

previous analysis. The NASA model predicts lower roll and higher pitch rates; the difference being due to the absence of the stabiliser bar from the actual NRC Bell 205 as opposed to the calculation of the linearised models in [34]. From Figures 3.9, 3.10, 3.11, 3.12, 3.13, and 3.14, the experimental data show that, as with virtually all low order helicopter models, the off-axis responses of the NASA model are in the opposite direction of the actual aircraft responses. This is one of the major problems in the rotary wing modelling area, and high order dynamics such as rotor flapping, inflow, tail fin blockage, tail rotor blade root cut-out states are required to enhance the predictions of the quasi-static description shown in equations (3.1).

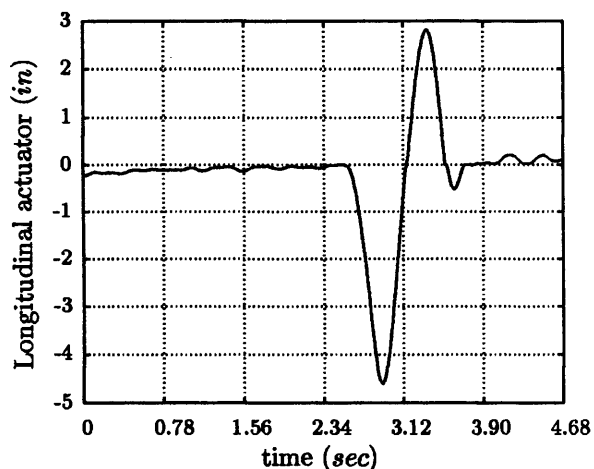


Figure 3.5 Time history of doublet input in longitudinal axis

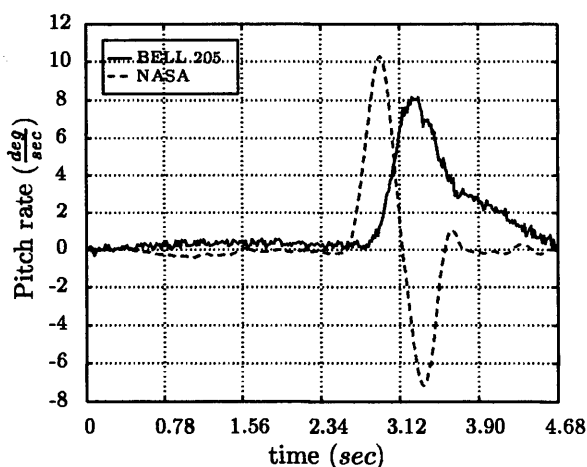


Figure 3.6 Comparison of flight test data and NASA 6DOF model responses to a doublet input in longitudinal axis

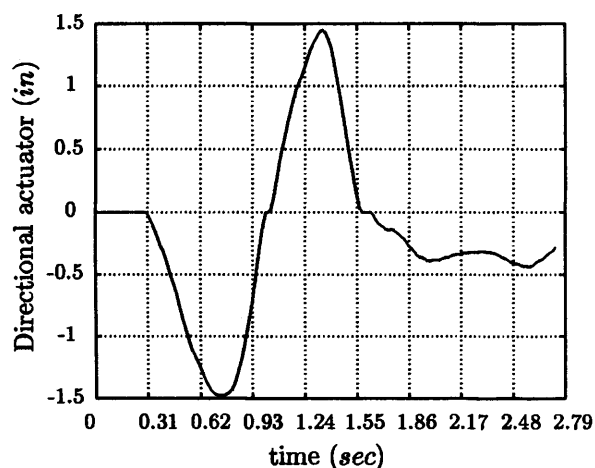


Figure 3.7 Time history of doublet input in yaw axis

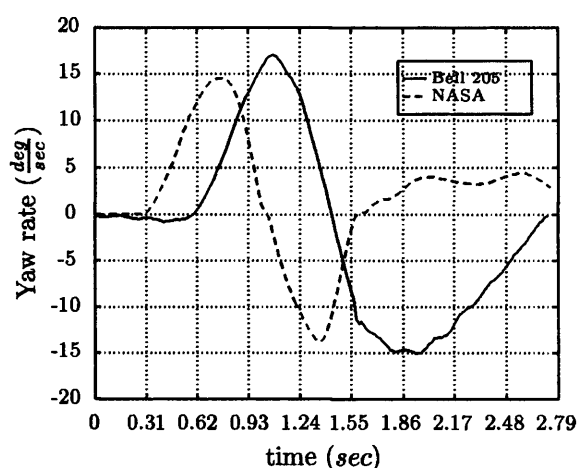


Figure 3.8 Comparison of flight test data and NASA 6DOF model responses to a doublet input to directional axis

From the time histories shown in Figures 3.4, 3.6, and 3.8, it can also be seen that there is a significant lag between the pilot input and the aircraft response, which is actually perceived as a pure time delay by the pilots. This is typical for teetering rotor helicopters where the fuselage is almost pendulously suspended from the rotor system and therefore the fuselage-mounted accelerometers pick up a lagged/delayed signal. From Figures 3.4, 3.6, and 3.8, the time constant characterising this lag can be estimated to be 150 msec for the pitch and roll axes and 180 msec in yaw. To describe in a mathematically appealing form this inherent lag in the aircraft dynamic response, it is possible to use a low order lag filter $\frac{1}{Ts+1}$ or first order Padé approximation to the time delay $\frac{2-Ts}{2+Ts}$, with the appropriate time constants, and to cascade it with the quasi-static description of equations (3.1). It is generally not clear from these time domain comparisons to decide whether a lag or a time delay can precisely characterise the aircraft motion. However, it is possible to identify

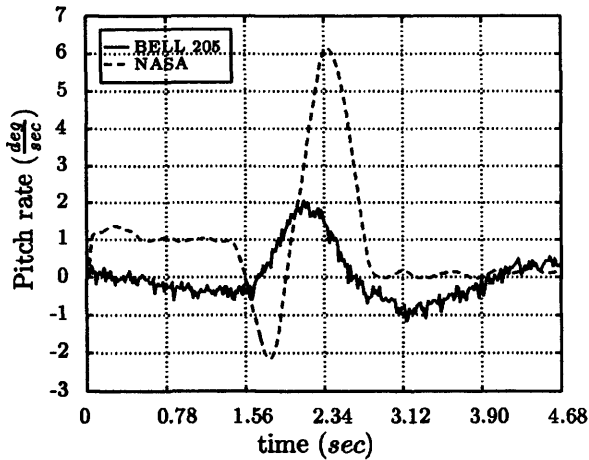


Figure 3.9 Comparison of flight test data and NASA 6DOF pitch axis responses to a doublet input in the lateral axis

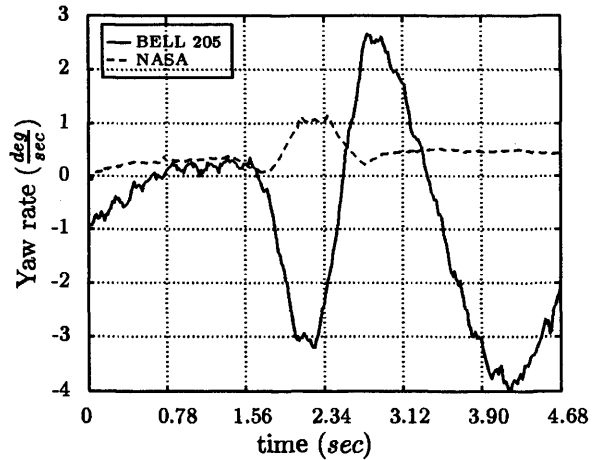


Figure 3.10 Comparison of flight test data and NASA 6DOF yaw axis responses to a doublet input in the lateral axis

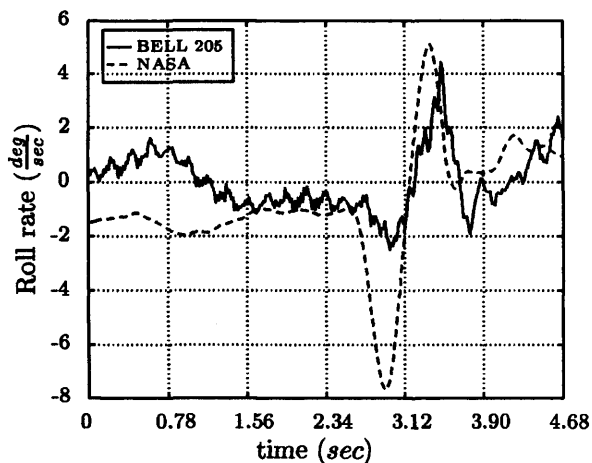


Figure 3.11 Comparison of flight test data and NASA 6DOF roll axis responses to a doublet input in the longitudinal axis

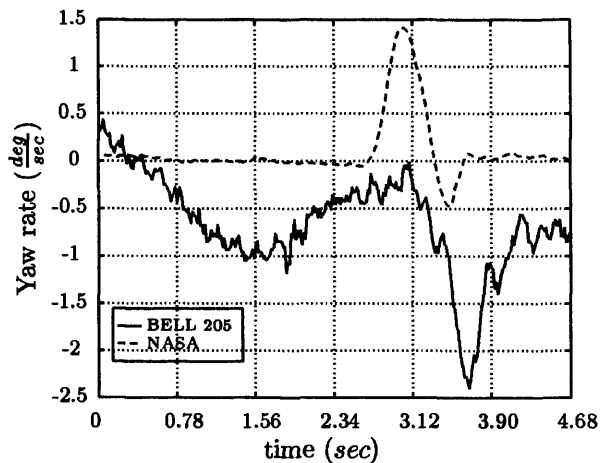


Figure 3.12 Comparison of flight test data and NASA 6DOF yaw axis responses to a doublet input in the longitudinal axis

the frequency-dependent phase difference between the modelled and the actual helicopter responses from frequency domain analysis as we shall see next.

To enable a frequency domain comparison of the quasi-static model and the actual helicopter responses, a set of open loop frequency sweeps was conducted at 60 *knots* IAS on the NRC Bell 205 helicopter and time histories of actuator activity, aircraft attitudes and angular rates were recorded. A frequency sweep is performed by starting from trim conditions and moving the inceptor in a sinusoidal trajectory starting with low frequency excursions and progressing to high frequency. Although the period of the sinusoid is constantly increasing, the magnitude of the inputs is varied to keep the states near the trim conditions around which model and aircraft comparisons are to be made. At least two frequency sweeps in each loop were performed to ensure a sufficient amount of recorded data for further analysis.

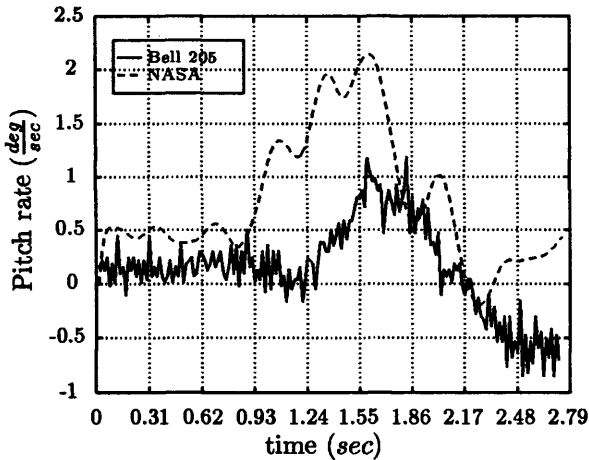


Figure 3.13 Comparison of flight test data and NASA 6DOF pitch axis responses to a doublet input in the directional axis

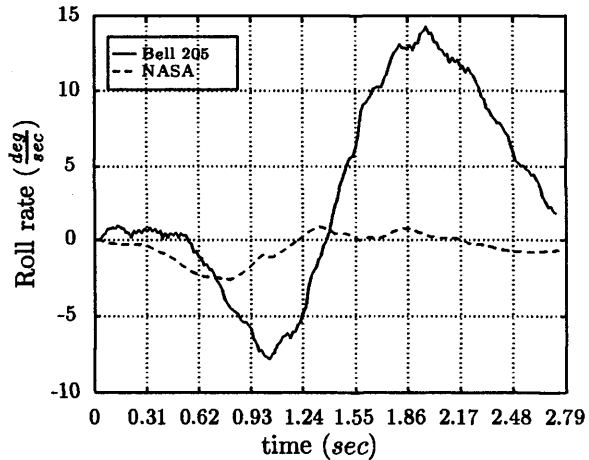


Figure 3.14 Comparison of flight test data and NASA 6DOF roll axis responses to a doublet input in the directional axis

The open loop flight test data were cropped to isolate only the response to the control input, zero mean de-trended to remove any trim offset and the inputs were linearly de-trended to remove the effects of drift caused by changes in the flight condition as a result of the test input. The processed data were then used to excite the NASA linear model, and Fast Fourier Transform spectral analysis was applied to the resulting input/output time histories in order to identify the frequency response magnitude and phase. For the measured input $u(t)$ and output $y(t)$, the estimated linear system frequency response function can be obtained as

$$G(j\omega) = \frac{P_{uy}}{P_{uu}} \quad (3.3)$$

where P_{uu}, P_{uy} are the auto and cross spectral density functions between $u(t)$ and $y(t)$ respectively.

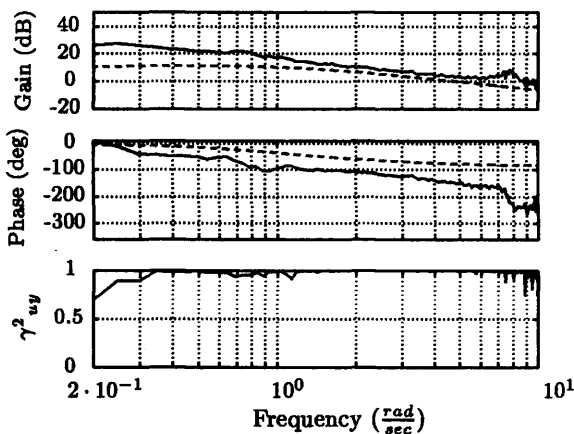


Figure 3.15 Comparison of open loop flight test data (solid) and NASA 6DOF model responses (dashed) to a frequency sweep input in lateral axis

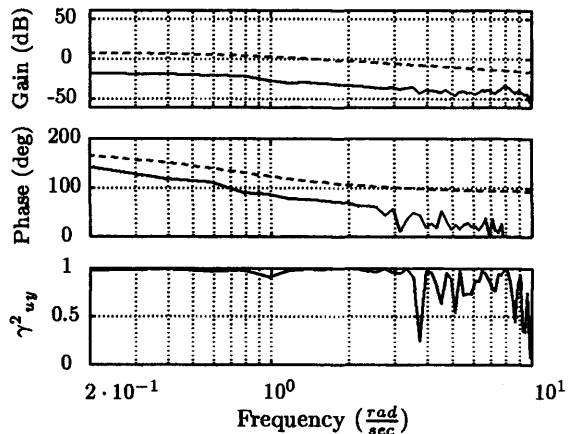


Figure 3.16 Comparison of open loop flight test data (solid) and NASA 6DOF model responses (dashed) to a frequency sweep input in longitudinal axis

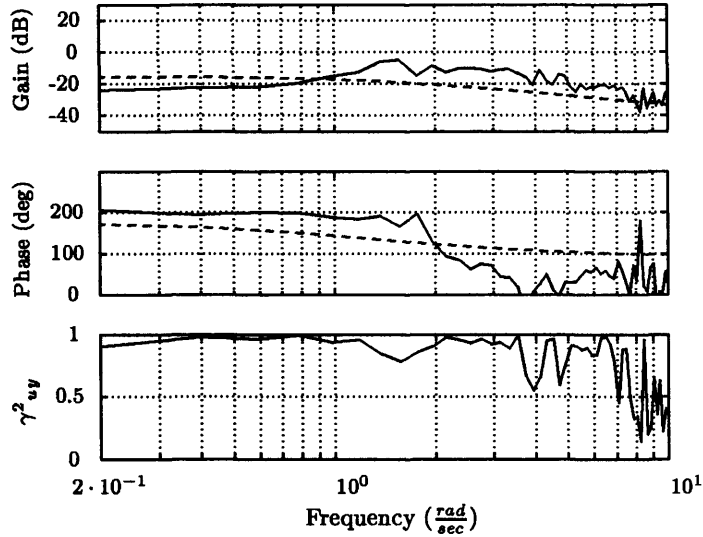


Figure 3.17 Comparison of open loop flight test data (solid) and NASA 6DOF model responses (dashed) to a frequency sweep input in yaw axis

Figures 3.15, 3.16 and 3.17 show a comparison of the flight test data (solid) and the NASA model (dashed) for a lateral, longitudinal and pedal frequency sweep respectively in terms of Bode magnitude and phase plots. To check that the approximation of the nonlinear input-output response does not introduce any unwanted phase errors a coherence function was calculated, indicating the fraction of the output spectrum which is linearly related to the the input $u(t)$. The coherence function $\gamma^2_{uy}(t)$ is defined as

$$\gamma^2_{uy} := \frac{|P_{uy}|}{P_{uu}P_{yy}}, \quad 0 \leq \gamma^2_{uy}(t) \leq 1 \quad (3.4)$$

A value of 1 indicates linear relationship between $y(t)$ and $u(t)$ while a value of 0 indicates that the input and output are uncorrelated. We shall see later in chapter 4 the importance of $\gamma^2_{uy}(t)$ in assessing the closed loop system performance of the designed H_∞ controller. At the present time, $\gamma^2_{uy}(t)$ is used only to ensure that the flight test data adequately represent the helicopter dynamic response. Figures 3.15 - 3.16 suggest that at 60 knots forward speed the phase differences in the lateral and longitudinal axes vary from a few degrees at 0.2 rad/sec up to 60° at 2 rad/sec respectively. Based on this observation a first order lag would account for up to 15° at 2 rad/sec and a first order Padé delay would ensure that up to 30° of phase difference (assuming a 150 msec time constant) is incorporated into the design model.

The use of a first order Padé approximation, as a means of explaining the phase difference in Figures 3.15 and 3.16, appears to be also valid from the flapping dynamics theory point of view. The main argument here involves the phase difference between the flapping response and the applied cyclic pitch [53, ch2]. According to the theory of the flapping

rotor in air, the flap equation of motion can be written as

$$\beta'' + \frac{\gamma}{8}\beta' + \lambda_\beta^2\beta = \frac{2}{\Omega} (p \cos(\psi) - q \sin(\psi)) + \frac{\gamma}{8} \left(\theta - \frac{4}{3} \frac{\nu_i}{\Omega R} + \frac{p}{\Omega} \sin(\psi) + \frac{q}{\Omega} \cos(\psi) \right) \quad (3.5)$$

with the applied blade pitch given by

$$\delta = \delta_0 + \delta_{long} \cos(\psi) + \delta_{lat} \sin(\psi) \quad (3.6)$$

where δ_0 , δ_{long} and δ_{lat} are the collective, longitudinal and lateral pitch respectively. Assuming that the control activity and the period of fuselage angular motion are an order of magnitude greater than the flap time constants, equation (3.5) can be written in a quasi-steady form as

$$\beta = \beta_0 + \beta_{long} \cos(\psi) + \beta_{lat} \sin(\psi) \quad (3.7)$$

where β_0 is the rotor coning angle and β_{long} and β_{lat} are the longitudinal and lateral flapping angles respectively, given by

$$\left. \begin{aligned} \beta_0 &= \frac{\gamma}{8\lambda_\beta^2} \left(\delta_0 - \frac{4}{3} \frac{\nu_i}{\Omega R} \right) \\ \beta_{long} &= \frac{1}{1+S_\beta^2} \left(S_\beta \delta_{long} - \delta_{lat} + \left(S_\beta \frac{16}{\gamma} - 1 \right) \frac{p}{\Omega} + \left(S_\beta + \frac{16}{\gamma} \right) \frac{q}{\Omega} \right) \\ \beta_{lat} &= \frac{1}{1+S_\beta^2} \left(S_\beta \delta_{lat} + \delta_{long} + \left(S_\beta + \frac{16}{\gamma} \right) \frac{p}{\Omega} - \left(S_\beta \frac{16}{\gamma} - 1 \right) \frac{q}{\Omega} \right) \end{aligned} \right\} \quad (3.8)$$

In equation (3.8), ν_i represents the constant approximation of the inflow velocity over the rotor disk, Ω is the rotor speed, R is the blade radius and S_β represents the blade stiffness, which can be written as a function of the Lock number γ and the flapping frequency ratio λ_β

$$S_\beta = \frac{8(\lambda_\beta^2 - 1)}{\gamma} \quad (3.9)$$

From the above equations it is possible to see that the flapping response has approximately 90° phase difference from the applied blade cyclic pitch. Since a Padé approximation introduces a 90° phase difference to the model used for control law design it appears that its use coincides with the general theory of flapping dynamics.

Despite the above analysis it is our belief that there is much more than a simple estimation of the phase difference between the modelled and the actual aircraft response. Recall that the experimental data analysis was performed at 60 *knots* IAS, where the aerodynamic loads on the fuselage and empennage are strong functions of forward velocity. Also, dihedral forces are very strong and it would not seem readily justifiable to extrapolate the results for the hover flight regime. Anyway, due to the absence of hover flight test data for more detailed analysis, the Padé approximation was used as a conservative¹ estimate of the time delay between the predicted and actual aircraft response.

From the above discussion it can be seen that to tolerate the high degree of uncertainty in the linear model, the subsequent controller synthesis has to be biased strongly towards

¹In the sense that a right half plane zero is introduced in the linear model imposing limitations on achievable performance. See equation (2.29) in chapter 2.

low/moderate bandwidth robust stability as opposed to high bandwidth performance. This limits the potential of the H_∞ loop shaping design procedure for high bandwidth control system design, but it is compatible with safety considerations which prefer a low bandwidth, when a prototype flight control system is first evaluated in-flight.

3.4 The controller architecture

The primary purpose of the controller architecture is to tailor the handling qualities of the vehicle to the appropriate mission task. The controller structure is, in principle, independent of the design method. However, certain properties of the control design method can be exploited to yield a modular and easily-implementable control law. Indeed, the state feedback observer-based H_∞ compensator (see equations (2.34) and (2.35) in chapter 2), can provide a generic controller architecture for both disturbance rejection and command tracking in real time applications.

This generic controller architecture is shown in an analogue form in Figure 3.18. The pilot demands are shown entering a dead-band and command shaping block. Dead-bands are important, particularly for rate command (RC) systems that might contain integral action in the command path, preventing the excitation of the controller dynamics with undesirable biodynamic interference caused by the n/rev rotor disturbances and structural mode excitations. Alongside dead-bands, shaping functions are used to tailor the stick sensitivity to the mission task and therefore they depend on the response qualities of the vehicle as well as the stick feel system. For instance, a RC response in pitch and roll should allow small amplitude responses and low rates to be achieved without any lags or over-sensitivity, while large amplitude demands should be executed with comfortable input forces. The shaping functions usually have non-linear character; however, harmonisation between the different response type requirements can also be achieved through linear functions, as it will be seen in the next chapter.

The frequency range of the input signals to be tracked by the control system is determined by the closed loop bandwidth. However, uncertainty in the design models makes the prediction of the closed loop bandwidth imprecise and therefore undesirable high frequency noise may be present in the command path. The low pass filter shown in the command path of Figure 3.18 (with cut-off frequency " ω " higher than the closed loop bandwidth) removes a large amount of high frequency noise and does not introduce significant lag into the control loop.

Next to the low pass filter, a scaling factor (S_f) guarantees zero steady-state error in the output response, and a command model (A_o, B_o) is utilised to tailor the aircraft response to the appropriate mission task. As in the design example presented in chapter 2, the command model responses are specified using the damping and natural frequency parameters of a second order model for ACAH response type according to the ADS-33D

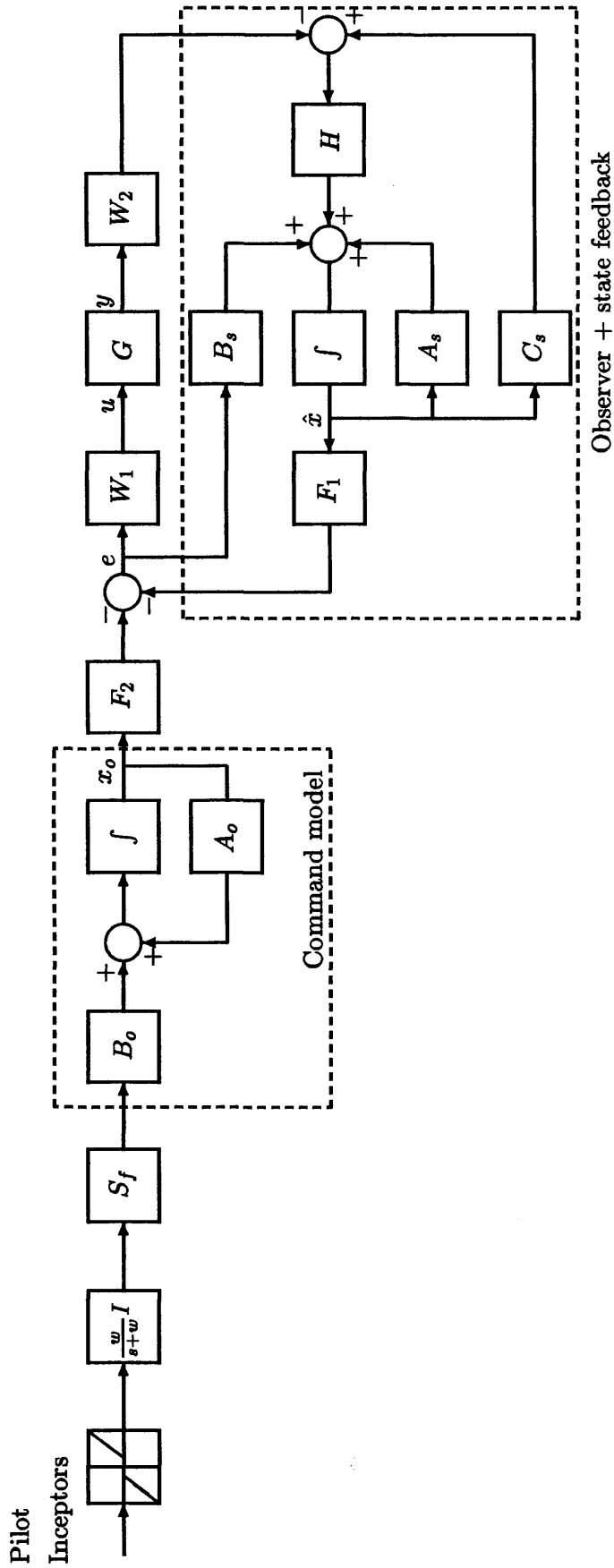


Figure 3.18 The H_∞ controller architecture

rotorcraft specifications [3]. In this case though, we also use the agility parameter (see equation (3.13)) to impose time domain requirements. The agility parameter is defined as the peak angular rate necessary to achieve a desired attitude response and therefore it is directly related to the rate signal generated by the feedback compensator. Thus, the designer can trade-off how much rate feedback will be used to achieve good control system performance.

The feed-forward gain matrix (F_2) in Figure 3.18 is the output injection gain from the solution of the H_∞ robust stabilisation problem. In the controller equations (2.34) and (2.35) it is represented by $F_2 = B_s^T X_{\infty 12}$. As in classical controller structures which use PID gains, this feed-forward element can be viewed as a “quickening” action on the command path demands in order to offset the feedback damping and open loop damping which would otherwise retard the command response.

The feedback signals are derived from the sensors and sensor noise may be filtered out via the frequency dependent filter W_2 . The design of this noise attenuation block is done independently of the overall controller synthesis and it is used to emphasise sensor bandwidths and measurement fidelity over the frequency range of interest. W_2 can also be used to remove the n/rev structural vibration measurements picked up by the sensors. Later in chapter 5 this filter is specified as a first order filter to fulfil the noise attenuation role within the loop shaping design procedure. It is important to note here that H_∞ optimisation and other robust multivariable methods can also address the robustness implications of using W_2 as an integral part of the design procedure.

As mentioned in the introduction, achieving robust high gain feedback in helicopter flight control system design is problematic because the rotor and fuselage are dynamically coupled in the frequency range of the desired closed-loop cross-over. It is widely known that if conventional rigid-body state feedback can be augmented with rotor state feedback, then robust control of the coupled body/rotor modes can be obtained at higher bandwidths than would otherwise be achievable. Ongoing experimental studies on a model-scale Experimental Rotor Rig Facility [26] have also suggested that - while based purely on output feedback from the rigid body dynamics - all observable states are reconstructed within an H_∞ synthesis and hence the resulting feedback controller will implicitly include rotor state augmentation if rotor dynamics are included in the design model. The observer scheme shown in Figure 3.18 is unique among H_∞ methods in the sense that the observer is not calculated in a separate procedure. Instead, a stabilising controller is synthesised which can, if required, be written as an exact estimator preserving all the properties the designer specified during the controller synthesis [60, 72].

Using a 6-DOF rigid body model for control system design limits the full potential of the H_∞ technique for including rotor state augmentation. This, however, does not undermine the attractiveness of H_∞ loop shaping as a control design method; the inherent robustness properties and the modularity of the observer state feedback structure offer great insight

to the helicopter control problem.

The pre-compensator W_1 is used primarily to boost the low frequency gain of the open loop frequency response and also to specify desired closed loop bandwidths. The structure of this pre-compensator is essentially a proportional plus integral (PI) element, derived from SISO loop shaping ideas. Recall from the previous chapter that the simpler this pre-compensator is, the lower its condition number can be. Thus, the better achievable bounds are obtained as described by relationships 2.12 over 2.17.

When maximum performance is a primary design specification, the uncertainty present in the models used for control law design may result in controllers that sometimes generate excessive rate or position demands. In these cases, actuator rate limiting may lead to pilot induced oscillations (PIO) that can compromise stability and performance. The designer uses extensive simulations to ensure that the actuators respect the vehicle limits and in most cases command path pre-filtering and reduction of the control gains (i.e. limiting the bandwidth) are obvious choices to prevent saturation. However, for invertible multivariable controllers, such as the two DOF H_∞ compensator designed in the previous chapter, the Hanus anti-windup procedure [57] offers a straightforward solution to the saturation problem. Applications of this anti-windup procedure can be found in [40, 65].

For the H_∞ controller shown in Figure 3.18 the remaining controller blocks are: the shaped plant ($W_2(s)G(s)W_1(s)$) in state-space form $(A_s, B_s, C_s, 0)$, the Riccati gains $F_1 = B_s^T X_{\infty 11}$, and H , which guarantee stability and performance against the normalised coprime perturbation description described in chapters 1 and 2. It has to be noted here that the designer's visibility in those blocks is lost due to their multivariable nature when compared to simple controllers using PID gains. However, this should not present a problem for implementation purposes since the implementation can be performed using state-space integration methods while the overall controller is viewed as a frequency response altering the vehicle's dynamics.

3.5 Controller design for the NRC Bell 205 FBW helicopter

The overall design aim was to provide the helicopter with level 1 handling qualities through the robust stabilisation and de-coupling of the aircraft's roll and pitch attitudes and yaw rate. In addition, it was decided to augment the heave axis in order to investigate to what extent the H_∞ controller could decouple all four axes of the aircraft. Due to the lack of state information data, however, the vertical velocity measurement w was chosen for feedback although heave velocity (\dot{H}) would be preferable as the tests would be carried out in the hover regime. The reasoning behind this is that pilots use ground-referenced cues for hovering tasks and therefore they "close the loop" around \dot{H} rather than w .

The design procedure started with the open loop singular values of the helicopter model being scaled to reflect the relative importance between the chosen outputs. Normalisation

with respect to the maximum variable range was used in this case. This choice was taken on the grounds that we did not have a nonlinear representation of the Bell 205 dynamics and therefore it was difficult to use normalisation with dynamic pressure. This will not be a problem though as in the next chapter we will see that this controller will perform satisfactorily (considering the available linear models) over a wide speed range. In addition, this control law concentrates on the hover flight regime as this speed region is the most challenging for the flight control system.

As in the design example in the previous chapter, the scaled plant was pre-multiplied with the dynamic matrix W_1 containing integral action to specify good tracking at low frequencies and disturbance attenuation at high frequencies. So, the pre-compensator W_1 was chosen to give a slope of -1 (i.e. 20 dB/decade) to the magnitude of the loop transfer function $W_2(j\omega)G(j\omega)W_1(j\omega)$ at high frequencies while a zero at -2 was used to reduce the roll-off rate around the cross-over region i.e.

$$W_1(s) = \begin{bmatrix} \frac{s+2}{s} & 0 & 0 & 0 \\ 0 & \frac{s+2}{s} & 0 & 0 \\ 0 & 0 & \frac{s+2}{s} & 0 \\ 0 & 0 & 0 & \frac{s+2}{s} \end{bmatrix} \quad (3.10)$$

Note that the zero at -2 is slightly higher than the frequency of the two unstable modes shown in table 3.1. It is not straightforward to justify this choice only from ground-based linear simulations. The designer should also bear in mind that the frequencies of these modes can be different at flight conditions. Of course, the classical loop shaping ideas described in section 2.3 are valid; however, the more uncertain the linear model is, the harder it is to arrive at a suitable weighting function. A diagonal matrix W_2 was used to enable pitch and roll rates to be fed back to the controller. The final form of W_2 was:

$$W_2 = \begin{bmatrix} 1 & 0 & 0 & 0 & 0 & 0 \\ 0 & 1 & 0 & 0 & 0 & 0 \\ 0 & 0 & 1 & 0 & 0 & 0 \\ 0 & 0 & 0 & 1 & 0 & 0 \\ 0 & 0 & 0 & 0 & 0.5 & 0 \\ 0 & 0 & 0 & 0 & 0 & 0.5 \end{bmatrix} \quad (3.11)$$

Note that pitch and roll rates (p and q respectively) are fed back weighted with 0.5 which specifies how much they will contribute to the damping of the feedback loop. The open loop cross-over frequency was set to a desired value by pre-multiplying the weight W_1 with an alignment gain matrix K_a . This constant matrix was calculated as the real approximate inverse of the augmented helicopter model $W_2G(j\omega)W_1(j\omega)$ at 4 rad/sec . The selection of this cross-over frequency requires that all the underdamped modes to be controlled must be well within the control bandwidth. If this frequency is high then the controller will reduce

the closed loop response lag and produce a stable closed loop insensitive to the feedback dynamics. However, the designer must have good knowledge of the actuator capabilities, so that excessive control action is avoided. A good rule of thumb is to push the cross-over frequency as high as possible until the robust properties, as viewed by the H_∞ stability margin $\gamma := \left\| \begin{bmatrix} K_\infty \\ I \end{bmatrix} (I - G_s K_\infty)^{-1} \tilde{M}_s^{-1} \right\|_\infty$, deteriorate. The gain (singular values) of the final shaped plant $W_2 G W_1 K_a$ is shown in Figure 3.19.

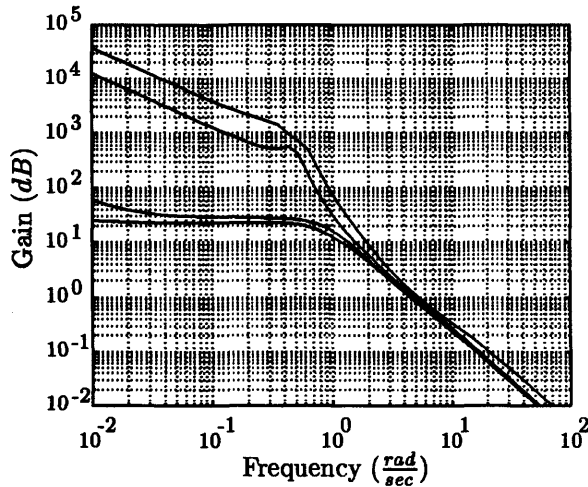


Figure 3.19 Shaped helicopter model

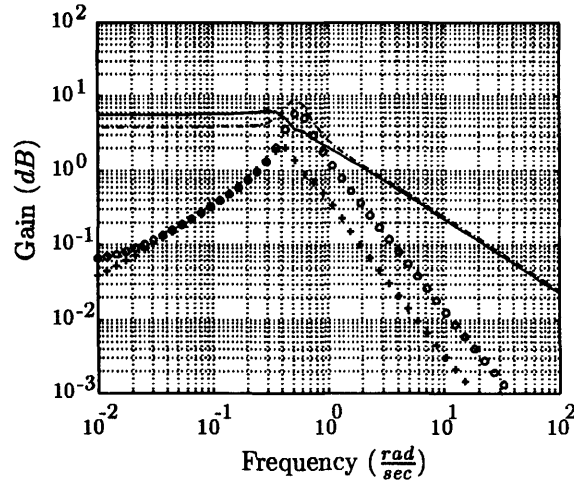


Figure 3.20 Open loop singular values from all the inputs to each of the outputs.

Remark 3.5.0.1 Ideally, it would be desirable to shape each open loop singular value without affecting the gain in the other loops. This is the reason for using a diagonal pre-compensator W_1 . However, in practice, this loop-by-loop shaping procedure can be hard to perform. Figure 3.20 shows the maximum singular values from all the inputs to each of the outputs i.e. the norms $\left\| \frac{y_1}{u_{1\dots 4}} \right\|_\infty$, $\left\| \frac{y_2}{u_{1\dots 4}} \right\|_\infty$, $\left\| \frac{y_3}{u_{1\dots 4}} \right\|_\infty$, $\left\| \frac{y_4}{u_{1\dots 4}} \right\|_\infty$. From this Figure, it can be seen that any combination of input gains intended to specify better tracking in pitch loop will unavoidably affect heave, especially between 0.9 and 1 rad/sec. So, there is a great possibility that by the time the low frequency gain in pitch is large enough for good tracking performance, the collective actuator may experience undesirably large control deflections. The alignment gain K_a essentially cross-feeds the required amount of gain to achieve a diagonally dominant specified loop shape $W_2 G(j\omega) W_1(j\omega)$ and thus to decouple the helicopter outputs to a large extent. When implementing the controller, this alignment matrix (alongside the input scaling) is absorbed into the diagonal pre-compensator.

Having found suitable loop shaping weights, the next step is to select a command model to reflect handling quality requirements. The command model for the chosen ACAH response type was represented by a standard second order transfer function (M_o) with

desired natural frequency (ω_n) and damping factor (ζ) for each of the controlled outputs:

$$M_o := \frac{\omega_n^2}{s^2 + 2\omega_n\zeta s + \omega_n^2} \quad (3.12)$$

The natural frequency parameter for each of the outputs was chosen to satisfy the minimum requirements on the peak angular rate necessary to achieve a desired pitch or roll attitude change which for a second order closed loop response is given by

$$\frac{Rate_{pk}}{\Delta Att_{pk}} = \frac{\omega_n e^{-\frac{\zeta}{\sqrt{1-\zeta^2}} \arcsin \sqrt{1-\zeta^2}}}{1 + e^{\frac{-\pi\zeta}{\sqrt{1-\zeta^2}}}} \quad (3.13)$$

Table 3.2 summarises the values used for this design example. The final controller was

	Heave	Roll	Pitch	Yaw
Damping (ζ)	0.9	0.9	0.9	0.7
Natural frequency (ω_n)	1.6	3.6	1.2	10.99
Agility ($\frac{P_{pk}}{\Delta\phi_{pk}}$)	0.63	1.41	0.47	4.8

Table 3.2 *Four-axes command model specifications*

calculated via the two-Riccati equation solution of [20] and a suboptimal controller achieving a minimum cost of $\gamma = 4.63$ was chosen for further analysis and implementation. Note the high γ value returned by the H_∞ optimisation procedure. This is typical of models which include time delays in their mathematical representation.

A thorough analysis of the suboptimal controller was conducted via frequency response analysis, linear simulations and ground-based piloted trials. Figures 3.21 and 3.22 show the sensitivity and complementary sensitivity functions respectively. Note the large positive

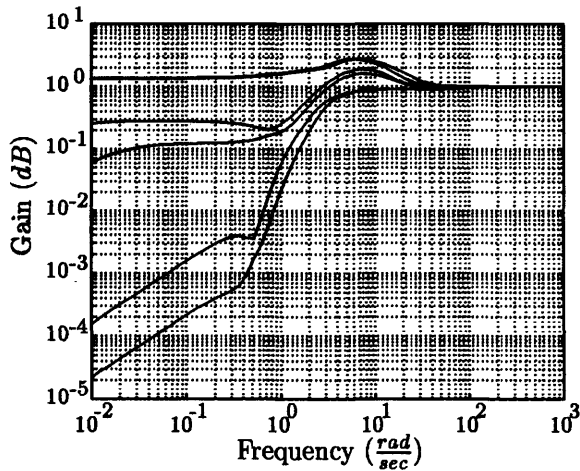


Figure 3.21 *Sensitivity function $S_o = (I - G_s K_2)^{-1}$ - Bell 205 control law*

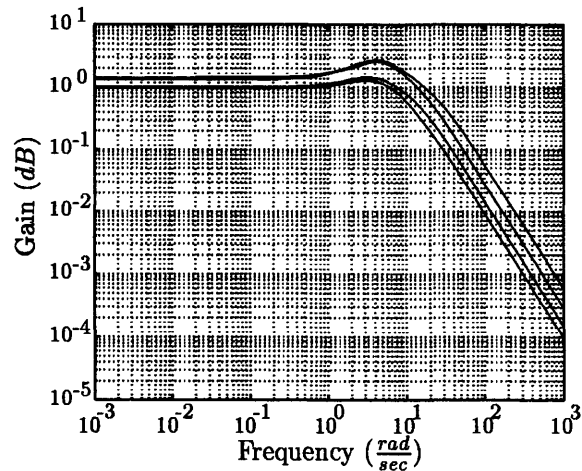


Figure 3.22 *Complementary sensitivity function $T_o = (I - G_s K_2)^{-1} G_s K_2$ - Bell 205 control law*

area under the sensitivity plot S_o . This is the so called waterbed effect and it is due to the

RHP zeros introduced by the first order Padé approximations to the time delay (see [63, ch5]). From the complementary sensitivity plot it is easy to deduce that the controller will reject all disturbances above 11 rad/sec. Thus, any excitation of the rotor rocking-mast mode above that frequency is unlikely to be caused from the sensors.

Figures 3.23 - 3.34 show the state and actuator responses of the Bell 205 to step demands on heave, pitch, roll and yaw controlled outputs. The primary loop responses are superimposed with the demands and the actuator deflections include the blade trim offsets in swashplate angular units. These Figures indicate a good design and as a consequence the controller was coded in FORTRAN and transferred to the Large Motion Simulator for piloted simulations.

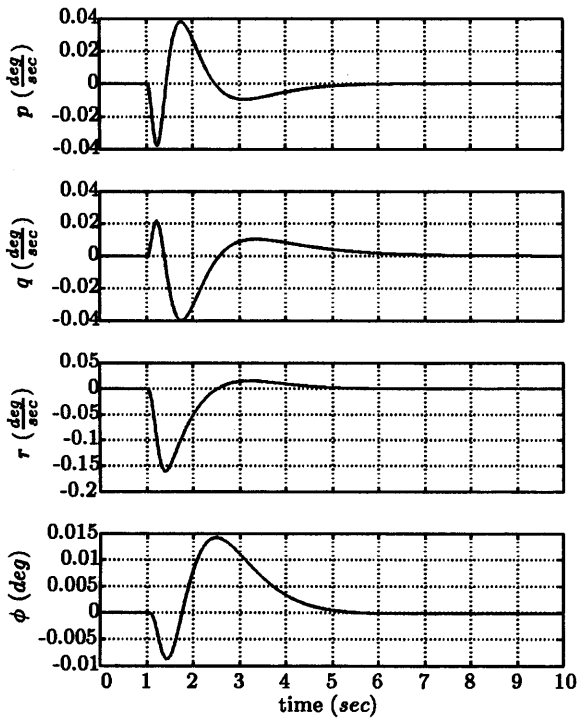


Figure 3.23 Time simulation, 5° heave demand

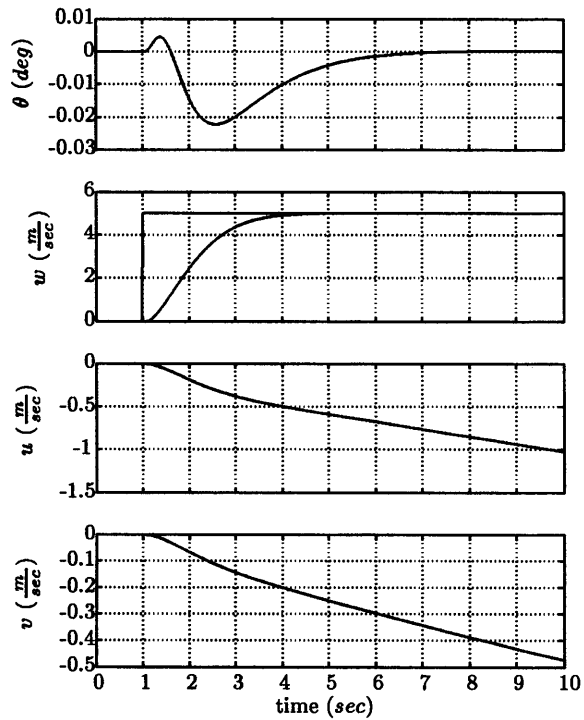


Figure 3.24 Time simulation, 5° heave demand

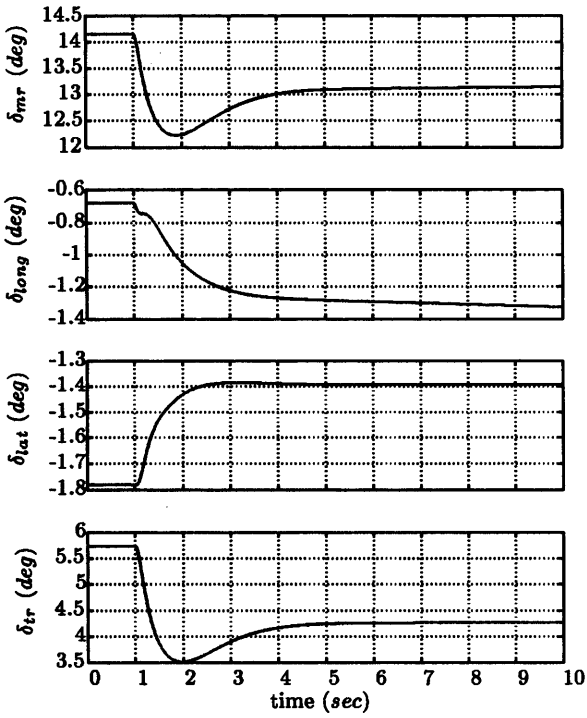


Figure 3.25 Time simulation, 5° heave demand - Actuator deflections

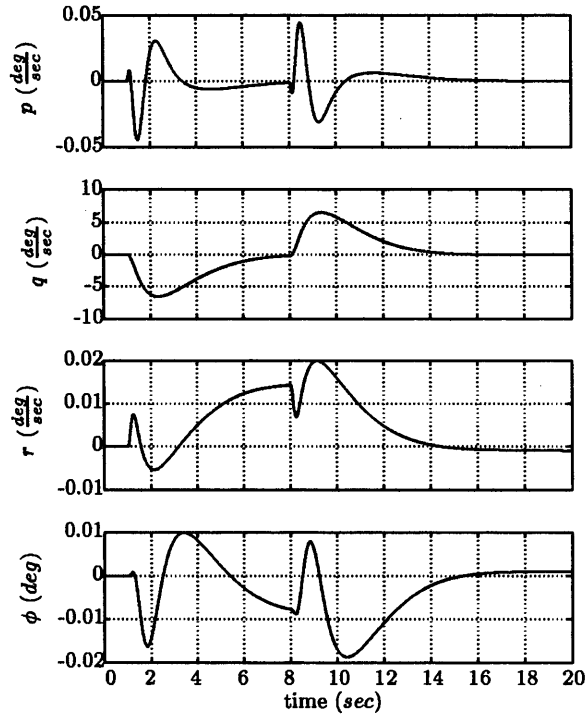


Figure 3.26 Time simulation, 5° pitch attitude demand

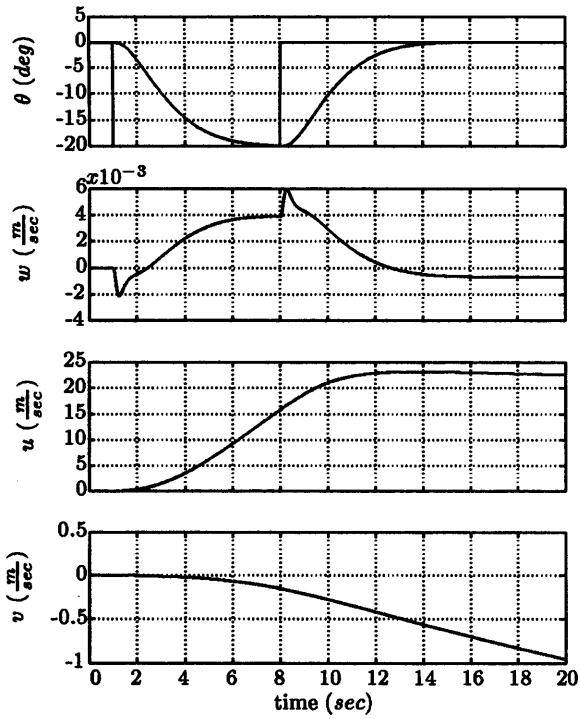


Figure 3.27 Time simulation, 5° pitch attitude demand

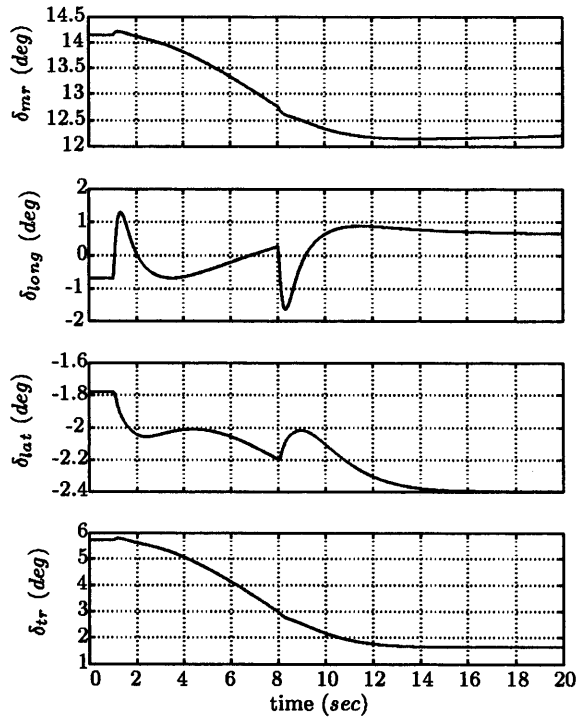


Figure 3.28 Time simulation, 5° pitch attitude demand - Actuator deflections

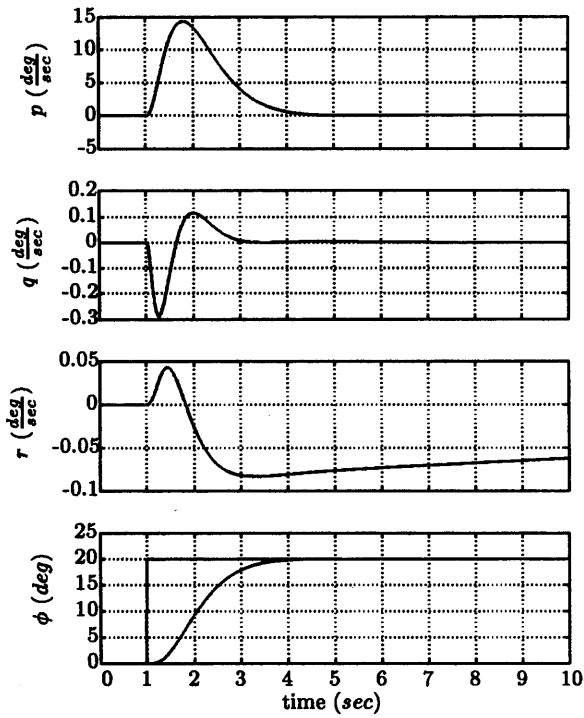


Figure 3.29 Time simulation, 5° roll attitude demand

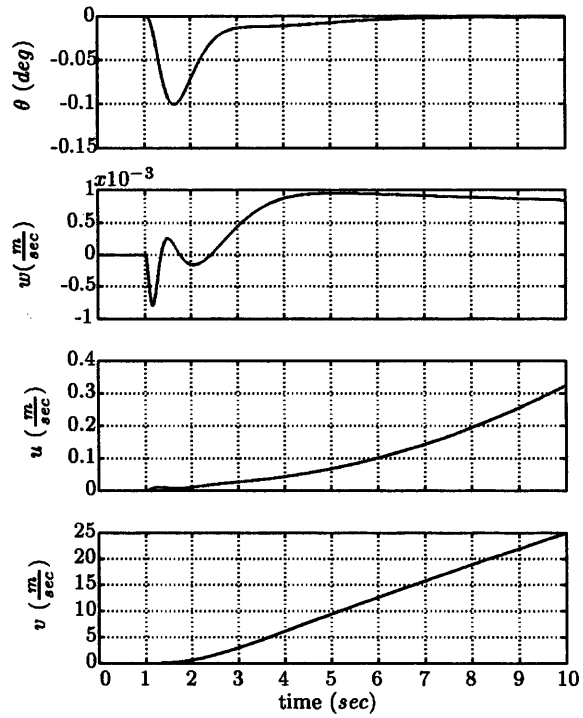


Figure 3.30 Time simulation, 5° roll attitude demand

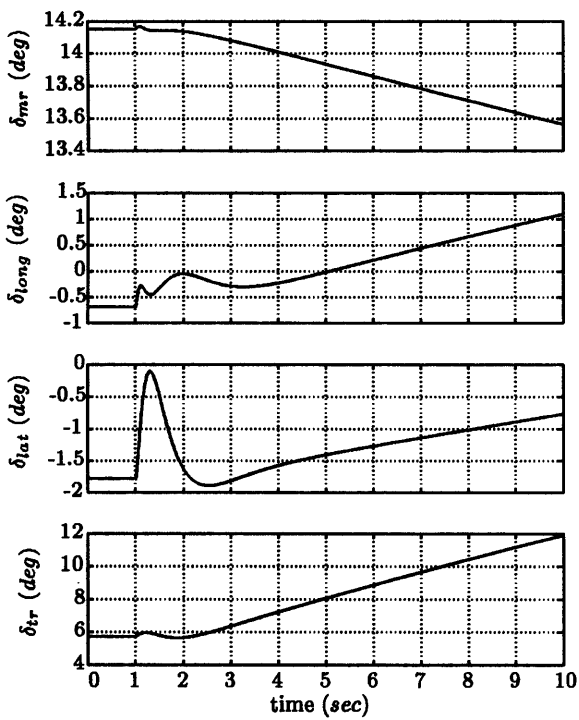


Figure 3.31 Time simulation, 5° roll attitude demand - Actuator deflections

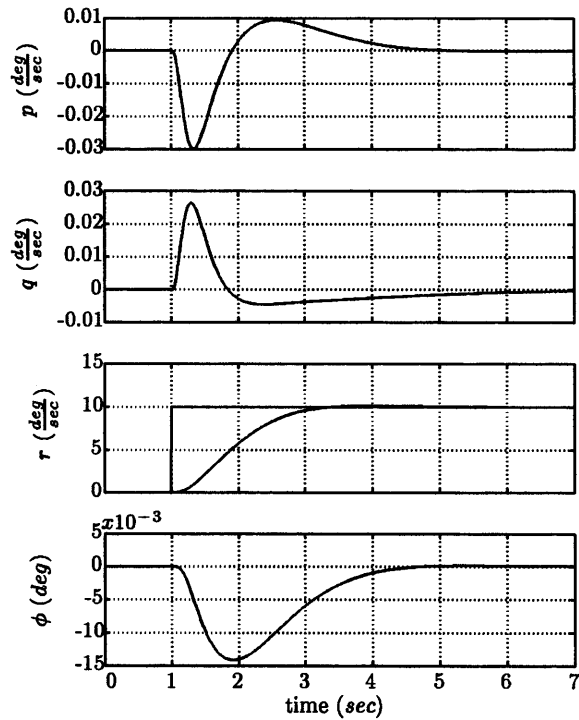


Figure 3.32 Time simulation, 5° yaw rate demand

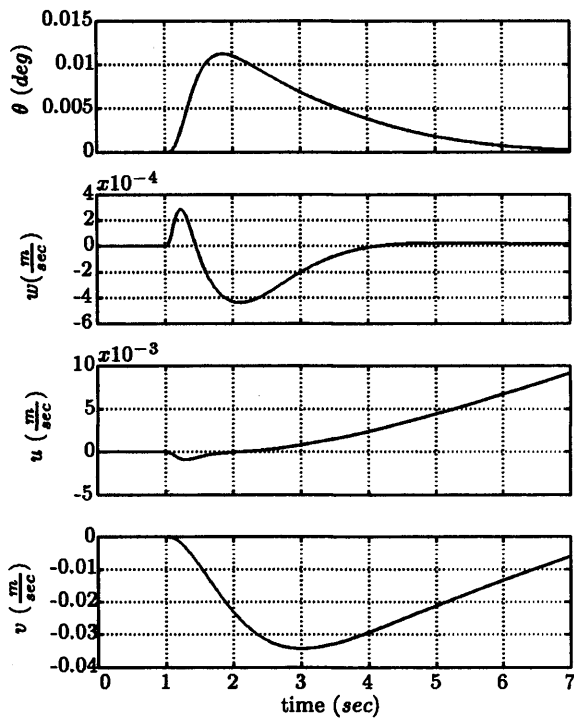


Figure 3.33 Time simulation, 5° yaw rate demand

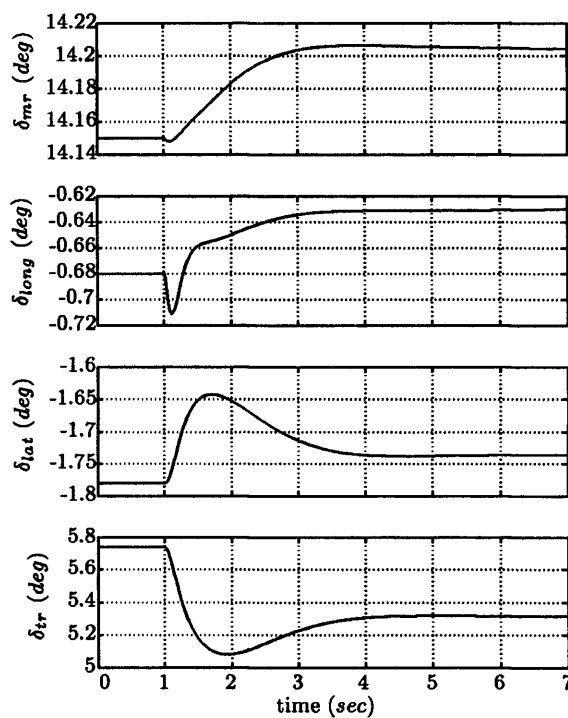


Figure 3.34 Time simulation, 5° yaw rate demand - Actuator deflections

3.6 Piloted simulation results

Whilst the design model was a linear quasi-static approximation of the helicopter, the model used for the piloted trials was the nonlinear HELISIM model [52], configured as a Bell 205 using data from [34] and [49] to provide a full flight envelope model for real-time ground-based piloted simulation. This was because the HELISIM Bell 205 configuration was not available at the time of the controller design process. The major modelling assumptions will be described later in chapter 5. For the moment, we just point out that comparisons of flight test data with the simulation model indicated that both model and actual vehicle behaved similarly in moderate speeds, but it was unknown how much uncertainty was present in the hover region. However, it was felt that the control law should be insensitive to these variations and that the closed loop simulation was adequate for HQ analysis.

The simulator configuration used a single-seat generic helicopter cockpit mounted on the Large Motion System which is capable of significant accelerations, velocities and displacements in pitch, roll, yaw and heave axes, and - depending on the orientation of the cockpit - either surge or sway axes. Visual cues were displayed via a photo-textured imaging system through five collimated cathode-ray-tube monitors mounted to approximate the field of view from the right hand seat of the helicopter. The image system provides a number of general landscape databases over which more detailed ADS-33D style task cues were superimposed. The single-seat cockpit was configured with standard cyclic, collective

and pedal controls with representative force-feel characteristics. The seat was dynamically driven to provide vibration and gravitational acceleration cueing along with audio cueing of rotor speed and blade flap. Standard attitude indicator, airspeed, barometric and radar altitude, compass and torque instruments were provided on two colour head-down multi-function displays. The transport delays of the visual system following a control input were not considered to affect the handling qualities since the delays contributed from the Bell 205's teetering rotor system are similar in length—approximately 120 – 150 *msec*.

The test scenario of the simulations involved the execution of a subset of ADS-33D manoeuvres primarily for hover and moderate speeds. The pilot was allowed some time to become familiar with the controller characteristics and functionality before specific tasks were performed. The analysis focused on the handling qualities for low, moderate, and high aggression tasks near the aircraft's limits. Comments on the closed loop system stability, inter-axis coupling, task performance and pilot workload were reported and Cooper-Harper ratings were recorded. The Cooper-Harper ratings scale shown in Figure 3.36 provided an appropriate mechanism for compiling pilot comment. On this scale ratings of 1-3 imply that achievable performance is satisfactory without improvement. Ratings of 7 or more mean that the controller has to be modified.

The controlled system's stability and performance were tested over a wide range of rotorcraft speeds until the linear controller robustness margins were "exhausted". It was found that degradation with speed was small and this gave confidence in moving onto a flight test. The operational envelope of the Bell 205 helicopter extends up to 120 *knots* IAS. However, in practice the speed envelope is limited to 90 – 95 *knots* as the teetering rotor system induces significant fuselage vibrations which result in increased stressing loads on the airframe. It was felt that a conservative approach would be the most appropriate in this case, and therefore it was decided that in-flight evaluation should present no problem for the hover regime and possibly moderate speeds.

Four Mission Task Elements (MTEs) were chosen as the basis for the control law simulation: bob-up, side-step, quick-hop and spot-turn. A description of each task and the relevant results are summarised below. A pictorial representation of the tasks can be found in appendix B.

Bob-up: This task is dominated by heave axis response; the pilot has to vertically translate the aircraft from a stabilised hover at 10 *m*, bob-up through 50 *ft* and establish a line-of sight between the top of the marker post and two marker boards positioned on the ground beyond. The task objective was to assess the primary heave response for damping and adequacy of control power, for different aggression levels, checking the torque limits and coupling into pitch, roll and yaw axes. Desired performance: to maintain plan position variations $\leq \pm 10$ *ft*, height variations $\leq \pm 5$ *ft*, heading excursions $\leq \pm 5^\circ$ and maintain torque $\leq 100\%$ (maximum continuous limit). Adequate performance: to maintain plan position variations $\leq \pm 15$ *ft*, height variations $\leq \pm 10$ *ft*, heading excursions $\leq \pm 10^\circ$ and

maintain torque $\leq 116\%$ (maximum transient limit)

Side-step: From a precision hover, the pilot was required to perform a side-step manoeuvre along a marked reference line give an initial roll attitude of 10° , 20° or 30° (defining low, moderate and high levels of aggression) to acquire and maintain a new precision hover at the far end of the course as quickly as possible. Desired performance: to maintain plan position variations $\leq \pm 10 \text{ ft}$, height variations $\leq \pm 10 \text{ ft}$, heading variations $\leq \pm 5^\circ$ ² and torque to be maintained $\leq 100\%$ (maximum continuous limit). Adequate performance: to maintain plan position variations $\leq \pm 15 \text{ ft}$, height variations $\leq \pm 15 \text{ ft}$, heading variations $\leq \pm 10^\circ$ and torque to be maintained $\leq 116\%$ (maximum transient limit)

Quick-hop (Acceleration - Deceleration): This task is similar to the side-step but pitch is the primary axis. From a stabilised hover the pilot was required to perform a 500 ft quick-hop manoeuvre along a marked reference line with an initial pitch attitude of 10° , 20° or 30° (defining low, moderate and high levels of aggression) to acquire and maintain a new precision hover at the far end of the course as quickly as possible. Desired performance: to maintain plan position variations $\leq \pm 10 \text{ ft}$, height variations $\leq \pm 10 \text{ ft}$, heading variations $\leq \pm 3^\circ$ and torque to be maintained $\leq 100\%$ (maximum continuous limit). Adequate performance: to maintain plan position variations $\leq \pm 15 \text{ ft}$, height variations $\leq \pm 15 \text{ ft}$, heading variations $\leq \pm 6^\circ$ and torque to be maintained $\leq 116\%$ (maximum transient limit).

3.7 Discussion

From the recorded pilot comments it was deduced that there were no major problems associated with the stability and vehicle limits that are of primary importance in a piloted assessment of a novel control law. There was some coupling in pitch (or more accurately in fore and aft directions), which was largely attributed to the vertical velocity measurement w being used to decouple the helicopter axes. As mentioned earlier, pilots use ground-based visual cues for hovering tasks and therefore it is more natural to “close the loop” around height rate (\dot{H}) using main rotor collective inputs. Therefore, selecting w as a primary feedback variable in the heave axis implied that the helicopter was displaced along the vertical velocity vector by the controller and the pilot needed to make adjustments in the fore and aft directions to correct the rotorcraft response with respect to height rate (\dot{H}). Although the coupling was not considered to be a significant problem, it was decided to leave the collective open loop for the first flight test. This was also a safety requirement of the flight test team - pilots prefer to have a direct command over main rotor torque forces and therefore they stay in touch with the aircraft.

The controller was designed with emphasis on robust stability and it generally gave slow

²According to ADS-33D document, heading has to be kept within $\pm 10^\circ$ for desired and $\pm 15^\circ$ for adequate performance. During the simulator trials this limit was reduced to $\pm 5^\circ$ and $\pm 10^\circ$. This practice seems justified on the grounds that on the simulator there are no wind gusts

responses which resulted in some overshoots. This is because the predictability of the rates of attitude changes becomes difficult for the pilot especially for aggressive manoeuvring. It is also known that a RC response type would be desirable for high aggression tasks, while ACAH is more appropriate for degraded visual environments ($UCE > 1$). In this work an ACAH response type was chosen over a RC because it provides greater levels of stability (rather than performance) which was seen as the main objective at this stage. Also, no turn coordination was provided as this could easily be added at a later stage. Further improvements in de-coupling and primary responses were made before the first flight on the Bell 205 aircraft. Figure 3.35 shows the pilot HQ ratings returned for each of the executed tasks. As the aggression level increased the controller performance deteriorated. It should

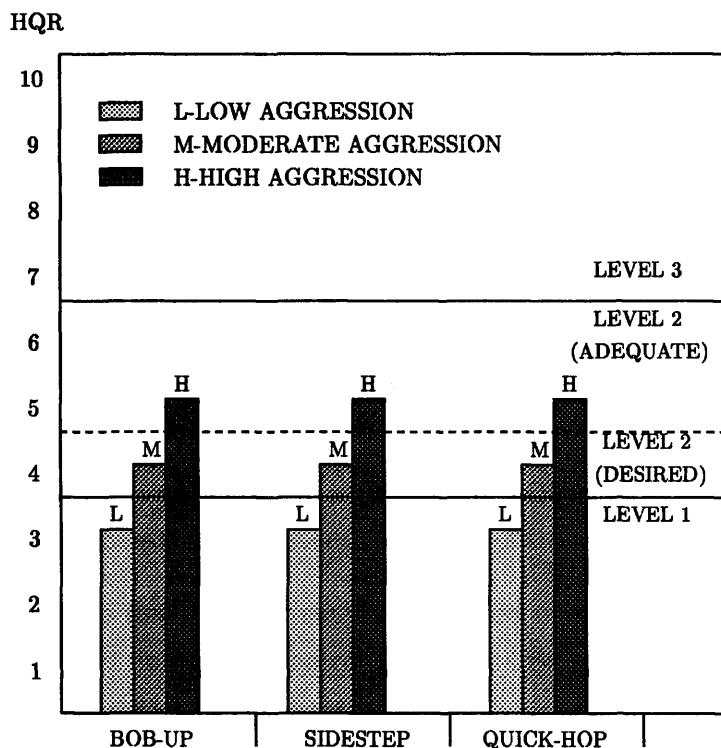


Figure 3.35 Handling Qualities Ratings: ground-based simulations for different aggression levels

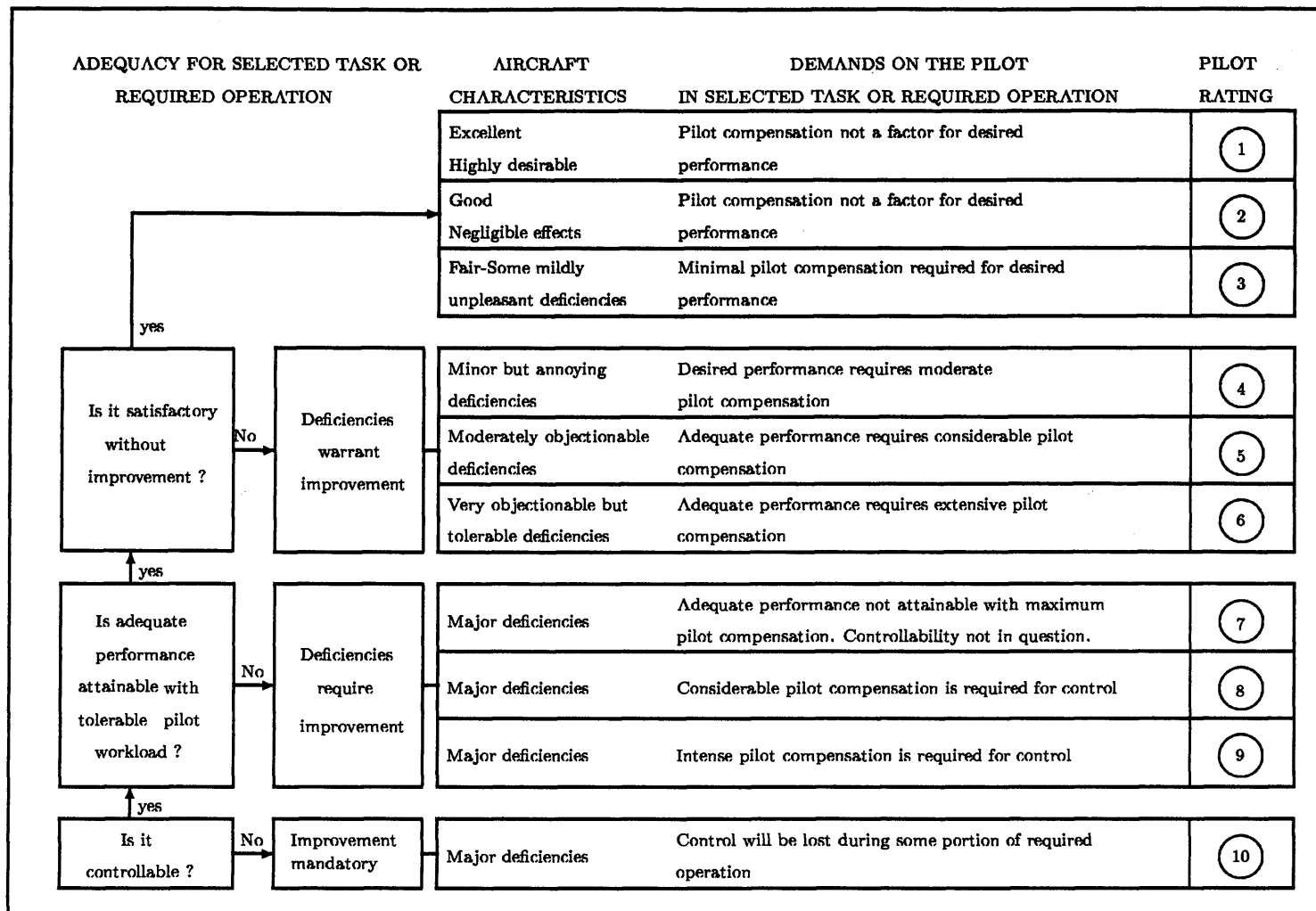
be noted here that the HELISIM model used in the piloted simulation was developed independently from the control law design (the latter was based on the NASA models) which boosted the designer's confidence about the controller's functionality. In general, the overall objectives of the trial were met and the test pilot gained sufficient experience about the control law behaviour.

So far, we have seen that piloted simulations are very useful in investigating the functionality of a novel control law and thus reducing the risks associated with the first flight. However, simulator trials are limiting in terms of conclusive statements about the controller performance and the handling qualities of the helicopter. Realistic atmospheric phenomena, such as wind gusts and turbulence, are difficult to model and hence to use in simulation. The

out-of-cockpit view and the other visual cues can be limiting for aggressive manoeuvring and therefore the necessity of a real flight test seems indisputable. However, a number of useful guidelines for designing and implementing *prototype* controllers on FBW helicopters *can* be drawn from the simulation trials. These guidelines follow closely the design philosophy reported in [39] for fixed-wing vehicles and can be summarised as follows:

- i) Design for low bandwidth capitalising on robust stability rather than performance. H_∞ and related methods are very attractive for this task since they deal explicitly with the unmodelled plant dynamics.
- ii) Use approximate integrators when implementing weighting functions containing integral action. Rounding errors and finite digit arithmetic can easily perturb some of the closed loop eigenvalues to the right half complex plane. If the feedback and forward parts of the controller are implemented using Euler integration in a single state space system then approximate integrators are necessary to guarantee the stability of the integration algorithm (see chapter 5 section 5.7 for more details).
- iii) During the first flights do not augment the heave loop. Pilots prefer a heave inceptor to function similarly to the manually flown aircraft. The demanded torque forces on the main rotor are of primary importance for structural integrity and safety of the helicopter.
- iv) Make sure that the core controller is functioning satisfactorily before designing any outer loops that complicate the overall response of the vehicle.
- v) Do not attempt to fine tune the control law based on the simulator trials alone. It is more effective to finalise the control law gains after qualitative feedback from the pilots and the inspection of the flight test data.

We shall see in the next chapter that this philosophy is clearly reflected in the test pilot's comments and the handling qualities evaluation. It will also be seen that following the above guidelines we will be able to build up on the success of the first flight and finally to obtain reasonable agreement between the piloted simulation and the flight test results.



Aggression	Minimal	Low	Moderate	High	Maximum
		□	△	◇	
Vehicle Characteristics	Satisfactory or better	Minor deficiencies	Moderate deficiencies	Objectionable deficiencies	Major deficiencies
Primary response	□ △	◇			
Stability	□ △ ◇				
Coupling		□ △	◇		
Vehicle limits	□ △		◇		
Task Performance	Clearly within desired limits	Marginally desired	Clearly within adequate limits	Marginally adequate	Adequate perf. not achievable
	□ ◇	△			
Task Workload	Minimal	Moderate	Considerable	Extensive	Intolerable
	□	△	◇		

Table 3.3 Handling qualities summary - Bob-up task

Bob-up task	Pilot comment
□	A little coupling into roll and yaw. One minor overshoot.
△	The pilot needs to get it right from the beginning of the manoeuvre. Minor fore and aft coupling.
◇	One overshoot. Coupling into yaw, heading wandered ± 5 degrees. Some fore and aft activity but not much coupling in roll. Vehicle limits difficult to observe and they limited the pilot's performance.

Table 3.4 Bob-up task: Low (□), moderate(△), high aggression (◇)

Aggression	Minimal	Low	Moderate	High	Maximum
		□	△		◇
Vehicle Characteristics	Satisfactory or better	Minor deficiencies	Moderate deficiencies	Objectionable deficiencies	Major deficiencies
Primary response	□	△	◇		
Stability	□ △ ◇				
Coupling	□	△	◇		
Vehicle limits	□ △ ◇				
Task Performance	Clearly within desired limits	Marginally desired	Clearly within adequate limits	Marginally adequate	Adequate perf. not achievable
	□ △			◇	
Task Workload	Minimal	Moderate	Considerable	Extensive	Intolerable
	□	△	◇		

Table 3.5 Handling qualities summary - Sidestep task

Sidestep task	Pilot comment
□	No problem. Easy to do.
△	A bit slow, it required some pilot anticipation to get the deceleration right. If you get it wrong you'd overshoot. Some fore and aft activity.
◇	Maximum aggression used (the pilot was limited by the stick displacement). Predictable, well de-coupled but not fast enough at the last stages of the manoeuvre. Some fore and aft coupling.

Table 3.6 Sidestep task: Low (□), moderate(△), high aggression (◇)

Aggression	Minimal	Low	Moderate	High	Maximum
		□	△	◇	
Vehicle Characteristics	Satisfactory or better	Minor deficiencies	Moderate deficiencies	Objectionable deficiencies	Major deficiencies
Primary response	□ △	◇			
Stability	□ △ ◇				
Coupling	□	△ ◇			
Vehicle limits	□ △ ◇				
Task Performance	Clearly within desired limits	Marginally desired	Clearly within adequate limits	Marginally adequate	Adequate perf. not achievable
	□ △ ◇				
Task Workload	Minimal	Moderate	Considerable	Extensive	Intolerable
	□	△	◇		

Table 3.7 Handling qualities summary - Quick-hop task

Quick-hop task	Pilot comment
□	Not a problem.
△	Coupling into roll, difficult to maintain track
◇	Again difficult to maintain track due to roll coupling. Considerable workload due to the poor field of view

Table 3.8 Quick-hop task: Low (□), moderate(△), high aggression (◇)

In this chapter, we describe the flight test results of the H_∞ controller, designed in chapter 3, on the Bell 205 FBW helicopter. Whilst the ground-based simulation trials are useful for an initial assessment of the controller, a reliable investigation of the controller's performance can be made only in flight. We shall address the issue of robust stability by repeating the experiments performed on the Motion Simulator on the real aircraft: the Canadian National Research Council (NRC) Bell 205 Airborne Simulator. The additional benefit of these flight tests is that apart from the qualitative assessment of the controller the recorded flight test data allow for a quantitative analysis of the controller performance. It should be remembered though that these assessments are valid only to the extent that the controller design model and the actual helicopter behaviour are similar.

The objectives of the experiments presented in the next two sections focus on three tasks, namely:

- Evaluation of the H_∞ controller in hover and at moderate speeds
- Assessment of the robust stability properties of the H_∞ -based control system
- Comparison of the in-flight performance and handling qualities ratings with:
 - i) desk-top computer-based predictions, in order to provide guidance for future designs based on H_∞ optimisation;
 - ii) motion-based piloted simulations to enable better models to be derived; and
 - iii) the latest handling qualities specifications ([3]) to assess overall performance.

The chapter concludes with a summary of the experimental findings from the evaluation of the H_∞ controller and a number of suggestions for further enhancement of the H_∞ -based system.

4.1 The Bell 205 fly-by-wire helicopter

The NRC Bell 205 airborne simulator shown in Figure 4.1 is an extensively modified version of the Bell 205A-1 general-purpose helicopter and serves as a fly-by-wire variable stability platform for the in-flight simulation of other aircraft, in-flight investigation of control system characteristics and investigation of cockpit systems. The standard Bell 205A-1 helicopter



Figure 4.1 The NRC Bell 205 Airborne Simulator

has an all-metal semi-monocoque fuselage and is powered by a single turbo-shaft engine. Since the arrival of the Bell 205 at the NRC, several modifications have been carried out to enable FBW capabilities. These modifications can be summarised as follows:

- The helicopter is configured to have a Safety Pilot (SP) flying from the left-hand seat and an Evaluation Pilot (EP) flying from the right-hand seat. The original aircraft actuators have been replaced with specially built dual mode electro-hydraulic actuators that can be either electrically or mechanically controlled. During normal flight these actuators behave the same way as the original actuators and are mechanically actuated. During FBW flight, these actuators are electrically controlled by the EP to change the swashplate angles, but can be mechanically overridden if the safety pilot exceeds a given control breakout force.
- The standard Bell 205A-1 stabiliser bar has been removed to enhance the control response of the teetering rotor and the cyclic-to-elevator has been fixed in position with the interlink to the cyclic removed.
- The tail rotor assembly has been replaced with a Bell 212 wide-cord, right side mounted tail rotor.

A more detailed description of the NRC Bell 205 facility can be found in [8, 59].

	Roll	Pitch	Yaw
Damping (ζ)	0.9	0.9	0.7
Natural frequency (ω_n)	3.6	1.2	10.99
Agility ($\frac{p_{pk}}{\Delta\phi_{pk}}$)	1.41	0.47	4.8

Table 4.1 *Rotational-axes command model specifications*

4.2 Flight test

Following the piloted simulation trials presented in the previous chapter, the controller was redesigned to accommodate the pilot's comments from the piloted simulations. The heave loop was left unaugmented so that the pilot has a direct "feel" of the resulting torque from the heave inceptor demands. Thus, the parameters of the ideal model used in the controller synthesis were fixed as shown in table 4.1 and a suboptimal controller achieving $\gamma = 4.9$, was finally synthesised. Frequency and time response analysis was performed and the resulting responses were similar to those in chapter 3 (see section 3.5).

4.2.1 Coding and software requirements

A "continuous-time" version of this controller was coded in C for the on-board computer of the Bell 205. The dynamic parts of the controller (the feedback observer, the ideal model and the weighting function W_1) were numerically integrated using Euler-type integration. The iteration rate was set at 15 msec, which is compatible with the clock rate of the NRC Bell 205 Motorola 68040 processor. The control law code used for the integration can be found in appendix A. It is out of the scope of this thesis to provide the whole listing of the flight control software. There are thousands of lines of code monitoring the overall FBW system within which the controller code was executed only once per cycle.

The headers describe roughly the sub-blocks of the routine. In the initialisation the sensitivity of the dead-banded pilot demands (DANET, DENET, DRNET) is reduced by a factor of five and the feedback variables are being trimmed at the required flight condition.

Variables FSW_REG and BIT_8 set the conditions for mixed rate feedback. This feedback provides delay-free predictor-type rate signals for the control system. The functionality of this feedback will be discussed in the next chapter. For the evaluations presented here the pilots disabled this feature.

The rest of the code integrates the continuous controller states as seen in the controller block diagram (see Figure 3.18 in chapter 3). Note that the number of states being integrated is: six for the ideal model, 14 for the feedback controller and three for the pre-compensator.

Several ground checks were carried out to ensure that the computational requirements of the overall on-board software did not exceed the available microprocessor computing power.

Testing of the controller on the ground revealed that with zero feedback signals any inceptor input would result in a fast unstable response (indeed, there is no reason why it shouldn't). To ensure that the instability arose from the zero feedback and not from the controller implementation, the original eight-state design model used for controller design was also programmed into the on-board computer and the controller was simulated in closed loop form. Playback of the recorded signals confirmed the similarity of the closed loop output responses observed in the computer simulations and the aircraft on-board computer, and subsequently the helicopter was rolled out for flight tests.

Successful engagement was achieved on the first flight and a total of 8 hours FBW time was accumulated in one week. The weather conditions for the handling qualities evaluation on the final day were recorded as: wind - westerly 5 – 25 *knots*; temperature 25 to 30° *Celsius*; visibility good (UCE=1); humidity 50 – 85%; typical fuel load, 1400 *lbs*.

4.2.2 Inceptor configuration

The Evaluation Pilot (EP) used a side-stick 2 + 1 + 1 configuration; a two-axis force sensing side-stick was used to command pitch and roll attitudes with a conventional collective lever. Unfortunately the active force-feel system for the conventional controls was unserviceable which meant that the evaluations were performed with zero spring force (non-centring pedals).

4.2.3 Instrument Configuration

The current configuration of the NRC Bell 205 helicopter incorporated a set of standard head down instruments, but no airspeed indication was available below 30 knots. At the time of the flight test Doppler ground speed information was also not available. The EP was provided with torque indicators which were driven electrically with a 5% bias upwards for safety margins.

4.2.4 Pilot experience

The evaluation pilot was a qualified test pilot who's flight hours were 3900 with 3700 on rotary wing aircraft. Previous experience on Bell 205s was limited with some 20 hours flown approximately 10 years before the evaluation.

4.2.5 Test manoeuvres

The flight test plan covered both open- and closed-loop evaluation at hover/low speed and informal assessment at higher forward speeds (> 45 *knots*) in the circuit around the NRC airfield. Open-loop testing consisted of step, doublet and frequency sweep inputs in each axis for model identification purposes. Data recorded from closed loop tests were used for

benchmarking against ADS-33D open-loop criteria as well as to provide the pilot with an overall feel of the dynamic performance of the controller. The core element of the handling qualities evaluation, were the hover/low speed flight test manoeuvres described in chapter 3 with the addition of one single-axis task in yaw and two multi-axis tasks as defined by the ADS-33D specification. A short description of the extra manoeuvres is given below:

Spot-turn (Turn-to-target): This manoeuvre is initiated from a precision hover at an altitude of approximately 50 *ft* with a rapid heading demand through 180° to acquire and track a stationary ground target, while maintaining plan position. The primary objective of the task is to check for ability to recover from a rapid turn with sufficient precision and to assess the cross coupling between the rotorcraft axes. Desired performance: to maintain plan rotorcraft position of a reference point on the ground within 6 *ft* to maintain altitude and heading within ± 3 *ft* and $\pm 3^\circ$ respectively, and to complete the turn in less than 5 *sec*. Adequate performance: to maintain plan position within 12 *ft*, altitude within ± 6 *ft*, heading within $\pm 6^\circ$ and to complete the turn in less than 10 *sec*.

Precision hover: From a ground speed between 6 and 10 knots the pilot is required to fly to the target point (at 45° from the aircraft heading) and establish a stabilised hover. Desired performance: to attain hover within 3 *sec* of the initiation of the deceleration and maintain a stabilised hover for at least 30 *sec*; to maintain plan position within ± 3 *ft* altitude within ± 2 *ft*, and heading below $\pm 5^\circ$. Adequate performance: to maintain plan position within ± 6 *ft* of the ground reference point, altitude below ± 4 *ft* and heading less than $\pm 10^\circ$.

Pirouette: From a stabilised hover the pilot is required to translate the rotorcraft along a circumference of a 100 *ft* radius circle at an altitude of 10 *ft*, keeping the aircraft nose pointed at the centre of the circle. Desired performance: to maintain a position of 10 *ft* from the circumference of the circle, to keep altitude less than ± 3 *ft*, to maintain heading with respect to the circle centre less than 10° and to complete the circle within 45 *sec*. Adequate performance: to maintain the position from the circumference of the circle within 15 *ft*, altitude within 10 *ft* heading within $\pm 15^\circ$ and to complete the circle within 60 *sec*.

4.3 Handling qualities evaluation

Initially, the pilot flew a few circles around the designated flight test area which gave an overall assessment of the aircraft handling up to 80 *knots* IAS. Although the control law did not incorporate any turn coordination signal - a basic requirement providing the appropriate response type in lateral/directional axes during forward flight. The following comments were made:

4.3.1 Forward flight - pilot observations

The longitudinal cyclic inputs were dead beat and predictable but a little sluggish. Roll response was lightly damped and the bank angle was limited to about $\pm 30^\circ$. Flight path control was easy and there was little coupling between the cyclic axes. Although the response was adequate for, say, instrument flight, the ability of the controller to maintain roll attitude was poor as the bank angle tended to wander about $3 - 5^\circ$. Pitch attitude hold was good and airspeed hold (through the pitch axis) was relatively good.

The aircraft responses to collective were as expected with small amounts of coupling into roll and yaw. These off-axis responses were suppressed with minimal pilot workload.

Pedal inputs were hard to coordinate in order to achieve the turn desired. The controller was found to be increasing the pilot workload due to two effects: the yaw rate response type in combination with the non-centring pedals made turn coordination a difficult manoeuvre to execute.

4.3.2 Mission task elements - pilot Observations

A number of practice runs (typically 2-3) were made on each MTE for familiarisation purposes before an evaluation was conducted. The evaluation was followed by a pilot self de-brief using a cockpit questionnaire similar to the ground-based trials. At the end of each sortie a more detailed de-brief was conducted with the engineers. It should be noted that all the MTEs were flown in the presence of a $15 - 20 \text{ knots}$ cross wind. Below is a brief summary of pilot comment.

Side-step: The right side-step was flown up to maximum aggression¹ and desired performance limits were achieved in all but the yaw axis. Demanded bank angles were up to 25° to initiate the manoeuvre and up to 30° to arrest the manoeuvre. The roll rate response was deemed adequate for the task, but the pilot found selecting a desired bank difficult with the force-sensing side-stick. During deceleration strong coupling with the pitch axis caused the aircraft to drift. However, it was possible to suppress this coupling with small but frequent longitudinal inputs. The dominant workload factor in this manoeuvre was poor heading control and only adequate performance was achieved in this axis. Also, torque monitoring contributed significantly to the pilot workload as the power margins were barely adequate; HQR 5.

Quick-hop: Similar to the side-step, the quick-hop task was flown to maximum aggression. However, in this case the torque limits were almost reached. Pitch response was crisp, predictable and satisfactory for the task. Commanded angles were $25 - 30^\circ$ and very little off-axis activity was noted. However, torque monitoring increased pilot workload. Deceler-

¹Maximum aggression denotes the force level that the pilot applied to the side-stick which does not necessarily imply that the aircraft reached its attitude limits. For cyclics with motion it means that the stick was deflected fully until the stop position

ating with 30° nose up required a lot of pedal activity and only marginal heading control performance was achieved. As the aircraft pitched down to the hover a large couple in to roll was observed and considerable pilot effort was necessary to establish a stabilised hover. Despite this, desired performance was achieved in all axes, but the yaw response made the execution of the task difficult; HQR 5.

Precision hover: The precision hover manoeuvre into the wind was easy to conduct and it was easy to achieve the desired performance. The roll hold was not as tight as the pilot would have liked and the bank angle oscillated by $\pm 2^\circ$. Significant pedal activity had to be used again to compensate for small heading excursions ($\pm 2^\circ$); HQR 4.

Pirouette: Considerable pilot workload was required to complete the task, especially to achieve the desired yaw rate, to maintain adequate yaw pointing task performance. Roll control was only just adequate and the ground speed was fairly constant. Frequent pitch inputs were necessary to compensate for the pitch transients as the rotorcraft was flown into and out of the wind. The overall performance was marginally adequate which resulted in extensive workload; HQR 5.

Turn-to-target: Very little cross coupling was observed during the initial pedal input. The yaw rate generated was satisfactory for the task and a 180° rotation was achieved in less than 5 sec. During more rapid turns some coupling between roll and yaw was observed and moderate pilot workload was required to compensate for this activity. Demanding opposite yaw rate to arrest the manoeuvre resulted in a smooth, predictable and well-damped response so that the required heading was repeatedly achieved (less than $\pm 2^\circ$) with a single input and no overshoots. The primary response was characterised as outstanding, ideal for rapid weapon aiming; HQR 4.

The above handling qualities ratings are summarised in Figure 4.2 and can be seen to be comparable to the ground-based piloted simulations.

4.4 Quantitative analysis of the flight test data

Figure 4.3 presents a flow chart of the data analysis procedure, for the set of data that were collected from the on-board sensors of the NRC Bell 205 helicopter. As shown in the chart, the primary objective of the test data analysis is to gain information about the achieved bandwidths and phase delays, and to provide qualitative and quantitative analysis of the helicopter handling qualities. For the tasks *A*, *B* and *C* (estimation of closed loop frequency responses) we shall use the transfer function estimation methods as in chapter 3; task *E* was completed in the previous section and the remaining task *D* (characterisation of the pilot workload) will be addressed using the Power Spectral Density (PSD) function of the input control activity. Figure 4.4 shows a typical PSD function consisting of two frequency components relating the input control activity to guidance and stabilisation tasks. The cut-off frequency on a PSD plot illustrates the pilot workload and it is defined as the frequency

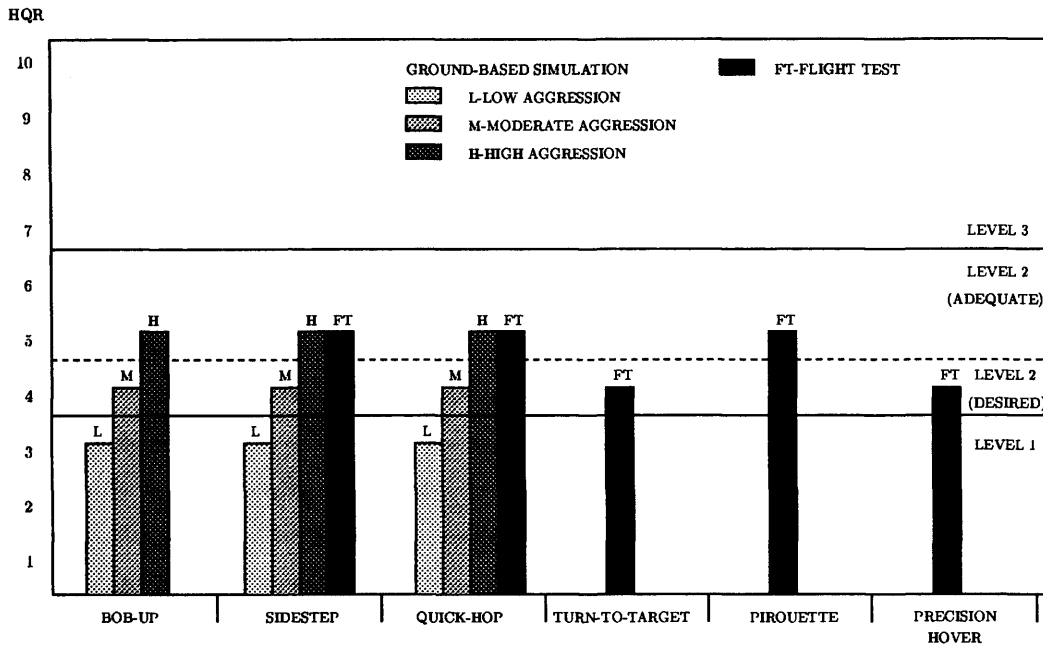


Figure 4.2 Handling Qualities Ratings: ground-based simulations vs flight test

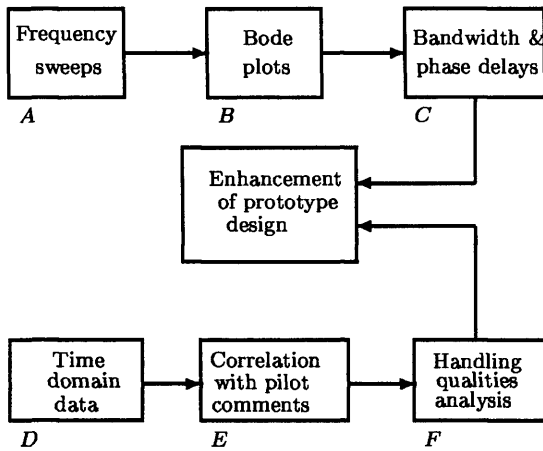


Figure 4.3 Test data analysis procedure

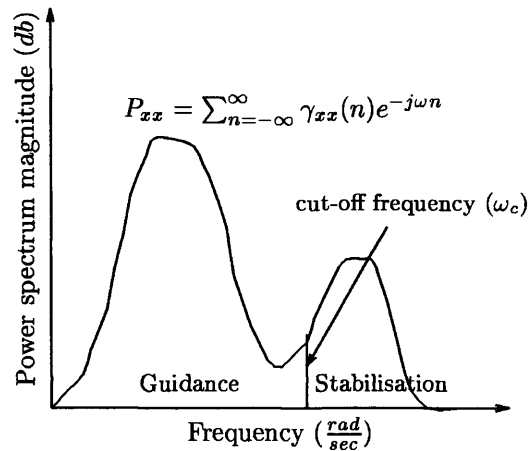


Figure 4.4 Power spectral density function

at which 70% of the energy has been accounted for². The stabilisation frequency is aircraft dependent (governed by rigid rotor inertia and rotor design) and remains constant. As the task difficulty increases, both the cut-off frequency and the magnitude of the navigation components will increase. When the guidance and stabilisation tasks overlap the increase in pilot workload is dramatic, which indicates high levels of aggression are needed to cope with the coupling and therefore an increased HQR is anticipated.

Forward flight: From the EP's comments it is evident that a tighter attitude hold loop would improve the rotorcraft response. It has to be noted here that the controller was designed using a hover linearisation from ([34]) and it was intended to be primarily for low speed. The fact that the helicopter could be flown with confidence up to 80 knots

²In a sense the cut-off frequency is analogous to the 3 dB cross-over frequency for servomechanisms

IAS is thought to be very encouraging for the evolution of the H_∞ -based control system. The increased pilot workload due to the inconsistency of the pedal inputs with the desired response type is not difficult to explain. In forward flight pilots can demand heading changes using pedals as well as lateral stick inputs. This is because the directional stability increases with airspeed and heading naturally changes through rolling demands. Therefore, the unaugmented aircraft has a naturally coordinated turn which was suppressed by the control law in order to achieve yaw rate tracking. To avoid this rate suppression it is customary to construct a turn coordination signal from the output measurements and cross-feed it to the pedal demands. However, as mentioned earlier, the evaluation was intended to be for hover speed and therefore a turn-coordination loop was not considered important.

Side-step: The difficulty in maintaining heading was primarily attributed to the non-centring pedals. The pilot had to make frequent and often large corrections which considerably increased his workload. Figure 4.5 shows the time histories of pitch, bank and heading angles during a side-step task. From the Figure it can be seen that as soon as the

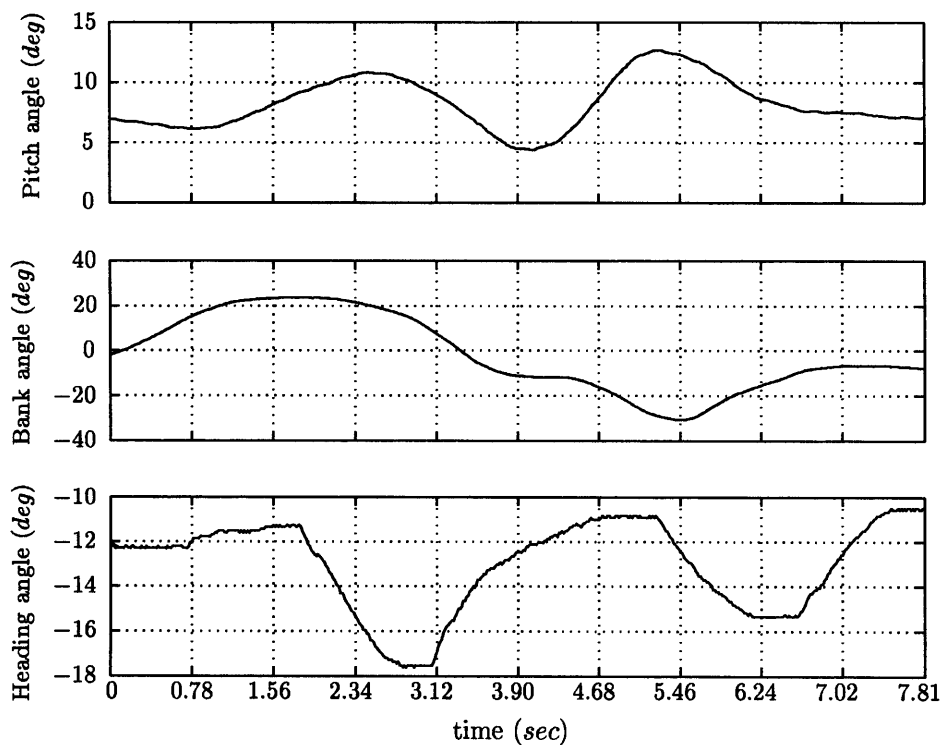


Figure 4.5 Time histories of the pitch, bank, and heading angles during side-step task

helicopter achieves $20-23^\circ$ of roll attitude there is an evident cross coupling into yaw which is maintained within desired performance limits³ only at the expense of high pilot workload. The achieved bank angles (23.6° and -30.5°) were reached within 1.7 and 5.4 sec from the initiation of the manoeuvre. Therefore, since the task was flown to maximum aggression, the roll rate generated by the controller should have been faster in order to achieve these

³Recall that heading has to be kept within $\pm 10^\circ$ for desired and $\pm 15^\circ$ for adequate performance

attitudes within 1.5 sec from the initiation of the positive and negative lateral accelerations as ADS-33D requires. The EP also commented on the difficulty in commanding roll angles with the side-stick inceptor. This is “almost” certainly the case as the bank attitude seems to be constant at -16° between 3.90 and 4.68 sec. The “almost” is justified on the grounds that the EP’s attention could also have been diverted to compensate for the pitch and heading attitude excursions which occurred around 3.90 sec. From the PSD plot of

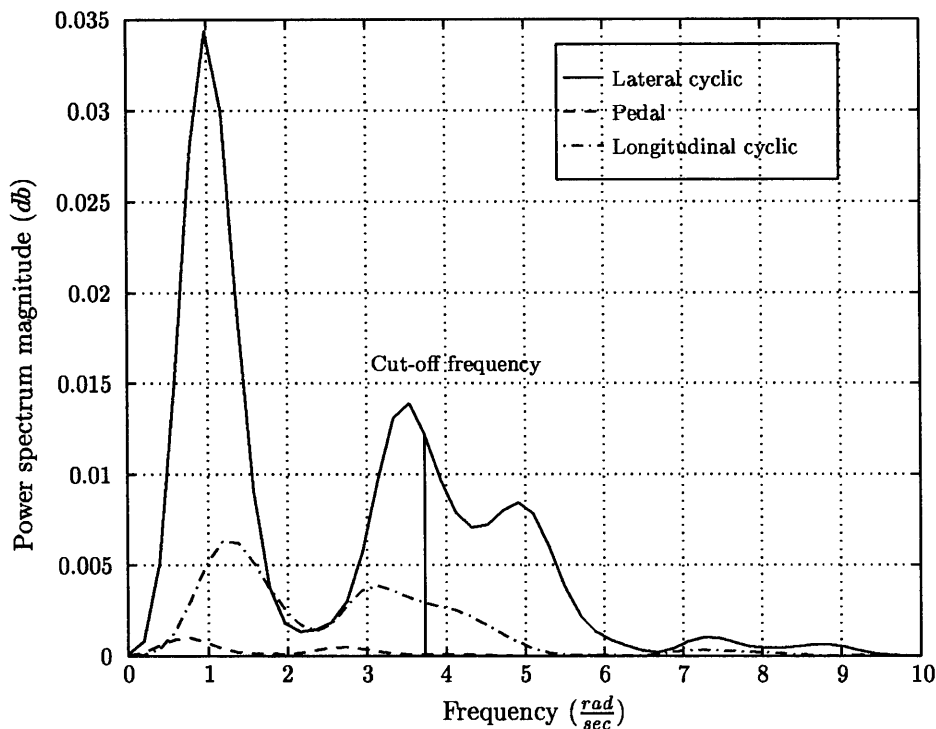


Figure 4.6 Power spectral estimates of input signals during side-step task

the of the pilot inputs (Figure 4.6) it can be observed that the activity in the longitudinal channel consists of one guidance region of large magnitude and two smaller peaks related to stabilisation frequencies. The pilot effort in the stabilisation frequencies was necessary to compensate for the strong pitch transients during the deceleration phase as reported by the test pilots. However, in the EP’s comments this longitudinal activity was of secondary importance as the heading excursions approached the limits of the desired performance. In any case, the HQR rating returned (HQR=5), was definitely representative of the pilot workload, since the EP’s effort in the stabilisation frequencies was considerable.

Quick-hop: Similar arguments to those employed on the side-step manoeuvre can be used to explain the yaw activity reported by the EP during the deceleration phase of the quick-hop manoeuvre. Figure 4.7 shows the time histories of the pitch, bank and heading attitudes during a quick-hop task. The helicopter, initially, achieved -19.6° of pitch attitude and a demand of 23.9° was required to decelerate the aircraft. Desired performance (in terms of cross-couplings) was achieved in all axes, but the controller was slow and the pitch

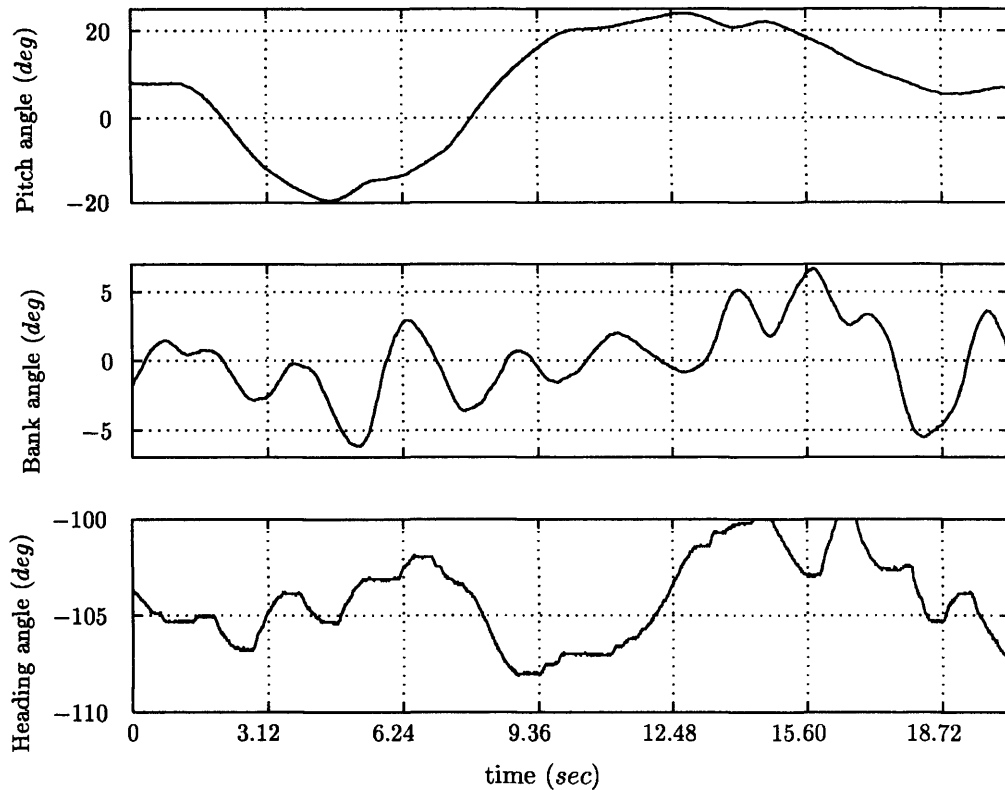


Figure 4.7 Time histories of the pitch, bank, and heading angles during a quick-hop task

rate generated was not adequate to meet the attitude quickness ($\frac{q}{\Delta\theta}$) requirements. Figure 4.8 shows the PSD plot of the input activity during the quick-hop task. It can be seen that frequent stick inputs in the lateral loop were of significant magnitude in the stabilisation frequencies and this was clearly reflected in the pilot's comments.

Pirouette: As with the other manoeuvres, demanding the required yaw rate with zero spring pedal stiffness imposed a high workload on the pilot. This workload was further increased by two factors: a) The aircraft was yawing into and out of the wind direction and the horizontal stabiliser was generating large pitching moments causing the aircraft to shift in the fore and aft directions. b) The combination of a force sensing side-stick with the particular H_∞ ACAH controller was unfamiliar to the EP. The controller had been designed for robust stability and not for performance and therefore, the control response of the aircraft was slow. Thus, the predictability of the commanded rates was poor, which did increase the overall workload.

Precision hover: Although the plan variation of the rotorcraft was not measured, due to the absence of GPS information, the data recorded confirm the pilot observations about the roll and heading variations. Figure 4.9 shows the bank and heading attitudes and indicated altitude (IA). Indeed, for most of the manoeuvre the bank and heading angles oscillated $\pm 2^\circ$, while IA varied only ± 1 ft. This motivates further the need for a heading hold loop as well as a tighter attitude hold as encountered in forward flight.

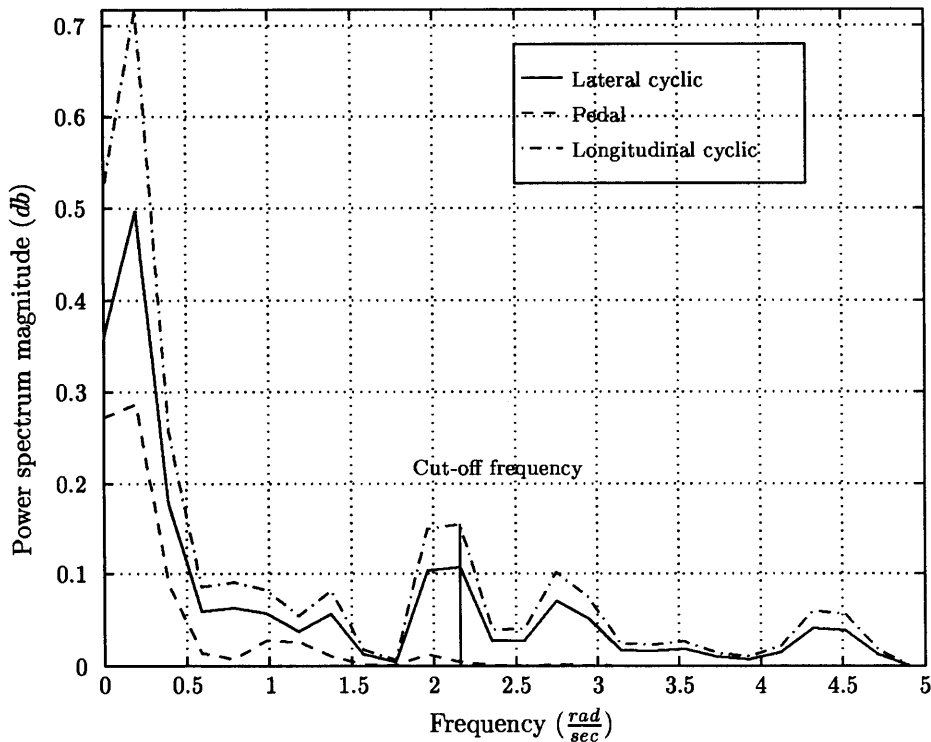


Figure 4.8 Power spectral estimates of input signals during a quick-hop task

Turn-to-target: In all the previous manoeuvres, the secondary task of heading control had been found to dominate pilot workload. However, for the turn-to-target manoeuvre where heading control was the primary task, the pilot commented very favourably on the outstanding ability to rapidly and precisely stabilise on a given heading. Figure 4.10 shows the pitch, roll and heading angles during a 180° turn-to-target manoeuvre. From Figure 4.10 it can be seen that the 180° turn was completed within 5.2 sec and the heading was stabilised within 2.5° from the chosen ground reference. The coupling into longitudinal and lateral loops was not of significant magnitude as in the previous tasks. This observation can also be confirmed from the PSD plot of the inceptor signals (Figure 4.11), where minor cross activity was required to maintain the plan position of the helicopter. Note that the small pilot effort in the stabilisation frequencies indicates that the yaw rate wash-out was highly predictable and well-damped. Therefore, given full attention, the pilot was able to compensate for the lack of force-feel on the pedals and desired performance was relatively easy to achieve.

Frequency sweep testing was conducted to establish the achievable bandwidths and phase delays for comparison with the desk-top simulations. At least two frequency sweeps were flown in each axis to ensure that good records were available for identification purposes. Figures 4.12, 4.14 and 4.16 show the frequency sweep inputs recorded from lateral, longitudinal and yaw inceptors, respectively. The data were pre-processed and Fast Fourier Transform spectral analysis was applied to the resulting input/output histories to identify

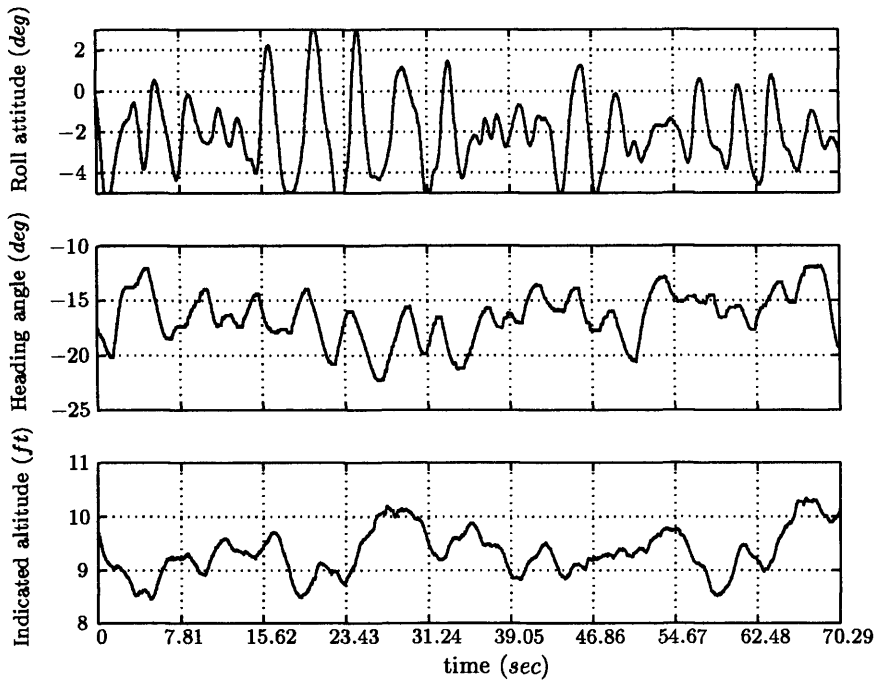


Figure 4.9 Time histories of the bank angle, heading angle and indicated altitude during a precision hover manoeuvre.

the closed loop frequency response magnitudes and phases. Figures 4.13, 4.15 and 4.17 show the estimated closed loop frequency Bode plots alongside their respective coherence function plots for these sweep inputs. Note that for the estimation of the pitch and yaw closed loop frequency responses the rate measurements were used (shifted by the inverse of the Laplace operator). This is because the rate sensors can provide less noisy signals (when compared with attitude measurements) as well as because heading crossed the 180° discontinuity during the frequency sweep. The coherence functions indicate that the identified linear responses are valid up to 5 rad/sec for roll, 7 rad/sec for pitch and 3.5 rad/sec for yaw. The reduced coherence values on Figures 4.13, 4.15 and 4.17 are primarily due to

- i) the non-linear relationship between input and output, and
- ii) the off-axis inputs required to trim the helicopter at the current flight condition.

Both these are of primary concern when evaluating control laws in-flight as argument i) relates to the level of compensation of the helicopter non-linearities in the primary axis and argument ii) is a measure of the de-coupling performance of the controller. From the definition of the coherence function $\gamma^2_{uy}(t) := \frac{|P_{uy}|}{P_{uu}P_{yy}}$ we can see that if the off-axis control is uncorrelated with the on-axis inputs there will be a resulting drop in the coherence values. On the other hand, if the off-axis control correlates to the input-output signals of interest, then the resulting coherence will not necessarily reflect the true errors in the transfer function estimates. Therefore, the inherent coupling between the four axes of the

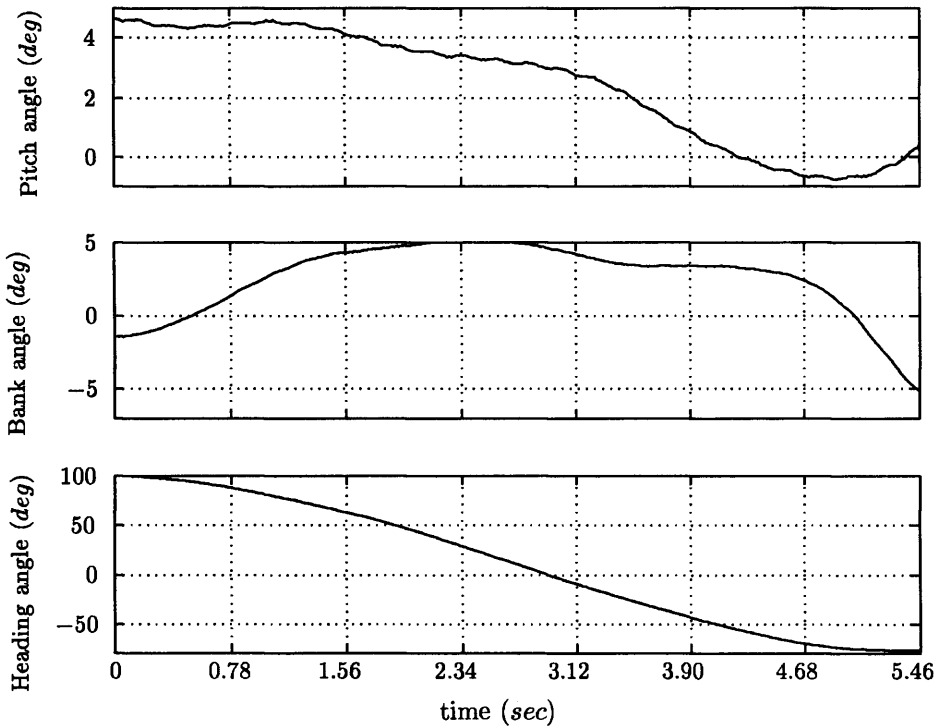


Figure 4.10 Time histories of the pitch, bank, and heading angles during a 180° turn-to-target manoeuvre.

helicopter has to be minimised by the pilot (or the flight control system in a closed loop setting) for meaningful frequency domain analysis to be carried out.

Based on the phase definition of the bandwidth⁴ the calculated closed loop bandwidths for the controlled axes are shown in table 4.2 alongside the predicted values from desk-top simulations of the previous chapter. These discrepancies again highlight the significant

	Pitch (rad/sec)	Roll (rad/sec)	Yaw (rad/sec)
Predicted	1.83	3.11	3.18
Achieved	1.50	1.90	1.51

Table 4.2 Predicted and achieved bandwidths

level of uncertainty in the design model and suggest that the controller needed more lead compensation for better phase response. The required lead compensation can be provided by using a mixed rates approach as shown in [8] where a predictor-type rate feedback is employed to avoid the inherent delay in the aircraft response.

⁴For flight control systems, a phase margin of at least 45° is required to ensure that the controller can tolerate the outer biodynamical loop of the human operator.

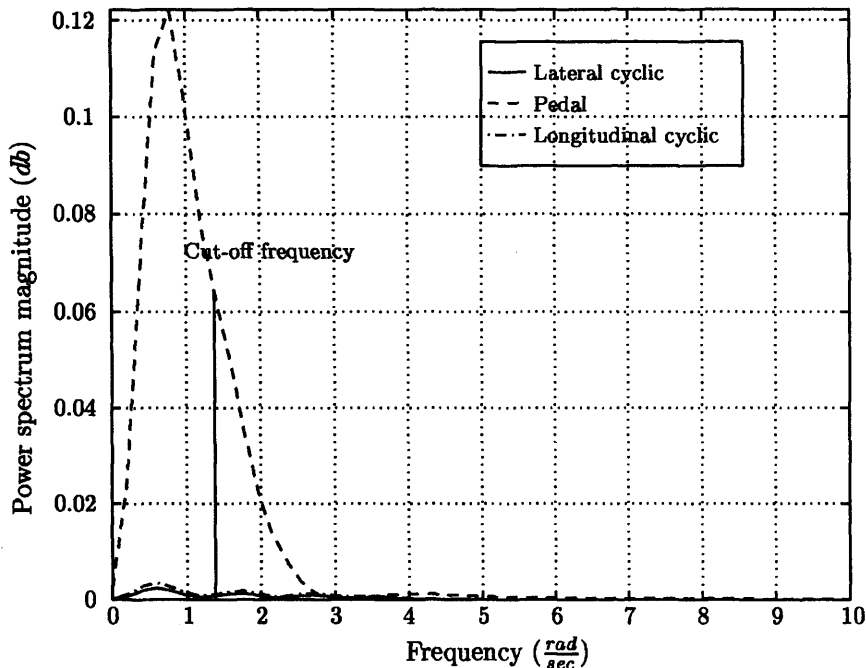


Figure 4.11 Power spectral estimates of input signals during a turn-to-target task

4.5 Force-feel system “transparency”

An important factor during the first flight test is the integration of the pilot inceptors with the flight control system. Extensive studies ([11]) have shown that sticks with even limited motion are superior to rigid force-sensing sticks in the real flight environment. The main reason is that pilots have a direct feel via the stick deflection of what is being demanded. The pilot should not be conscious about the stick even during a first flight - and in these flight trials the EP *did* express difficulty in applying a desired force (i.e issuing the appropriate attitude demand). The F-16 late modifications also support this point of view⁵. In addition, human operators are rarely able to make precise demands along strictly Cartesian axes i.e fore-aft and left-and-right. Conventional sticks employing motion produce less inter-axis cross-talk than those with no displacements. Unfortunately the angles between the axes of the stick arm were not measured to check whether they were rotated to the left to align them with the right forearm. Therefore, it is hard to say with confidence if some of the cross-axis activity recorded in flight is due to undesired off-axis inputs⁶. On the other

⁵The early versions of the F-16 used a force-sensing stick from the A-7 Corsair aircraft, but it was later replaced by a stick with small amount of movement which greatly improved the perceived aircraft characteristics.

⁶An extreme example of off-axis inputs was the Grippen disaster during its first flight. The Grippen stick axes were rotated 18° to the left to align the grip with the arm and reduce wrist fatigue. During the flight tests, to avoid a severe divergent PIO, at low altitude, the pilot reverted to an instinctive fore and aft arm action, applying simultaneous full nose up and roll demands which resulted in the left wing tip striking the ground.

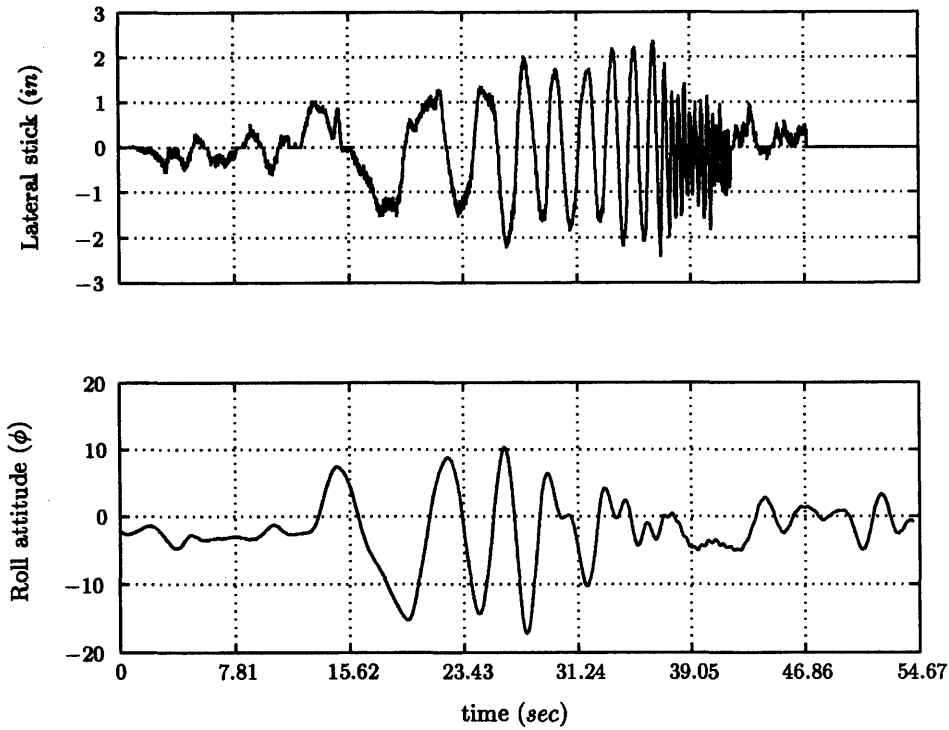


Figure 4.12 Roll axis frequency sweep: Input - Output time histories

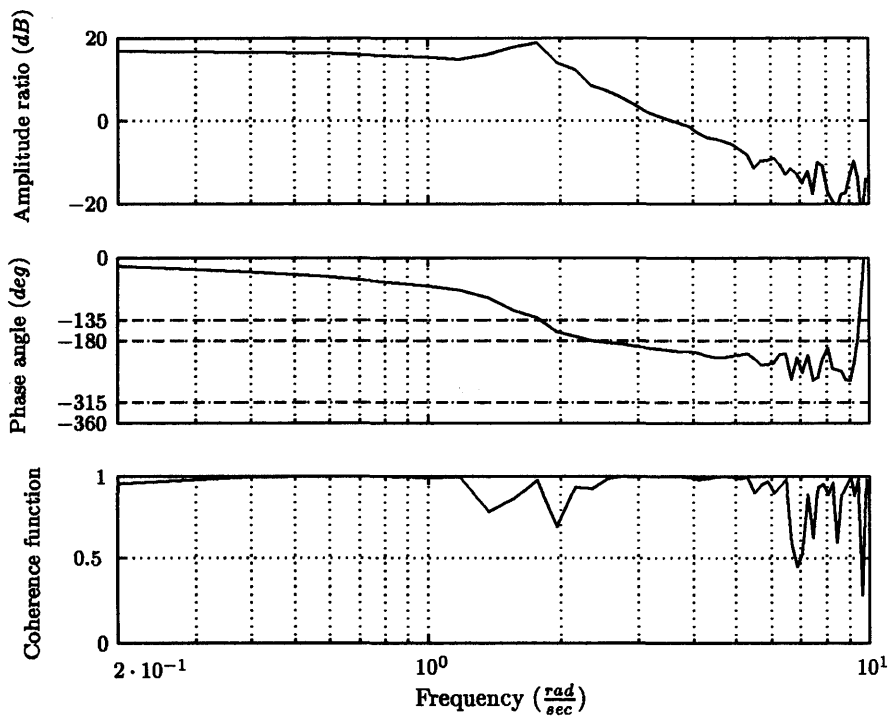


Figure 4.13 Lateral cyclic to roll attitude estimated closed loop frequency response

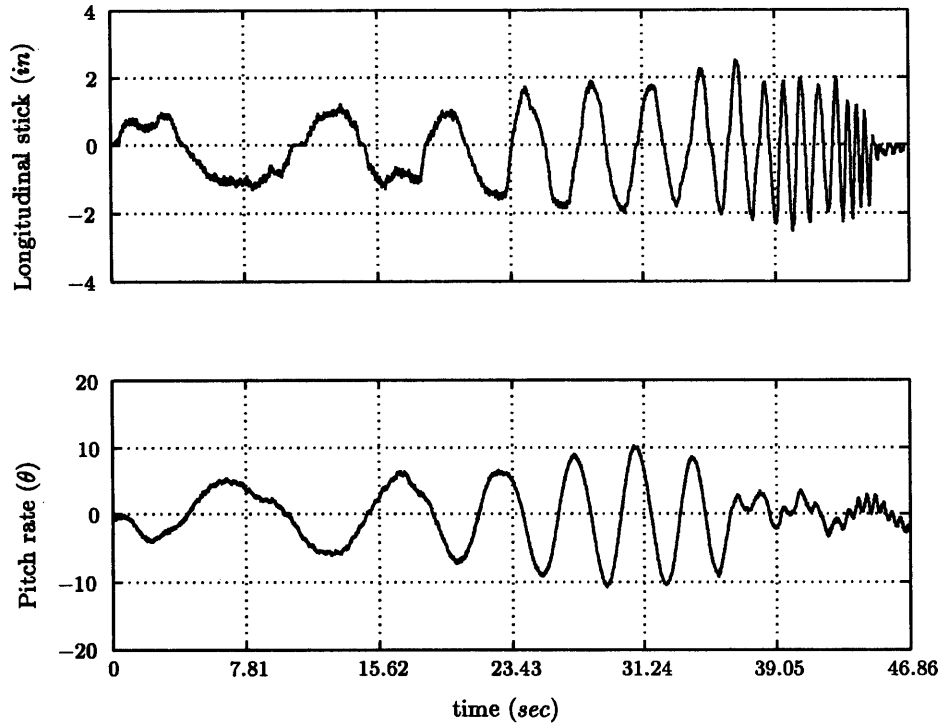


Figure 4.14 Pitch axis frequency sweep: Input - Output time histories

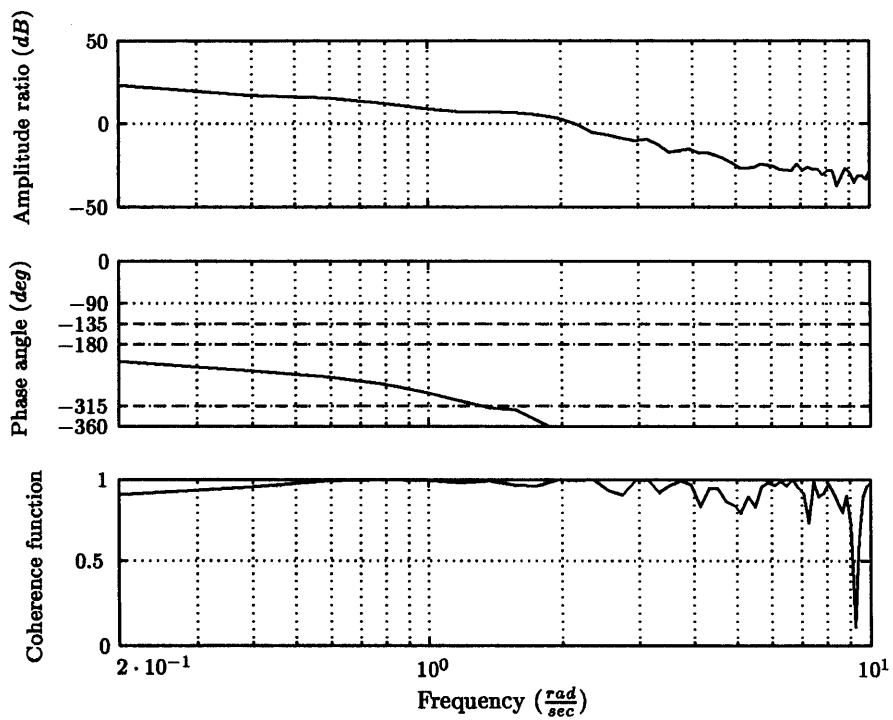


Figure 4.15 Longitudinal cyclic to pitch attitude estimated closed loop frequency response

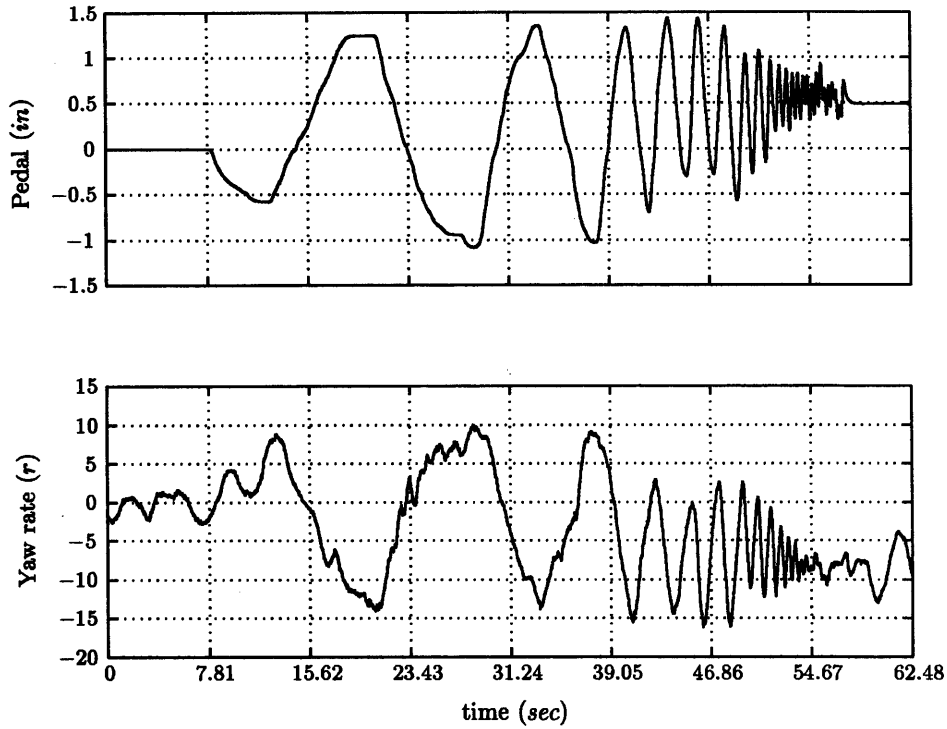


Figure 4.16 Yaw axis frequency sweep: Input - Output time histories

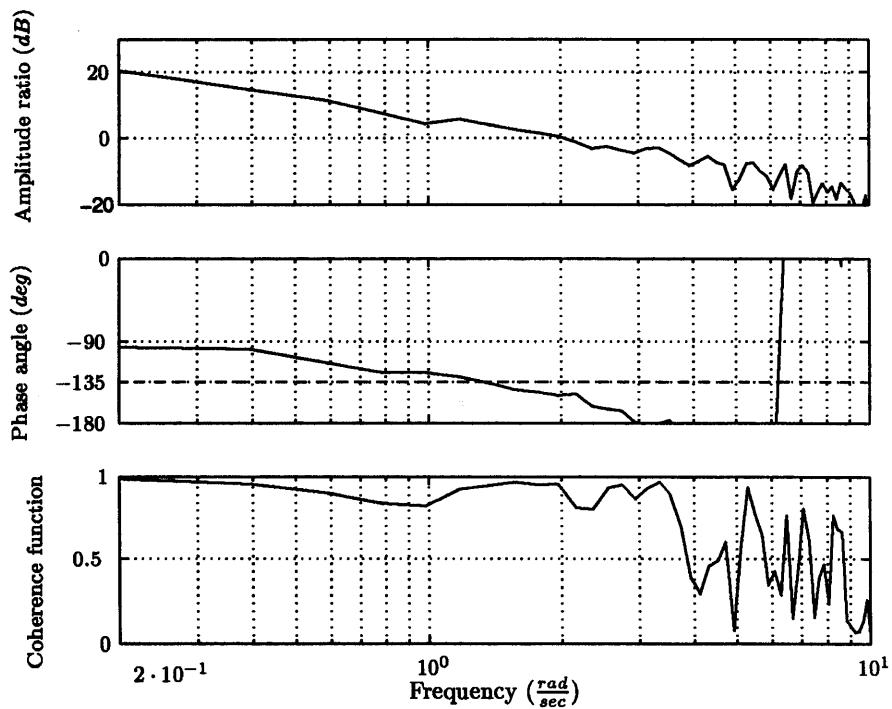


Figure 4.17 Pedal to heading estimated closed loop frequency response

hand, experiments on the NRC Bell 205 helicopter with force-sensing side-sticks have shown exactly the opposite - handling qualities Level 1 performance *is* achievable with a force-sensing side-stick. There is an evident contradiction here between the pilot’s comments and previous experience with force-sensing side-sticks which may be attributed to the following: without undermining the importance of both views it is believed that the problem stems from the combination of the force-feel system with the H_∞ flight control system. The ACAH controller was designed for low bandwidth, which made the predictability of the rate of attitude changes hard. This problem was further exaggerated by the unfamiliarity of the EP with the force-sensing stick and the lack of the pedal spring stiffness. Therefore, it can be concluded that these unharmonised force-feel characteristics masked some of the performance potential of the H_∞ controller.

Towards the end of the July 1997 H_∞ flight test campaign, several modifications to the controller were proposed to enhance the observed performance. Better integration of the force-feel system with the controller seems to be an obvious improvement. Ideally, a centre stick would be needed to correlate the findings with the ground-based simulations. We will describe briefly this experiment in the next chapter in section 5.5.4. A heading hold function also needs to be designed and implemented either within the H_∞ controller or as an outer loop which is engaged when yaw rate demands fall below a given threshold representing the pedal centring area. In addition, it would be possible to further alleviate the pilot workload, due to the high torque activity, if some form of heave augmentation is used to enable carefree handling. However, the first priority for the control law enhancement is to remove the limiting quasi static assumptions of chapter 3 (section 3.2.2), by including rotor state information to the mathematical description of the design model. This is because the rate sensors essentially provide a feedback signal, which contains high order rotor modes such as flapping motion. The inherent lag in this feedback signal, combined with uncertain structural modes, not only limits the achievable performance of the helicopter, but it can also result into a divergent closed loop response of the system. Thus, alongside the modelling of the high order modes, provisions to use a predictor-type rate feedback were also thought to be important to avoid possible excitation of uncertain structural modes by the control system. By predictor-type rate feedback we mean a feedback signal reconstructed from the low frequency component of the actual sensor output and the high frequency section of a lag-free model of the helicopter. We will see the details of such a reconstruction in section 5.3.1.

Helicopter handling qualities improvement using rotor dynamics and H_∞ optimisation. Design, analysis and flight test results

5.1 Introduction

The justification for using the six-degrees-of-freedom linear time invariant (LTI) model described in section 3.2, was largely based on the quasi-steadiness assumptions of the rotor dynamics. That is, the dynamic characteristics of the tip-path-plane have the same angular velocity as the rotor shaft; cyclic inputs are instantaneously converted to tip-path-plane angles. Of course, the Padé approximations accounted for the time delay between the aircraft responses and the cyclic input, but this doesn't imply that the transient behaviour of these responses was predicted adequately. Recalling the flapping equation (3.5), note that the tip-path-plane motion is governed by a second order differential equation, which includes not only inertial dynamics, but also aerodynamic damping. These effects give rise to rotor motions with natural frequencies close to the aircraft control system bandwidth. Thus, including the high order rotor dynamics to the controller design and analysis can have a significant impact on the achievable aircraft responses.

Similar arguments can be found in early research efforts by Ellis [24] and Heimbold [35]. Both authors suggested that any analysis of high gain feedback should include the dynamics of the rotor as the aircraft without them gives a deceptive impression of high stability. More recently, Takahashi in [67] used a mixed sensitivity formulation to the H_∞ optimisation problem to compare flight control laws designed with and without rotor state feedback. It was observed that the controller designed without rotor state feedback not only was more sensitive to gain variations as opposed to the controller synthesised with state feedback, but it also had the potential to pass approximately twice as much noise to the actuators near the one-per-rev frequency.

In this chapter, we will go a little further by presenting flight experiments substantiating the above claims. Of course, the main objective of the chapter is to improve the achieved handling qualities of section 4.3.2. However, instead of using mixed sensitivity formulation for the controller synthesis, we will rely on the appealing form of the two DOF H_∞ loop

shaping compensator and on model improvements from the inclusion of rotor dynamics to the design model.

As a first approximation of the higher order dynamics consider the equivalent centre spring model of a helicopter rotor. In terms of this centre spring model the flap frequency ratio λ_β can be written as

$$\lambda_\beta = 1 + \frac{K_\beta}{I_\beta \Omega^2} \quad (5.1)$$

where K_β , I_β , and Ω are the rotor stiffness, flapping inertia, and rotorspeed respectively. For the teetering rotor of the Bell 205 (see Figure 3.1) the two blades are connected to the rotor shaft via a single flap hinge. There is no transfer of moments to the hub and the spring stiffness of the equivalent centre spring model can be assumed to be zero. Therefore, the flapping frequency ratio λ_β can be set to unity. This implies that the flapping frequency λ equals the rotorspeed, which for the Bell 205 helicopter is 33 rad/sec . In practice, however, this value is much lower due to the coupling of the rotor dynamics with the fuselage motion. Using the method of Chen in [15] it can be shown that the resulting regressing and advancing flapping modes have undamped natural frequencies of 13.5 and 64 rad/sec , respectively. Of these modes, the regressing flap is most important since its frequency is low enough to restrict the achievable aircraft bandwidths. This value appears to be much higher than the bandwidths of the Bell 205 helicopter, however, from the sensitivity plot in Figure 3.22, (chapter 3), we can see that to achieve bandwidths between $1 - 2 \text{ rad/sec}$ in-flight the complementary sensitivity had to be rolled-off just before 11 rad/sec . Thus, it is of primary importance that the linear models predict “reasonably well” these low frequency flapping dynamics and as we shall see later in the chapter this is crucial in achieving improved handling characteristics of the aircraft.

5.2 A High order model for the NRC Bell 205 helicopter

The aims of this section are two-fold: to show the main modelling assumptions incorporated in the high order model and to compare the resulting linear model with open loop flight test data. Identifying those attributes that have a direct impact on control law design, it is possible not only to design a successful control law, but also to give a qualitative description of the handling quality assessment results presented later in this chapter.

The nonlinear model has its origins in a generic helicopter simulation model called HELISIM. The HELISIM code is an implementation of the dynamic equations of motion for a single rotor helicopter developed in [52]. The overall aircraft equations are formulated using a Newtonian approach with respect to the body axes and integrated numerically. In the next two sections we shall give a brief description of the Bell 205 HELISIM-based model in terms of rotor and body components.

5.2.1 Rotor

The main rotor has been modelled using an equivalent centre spring model with zero stiffness with respect to the shaft axis system. The rotor assumes only flapping and coning modes whilst lag dynamics, air compressibility, blade stall, tip losses and unsteady aerodynamics are neglected. The lag motion in zero stiffness rotors is very small and therefore neglecting it appears to be justified. Stall and compressibility effects can be ignored because the operational flight envelope of the Bell 205 helicopter is limited up to 90 *knots*. If tip losses and unsteady aerodynamics are modelled the resulting equations become very complex with little gain in terms of performance and response predictions. Root and tip lift losses account for only a small per cent of total power, and unsteady aerodynamics require extensive wind tunnel testing and empirical adjustment to predict accurately airfoil-induced moments (see for example Goman in [23, ch8]). In addition, these approximations allow relatively simple closed form solutions of the acting forces and moments to be obtained.

Using the above simplifications the lift (c_l) and drag (c_d) coefficients can be written as

$$c_l = a_0 \alpha \quad (5.2)$$

$$c_d = c_{d0} + c_{d1} \alpha^2 \quad (5.3)$$

That is, c_l is just a linear function of the local blade incidence α and c_d is given in terms of a mean value c_{d0} and a term to account for the changes in α .

The dynamics describing the flapping response of the rotor have already been introduced in chapter 3 (see section 3.2, equation (3.5)). From this second order differential equation, it is not difficult to see that obtaining flapping solutions of the form

$$\beta = \beta_0 + \beta_{long} \cos(\psi) + \beta_{lat} \sin(\psi) \quad (5.4)$$

requires that p , q and ψ behave in a quasi static manner. In other words, to use the mathematically appealing form of equation (5.4), we need to assume that flapping dynamics have a negligible effect on the stability and control of the helicopter. At first glance, this seems to be a “contradiction”, since one of the motivations for introducing flap motion to the model is to remove the limiting quasi static assumptions in the system description. However, these assumptions are valid *only* for small flapping angles achieving a new steady state one-per-rev following each incremental change in control activity and fuselage angular motion. Mathematically, this means that for a small integration step, equation (5.4) gives accurate solutions to the flapping equation (3.5). For the Bell 205 helicopter the 33 *rad/sec* rotor speed corresponds to 0.19 *sec* for one blade revolution. Thus, if the fuselage response is less than 0.19 *sec* the above assumptions are justified. This can be easily seen from the comparisons of the flight test data and the NASA quasi static model of chapter 3. The fuselage responses to pilot doublet inputs were approximately 0.15 *sec* delayed for both pitch and roll loops (see Figures 3.4 and 3.6). The final form of the three dominant rotor modes

(coning, longitudinal and lateral flapping) has been expressed in multi-blade coordinates and it can be found in [52, appendixD]. Note that engineering experience suggests that the coning angle can be neglected for a teetering rotor; the blades are rigidly coupled and coning motion is very small. However, setting β_0 to zero does not give any significant gain in terms of mathematical simplification of the model and thus coning has been left in the description of the system.

Similar to the main rotor, the tail rotor is also of a teetering type, consisting of two blades attached to their shaft via a single flap hinge. The aerodynamics of the tail rotor blades are governed by the same assumptions as described earlier, however, blade flapping is almost negligible for the tail rotor and therefore has been left out of the model. In addition, a tail/fin blockage and tail rotor cut-out scale factor have been introduced to account for the effects of the vertical fin on the rotor-exerted side-force.

5.2.2 Fuselage, tailplane and fin

The equations of fuselage, tailplane and fin force and moment contributions have already been introduced in chapter 2 (see equations (2.39), (2.40)). From these expressions it can be seen that for a given rotorspeed (assuming constant air density), the lift coefficients $c(\alpha, \beta)$ determine the aircraft behaviour. From the existing data, the forces and moments have been represented by first order functions of α and β and implemented in a look up table form.

The overall eight degrees-of-freedom helicopter mathematical description in the body axis system can be written in the standard form:

$$\left. \begin{aligned} \dot{u} &= -(wq - vr) + \frac{X}{M} - g \sin(\theta) \\ \dot{v} &= -(ur - wp) + \frac{Y}{M} - g \cos(\theta) \sin(\phi) \\ \dot{w} &= -(vp - uq) + \frac{Z}{M} - g \cos(\theta) \sin(\phi) \end{aligned} \right\} \quad (5.5)$$

$$\left. \begin{aligned} I_{xx}\dot{p} &= (I_{yy} - I_{zz})qr + I_{xz}(\dot{r} + pq) + L \\ I_{yy}\dot{q} &= (I_{zz} - I_{xx})rp + I_{xz}(r^2 - p^2) + M \\ I_{zz}\dot{r} &= (I_{xx} - I_{yy})pq + I_{xz}(\dot{p} - qr) + N \end{aligned} \right\} \quad (5.6)$$

$$\left. \begin{aligned} \dot{\phi} &= p + q \sin(\phi) \tan(\theta) + r \cos(\phi) \tan(\theta) \\ \dot{\theta} &= q \cos(\phi) - r \sin(\phi) \\ \dot{\psi} &= q \sin(\phi) \frac{1}{\cos(\theta)} + r \cos(\phi) \frac{1}{\cos(\theta)} \end{aligned} \right\} \quad (5.7)$$

where X, Y, Z, L, M, N are the force and moment contributions from all the body components (fuselage, tailplane, fin). Note that in the Euler equations (5.7) the cross couplings are fully modelled, unlike in the NASA six degrees of freedom representation of (3.1).

5.3 Comparisons with flight test data

The 19 nonlinear equations of the Bell 205 (9 body, 4 actuators and 6 flapping states) were trimmed and linearised at 60 *knots* flight condition for comparisons with flight test data. As in section 3.3, time and frequency domain analysis was used to give a qualitative description of the differences between the aircraft response and the open loop linearisations. The actuator signals used to drive the high order models are the same with those used in chapter 3 and they are shown in Figures 3.3, 3.5 and 3.7 for the lateral, longitudinal and pedal inputs respectively. Figures 5.1, 5.2 and 5.3 show the primary and the off axis responses to a lateral doublet input in time domain. From these Figures it can be seen

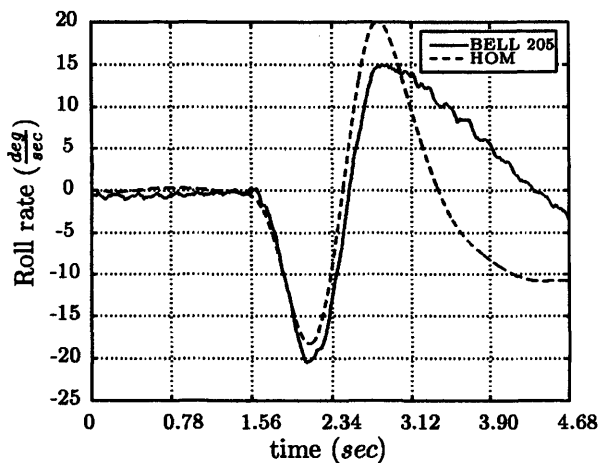


Figure 5.1 Comparison between flight test data and high order model roll rate responses to a doublet input in lateral axis

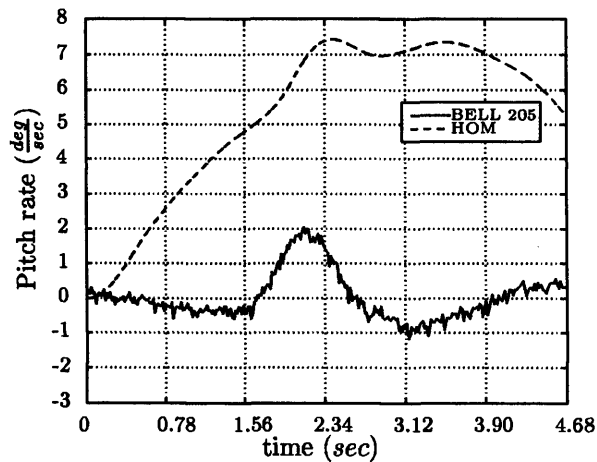


Figure 5.2 Comparison between flight test data and high order model pitch rate responses to a doublet input in the lateral axis

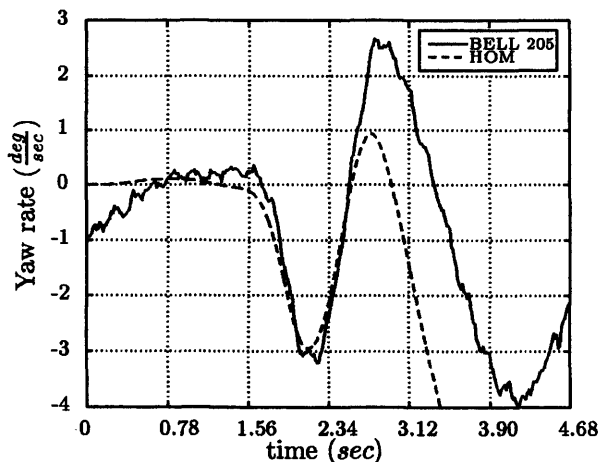


Figure 5.3 Comparison between flight test data and high order model yaw rate responses to a doublet input in the lateral axis

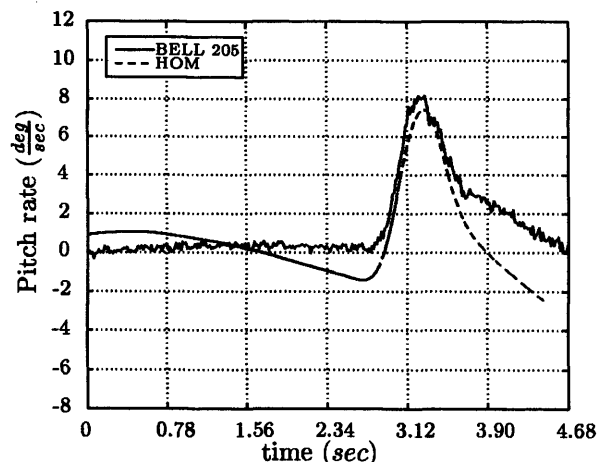


Figure 5.4 Comparison between flight test data and high order model pitch rate responses to a doublet input in longitudinal axis

that the high order model predicts the aircraft response reasonably well. In particular, the inclusion of the actuator and flapping states has resulted in a response with virtually

no lag characteristics and better predictions of the achievable roll rate, as opposed to the NASA model response shown in Figure 3.4. Good agreement between flight data and high order model responses can also be observed in the roll-to-yaw cross coupling prediction. Figure 5.3 illustrates the yaw rate response to the doublet input in lateral axis. The initial response of the model follows very well the aircraft response for at least 1 sec. The discrepancies between 2.34 and 3.90 sec are possibly due to absence of the rotor wake in the model description. In spite of these deficiencies, the anticipated cross coupling appears to be substantially improved from the NASA model predictions in Figure 3.10. However, the roll-to-pitch coupling does not seem to be in very good agreement as shown in Figure 5.2. When compared to the responses of Figure 3.9 one can see that even before the doublet input, around 1.56 sec, there is a significant residual in pitch rate in the nonlinear model predictions. We will see similar pitch rate discrepancies later in the pitch-to-yaw and yaw-to-pitch response predictions, which lead us to the speculation that the actuator trim position of the longitudinal actuator (as calculated from the trimming procedure) is not very close to the actual aircraft trims during these manoeuvres. As for the magnitude of the discrepancies between the flight data and the linearisations, in both quasi static and high order models, the over-sensitivity of the model can be partly explained due to the rotor wake effects on the tailplane. However, despite these discrepancies, the high order model has captured the correct sign of the aircraft pitch rate response.

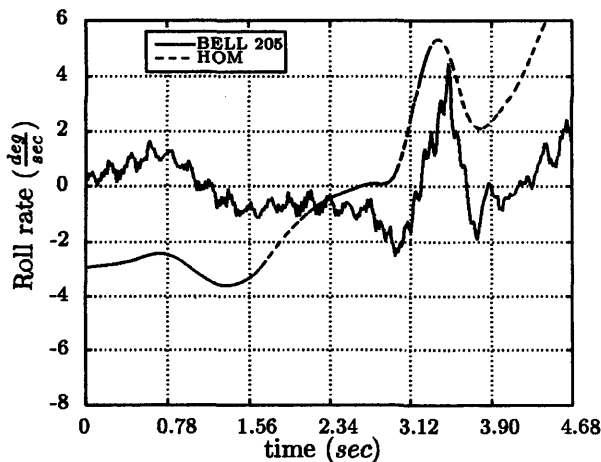


Figure 5.5 Comparison between flight test data and high order model roll rate responses to a doublet input in the longitudinal axis

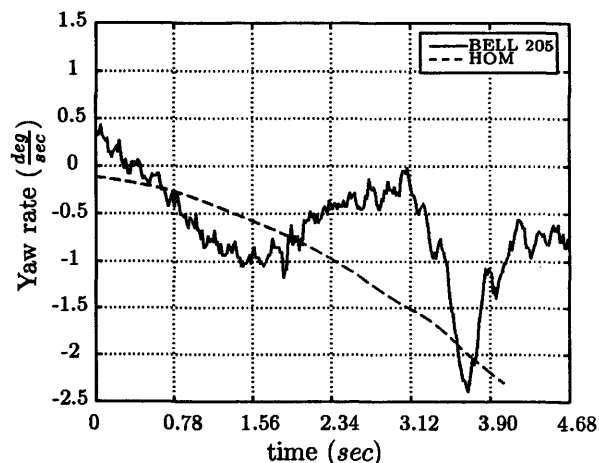


Figure 5.6 Comparison between flight test data and high order model yaw rate responses to a doublet input in the longitudinal axis

Figures 5.4, 5.5 and 5.6 show the on-axis and off-axis responses to a doublet input in longitudinal loop. Despite the high order model transient response before the input was applied (around 2.34 sec), the pitch rate response follows very closely the aircraft behaviour and seems to be significantly improved, when compared with its quasi-static counterpart in Figure 3.6. The inherent aircraft lag is accurately captured and the peak rate generated after the initial input has minor differences with the actual aircraft response. However, in

both off-axis responses significant discrepancies can be observed. Firstly, in Figure 5.5 the high order model seems to be less responsive than the quasi static linearisation in Figure 3.11. As a result, it cannot follow closely the aircraft movement below 3.12 sec. Secondly, the pitch-to-yaw coupling shown in Figure 5.6 seems to be less predictable considering that at 60 knots flight condition with a 4 deg/sec pitch rate, the response in yaw loop should not be very large. Similar rate unpredictability in pitch loop during yaw doublet input can be seen in Figure 5.9. These differences were somewhat unexpected, since all primary responses including some off-axis couplings are very well predicted. As an example, Figures 5.7 and 5.8 illustrate the yaw and roll rates generated during a directional doublet input. Thus, it is evident that the high order model responses represent very well the aircraft dynamics in the primary loops, however, the cross couplings to pitch rate are poorly modelled.

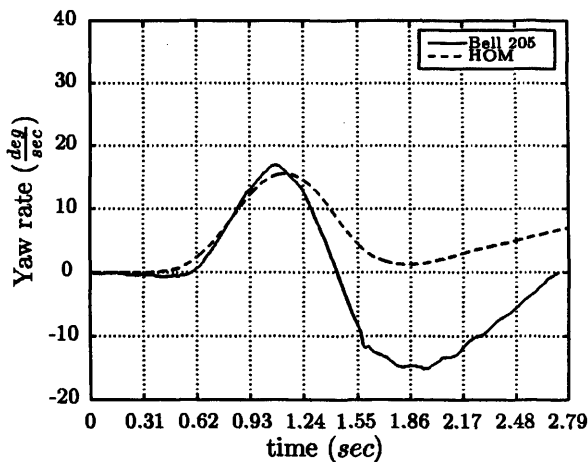


Figure 5.7 Comparison between flight test data and high order model yaw rate responses to a doublet input in directional axis

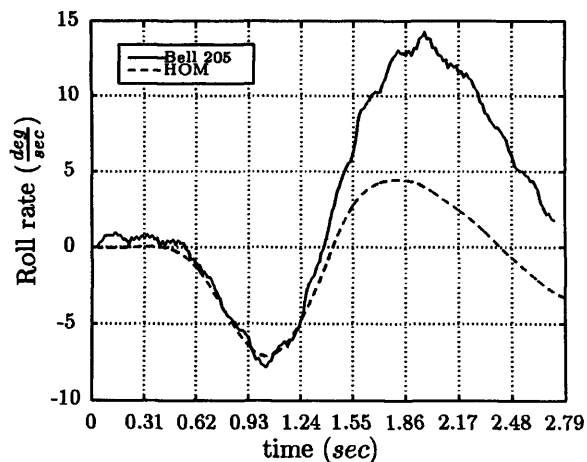


Figure 5.8 Comparison between flight test data and high order model roll rate responses to a doublet input in the directional axis

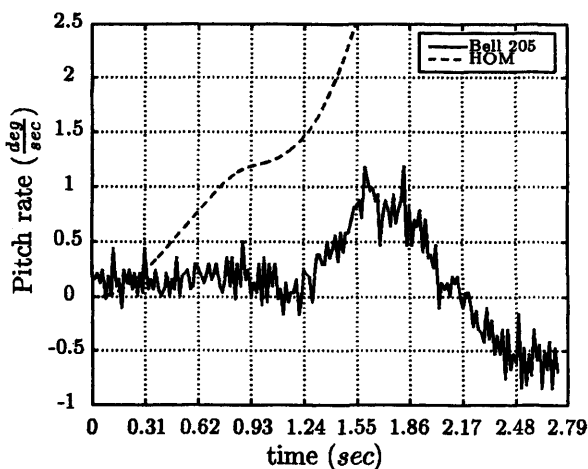


Figure 5.9 Comparison between flight test data and high order model pitch rate responses to a doublet input in the directional axis

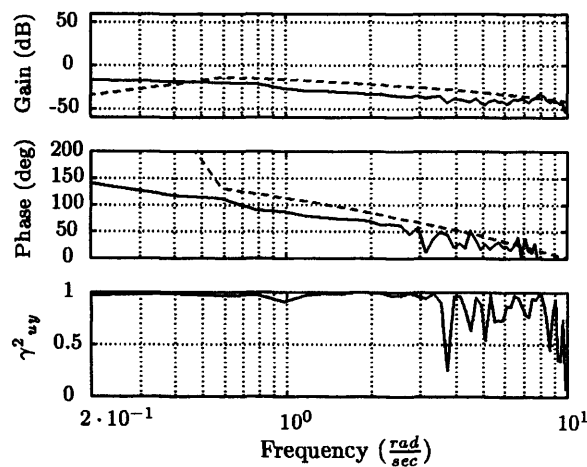


Figure 5.10 Comparison between open loop flight test data (solid) and nonlinear model responses (dashed) to a frequency sweep input in longitudinal axis

To complete the analysis we present the relative comparisons of the high order model and aircraft responses in the frequency domain. Similar to chapter 3 (section 3.3) longitudinal, lateral and pedal sweeps were performed and the results are shown in Figures 5.10, 5.11 and 5.12, respectively. For all the primary loops both the gain and phase plots show significant improvement, when compared to the early quasi static representations in Figures 3.16, 3.15 and 3.17.

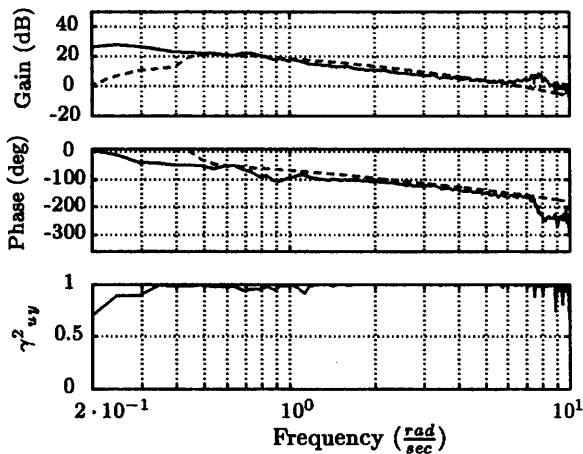


Figure 5.11 Comparison between open loop flight test data (solid) and nonlinear model responses (dashed) to a frequency sweep input in lateral axis

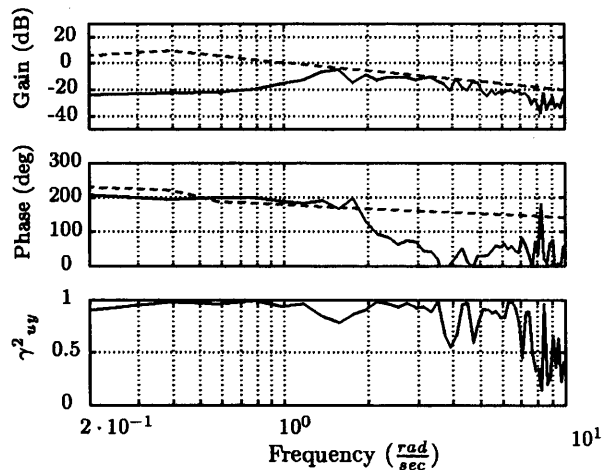


Figure 5.12 Comparison between open loop flight test data (solid) and nonlinear model responses (dashed) to a frequency sweep input in directional axis

To summarise, the high order nonlinear model predicts the actual aircraft responses better than the quasi static representation used to design the control laws in chapter 3. There is an improvement in each of the primary loops, however, some off-axis responses (especially those involving significant pitch motion) still remain in error. Due to the highly nonlinear plant behaviour, it is generally very difficult to justify with certainty how these predictions can be improved. For example in [17] and [44], the lateral distribution of induced velocity produced by the main rotor was identified as a primary source of strong pitch-yaw cross coupling. Thus, it is likely that the identified deficiencies of the model are due to other interactional aerodynamic phenomena not captured by the current linearisations. Despite that, we will see that the synthesised controller in section 5.4.3 improves the perceived performance of the helicopter and thus achieves good ratings by the test pilots.

5.3.1 Feedback Signals

The feedback signals include pitch and roll attitudes (θ , ϕ) and rates (q , p). In the heading loop, yaw rate (r) was used as a primary feedback variable and heading angle (ψ) along with indicated airspeed (U_i) were also fed back to enable a heading hold function.

In chapter 4, we motivated the use of a predictor-type rate signal for pitch and roll loops. The rationale behind this feedback is that the structural noise from the high frequency

angular variables can be “filtered-out” using a complementary filter with a cut-off frequency (ω_c) at 11 *rad/sec* (just before the aircraft mast-rocking mode). For example, if q is the measured pitch rate signal and q_m the output of a longitudinal transfer function model of the helicopter, the overall feedback signal q_f can be written as

$$q_f = q \frac{\omega_f}{s + \omega_f} + q_m \frac{s}{s + \omega_f} \quad (5.8)$$

where q_m is given by

$$q_m = \frac{\delta_{long} L_{\delta_{long}}}{s + M_q} \quad (5.9)$$

Here, δ_{long} represents the longitudinal actuator input and M_q , $L_{\delta_{long}}$ are the primary roll damping and control derivatives respectively¹. On the on-board computer of the Bell 205 both derivatives are implemented via a second order function of indicated airspeed. Note that the use of primed² instead of their unprimed counterparts makes no difference in the real time implementation of the feedback signal q_f . This is because the lateral-directional expressions in 5.6 are independent of the form in which the derivatives appear in the linearised equations of motion.

Experience in using the mixed-rate feedback was originally reported in [8], where a Linear Quadratic Regulator (LQR) was designed for the Bell 205 aircraft. The LQR control law was found to be unstable in flight without the use of a predictor-type signal. A similar experiment was carried out with an H_∞ controller, which was designed using a quasi-static linearisation of the Bell 205 helicopter. The bandwidths of the H_∞ controller were slightly higher than the predicted bandwidths shown in Table 4.2, in chapter 4. When tested in flight, the controller was found to be unstable in pitch direction. However, when mixed rate signals were used for feedback the controller was stable, although not worth evaluating. This suggests that the mixed rate feedback *did* filter-out some of the undesirable noise picked up by the sensors, and therefore, it is a useful tool when designing compensators using quasi-static linearisations.

5.4 Controller design

Before proceeding with the description of the control law tested on the Bell 205 aircraft in August 1998, it is necessary to substantiate a number of observations made in chapters 2 and 3. These observations referred to the benefits of using a single or a two DOF H_∞ loop shaping procedure to satisfy the ADS-33 Handling Qualities requirements [3]. We know for example, that within the one DOF methodology, it is possible to use a W_2 weighting function to explicitly impose disturbance rejection requirements on the controller input. On

¹The term “damping” refers to the aerodynamic properties of the airframe for different values of M_q and not to the damping factor within a pure control context.

²Primed derivatives eliminate the appearance of the inertia terms in the equations of motion. For details see [34].

the other hand, using a two DOF procedure enables the designer to achieve better output decoupling - at least in the ground-based simulations. Thus, the objective of this section is to provide evidence, from the experimental point of view, as to which formulation is best applicable to the helicopter stabilisation problem. To make valid comparisons though, the different compensators should be designed to achieve the same bandwidth specifications and, of course, flight tested under the same conditions.

The model for the two designs was a 19th order hover linearisation equivalent to the 60-*knot* model described earlier. Admittedly, using a high order design model leads to compensators of large dimensions, which can be difficult to implement within the time frame requirements of the flight control computer. Thus, a smaller dimension system was obtained by residualising heading (ψ), the collective actuator (δ_{coll}) and the two coning states ($\beta_0, \dot{\beta}_0$). Each of the above residualisations is justified on different grounds, however, care must be taken so the original model dynamics are not altered significantly in the frequency range of interest. For example, the collective actuator was omitted since the heave loop was to be unaugmented. Also, heading is independent from the short period stabilisation problem and alongside the small coning angles for the teetering rotor (see section 5.2.1) it does not have any significant effect on the model dynamics.

Figure 5.13 shows the model frequency responses of the 19-state high order linearisation (solid line) and the 15-state residualised model (dashed line). The frequency responses of the two models coincide over the plotted frequency range. Further reduction of the model can be achieved by truncating the longitudinal and lateral flapping derivatives $\dot{\beta}_{long}$ and $\dot{\beta}_{lat}$. The resulting 13-state realisation is also shown in Figure 5.13 (* line)³

5.4.1 Mode description

Eigenvalue decomposition of the final 15-state linearisation shows that it is considerably more difficult to identify the dynamic modes of the aircraft motion as opposed to the quasi-static realisation of chapter 3. From table 5.1 it is straightforward to identify the two flapping and the actuator modes because of their high frequency and their time constants respectively. However, the effects of the main rotor on the fuselage modes give rise to subsidences, which are difficult to characterise in terms of classical aircraft motions. For example, mode 7 represents a well damped flap-roll motion which is considerably faster (due to the lower fuselage inertia in roll) than the flap-pitch motion shown as mode 3.

Examination of the final 3-input 5-output system revealed that there are also three left-half-plane (LHP) zeros at -0.38 , -0.0010 and $-2 \cdot 10^{-5}$. Although not constraining the achievable performance of the closed loop system, the magnitude of these LHP zeros

³Balanced truncation of the plant normalised coprime factors is more effective in truncating a high order model. However, the resulting state space system is an equivalent realisation of the original model and it is not possible to relate the states of the reduced model to the physical system. For details see [33].

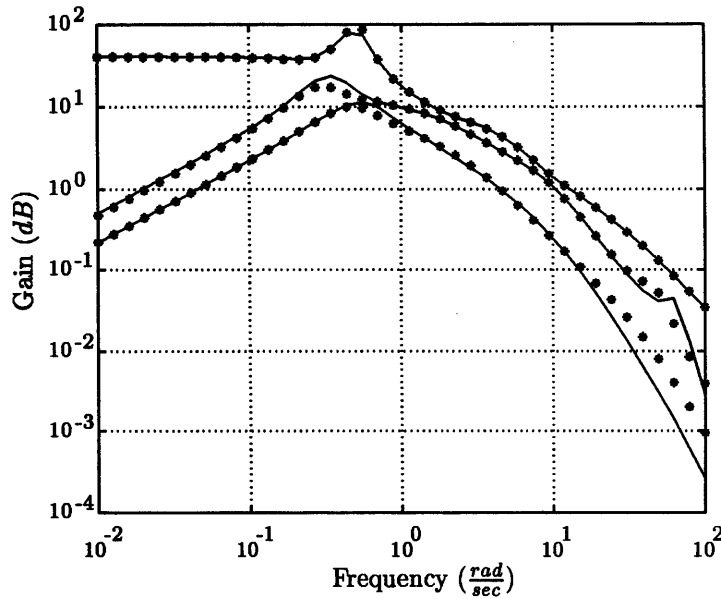


Figure 5.13 Frequency responses of the high order model (solid), 15th order residualised (dashed) model and 13th order model (*).

can impose severe limitations during the controller implementation. This will be analysed in detail in section 5.7.

5.4.2 One degree-of-freedom synthesis

To achieve closed loop bandwidths between 2 – 3 rad/sec the pre-compensator W_1 was chosen to give a slope of 20 $dB/decade$ to the magnitude of the loop transfer function $W_2(j\omega)G(j\omega)W_1(j\omega)$ with a zero at -2 around the cross-over region i.e.

$$W_1(s) = \begin{bmatrix} \frac{s+2}{s} & 0 & 0 \\ 0 & \frac{s+2}{s} & 0 \\ 0 & 0 & \frac{s+2}{s} \end{bmatrix} \quad (5.10)$$

The position of the zero here is justified using inspection of the closed loop damping and steady state errors of the output responses. An alignment matrix at 2.5 rad/sec was also used to give the desired cross over of the open loop frequency responses. Note that the alignment frequency is located well within the targeted closed loop bandwidths, as opposed to the higher cross over used in the design of chapter 3. Design experience shows that this is good practice when rotor state information is included in the design model. This is probably because the additional rotor states enable good models to be obtained at high frequencies. This implies that the discrepancies between the predicted and achieved closed loop bandwidths should be reasonably small since the ball of uncertainty the controller has to compensate for is smaller.

The post-compensator W_2 was defined as first order filter to accommodate the low pass section of the feedback signal described in equation (5.8). The cut-off frequency ω_f was set

Mode	Real	Imaginary	Frequency	Damping	
1	-0.354	0	0.354	1	Heave subsidence
2	0.132	-0.347	0.372	-0.35	Phygod
	0.132	0.347	0.372	-0.35	
3	-0.413	0	0.413	1	Flap/Pitch
4	-0.091	-0.499	0.507	0.18	Dutch Roll
	-0.091	0.499	0.507	0.18	
5	-1.033	0	1.033	1	Roll subsidence
6	-4.433	-2.295	4.992	0.88	Regressing flap
	-4.433	2.295	4.992	0.88	
7	-5.560	0	5.560	1	Flap/roll
8	-12.579	0	12.579	1	Longitudinal
9	-12.579	0	12.579	1	Lateral
10	-25.000	0	25.000	1	Pedal
11	-7.564	-66.794	67.221	0.11	Advancing flap
	-7.564	66.794	67.221	0.11	

Table 5.1 High order model Bell 205 modes

at 11.5 rad/sec, just below the frequency of the mast rocking mode of the aircraft. The final W_2 post-compensator had the form

$$W_2 = \begin{bmatrix} 1 & 0 & 0 & 0 & 0 \\ 0 & 1 & 0 & 0 & 0 \\ 0 & 0 & \frac{\omega_f}{s+\omega_f} & 0 & 0 \\ 0 & 0 & 0 & \frac{\omega_f}{s+\omega_f} & 0 \\ 0 & 0 & 0 & 0 & \frac{\omega_f}{s+\omega_f} \end{bmatrix} \quad (5.11)$$

The singular value gains of the final shaped plant $W_2GW_1K_a$ are shown in Figure 5.14. The solution of the robust stabilisation problem gave a 21-state controller which achieved a minimum cost γ of 2.5. Table 5.2 shows the predicted bandwidths and phase delays calculated according to the ADS-33 requirements [3].

	Pitch	Roll	Yaw
Bandwidth	2.36	2.56	2.22
Phase Delay	0.20	0.20	0.07

Table 5.2 Bandwidths and Phase delays of the single DOF compensator

5.4.2.1 Nonlinear simulations

Typical step inputs in all controlled axes were simulated to check the operation of the control law. Figures 5.15 - 5.17 show the output responses to input demands on collective

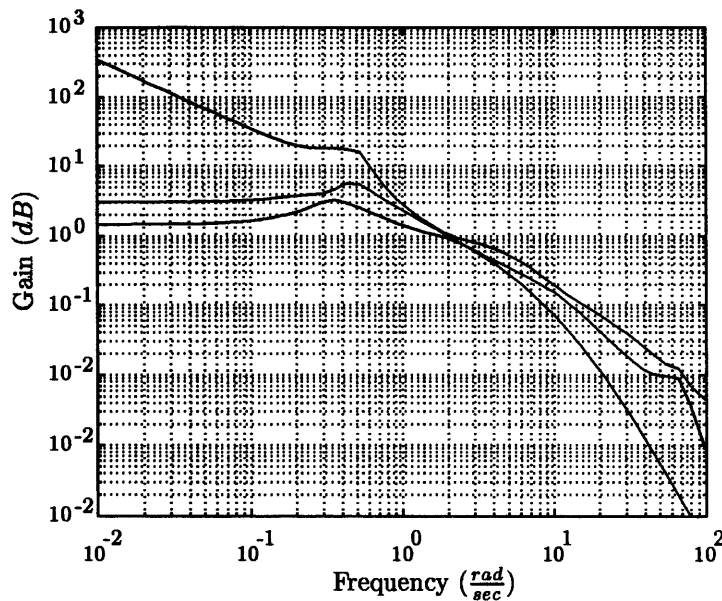


Figure 5.14 *Weighted frequency response of the Bell 205 helicopter*

actuator. From these Figures it can be seen that the coupling between the controlled variables θ , ϕ and heave loop is negligible. In particular, heading changes do not exceed 5° although much better decoupling could be achieved if the heave loop was also augmented. Similarly, Figures 5.18 - 5.20 show the nonlinear time domain output responses to step inputs of $\pm 20^\circ$ in pitch loop. Again the off axis couplings into pitch are minimal. For example, in Figure 5.18 roll attitude excursions reach 2° at 9 sec into the manoeuvre. This is indeed very small interaction considering that at that moment the helicopter is already flying with an airspeed above 20 m/sec. In all the other cases, decoupling is also very good. Step inputs in roll attitude and yaw rate (Figures 5.21 - 5.23 and 5.24 - 5.26 respectively) show the primary variables being tracked satisfactorily and the attitudes being captured without significant overshoots or steady state errors.

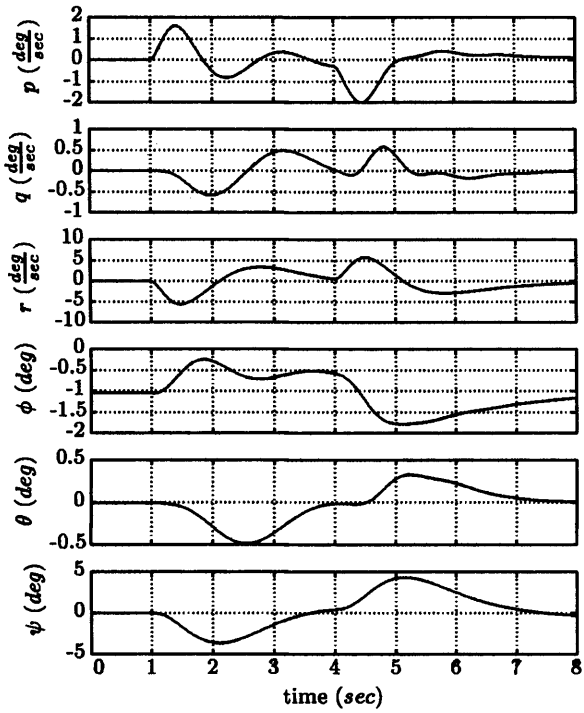


Figure 5.15 One degree-of-freedom compensator, -2° heave demand

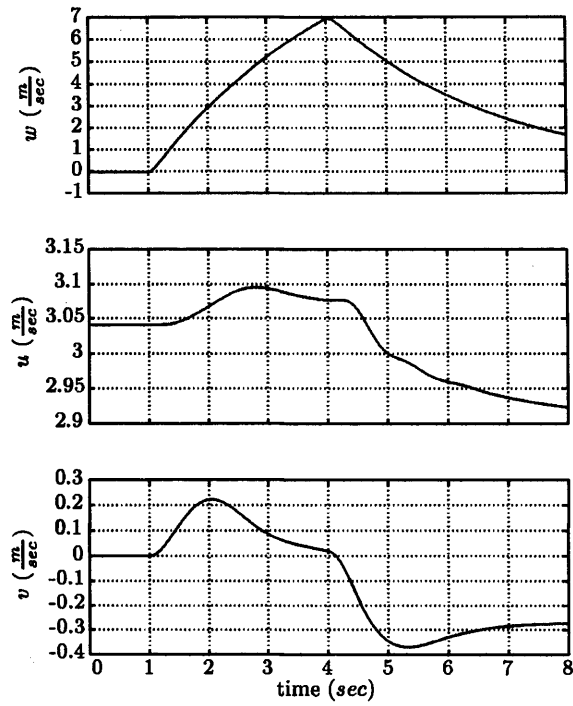


Figure 5.16 One degree-of-freedom compensator, -2° heave demand

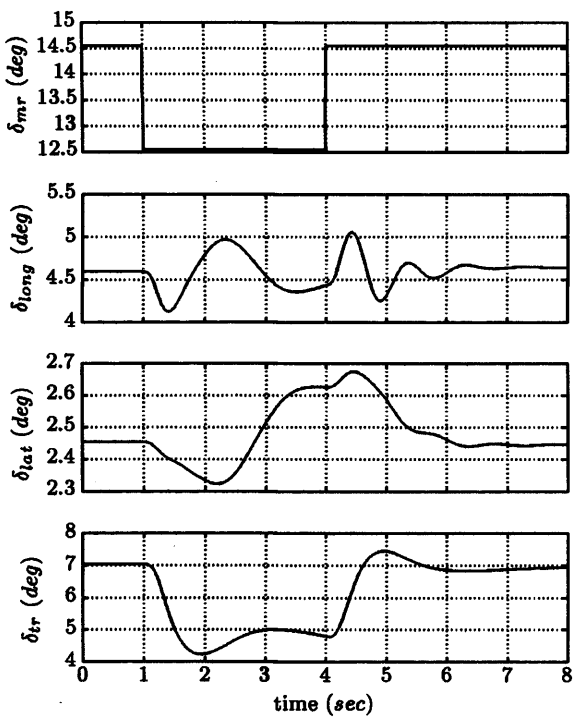


Figure 5.17 One degree-of-freedom compensator, -2° heave demand - Actuator deflections

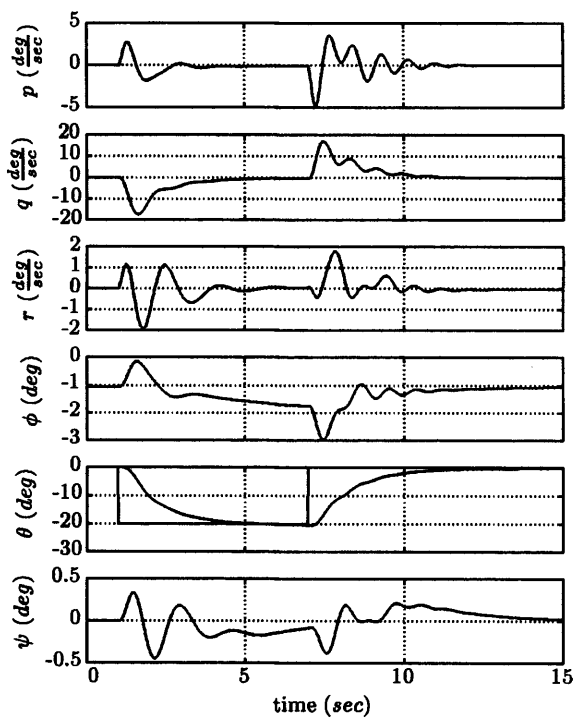


Figure 5.18 One degree-of-freedom compensator, -20° pitch attitude demand

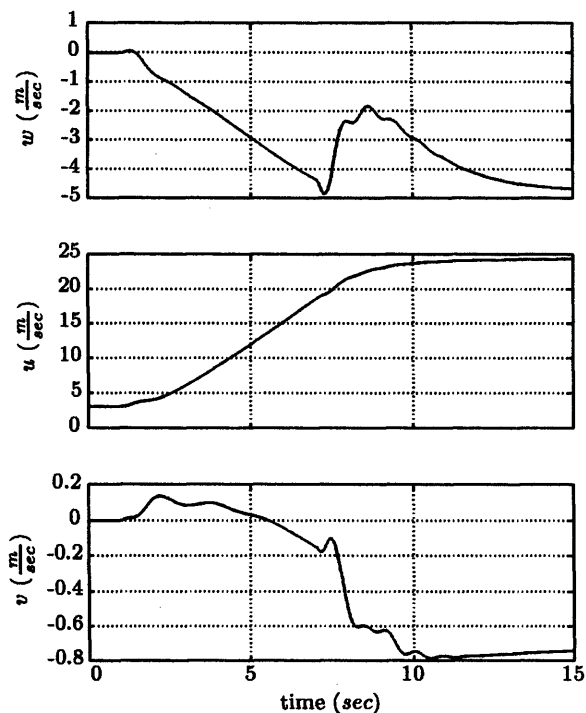


Figure 5.19 One degree-of-freedom compensator, -20° pitch attitude demand

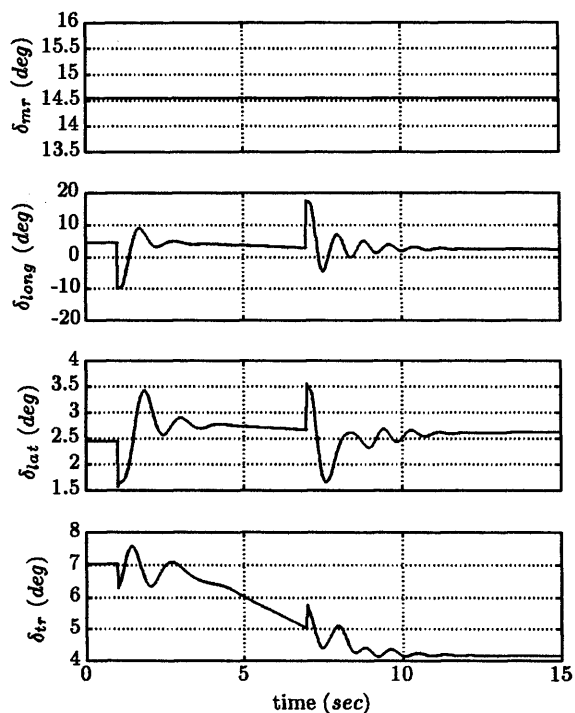


Figure 5.20 One degree-of-freedom compensator, -20° pitch attitude demand - Actuator deflections

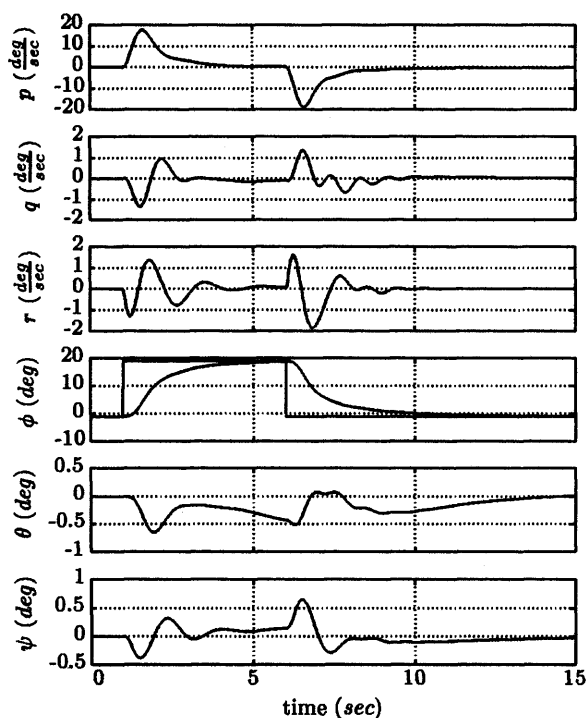


Figure 5.21 One degree-of-freedom compensator, 20° roll attitude demand

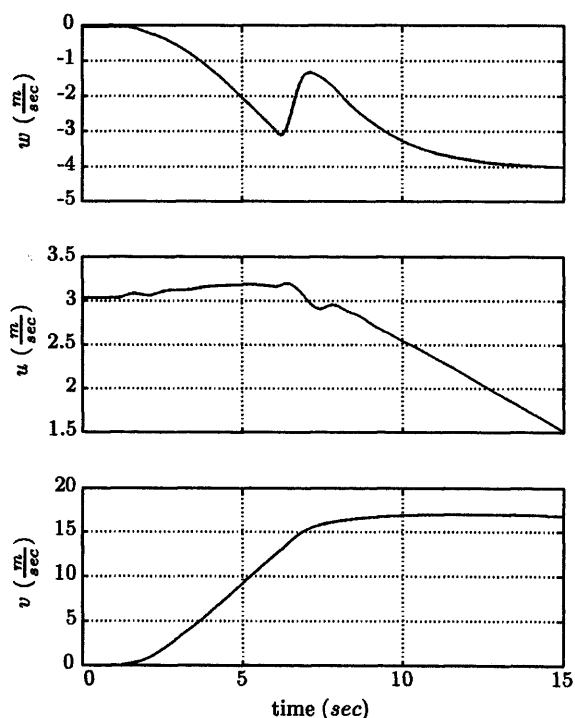


Figure 5.22 One degree-of-freedom compensator, 20° roll attitude demand

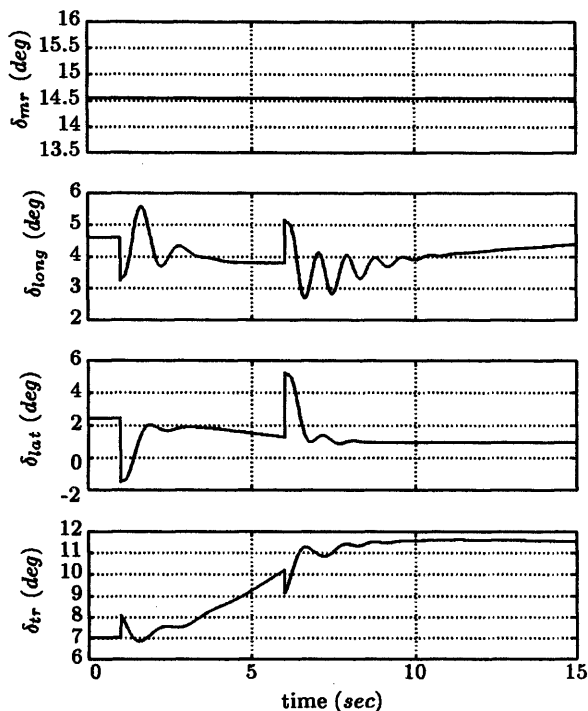


Figure 5.23 One degree-of-freedom compensator, 20° roll attitude demand - Actuator deflections

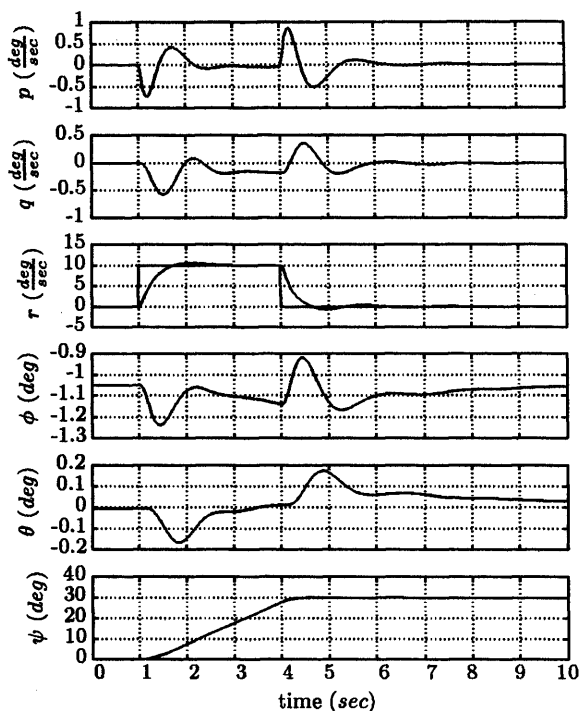


Figure 5.24 One degree-of-freedom compensator, 10°/sec yaw rate pulse input

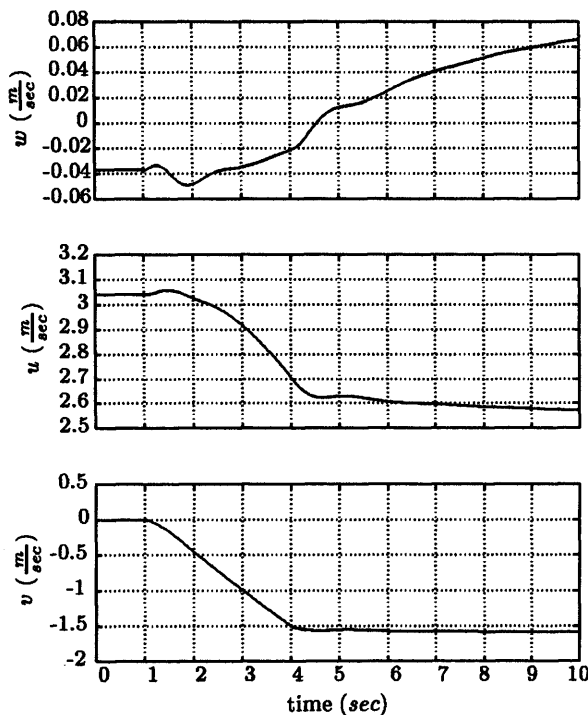


Figure 5.25 One degree-of-freedom compensator, 10°/sec yaw rate pulse input

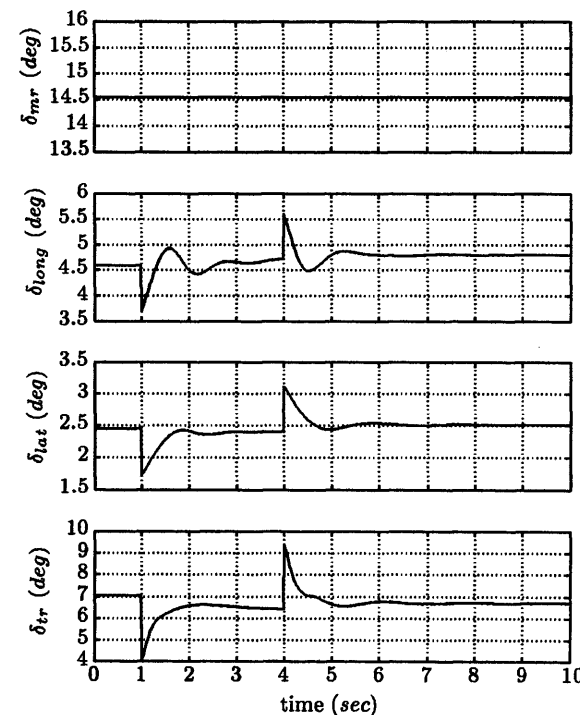


Figure 5.26 One degree-of-freedom compensator 10°/sec yaw rate pulse input - Actuator deflections

5.4.3 Two degrees-of-freedom synthesis

Having analysed the performance of the one degree-of-freedom compensator it was decided to lower the pre-compensator integral gains and to eliminate the W_2 weighting function from the controller synthesis. The final pre-compensator had the form

$$W_1(s) = \begin{bmatrix} \frac{s+0.25}{s} & 0 & 0 \\ 0 & \frac{s+0.25}{s} & 0 \\ 0 & 0 & \frac{s+0.5}{s} \end{bmatrix} \quad (5.12)$$

A second order reference model was defined to enable model following controller synthesis to be performed. As in the previous chapter the ideal model consisted of second order transfer functions the parameters of which are shown in Table 5.3 below

	Roll	Pitch	Yaw
Damping (ζ)	0.9	0.9	0.7
Natural frequency (ω_n)	4.0	1.2	9
Agility ($\frac{p_{pk}}{\Delta\phi_{pk}}$)	1.57	0.47	3.94

Table 5.3 *Command model specifications - Design models include rotor state information*

Note that the specifications above are slightly different than the ones shown in chapter 4 (table 4.1). This is because the inner loop was modified, and thus the reference model had also to be altered to trade off achievable output response characteristics. The trade-off was performed according to the standard H_∞ two DOF methodology. If, for example, the stability margin γ was sufficiently small (large) and the speed of the output response had to be made faster (slower), the ideal model parameters were used alongside the model matching parameter ρ to achieve this objective. For this design example $\rho = 1.9$ for all the primary loops and the natural frequency parameters were used to tune the H_∞ controller. The resulting suboptimal stability margin was $\gamma = 3.9$ and the sensitivity and complementary sensitivity functions are shown in Figures 5.27 and 5.28 respectively. Table 5.4 shows the predicted bandwidths and phase delays calculated according to the ADS-33 requirements.

	Pitch	Roll	Yaw
Bandwidth	1.59	3.16	3.49
Phase Delay	0.24	0.20	0.08

Table 5.4 *Predicted bandwidths and phase delays of the two DOF compensator*

5.4.3.1 Nonlinear simulations

As in the previous section, step inputs in all controlled axes were simulated to ensure that the controller provides adequate decoupling between the three primary axes of the Bell 205 helicopter. Figures 5.29 - 5.31 show the output responses to input demands of $\pm 2^\circ$ to the

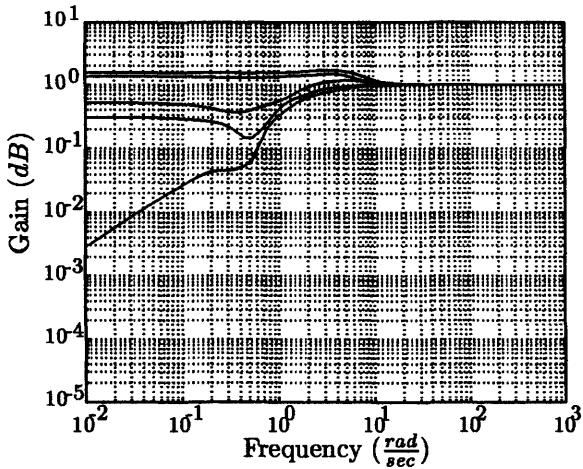


Figure 5.27 *Two degree-of-freedom compensator, output sensitivity function*

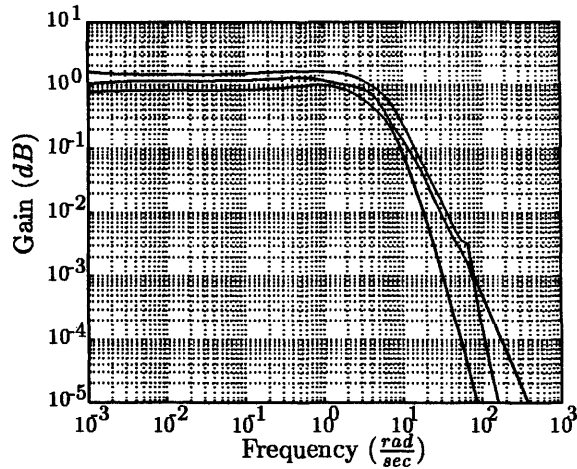


Figure 5.28 *Two degree-of-freedom compensator, complementary sensitivity function*

collective actuator. The heading coupling is minimal not exceeding 2.2° . Figures 5.32 - 5.34 show a simulated acceleration manoeuvre consisting of a pulse input of $\pm 20^\circ$ in pitch loop. Again the off axis couplings into pitch are minimal. Roll attitude excursions reach just 1.8° at 7 sec while the airspeed is more than 20 m/sec. Step inputs in roll attitude and yaw rate are shown in Figures 5.35 - 5.40. Note the attitude capture in both manoeuvres. The controller has minimised the inherent aircraft roll-to-yaw coupling, which implies that it should also minimise the pilot workload in the lateral-directional tasks.

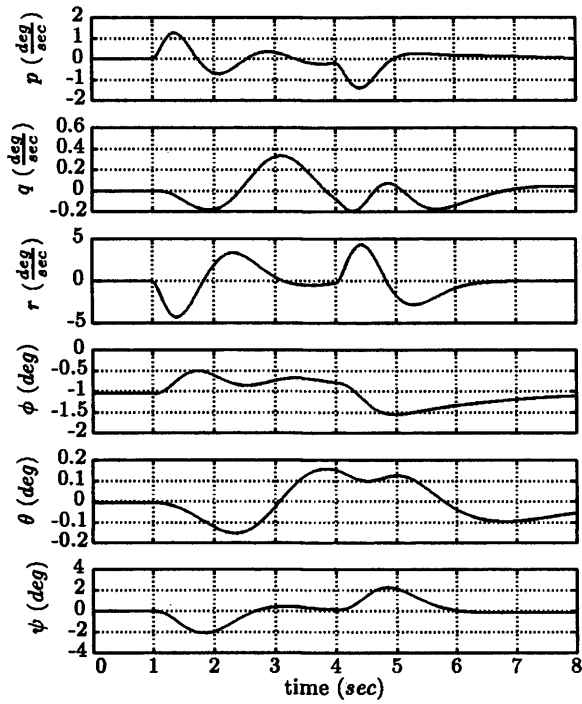


Figure 5.29 Two degrees-of-freedom compensator, 2° heave demand

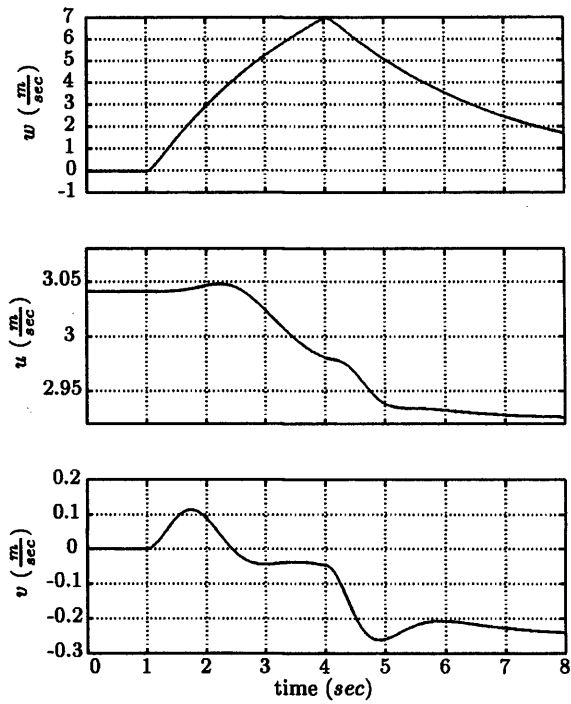


Figure 5.30 Two degrees-of-freedom compensator, 2° heave demand

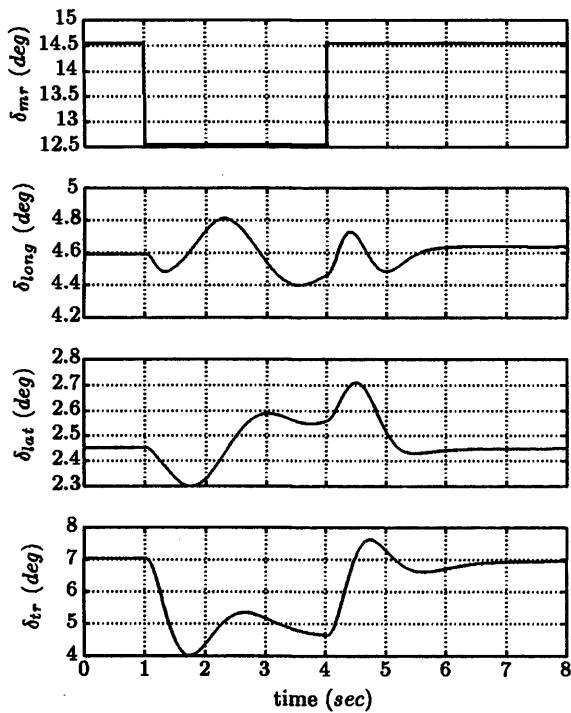


Figure 5.31 Two degrees-of-freedom compensator, 2° heave demand - Actuator deflections

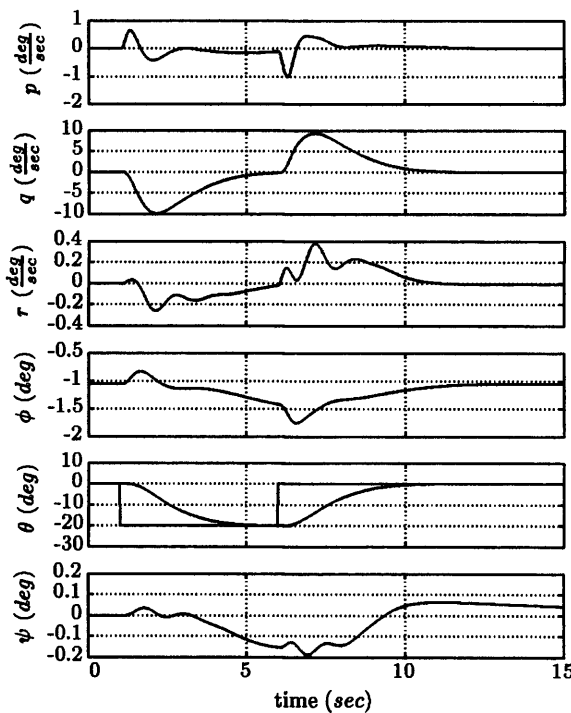


Figure 5.32 Two degrees-of-freedom compensator, -20° pitch attitude demand

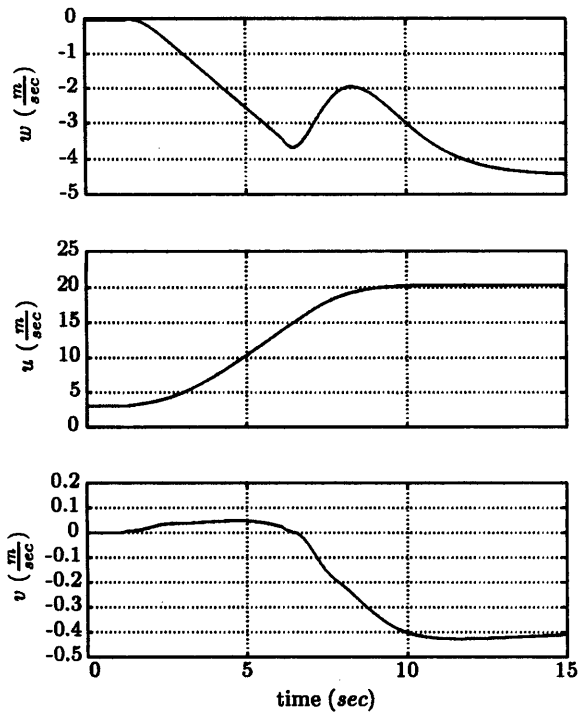


Figure 5.33 Two degrees-of-freedom compensator, -20° pitch attitude demand

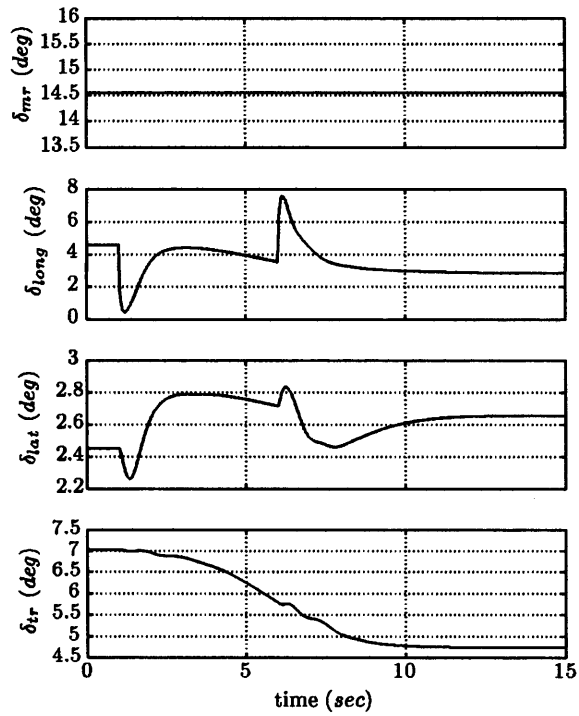


Figure 5.34 Two degrees-of-freedom compensator, -20° pitch attitude demand - Actuator deflections

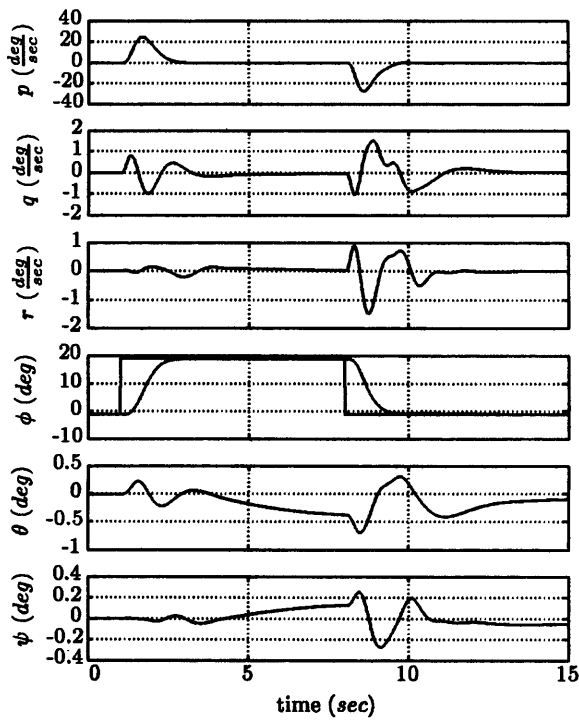


Figure 5.35 Two degrees-of-freedom compensator, 20° roll attitude demand

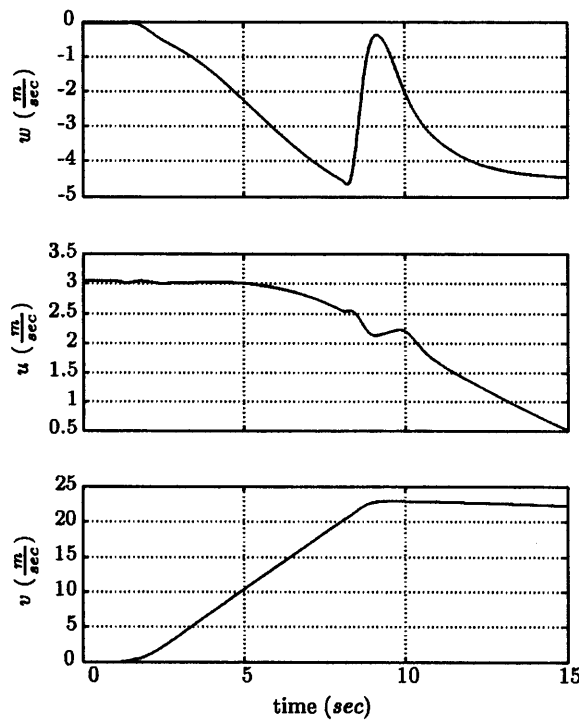


Figure 5.36 Two degrees-of-freedom compensator, 20° roll attitude demand

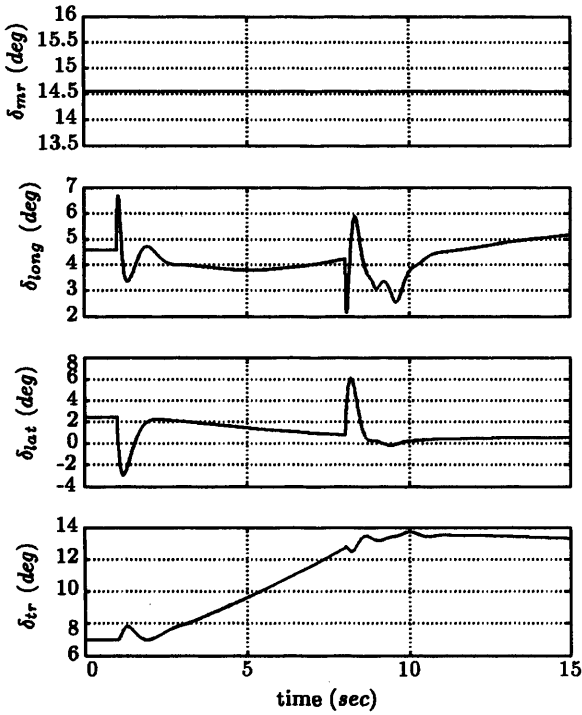


Figure 5.37 Two degrees-of-freedom compensator, 20° roll attitude demand - Actuator deflections

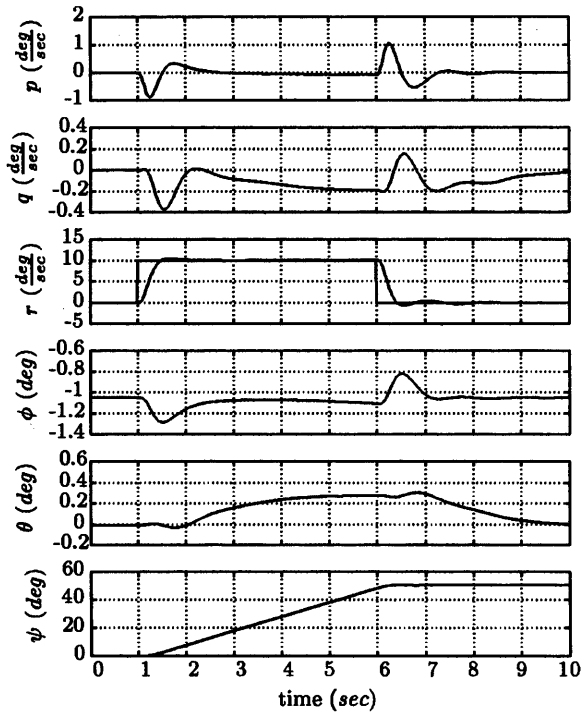


Figure 5.38 Two degrees-of-freedom compensator, 10°/sec yaw rate pulse input

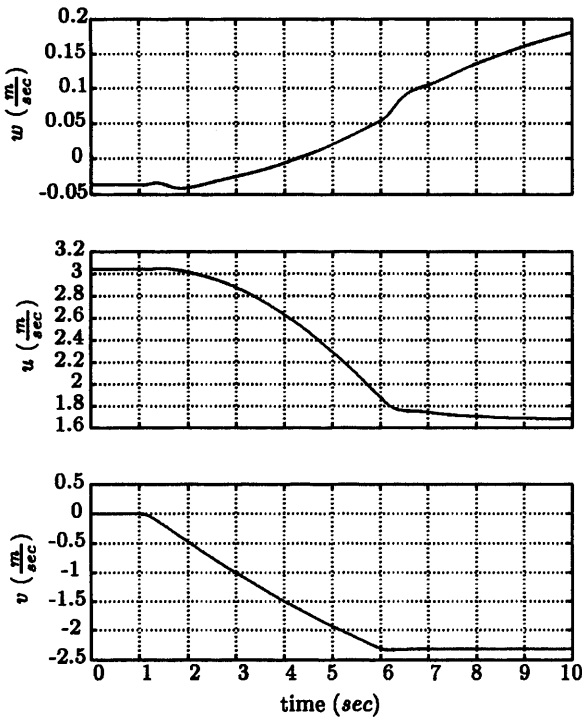


Figure 5.39 Two degrees-of-freedom compensator, 10°/sec yaw rate pulse input

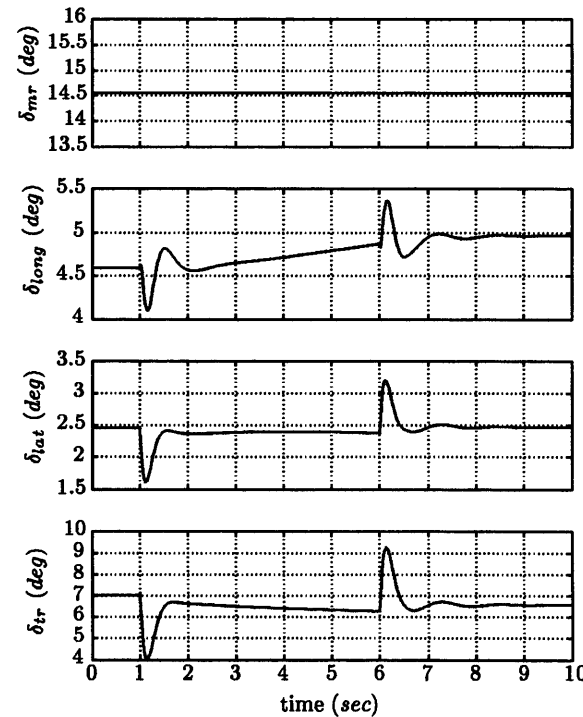


Figure 5.40 Two degrees-of-freedom compensator, 10°/sec yaw rate pulse input - Actuator deflections

5.4.4 Implementation and testing

Three controllers were implemented on the Bell 205 aircraft: the one and two DOF compensators described earlier and a two DOF controller designed using the 13-state truncated model described in section 5.4. Provisions were made so that each of these controllers could be engaged from the aircraft console with or without the mixed rate feedback signals. For the one DOF controller though, only the high frequency part of equation (5.8) was fed back to the controller since the low frequency filter was incorporated in the weighting function W_2 (see equation (5.11)).

Earlier in section 4.2.1 the implemented two DOF H_∞ controller was integrated using Euler-type numerical techniques. However, the stability of a numerical integration using Euler-type methods does not depend only on the relationship between the sampling rate and the largest controller eigenvalue, but also on the ratio of the largest and the smallest controller eigenvalues. When this ratio is very large, Euler-type integration techniques are insufficient to guarantee the required accuracy of the integration algorithm. This will be discussed in detail in section 5.7. For the moment we merely point out that the feedback compensators were discretised and updated as a set of difference equations within the time frame of the overall flight control law. As before, the code was written in ANSI standard C and debugged using a pre-programmed linear model on the on-board computer of the Bell 205 aircraft. The closed loop simulation ensured that the implemented compensator was functioning as intended and the aircraft was rolled out of the hangar for flight tests.

5.5 Flight test

The objective of the test plan was to evaluate the best of the three implemented compensators according to the ADS-33 standard [3]. It should be noted here that to judge which of the three controllers was best for in-flight evaluation test pilots were asked to familiarise themselves with each flown configuration using a variety of small and moderate amplitude inputs in all axes, at different frequencies. Upon completion of this preliminary investigation a full evaluation of the best implemented controller was conducted by flying standard ADS test manoeuvres (see for example section 4.2.5).

5.5.1 Inceptor configuration

The Evaluation Pilot (EP) used a centre-stick 2 + 1 + 1 configuration; that is, a two-axis centre-stick was used to command pitch and roll attitudes, spring centred pedals to command yaw rate and a conventional collective lever. The three-inceptor configuration is shown in Figure 5.41.

Figure 5.41 *The three-inceptor configuration*Figure 5.42 *The central console*

5.5.2 Instrument configuration

The flight instruments were laid in the cockpit in a standard Bell 205 set-up. Figure 5.42 shows the central console of the B205 experimental aircraft (see also chapter 4, section 4.2.3).

5.5.3 Pilot experience

The evaluation pilot was a qualified test pilot who had 1500 flying time on rotary wing aircraft. Previous experience on Bell 205s exceeded 500 hours flown approximately 5 years before the evaluation.

5.5.4 Handling qualities evaluation

The evaluation presented in this section is primarily based on qualitative pilot comments rather than quantitative analysis of the flight test data. This is because during the evaluation flight a system fault resulted in the data being unreadable from the Bell 205 data recorder facility.

Initial engagement of the controllers confirmed that all of them were working satisfactorily with or without mixed feedback rates. This was consistent with the designer's expectations since rotor state information was included in the design model.

Engagement of the one DOF controller quickly showed that there was significant inter-axis coupling between roll and yaw loops that required extensive pilot workload to be compensated for. The aircraft responses were not very predictable, which was a good indication that the control law did not have sufficient bandwidth to allow the pilot high frequency compensation. In addition, the safety pilot cyclic stick (see Figure 5.42) was slightly oscillatory in pitch direction at around 3 Hz. This was evidence that the integral gains in the pitch loop may have been too high. However, there is another equally important argument explaining the pitch oscillations. Earlier in section 5.3 Figures 5.6 and 5.9 suggested that the pitch and yaw loop cross couplings are poorly predicted by the model. Thus, any at-

tempt to push the roll and yaw bandwidths reasonably high (in order to enable the pilot to “get in the loop”) can result in excessive gain being injected into the pitch channel. As pitch is the slowest loop, which is bandwidth-limited by the dynamics of the rotor system, the developed pitch oscillation was perceived as an early warning of the mast-rocking mode being excited. Based on this, one can argue that MIMO controllers, which compensate for all the model cross couplings (even the erratic ones), are limiting if the couplings are poorly modelled. However, in the author’s opinion the accurate modelling of a flying vehicle is (and should be) very much part of the controller design loop. The key point is to synthesise feedback compensators by taking into account as many model inaccuracies as possible. Some examples can be found in [23, ch8,ch9]. For the moment we just point out that one route alleviating the erroneous cross compensation is to design a pitch controller separately from the lateral-directional loops.

Engagement of the two DOF controllers confirmed that both of them were very similar and minor differences could be identified by the test pilots. These differences were related to the activity of the safety pilot cyclic stick and the damping of the helicopter responses. In particular, the compensator designed using rigid body measurements alongside flapping angles and their derivatives, provided better damping and less actuator activity when compared to the compensator designed without the flapping derivatives. Of course, on the basis of a single flight experiment one cannot draw conclusive statements about the use of rotor states and their derivatives for high bandwidth feedback systems - especially when basic cross couplings are not well predicted by the design model. However, the fact that both controllers were insensitive to mixed feedback rates (as opposed to the experience reported in [8] and in section 5.3.1), coupled with the test pilot’s comments about the difference between the two compensators, *does* suggest that the more rotor states are used in the controller design process, the more insensitive the controller is to gain variations, and thus, the bigger the potential for disturbance rejection and high bandwidth flight control laws.

From the preliminary flight tests on each of the three implemented control laws it was decided finally to proceed with a full evaluation of the two DOF compensator designed using rigid body measurements with flapping angles and their derivatives. The following section describes the findings from the in flight evaluation according to the ADS-33 standard.

5.5.5 Mission task elements - pilot observations

Similar to section 4.3.2, each Mission Task Element (MTE) was flown a couple of times before an evaluation was conducted. All MTEs were flown on the same day with a temperature of 26° in a 5 – 10 *knots* cross wind. The aircraft was approximately 3330 *kg* with a slightly shifted centre of gravity in the aft direction. Below is a brief summary of pilot comment.

General comments: The controller was borderline level 1, but still slightly unpredictable in roll axis. Heading appeared slightly oscillatory during the arrest of the manoeuvre. The performance during the precision hover task was satisfactory, but all the controlled axes could be faster for high gain tasks.

Side-step: In general, the transient response was slow and some small amplitude high frequency oscillations were observed; despite that, the attitude capture was good. The aircraft required one to two additional pilot inputs to generate the desired roll rate. Because of this it was difficult to achieve the highest level of aggression. Some coupling into heading was observed (especially in the left side-step) which was not difficult to compensate for; HQR = 4.

Quick-hop: In the primary loop the acceleration was predictable but a little slow. As a result it seemed difficult to stop the aircraft at the desired position. During deceleration roll loop appeared to be a little oscillatory similarly to the side-step task although it was not a problem for the pilot to compensate for these oscillations. During acceleration some coupling into heading loop was detected, however, heading was kept within borderline performance at the expense of increased pilot workload. Because of this the resulting HQR was 4.

Precision Hover: For low gain tasks the performance was satisfactory. However, for high aggression inputs the aircraft seemed to respond slowly. Despite the fact that the pilot was using almost half the precision hover box (see Figure B.3 in appendix B) stabilising the helicopter required extensive effort. Heading loop also appeared slightly slow and required considerable pilot attention; HQR = 4.

Pirouette: Small frequent pedal inputs were required to compensate for heading changes and the ground speed seemed to be slightly oscillatory (in a sense that frequent pilot inputs were necessary to keep the speed constant during the manoeuvre). The pilot didn't like the fact that too much time was necessary to stop the aircraft from oscillating. Also performing the left pirouette was a little harder. However, the controller seemed to provide adequate angular rates and the pilot could successfully compensate for any undesirable cross couplings; HQR = 4.

Turn-to-target: There were some objectionable deficiencies in the primary response due to the inability of the controller to capture heading accurately during deceleration; the 5 sec limit was feasible only with extensive pilot workload. Despite the large overshoots in the primary loop no significant coupling was detected and the rate generated by the controller was adequate. There was also some minor translational motion which required some cyclic activity; HQR = 5.

The above handling qualities ratings are summarised in Figure 5.43.

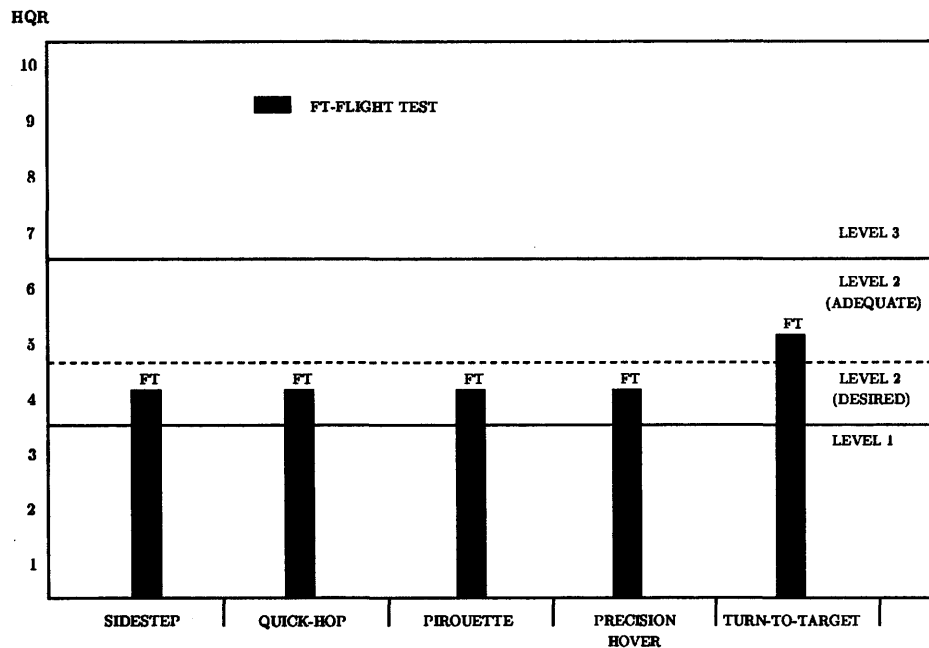


Figure 5.43 Handling Qualities Ratings - two degrees-of-freedom compensator

5.6 Discussion

Side-step: The primary concern here is the slow roll rate generated by the controller. This is an indication that the roll bandwidth may have been less than required by the helicopter for aggressive manoeuvring. The cause of the high frequency small amplitude oscillations (or ratcheting in flight test jargon) is difficult to pinpoint accurately. Previous research suggested that roll ratcheting is linked to the aircraft force-feel system [32]. However, roll ratchet tendencies are most severe with force-sensing side-sticks and in this experiment the roll inceptor was a centre-stick. Thus, it is more likely that the reason for the oscillatory roll behaviour was a small lateral PIO.

Quick-hop: From the pilot's comments it is evident that there was significant coupling into heading which resulted in the awarded HQR. This was not surprising considering the erroneous predictions of the cross coupling between pitch and yaw loops (see Figure 5.6). The reason that it was difficult to stop the aircraft during deceleration was more likely a combination of poor heading control and the lack of visual cues to the pilot when the aircraft had a pitch angle more than 15 – 20 degrees. From the pilot's point of view the visual cues become available when the aircraft nose drops significantly. Also, it seems that the heading loop does not provide sufficient bandwidth to enable the pilot to quickly compensate for the subsequent heading errors.

Precision Hover: In this task the pilot's comments suggest that the initial accelerations provided by the controller are not adequate for high gain inputs. To achieve high accelerations as required, the rate generated by the controller should have been much higher.

Redesigning for higher pitch loop bandwidth seems to be an obvious solution to the problem. Given a faster rate response the acceleration would be closer to what the test pilots would have liked. In addition, further improvement could be achieved by using a lower order ideal model in the model matching part of the H_∞ synthesis. Despite the fact that a second order output response is what we aim to achieve, the overall aircraft behaviour might contain additional dynamics - usually unmodelled modes that the controller can not compensate for. This results in flight controllers with excessive lag and/or very small initial acceleration. Therefore, using a smaller dimension ideal model can alleviate this problem to a large extent.

Pirouette: In this multi-axis manoeuvre, heading seems to be less of an issue since the pilot's attention is diverted to pitch and roll axis at the same time. The ground speed oscillations are more likely to be caused by a slightly under-damped lateral mode coupled with the wind direction. If the aircraft's attitude capture is oscillatory, the horizontal lift vector component from the main rotor (which induces the aircraft's translational motion) will not be constant in magnitude and direction. Thus, ground speed oscillations can easily occur especially when the aircraft flies out of the wind direction.

Turn-to-target: The objectionable pilot comments during this task remain largely unexplained. Although the model prediction in the yaw axis seemed very good and simulations showed that the controller should perform satisfactorily (see Figures 5.7 and 5.38 respectively), it is difficult to explain why the primary helicopter response had objectionable deficiencies. The translational motion, however, is easily explained. Pilots perform the turn-to-target task starting from the wind direction flying into the wind (see the manoeuvre description in chapter 4, section 4.2.5). Thus, as the aircraft oscillates around the targeted heading angle a fair amount of translational motion is exerted by the impinging wind on the fuselage surfaces.

Although the above discussion is based only on qualitative results, several conclusions can be made. Firstly, comparing the achieved HQRs with the HQRs obtained in the previous chapter there was an obvious improvement in the perceived aircraft responses. This improvement could be partially attributed to the inclusion of high order rotor dynamics in the controller design process. Secondly, careful consideration of high order dynamics (alongside guaranteed frequency response bounds by the controller synthesis method), can eliminate the need for predictor-type filters and make the control system more robust to high frequency uncertainty. Using such filtering methods can be more beneficial when designing compensators based only on low-frequency rigid body dynamics and actuator states. Finally, the last flight test campaign gave better insight on how to modify weighting functions in H_∞ optimisation to achieve bandwidth improvements. This is because the weight selection procedure becomes more effective when an accurate model is used for control law design.

5.7 Multivariable compensators and stability of euler-type integration algorithms

The aim of this section is to justify the choice we made to approximate the continuous time differential equations of the controller using difference equations. According to Shannon's theorem (or sample rate rule) [61, ch10], when a control law is implemented on a digital computer, the system is expected to give adequate performance if the sample rate is at least 2 times faster than the largest controller eigenvalue. When a compensator is designed "by hand", using graphical techniques, Shannon's rule is satisfied implicitly or explicitly. However, for multivariable controllers (e.g. H_∞ , μ) this requirement can be met only indirectly by solving the suboptimal synthesis problems or residualising any undesired fast controller dynamics. The key question we shall be addressing here is "whether the sample rate rule is sufficient to guarantee that a MIMO compensator will perform adequately when implemented on a digital computer with Euler-type integration techniques?" The answer is surprisingly simple. Unlike the popular understanding, Shannon's theorem does not guarantee satisfactory operation of the compensator unless the ratio of the largest to the smallest compensator eigenvalues is not very "large". Given a sufficiently small sample rate, the designer has to take into account the accuracy of the integration algorithm to ensure proper control law functionality. This is very important for H_∞ compensators since the poles of the feedback compensator tend to have the same magnitudes with the LHP transmission zeros of the design model (see remark 2.4.0.1 in chapter 2).

To justify the above arguments consider the second order system described by

$$\frac{y}{u} = \frac{1}{(s+M)(s+m)} = \frac{1}{s^2 + (M+m)s + Mm} \quad (5.13)$$

or in state space form by

$$\dot{x} = \begin{bmatrix} 0 & 1 \\ -mM & -(m+M) \end{bmatrix} x + \begin{bmatrix} 0 \\ 1 \end{bmatrix} u, \quad y = [1 \quad 0] \quad (5.14)$$

In equation (5.14), M and m represent the largest and the smallest eigenvalues of the system, s is the Laplace operator and x, u are the state and control vectors respectively. It can easily be shown that the evolution of the states can be written as

$$x(t) = C_1 e^{-Mt} [v_1] + C_2 e^{-mt} [v_2] \quad (5.15)$$

where (v_1, v_2) are the eigenvectors and C_1, C_2 depend on the initial conditions $x(0)$.

Define the ratio of the largest to the smallest eigenvalues as $\frac{M}{m} = \alpha \Leftrightarrow M = \alpha m$. Then, the controller state derivative \dot{x} can be written as

$$\begin{aligned} \dot{x}(t) &= -MC_1 e^{-Mt} [v_1] - mC_2 e^{-mt} [v_2] \\ &= -\alpha m C_1 e^{-Mt} [v_1] - mC_2 e^{-mt} [v_2] \\ &= -m \{ \alpha C_1 e^{-Mt} [v_1] + C_2 e^{-mt} [v_2] \} \end{aligned} \quad (5.16)$$

In equation (5.16) C_1 and C_2 are assumed to be constants, $M \gg m$ such that $M + m \simeq M$.

Let ΔT represent the integration step. Ignoring the constants C_1 and C_2 from the exponential terms of equation (5.16), we can see that for a sufficiently small ΔT , (say $\Delta T = 10^{-2}$), term $e^{-m\Delta T}[v_2]$ is finite and term $\alpha e^{-M\Delta T}[v_1]$ also converges. However, for large values of M the final value of $e^{-M\Delta T}$ does not approach zero and given that the ratio $\frac{M}{m} = \alpha$ is "large" the resulting controller state derivatives can take very large values.

To illustrate the above assume that $M = 20$, $m = 10^{-4}$ and $\Delta T = 10^{-2}$. Then the term $\alpha e^{-M\Delta T} = 200000e^{-20 \cdot 0.01} = 1.62 \cdot 10^5$ (see Figure 5.44).

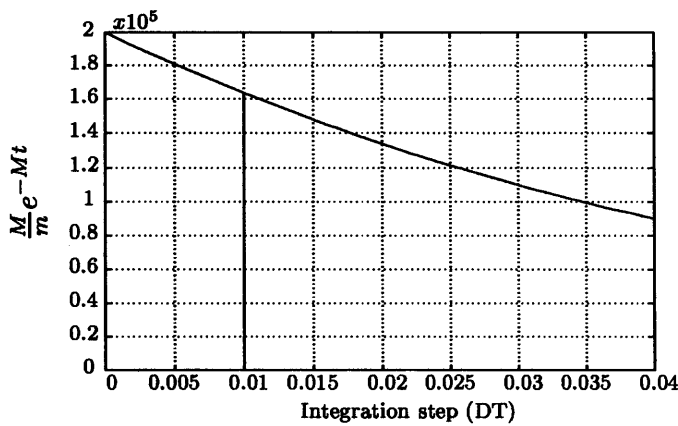


Figure 5.44 Convergence of $\alpha e^{-M\Delta T}$

The values in the above example were not chosen arbitrarily. In fact they are comparable with the smallest and the largest eigenvalues of the two DOF controller designed in section 5.4.3 (see the MATLAB script below).

```
>>rifd(spoles(K))
```

real	imaginary	frequency	damping
-2.8537e-005	0.0000e+000	2.8537e-005	1.0000e+000
-1.1101e-003	0.0000e+000	1.1101e-003	1.0000e+000
-2.4682e-001	0.0000e+000	2.4682e-001	1.0000e+000
-2.4901e-001	0.0000e+000	2.4901e-001	1.0000e+000
-3.8671e-001	0.0000e+000	3.8671e-001	1.0000e+000
-9.9039e-001	0.0000e+000	9.9039e-001	1.0000e+000
-1.0811e+000	-5.2360e-001	1.2012e+000	9.0000e-001
-1.0811e+000	5.2360e-001	1.2012e+000	9.0000e-001
-1.7977e+000	0.0000e+000	1.7977e+000	1.0000e+000
-2.6821e+000	0.0000e+000	2.6821e+000	1.0000e+000
-3.6037e+000	-1.7453e+000	4.0041e+000	9.0000e-001
-3.6037e+000	1.7453e+000	4.0041e+000	9.0000e-001
-5.3589e+000	-5.8228e+000	7.9135e+000	6.7718e-001
-5.3589e+000	5.8228e+000	7.9135e+000	6.7718e-001

-6.3000e+000	6.4273e+000	9.0000e+000	7.0000e-001
-6.3000e+000	-6.4273e+000	9.0000e+000	7.0000e-001
-7.1853e+000	7.5176e+000	1.0399e+001	6.9095e-001
-7.1853e+000	-7.5176e+000	1.0399e+001	6.9095e-001
-1.3241e+001	0.0000e+000	1.3241e+001	1.0000e+000
-1.4709e+001	0.0000e+000	1.4709e+001	1.0000e+000
-1.5826e+001	0.0000e+000	1.5826e+001	1.0000e+000
-2.1522e+001	0.0000e+000	2.1522e+001	1.0000e+000
-7.5614e+000	-6.6787e+001	6.7214e+001	1.1250e-001
-7.5614e+000	6.6787e+001	6.7214e+001	1.1250e-001

There are several ways of avoiding the effects of the large exponential term $\alpha e^{(-M\Delta T)}$. Firstly, the step size can be increased so that the initial derivatives have smaller values. However, it can easily be shown using time domain analysis, that in that case, updating the controller states according to the rule $x(\Delta T) = x(0) + \dot{x} \cdot \Delta T$, the integration error becomes very large. In other words Shannon's theorem is violated. Secondly, the designer can use a different integration technique (such as Runge-Kutta or backward Euler methods). In the latter case though, the computational demands on the flight control computer are increased and the controller coding task becomes cumbersome.

Given a continuous time controller, in the author's opinion, the best remedy to alleviate the Euler integration problem is to use difference equations to approximate the continuous time derivatives with their discrete time counterparts. It is believed that the resulting computational delay did not have a large effect on the handling qualities evaluation because it was small compared to the delays contributed by the teetering rotor and swashplate systems.

5.8 Concluding remarks

In this chapter we investigated, primarily, the use of rotor states to achieve better handling qualities than in chapter 4, where quasi-static models were employed for controller design. Pilots reported improved HQRs with compensators designed on models, which included both first and second order main rotor flapping states. In turn, these compensators achieved better disturbance rejection than their "quasi-static counterparts", which do not function satisfactorily without the use of mixed rate feedback signals. The results seem to coincide with theoretical observations based on ground-based simulations. In addition, we gave experimental evidence on the advantages of the two DOF loop shaping over, the original, one DOF H_∞ LSDP method for the helicopter control problem. This also confirms design experience from previous research efforts. Finally, it was shown that Shannon's theorem does not guarantee adequate performance of a MIMO compensator, when the controller is implemented using Euler-type integration techniques. The designer has also to take into

account the ratio of the largest to the smallest controller eigenvalues to ensure the stability of the integration algorithm.

The pilot comments about the helicopter behaviour in chapter 4 (section 4.4) as well as in chapter 5 indicated that although the controller was flown up to 80 *knots* in forward flight, its performance was not satisfactory. In this case, it is common practice to design another compensator for the high speed region ($> 45 - 50$ *knots*). “Linking” (or gain scheduling) the two H_∞ compensators can be done in a linear fashion for simplicity (see [40]), however, with no guarantees about the stability (let alone the performance) of the closed loop system. In the next chapter, a *systematic* methodology will be presented for the optimal design of a gain scheduled H_∞ loop shaping compensator, which not only stabilises the linearised plants in the blending region, but also achieves H_∞ performance control objectives.

Optimal design of multivariable, observer-based, gain-scheduled compensators

6.1 Introduction

Linear controller design techniques are the most commonly used design tools in industry. They are easy to apply and the control solution is fairly visible to systems engineers. However, for helicopters with large operating envelopes, linear designs are quite often driven beyond their limits. The assumptions regarding small deviations from nominal conditions are no longer satisfied. Airspeed dependent dynamics and different loading configurations may degrade significantly the guaranteed performance.

Over the last decade research in multivariable control laws seems to have tackled partially the problem of deviations from nominal conditions by improving the robustness of the control laws. Indeed, guaranteeing robustness against modelling errors and excursions from the design point proves a very effective tool in reducing the number of linear designs required across the flight envelope.

The purpose of gain-scheduled control, in general, is to design a time-varying controller K scheduled upon a parameter vector $\zeta(t)$ to achieve desired closed-loop performance (from $w \rightarrow z$, see figure 6.1) throughout the region of operation.

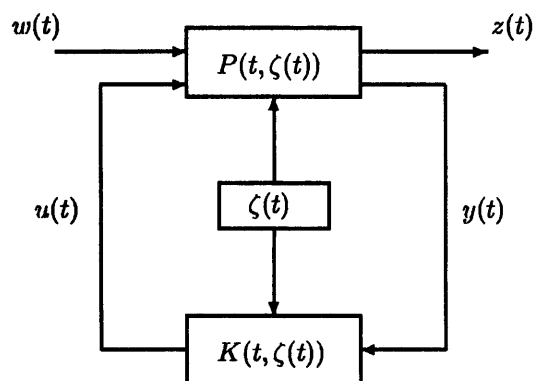


Figure 6.1 *Gain-scheduling control: general case*

A number of linear parameter-varying (LPV) controller design methods for LPV plants have recently appeared in the literature. These methods make use of a fixed Lyapunov function to characterize stability and performance. There are two general frameworks. The first framework concerns LPV plants with a linear fractional dependence on the scheduling parameter vector ζ ; parameter variations are treated as equivalent uncertainties, and a single robust controller is designed and scheduled upon these special uncertainties ([51], [5], [6]). The second framework is based on the notion of quadratic H_∞ performance; it uses directly the LPV form of the gain-scheduled controller with the same parameter dependence as the plant to bound the performance of the LPV system in an L_2 -norm sense ([7], [10]). In addition, gain-scheduling approaches based on the concept of parameter-dependent Lyapunov functions have appeared in [4], [36], [76].

These LPV approaches usually produce conservative designs, due to the large number of scheduling parameters that has to be considered in the problem. In addition, the original LPV methods provide no guarantee that an LPV controller can be determined for a given LPV plant and a scheduling variable region. In the present work, the interest is on the two-step approach that involves an interpolation process to schedule linear point controllers. First, a set of linearised plants is obtained for a set of values of the scheduling parameters, and linear controllers for these linearised plants are designed. Then, a schedule is designed that links these controllers as the operating envelope is traversed. This approach has been used in [41], [40], [50], with no guarantee, however, that the resulting interpolated controller stabilises the corresponding linearised plant. Lately, stability preserving controller interpolation schemes have appeared in [47], [66] for observer-based compensators and in [64] a new idea was presented, which minimised an H_∞ cost function in order to determine an optimal-like scheduling function for a helicopter control problem.

In this chapter, we present a realistic optimisation method for gain-scheduling observer-based controllers that not only guarantees stability, but also achieves H_∞ performance objectives along the ideas of [64]. The method can be used to maintain a smooth transition from low to high speed flight conditions in a predictable manner. In other words, the designer can ensure that blending between low and high speeds is done smoothly without causing discomfort to the pilot.

6.2 An interpolation and robust control framework

6.2.1 Stability preserving interpolation

For any pair (A, B) of state-space matrices, under certain conditions, a number of stabilising matrices $\{K_i, i = 1, \dots, r\}$ can be selected such that all eigenvalues of $(A + BK_i)$ are located in the left half plane. In what follows, we will need to determine a composite, interpolating state feedback gain that will include all individual gains K_i discussed above. The following lemma has been proven in [66]:

Lemma 6.2.1 *Suppose that $\{K_i, i = 1, \dots, r\}$ stabilize (A, B) , that is $(A + BK_i)$ is asymptotically stable for each $i = 1, \dots, r$. There exist symmetric, positive definite matrices $\{W_i, i = 1, \dots, r\}$ such that for any constants $\{\lambda_i \geq 0, i = 1, \dots, r\}$, not all zero, the interpolating matrix*

$$K = (\lambda_1 K_1 W_1 + \dots + \lambda_r K_r W_r) (\lambda_1 W_1 + \dots + \lambda_r W_r)^{-1} \quad (6.1)$$

stabilises (A, B) .

Note that the symmetric, positive definite matrices above are such that the following matrix inequalities hold

$$W_i (A + BK_i)^T + (A + BK_i) W_i < 0, \quad i = 1, \dots, r \quad (6.2)$$

As a direct result of the above lemma, for the case of two stabilising gains K_1 and K_2 , there exist symmetric, positive definite matrices W_1 and W_2 such that for the interpolating gain

$$K = (\lambda K_1 W_1 + (1 - \lambda) K_2 W_2) (\lambda W_1 + (1 - \lambda) W_2)^{-1} \quad (6.3)$$

the matrix $(A + BK)$ remains asymptotically stable for all values of λ in $[0, 1]$.

The results above determine the interpolating matrix for a fixed pair of matrices (A, B) . These results can be extended to the case where a set of such pairs of matrices are available; these matrices could be obtained, for example, from linearisations of a nonlinear plant at a fixed set of values of the scheduling parameters.

Consider a single scheduling parameter ζ varying in $[\zeta_1, \zeta_2]$. A pair of feedback gains K_1, K_2 has been determined which stabilises $(A(\zeta_1), B(\zeta_1))$ and $(A(\zeta_2), B(\zeta_2))$ respectively. Assuming that there is an overlapping region $[\alpha_1, \beta_1]$ within $[\zeta_1, \zeta_2]$ such that K_1 stabilises $(A(\zeta), B(\zeta))$ for every $\zeta \in [\zeta_1, \beta_1]$, and K_2 stabilises $(A(\zeta), B(\zeta))$ for every $\zeta \in [\alpha_1, \zeta_2]$; we say that (K_1, K_2) cover $[\zeta_1, \zeta_2]$.

The design objective is to determine an optimal continuous feedback gain with dependence upon the scheduling parameter $K(\zeta)$ which stabilises $(A(\zeta), B(\zeta))$ for any distinctive value of ζ in $[\zeta_1, \zeta_2]$. In view of Lemma 6.2.1, we can define such a continuous gain as follows

$$K(\zeta) = \begin{cases} K_1 & \zeta \in [\zeta_1, \alpha_1) \\ [\lambda(\zeta) K_1 W_1 + (1 - \lambda(\zeta)) K_2 W_2] [\lambda(\zeta) W_1 + (1 - \lambda(\zeta)) W_2]^{-1}, & \zeta \in [\alpha_1, \beta_1] \\ K_2, & \zeta \in (\beta_1, \zeta_2] \end{cases} \quad (6.4)$$

Note that it is the optimal selection of $\lambda(\zeta)$ in the entire region $[\alpha_1, \beta_1]$ to additionally meet specific H_∞ performance criteria that is of interest here. When only stability is considered, it is quite common to select $\lambda(\zeta) = \frac{\beta_1 - \zeta}{\beta_1 - \alpha_1}$; note that this reduces to the case of linear interpolation [66].

Similar to the state feedback case, results can be obtained for an interpolating state observer gain matrix which includes state observer gains that individually stabilise a pair (A, C) . The following lemma holds:

Lemma 6.2.2 *Suppose that $\{L_i, i = 1, \dots, r\}$ stabilise (A, C) , that is $(A + L_i C)$ is asymptotically stable for each $i = 1, \dots, r$. There exist symmetric, positive definite matrices $\{P_i, i = 1, \dots, r\}$ such that for any constants $\{\mu_i \geq 0, i = 1, \dots, l\}$, not all zero, the interpolating matrix*

$$L = (\mu_1 P_1 + \dots + \mu_l P_l)^{-1} (\mu_1 P_1 L_1 + \dots + \mu_l P_l L_l) \quad (6.5)$$

stabilises (A, C) .

For the state observer case, the symmetric, positive definite matrices above satisfy the following matrix inequalities

$$(A + L_i C)^T P_i + P_i (A + L_i C) < 0, \quad i = 1, \dots, l \quad (6.6)$$

Again, for a single scheduling parameter ζ varying in $[\zeta_1, \zeta_2]$, we consider a pair of state observer gains L_1, L_2 which stabilises $(A(\zeta_1), C(\zeta_1))$ and $(A(\zeta_2), C(\zeta_2))$ respectively. Assuming an overlapping region $[\alpha_1, \beta_1]$ within $[\zeta_1, \zeta_2]$ such that L_1 stabilises $(A(\zeta), C(\zeta))$ for every $\zeta \in [\zeta_1, \beta_1]$, and L_2 stabilises $(A(\zeta), C(\zeta))$ for every $\zeta \in [\alpha_1, \zeta_2]$, we can easily select a continuous state observer gain $L(\zeta)$ that stabilises $(A(\zeta), C(\zeta))$ for any value of ζ in $[\zeta_1, \zeta_2]$ as follows

$$L(\zeta) = \begin{cases} L_1, & \zeta \in [\zeta_1, \alpha_1] \\ [\mu(\zeta)P_1 + (1 - \mu(\zeta))P_2]^{-1} [\mu(\zeta)P_1 L_1 + (1 - \mu(\zeta))P_2 L_2], & \zeta \in [\alpha_1, \beta_1] \\ L_2, & \zeta \in (\beta_1, \zeta_2] \end{cases} \quad (6.7)$$

Note that similar stability preserving interpolation results have appeared in [47], where an observer-based controller structure is used, as in the sections that follow.

6.2.2 Right coprime factorisation

Suppose $G(s)$ is a strictly proper real-rational matrix with a stabilisable and detectable realisation

$$G_s = \left(\begin{array}{c|c} A_s & B_s \\ \hline C_s & 0 \end{array} \right) \quad (6.8)$$

Then, a normalised right coprime factorisation of $G_s(s)$ has a realisation

$$\begin{pmatrix} N_s \\ M_s \end{pmatrix} \stackrel{s}{=} \left(\begin{array}{c|c} A_s + B_s F & B_s \\ \hline C_s & 0 \\ F & I \end{array} \right) \quad (6.9)$$

where N_s, M_s satisfy equations (2.11) and (2.19) (see chapter 2, section 2.1.1); $F = -B_s^T X$, and $X = X^T > 0$ is the unique stabilising solution to the *Generalised Control Algebraic Riccati Equation* (GCARE)

$$A_s^T X + X A_s - X B_s B_s^T X + C_s^T C_s = 0 \quad (6.10)$$

We consider the class of perturbed plants described by

$$G_P = (N_s + \Delta_{N_s})(M_s + \Delta_{M_s})^{-1} \quad (6.11)$$

where $\Delta_{M_s}, \Delta_{N_s} \in \mathcal{H}_\infty^+$. The generalised plant $P(s)$ for this case of perturbations is given by

$$\begin{pmatrix} d \\ y \end{pmatrix} = \left(\begin{array}{cc|c} 0 & -M_s^{-1} & M_s^{-1} \\ I & -G & G \end{array} \right) \begin{pmatrix} w_1 \\ w_2 \\ u \end{pmatrix} \quad (6.12)$$

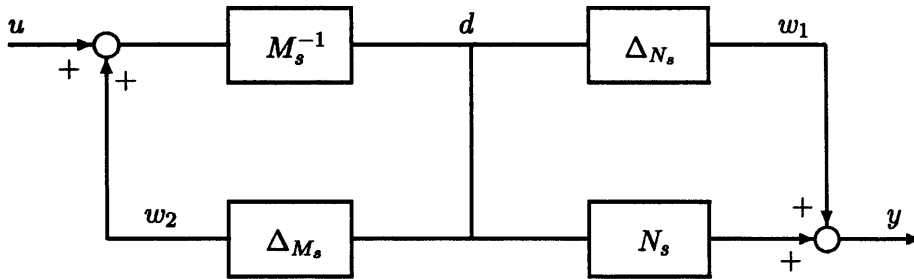


Figure 6.2 Right coprime configuration

where, as illustrated in Figure 6.2, the exogenous signals are defined as

$$w = \begin{pmatrix} w_1 \\ w_2 \end{pmatrix} = \begin{pmatrix} \Delta_{N_s} \\ \Delta_{M_s} \end{pmatrix} d = \Delta d \quad (6.13)$$

In state-space form, the generalised plant $P(s)$ from equation (6.12) is given by

$$P = \left(\begin{array}{c|cc} A_s & 0 & B_s & -B_s \\ \hline F & 0 & -I & I \\ -C_s & I & 0 & 0 \end{array} \right) \quad (6.14)$$

Assuming that a controller K internally stabilises the nominal system $G_s = N_s M_s^{-1}$ then the system is robustly stable if and only if

$$\|F_l(P, K)\|_\infty = \left\| M_s^{-1} (I - K G_s)^{-1} \begin{pmatrix} K & -I \end{pmatrix} \right\|_\infty \leq \gamma = \frac{1}{\epsilon}, \epsilon > 0 \quad (6.15)$$

where $F_l(\cdot)$ denotes a *Lower Linear Fractional Transformation* (LLFT). The closed-loop configuration of the generalised uncertainty model with a feedback controller is illustrated in Figure 6.3.

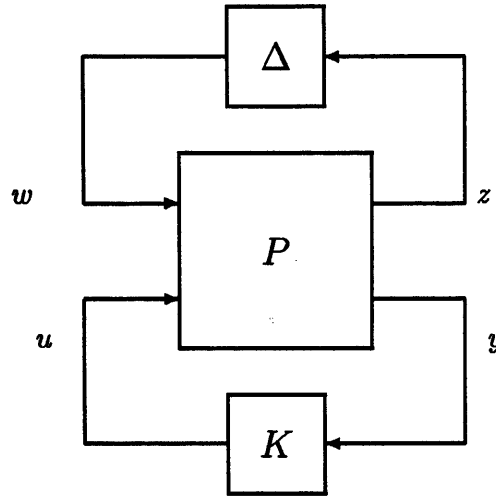


Figure 6.3 Generalised uncertainty model with feedback controller

A particular controller satisfying the cost function of equation (6.15) can be implemented in an observer form of McMillan degree equal to that of the plant. This so-called *central* or *maximum entropy* controller has the following state-space form [71]

$$K = \left(\begin{array}{c|c} A_s + B_s F + H C_s & -H \\ \hline F & 0 \end{array} \right) \quad (6.16)$$

where F is as defined before,

$$H = \gamma^2 [(1 - \gamma^2)I + Z X]^{-1} Z C^T \quad (6.17)$$

and $Z = Z^T > 0$ is the unique stabilising solution to the *Generalised Filtering Algebraic Riccati Equation* (GFARE) (see equation (2.21) in chapter 2). Note that with F , H as defined above, the eigenvalues of $(A_s + B_s F)$ and $(A_s + H C_s)$ have strictly negative real parts [71].

6.2.2.1 Closed-loop system

Consider the generalised plant P as in equation (6.14), and the controller $u = K(s)y$ from (6.16). The closed-loop system of Figure 6.3, that is the transfer function T_{zw} from the exogenous signal w to the error signal z , has the following state-space form

$$\begin{aligned} T_{zw} = F_l(P, K) &= \left(\begin{array}{c|c} A_{cl} & B_{cl} \\ \hline C_{cl} & D_{cl} \end{array} \right) \\ &= \left(\begin{array}{cc|cc} A_s & -B_s F & 0 & B_s \\ H C_s & A_s + B_s F + H C_s & -H & 0 \\ \hline F & F & 0 & -I \end{array} \right) \end{aligned} \quad (6.18)$$

It is easy to show that

$$\begin{aligned}
 \text{eig}(A_{cl}) &= \text{eig} \begin{pmatrix} A_s & -B_s F \\ HC_s & A_s + B_s F + HC_s \end{pmatrix} \\
 &= \text{eig} \begin{pmatrix} A_s + B_s F & -HC_s \\ 0 & A_s + HC_s \end{pmatrix} \\
 &= \text{eig}(A_s + B_s F) \cup \text{eig}(A_s + HC_s)
 \end{aligned} \tag{6.19}$$

So, if F and H are selected such that the eigenvalues of $(A_s + B_s F)$ and $(A_s + HC_s)$ have strictly negative real parts, then in view of equation (6.19), the closed-loop system T_{zw} of (6.18) is asymptotically stable.

6.2.3 Gap metric

The gap metric [79, 70, 30, 31], has extensively been used over the last decade to quantify the distance between uncertain feedback systems. The ν -gap metric of Vinnicombe [71], is of interest here since it admits a frequency response interpretation. According to this interpretation, the distance between any two linear systems $G_1(s)$, $G_2(s)$, that have the same number of inputs and outputs, can be calculated from their frequency responses, provided that an encirclement condition is met.

$$\delta_\nu(G_1, G_2) = \begin{cases} \|\Psi(G_1, G_2)\|_\infty, & \text{if } \det(I + G_2^* G_1) \neq 0 \forall \omega, \text{ and} \\ & \text{wno}(\det(I + G_2^* G_1)) + \eta(G_1) - \eta(G_2) - \eta_0(G_2) = 0, \\ 1, & \text{otherwise.} \end{cases} \tag{6.20}$$

with

$$\Psi(G_1, G_2) = (I + G_2 G_2^*)^{-\frac{1}{2}} (G_1 - G_2) (I + G_1^* G_1)^{-\frac{1}{2}}, \tag{6.21}$$

where $\text{wno}(g)$ is the winding number of a scalar transfer function $g(s)$, that is the number of counterclockwise encirclements around the origin by $g(s)$ evaluated on the Nyquist contour indented around the right of any imaginary axis poles of $g(s)$; $\eta(G)$ and $\eta_0(G)$ denote the number of open right-half plane and imaginary axis poles respectively of a matrix transfer function $G(s)$. More details on the ν -gap metric and its computation can be found in [71], [80], where an alternative definition in terms of normalised coprime factorisations is also given.

In the context of section 6.2.2, for a plant $G(s)$ and a controller $K(s)$, we define a generalised stability margin, $b_{G,K}$, in terms of an H_∞ norm of the size of the transfer function from signals w_1 and w_2 to signals u and y , in Figure 6.2; [60, 71, 80]

$$b_{G,K} = \begin{cases} \left(\left\| \begin{bmatrix} I \\ K \end{bmatrix} (I - GK)^{-1} \begin{bmatrix} G & I \end{bmatrix} \right\|_{\infty} \right)^{-1}, & \text{if } K \text{ stabilises } G \\ 0, & \text{otherwise} \end{cases} \quad (6.22)$$

The following robust stability result, initially shown for the gap metric in [31], can be found in [71] for the ν -gap metric:

Theorem 6.2.3 *Given a nominal plant G_1 , a compensator K , and a number ξ , then: $[G_2, K]$ is stable for all plants G_2 satisfying $\delta_{\nu}(G_1, G_2) \leq \xi$ if, and only if, $b_{G_1, K} > \xi$.*

The above theorem implies that any compensator K that stabilises a nominal plant G_1 with a stability margin $b_{G_1, K} = \xi$, will also stabilise any plant at a distance less than ξ , as measured by the ν -gap metric $\delta_{\nu}(G_1, G_2)$. The usefulness of this result will be exploited as an analysis tool in section 6.4.2.

6.3 Gain-scheduling

Our design goal is to determine an optimal gain-scheduling function for a family of linear plants, where the scheduling variable $\zeta \in [\zeta_1, \zeta_2]$. Note that the analysis that follows is not application-specific; the proposed optimisation methodology to gain-scheduling has been motivated from a helicopter control problem, but it can be applied to any other family of linear plants.

To demonstrate the applicability of the scheduling algorithm in section 6.3.3, we will use, the 12th-order Westland Lynx Mk7 helicopter model from the design example of chapter 2 (see section 2.5). The reason for using a Lynx-like rather than the Bell 205 helicopter here is that the former is much more agile (due to the main rotor system) and thus it is a more challenging problem in terms of performance requirements.

The 12-state Lynx representation was trimmed at different values of the forward speed U (which was chosen to be the scheduling variable ζ). This choice was justified on heuristic grounds, primarily for two reasons. Firstly, the scheduling variable must vary slowly with the plant dynamics. Secondly, it should capture the plant nonlinearities. For a helicopter, the dynamic pressure (and therefore forward speed) are the most important parameters affecting its dynamics. These effects have already been discussed in chapter 2 (see section 2.5, equations (2.39) - (2.40)).

6.3.1 Justification of blending region

Using a single controller at hover (and at negative airspeeds) is highly desirable as robust stabilisation has to be maximised. Earlier experience in [19] suggests that for a Lynx

helicopter a controller designed at hover can be successfully flown up to 80 *knots*. Therefore, a second linear controller was designed at 80 knots, which was used until the upper edge of the flight envelope.

However, as the aircraft accelerates from hover to high speed flight, it becomes more stable (due to the fuselage lift and the impingement of the rotor airflow on the horizontal stabiliser). Consequently the flight control system has to “adapt” to the new conditions in the transition period. Thus, the choice of the blending region $[\alpha_1, \beta_1]$ is not arbitrary. The designer must ensure that blending between low and high speeds can be done in a predictable manner to the pilot. The term “predictability” here refers to the way the human operator flies the helicopter. From the pilot’s point of view the controller should ensure a natural response of the vehicle as well as minimal workload during the transition from low to high speed flight. In our design study, this blending region was chosen between 14 and 26 m/sec ($\alpha_1 = 28$ and $\beta_1 = 52$ *knots* respectively). Note that the lower limit of this blending region is just when aerodynamic measurements become available and the upper limit reflects the speed region where the helicopter becomes aerodynamically stable.

6.3.2 Controller structure

Recall from chapter 2 that the models $\{G_i(s), i \in \overline{\zeta_1, \zeta_2}\}$ have the following state-space form

$$\begin{aligned}\dot{x} &= A(U)x + B(U)u \\ y &= C(U)x\end{aligned}\tag{6.23}$$

where the state and control vectors are

$$\begin{aligned}x &= (p \ q \ r \ \theta \ \phi \ \psi \ u_b \ v_b \ w_b \ \Theta_{lat} \ \Theta_{long} \ \Theta_{pedal})^T \\ u &= (\delta_{lat} \ \delta_{long} \ \delta_{pedal})^T\end{aligned}$$

Five of the above states comprise the output vector, namely ϕ, θ, r, p, q .

The *Loop Shaping Design Procedure* (LSDP), was used to shape the linearised plants above, as described in chapters 2, 3 and 5. The weights specifying good tracking performance at low frequencies and disturbance rejection at high frequencies were

$$W_1 = \frac{s+2}{s}I_3, \quad W_2 = \text{diag}(0.05, 0.05, 0.05, 0.025, 0.025)\tag{6.24}$$

which resulted in shaped plants given by $G_{s_i} = W_2 G_i W_1$. For simplicity, the same weights have been used for all the linearised plants.

For each linearised plant¹

$$G_i^s = \left(\begin{array}{c|c} A_i^s & B_i^s \\ \hline C_i^s & 0 \end{array} \right) = N_i^s (M_i^s)^{-1}, \quad i \in \overline{\zeta_1, \zeta_2} \quad (6.25)$$

the right coprime framework of the previous section is considered, and the central controller of equation (6.16) for F, H defined in terms of the solutions X, Z of GCARE (6.10) and GFARE (6.17) respectively can be implemented, as illustrated in Figure 6.4.

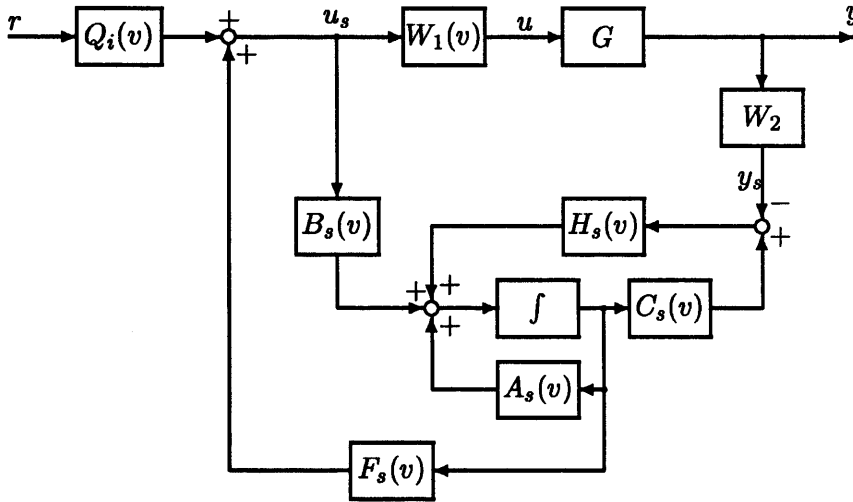


Figure 6.4 H_∞ controller in observer form

As discussed in [71, 58], it is this particular observer form of the controller that makes the right coprime factorisation for a plant $G_i^s = N_i^s M_i^s{}^{-1}$ appealing, since the injection of reference signals r in the fashion illustrated in Figure 6.4 results in $y = N_i^s Q_i$. The filter gain Q_i can easily be computed to give zero steady state tracking error. Therefore, such a controller implementation results in a closed-loop system that is not only robustly stable to perturbations (6.11) in G_i^s , but also maintains a well-behaved tracking response.

6.3.3 An optimisation approach to gain-scheduling

From the previous section, it is apparent that for each linearised plant G_i^s , the robust controller of (6.16) can easily be computed in terms of the state-space matrices of G_i^s via the Riccati equations (6.10), (6.17). Therefore, for each linearisation point, the stabilising controller can be fully described by the set of matrices $(A_i^s, B_i^s, C_i^s, F_i, H_i)$. In the next section we summarise a gain scheduling algorithm which uses this set of stabilising controllers to ensure the stability of the closed-loop system, and also maintain a certain control performance.

¹Note that the subscript $(\cdot)_s$ is replaced by $(\cdot)^s$ for notational convenience. Thus, M_s is written as M^s , N_s as N^s etc. “ i ” represents distinct linearisation points.

Step 1 (matrix interpolation) As a first step, we perform a high order polynomial fitting with respect to the scheduling variable U through the state-space matrices of the shaped linearised models $\{G_i^s, i = \zeta_1, \dots, \zeta_2\}$. As a result, we obtain continuous matrix functions $A_{in}(U)$, $B_{in}(U)$, $C_{in}(U)$ for all values of the scheduling variable within the flight region $[\zeta_1, \zeta_2]$; in other words, we define

$$G_{in}(U) = \left(\begin{array}{c|c} A_{in}(U) & B_{in}(U) \\ \hline C_{in}(U) & 0 \end{array} \right), \quad U \in [\zeta_1, \zeta_2] \quad (6.26)$$

For integer values of U , this polynomial fitting should result in an accurate approximation of the models described by

$$G_i^{in} = \left(\begin{array}{c|c} A_i^{in} & B_i^{in} \\ \hline C_i^{in} & 0 \end{array} \right), \quad i \in \overline{\zeta_1, \zeta_2} \quad (6.27)$$

For our design example a third order polynomial fitting was adequate to capture the nonlinearities of the models in (6.27). It will be shown later using gap metric analysis (see section 6.4.2), that these approximation models G_i^{in} are very close to the ideal linearised plants G_i^s . From now on, we consider these approximation models G_i^{in} , in our study, in place of the ideal models G_i^s . Note that with this assumption the results of section 6.2.2.1 can directly be used as shown in the following steps; the validity of this assumption will be confirmed again by the gap metric analysis in section 6.4.2.

Step 2 (stability preserving gains) In this part, the objective is to find a pair of stabilising control gains (F_L, F_R) for $A_{in}(U), B_{in}(U)$ that cover the transient flight region $[\alpha_1, \beta_1]$ in the sense of section 6.2.1; in other words, these two gains need to stabilise $(A_{in}(U), B_{in}(U))$ for all $U \in [\alpha_1, \beta_1]$ in the fashion of (6.4). Similarly, we need to determine a pair of filter gains (H_L, H_R) that stabilise $(A_{in}(U), C_{in}(U))$ for all $U \in [\alpha_1, \beta_1]$ in the fashion of (6.7).

These control gains are computed in terms of the solutions of (6.10) for the shaped linearised plants $G_{\alpha_1}^s$ and $G_{\beta_1}^s$ respectively, in the control scheme illustrated in Figure 6.4. Note that F_{α_1} is designated as the low-speed control gain, since it stabilises $(A_{in}(U), B_{in}(U))$ for $U \in [\zeta_1, \beta_1]$, and F_{β_1} is designated as the high-speed control gain, since it stabilizes $(A_{in}(U), B_{in}(U))$ for $U \in [\alpha_1, \zeta_2]$. Therefore, as discussed in section 6.2.1, a continuous control gain $F(U)$ which stabilises $(A_{in}(U), B_{in}(U))$ for all values of $U \in [\zeta_1, \zeta_2]$ is given by

$$F(U) = \begin{cases} F_{\alpha_1}, & U \in [\zeta_1, \alpha_1) \\ [\lambda(U)F_{\alpha_1}W_{\alpha_1} + (1 - \lambda(U))F_{\beta_1}W_{\beta_1}] [\lambda(U)W_{\alpha_1} + (1 - \lambda(U))W_{\beta_1}]^{-1}, & U \in [\alpha_1, \beta_1] \\ F_{\beta_1}, & U \in (\beta_1, \zeta_2] \end{cases} \quad (6.28)$$

where the symmetric positive definite matrices W_{α_1} , W_{β_1} are such that

$$\left. \begin{aligned} W_{\alpha_1} (A_i^{in} + B_i^{in} F_{\alpha_1})^T + (A_i^{in} + B_i^{in} F_{\alpha_1}) W_{\alpha_1} &< 0 \\ W_{\beta_1} (A_i^{in} + B_i^{in} F_{\beta_1})^T + (A_i^{in} + B_i^{in} F_{\beta_1}) W_{\beta_1} &< 0 \end{aligned} \right\}, \quad i = \alpha_1, \dots, \beta_1 \quad (6.29)$$

Similar to the control gains, $(H_{\alpha_1}, H_{\beta_1})$ were found to be pair of such filter gains as described above, computed in terms of the solutions of (6.17) for the shaped linearised plants $G_{\alpha_1}^s$, $G_{\beta_1}^s$ respectively. Note that H_{α_1} , the low-speed filter gain, stabilises $(A_{in}(U), C_{in}(U))$ for $U \in [\zeta_1, \beta_1]$, and H_{β_1} , the high-speed filter gain, stabilises $(A_{in}(U), C_{in}(U))$ for $U \in [\alpha_1, \zeta_2]$. Therefore, as discussed in section 6.2.1, a continuous stabilising filter gain $F(U)$ for all values of $U \in [\zeta_1, \zeta_2]$ is given by

$$H(U) = \begin{cases} H_{\alpha_1}, & U \in [\zeta_1, \alpha_1] \\ [\mu(U)P_{\alpha_1} + (1 - \mu(U))P_{\beta_1}]^{-1} [\mu(U)P_{\alpha_1}H_{\alpha_1} + (1 - \mu(U))P_{\beta_1}H_{\beta_1}], & U \in [\alpha_1, \beta_1] \\ H_{\beta_1}, & U \in (\beta_1, \zeta_2] \end{cases} \quad (6.30)$$

where

$$\left. \begin{aligned} (A_i^{in} + H_{\alpha_1} C_i^{in})^T P_{\alpha_1} + P_{\alpha_1} (A_i^{in} + H_{\alpha_1} C_i^{in}) &< 0 \\ (A_i^{in} + H_{\beta_1} C_i^{in})^T P_{\beta_1} + P_{\beta_1} (A_i^{in} + H_{\beta_1} C_i^{in}) &< 0 \end{aligned} \right\}, \quad i = \alpha_1, \dots, \beta_1 \quad (6.31)$$

The optimal selection of these nonlinear scheduling functions $\lambda(U)$, $\mu(U) \in [0, 1]$ to additionally satisfy H_∞ performance objectives is discussed in the next step. First, we define the controller in terms of the state-space matrices of the approximation linearised models $G_{in}(U)$ and the control, filter gains $F(U)$, $H(U)$ of (6.28), (6.30), as follows

$$K_{in}(U) = \left(\begin{array}{c|c} \frac{A_{in}(U) + B_{in}(U)F(U) + H(U)C_{in}(U)}{F(U)} & -H(U) \\ \hline & 0 \end{array} \right), \quad U \in [\alpha_1, \beta_1] \quad (6.32)$$

Step 3 (optimal selection of scheduled gains) For each linearisation point, we consider the controller

$$K_i = K_{in}(U_i) = \left(\begin{array}{c|c} \frac{A_i^{in} + B_i^{in}F(U_i) + H(U_i)C_i^{in}}{F(U_i)} & -H(U_i) \\ \hline & 0 \end{array} \right), \quad i = \alpha_1, \dots, \beta_1 \quad (6.33)$$

As discussed in section 6.2.2.1, the poles of the closed-loop configuration of the approximation plants G_i^{in} with the above controllers K_i are determined by the eigenvalues of $(A_i^{in} + B_i^{in}F(U_i))$ and $(A_i^{in} + H(U_i)C_i^{in})$. It should now be apparent why the approximation models G_i^{in} were preferred in place of the ideal models G_i^s in step 1. Therefore, the

selection of $F(U)$, $H(U)$ as in equations (6.28) and (6.30), ensures the asymptotic stability of the closed-loop system $F_l(P_i^{in}, K_i)$, as in (6.18), with

$$P_i^{in} = \left(\begin{array}{c|cc|c} A_i^{in} & 0 & B_i^{in} & -B_i^{in} \\ \hline F(U_i) & 0 & -I & I \\ \hline -C_i^{in} & I & 0 & 0 \end{array} \right) \quad (6.34)$$

Our objective is to determine the scheduling functions $\lambda(U_i)$, $\mu(U_i)$ in (6.28), (6.30) for each integer value U_i of the scheduling variable U in the blending region $[\alpha_1, \beta_1]$ such that a satisfactory H_∞ control performance is also achieved. Therefore, $\lambda(U_i)$, $\mu(U_i)$ can be chosen to minimise the effect of the exogenous signals w on the error signal z , that is to minimise the H_∞ performance cost $\|F_l(P_i^{in}, K_i)\|_\infty$. Clearly, this is a minimisation problem that has to be solved by a parameter optimisation approach. However, due to numerical inefficiency in minimising the $\|\cdot\|_\infty$ norm function ($\|\cdot\|_\infty$ is not defined on the $j\omega$ -axis) we have chosen to minimise the following cost:

$$\min_{\{\lambda(U_i), \mu(U_i)\}} J_i = \frac{1}{N} \sum_{n=1}^N \left(\max \left\{ 0, \left[\sigma_{max} \left(F_l(P_i^{in}, K_i)(j\omega) \Big|_{\omega=\omega_n} \right) - \gamma \right] \right\} \right)^2 \quad (6.35)$$

where $\{\omega_n, n = 1, \dots, N\}$ is a sufficient set of N frequency points within the “significant” frequency range (typically where the pilot workload is high), γ is the desired value for the H_∞ cost $\|F_l(P_i^{in}, K_i)\|_\infty$, and the scheduling parameters λ, μ are limited in $[0, 1]$. Note that a minimum cost $J_i = 0$ implies that $F_l(P_i^{in}, K_i)(j\omega) \Big|_{\omega=\omega_n} \leq \gamma$, for $n = 1, \dots, N$. Therefore, the frequency grid defined by $\{\omega_n, n = 1, \dots, N\}$ should be appropriately chosen such that for a zero cost J_i , the performance criterion $\|F_l(P_i^{in}, K_i)\|_\infty \leq \gamma$ can readily be determined. It should be noted that similar cost functions have been used in [62], [48].

The minimisation of the above cost functions $\{J_i, i \in \overline{30, 50}\}$ determines the values of the scheduling functions $\{[\lambda(U_i), \mu(U_i)], i = 30, \dots, 50\}$ for all the integer values of the scheduling variable U in the desired blending region ($\alpha_1 = 28, \beta_1 = 52$ knots). Polynomial fittings with respect to the scheduling variable U are performed through these distinct values of λ, μ resulting in continuous functions $\lambda(U), \mu(U)$ for $U \in \overline{28, 52}$, which in turn define the control and filter gains $F(U), H(U)$ as in (6.28), (6.30) respectively. With these gains, as discussed before, the closed-loop system is robustly stable and also achieves desired H_∞ control performance. An illustrative example is given in the following section.

6.4 Gain scheduling optimisation results

The results of the three-step optimisation approach to gain-scheduling of section 6.3.3 to the helicopter linearised models of section 6.3 are presented next.

6.4.1 Optimisation results

The minimisation of the cost functions $\{J_i, i \in \overline{30, 50}\}$ is performed using standard routines from the MATLAB Optimisation Toolbox [14]. Note that the chosen grid of frequencies consists of $N = 100$, equally spaced logarithmic frequency points $\{\omega_n, n = 1, \dots, 100\}$ in the frequency region $[10^{-2}, 10^1]$ rad/sec. The desired value for the H_∞ cost $\|F_l(P_i^n, K_i)\|_\infty$ was selected as $\gamma = 3.2$. Note that this is a reasonable target value for γ considering the fact that the optimal value of the H_∞ cost (6.15) for all the ideal linearised helicopter plants G_i^s of (6.25) with the weight functions of (6.24) has been computed, [46], to be within the range 2.75 ± 0.03 .

The results of the optimisation procedure for the optimal values of $\lambda(U_i)$, $\mu(U_i)$ are illustrated in Figure 6.5. As discussed in section 6.3.3, these distinct values of the scheduling functions are polynomially fitted with respect to U to give continuous scheduling functions $\lambda(U)$, $\mu(U)$ in the blending region $[14, 26]$ m/sec. Therefore, in view of (6.28), (6.30), we can easily implement the interpolating controller (6.32) for this region that will ensure a smooth transition from the low-speed, defined in terms of $(F_{\alpha_1}, H_{\alpha_1})$, to the high-speed controller, defined in terms of $(F_{\beta_1}, H_{\beta_1})$.

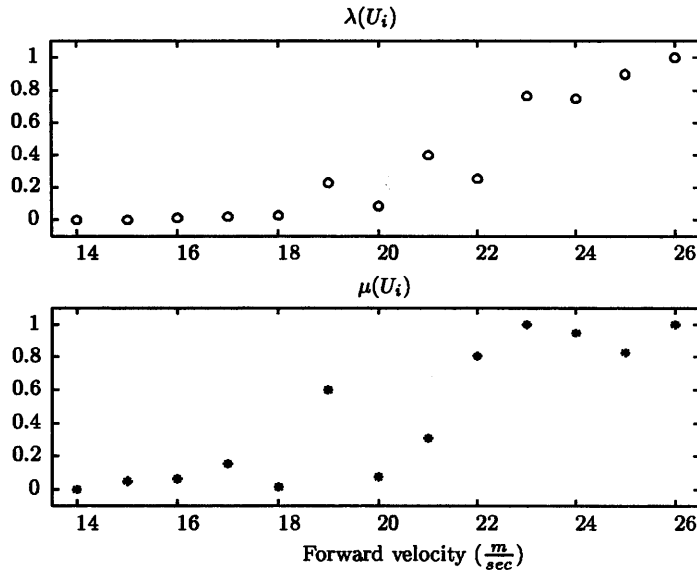


Figure 6.5 Optimal values for $\lambda(U_i)$, $\mu(U_i)$

Figure 6.6, shows a frequency domain comparison between the ideal shaped plants ($G_{20}^s K_{20}^{id}$) and the loop gains achieved from the proposed optimisation procedure ($G_{20}^s K_{20}$) at 20 m/sec; i.e. within the blending region of the gain schedule. Note that G_{20}^s is the helicopter linearised model as in (6.25), K_{20}^{id} the *central* controller in the control configuration of Figure 6.4, computed as in (6.16) in terms of the solution of GFARE (6.17), and K_{20} is the interpolating controller as determined by the optimisation procedure. It is quite apparent that the interpolating controller K_{20} results in loop gains close to the ones obtained by the ideal controller K_{20}^{id} . Similar plots are obtained when comparing the loop gains at different

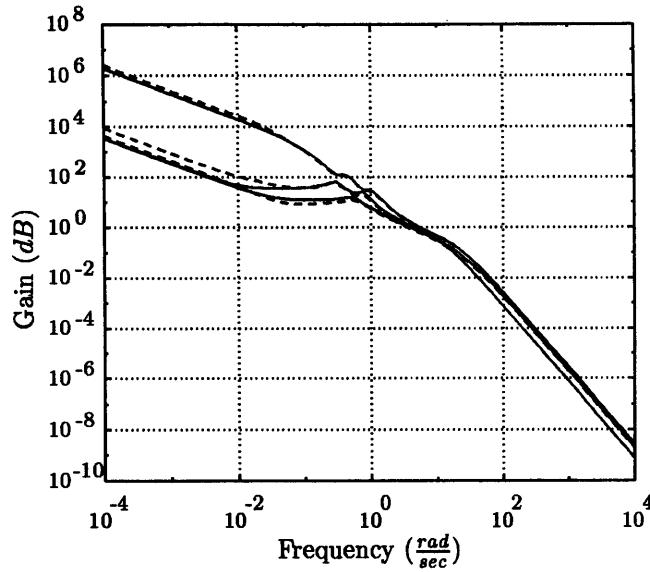


Figure 6.6 Comparison of ideal ($G_{20}^s K_{20}^{id}$) and optimised ($G_{20}^s K_{20}$) loop gains

speeds in the scheduling region $[\alpha_1, \beta_1]$.

6.4.2 Gap metric analysis

In section 6.3.3, we stated that the proposed optimisation approach was in terms of the approximation models G_i^{in} (6.27) instead of the ideal linearisation models G_i^s (6.25). As a result, we have the same state-space matrices $\{A_i^{in}, B_i^{in}, C_i^{in}\}$ for both the shaped plant G_i^{in} (6.27) and the observer-based controller K_i (6.33) in the control configuration of Figure 6.4. As discussed in section 6.2.2.1, this directly implies that the asymptotic stability of the closed loop $F_i(P_i^{in}, K_i)$, with P_i^{in} as in (6.34), is determined by the asymptotic stability of $[A_i^{in} + B_i^{in}F(U_i)]$ and $[A_i^{in} + H(U_i)C_i^{in}]$. Therefore, by selecting $F(U)$, $H(U)$ as in (6.28) and (6.30) respectively, with $\lambda(U)$, $\mu(U)$ determined by the minimisation of (6.35), the eigenvalues of $[A_i^{in} + B_i^{in}F(U_i)]$, $[A_i^{in} + H(U_i)C_i^{in}]$ are guaranteed to have negative real parts, and therefore the asymptotic stability of $F_i(P_i^{in}, K_i)$ is guaranteed as well.

It is evident that upon completion of the design procedure of section 6.3.3, we need to make sure that the determined optimal controllers K_i for the approximation models G_i^{in} (6.27) also stabilise the ideal models G_i^s in equation (6.25). In other words, we need to show that the *stability margin* of the closed-loop configuration involving (G_i^{in}, K_i) is such that the ideal model G_i^s , whose approximation G_i^{in} is, can also be stabilised by the same controller K_i .

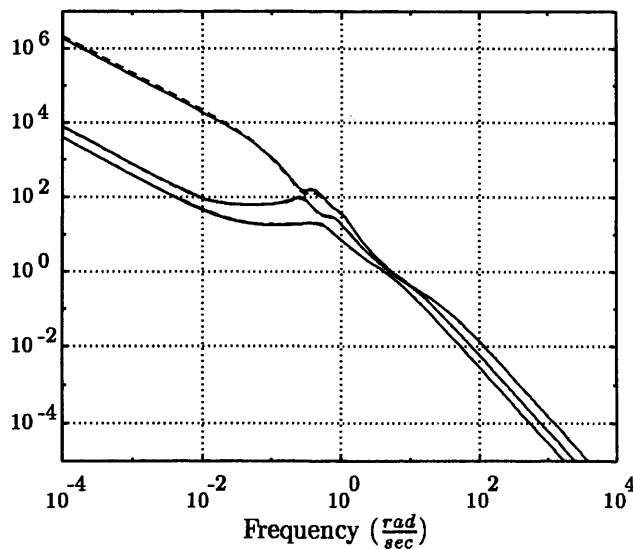
Taking into account the ν -gap metric of section 6.2.3, it suffices to show that the robust stability margin $b_{G_i^{in}, K_i}$ for the closed-loop configuration of (G_i^{in}, K_i) is larger than the ν -gap metric $\delta_\nu(G_i^{in}, G_i^s)$ that measures the distance between the ideal and approximation shaped plants G_i^s and G_i^{in} respectively. The results are shown in Table 6.1. We can clearly see that for all linearisation points, the stability margins $b_{G_i^{in}, K_i}$ are significantly larger than the

distances between the plants as measured by $\delta_\nu(G_i^{in}, G_i^s)$; and so the optimal controllers K_i do indeed stabilise the ideal linearisation models G_i^s (6.25). Therefore, we can conclude that the optimal controller $K_{in}(U)$ (6.32) determined by the proposed optimisation methodology stabilises the helicopter shaped plants G_i^s (6.25).

U_i (m/sec)	$\delta_\nu [G_i^{in}, G_i^s]$	$b_{G_i^{in}, K_i}$
14	0.0056	0.1492
15	0.0034	0.1855
16	0.0042	0.2876
17	0.0045	0.2650
18	0.0050	0.2478
19	0.0055	0.2183
20	0.0056	0.2692
21	0.0155	0.2544
22	0.0166	0.2805
23	0.0201	0.2782
24	0.0102	0.2853
25	0.0090	0.2758
26	0.0056	0.2824

Table 6.1 Gap metric analysis

Note that the effectiveness of the matrix interpolation of the shaped linearised models $\{G_i^s, i = \zeta_1, \dots, \zeta_2\}$ in step 1 of section 6.3.3, in other words the closeness of the interpolated linearised plants G_i^{in} to the ideal linearised plants G_i^s , is also demonstrated in Figure 6.7 for $U = 20$ m/sec. Similar plots are obtained for all values of U in the blending region $[\alpha_1, \beta_1]$.

Figure 6.7 Comparison of ideal G_{20}^s and interpolated G_{20}^{in} shaped plants

6.4.3 Gain-scheduled controller in simulation

The gain-scheduled controller, designed in the previous section, was tested in simulation on the nonlinear Lynx Mk7 model trimmed at 20 m/sec. Manoeuvres in the roll, pitch, and yaw axis have been performed, and the results are given in Figures 6.8 over 6.16 below. Figures 6.8 over 6.10 and Figures 6.11 to 6.13 show the output responses to input demands in the roll and pitch attitudes respectively, whereas Figures 6.14 to 6.16 give the responses to a yaw rate demand.

We can see that the controller achieves a relatively good tracking performance for all three axes manoeuvres. Note that the coupling into the other loops (especially during the rolling manoeuvre) is due to the dihedral forces around the aircraft at 40 *knots* forward speed. The rate of change of the control deflections observed is typical for controllers with static gains at the pilot inputs. This is usually addressed with command path prefiltering. In general, we can conclude that the optimal gain-scheduled controller provides smooth transition from low to high speed flight conditions, which was the objective of this work.

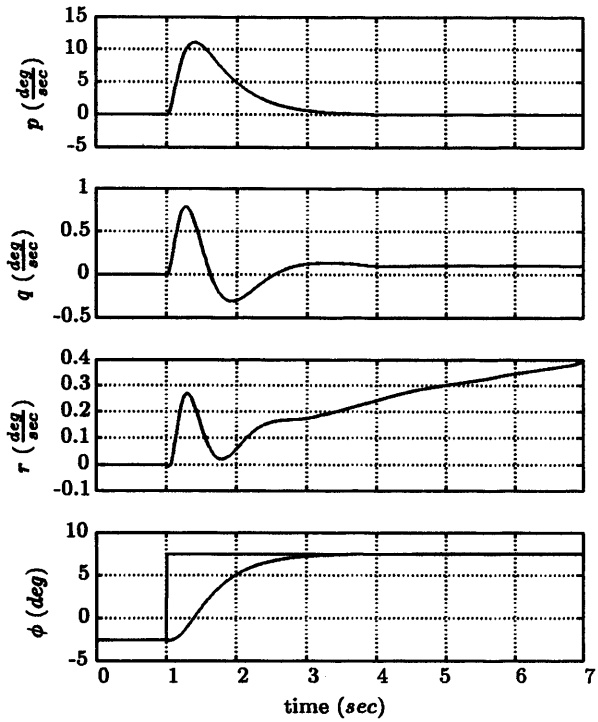


Figure 6.8 Roll manoeuvre: roll rate p , pitch rate q , yaw rate r , and roll angle ϕ

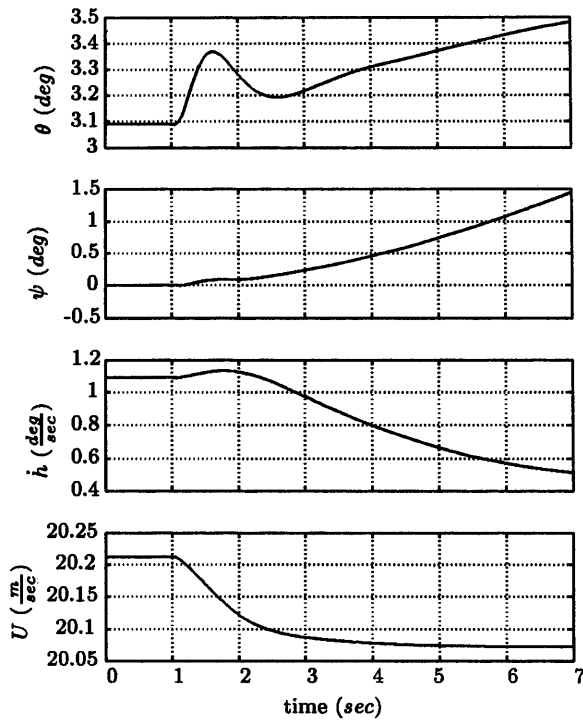


Figure 6.9 Roll manoeuvre: pitch angle θ , yaw angle ψ , heave velocity h , forward speed U

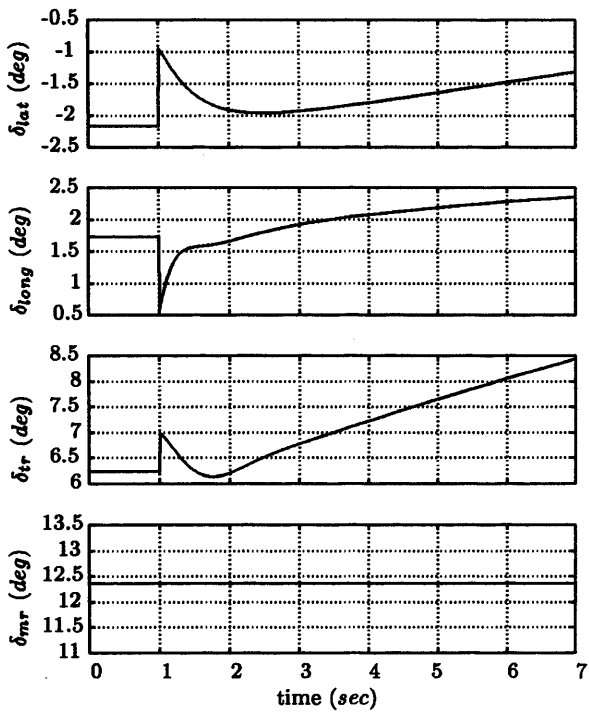


Figure 6.10 Roll manoeuvre: lateral cyclic δ_{lat} , longitudinal cyclic δ_{long} , pedal δ_{pedal} , and collective δ_{coll} inputs

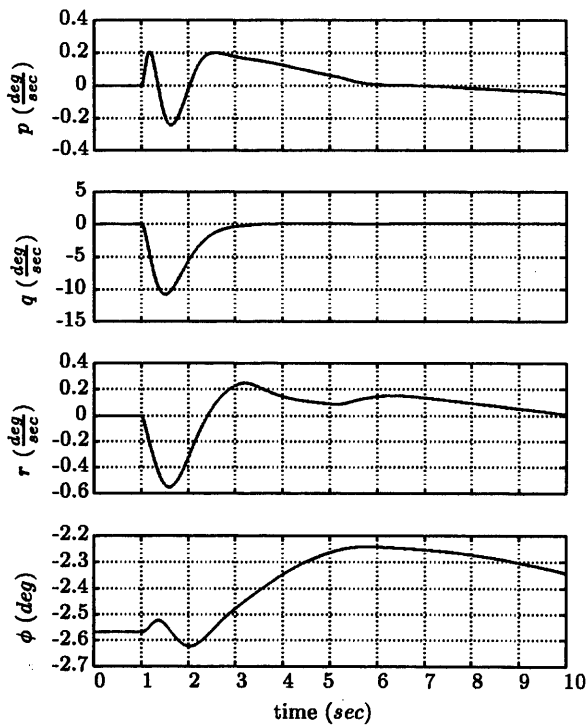


Figure 6.11 Pitch manoeuvre: roll rate p , pitch rate q , yaw rate r , and roll angle ϕ

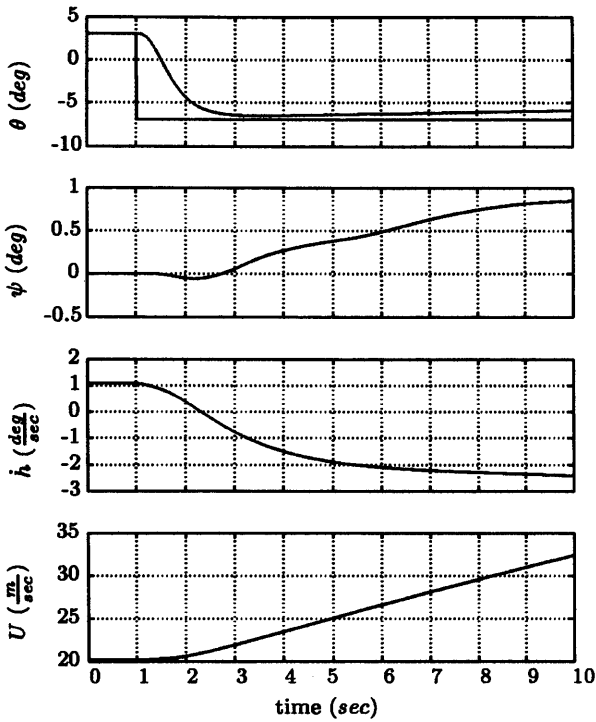


Figure 6.12 Pitch manoeuvre: pitch angle θ , yaw angle ψ , heave velocity \dot{h} , forward speed U

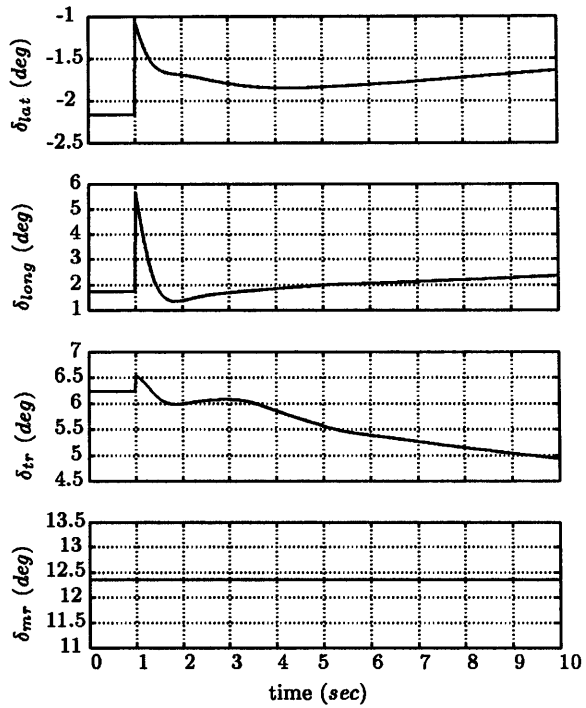


Figure 6.13 Pitch manoeuvre: lateral cyclic δ_{lat} , longitudinal cyclic δ_{long} , pedal δ_{pedal} , and collective δ_{coll} inputs

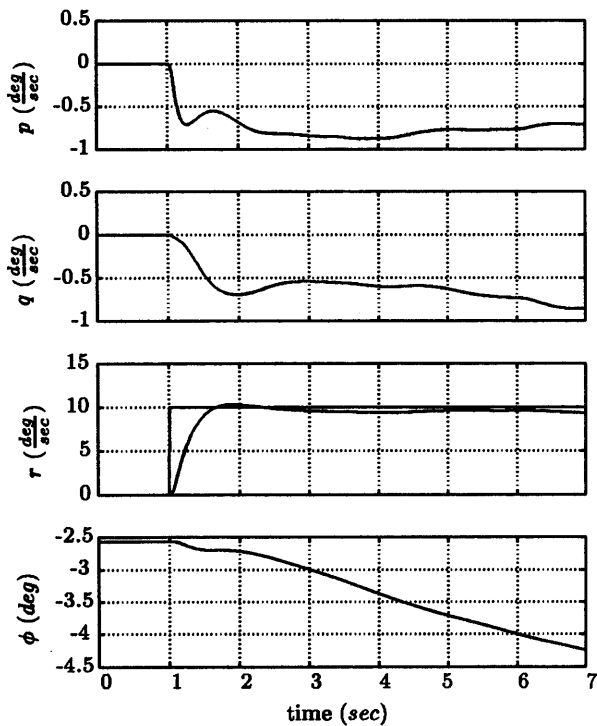


Figure 6.14 Yaw manoeuvre: roll rate p , pitch rate q , yaw rate r , and roll angle ϕ

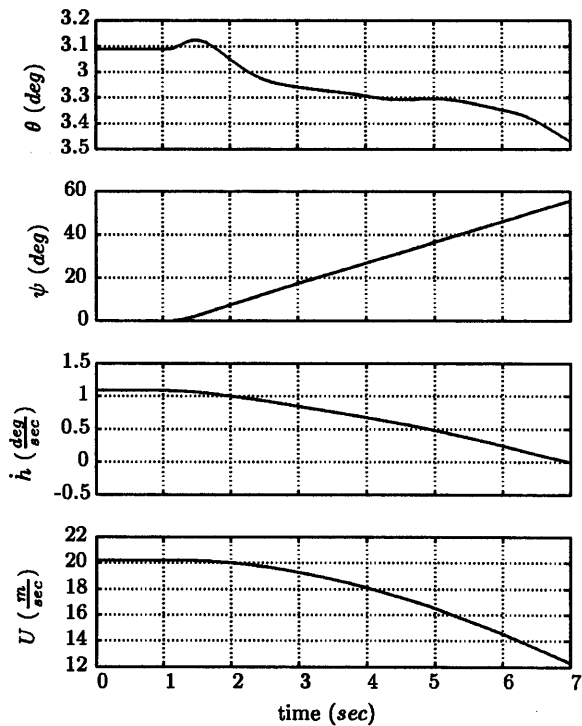


Figure 6.15 Yaw manoeuvre: pitch angle θ , yaw angle ψ , heave velocity \dot{h} , forward speed U

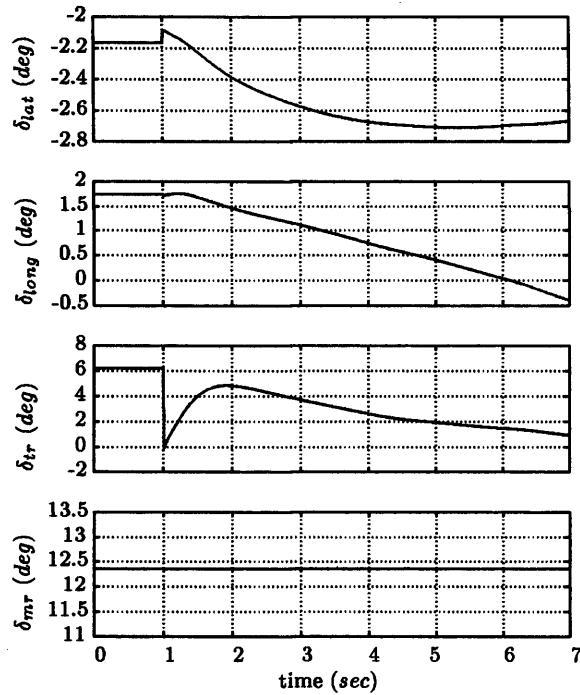


Figure 6.16 *Yaw manoeuvre: later cyclic δ_{lat} , longitudinal cyclic δ_{long} , pedal δ_{pedal} , and collective δ_{coll} inputs*

6.5 Summary

A systematic methodology has been presented for the optimal design of gain-scheduled observer based compensators for a family of linear plants. These plants are usually linearisations derived from a nonlinear model for frozen values of the scheduling parameters. The proposed methodology determines a gain-scheduled controller that not only stabilises the linearised plants within the scheduling variable region, but also achieves H_∞ performance control objectives.

Conclusions and suggestions for future research

7.1 Summary

This thesis describes the world's first H_∞ control law, which was designed and tested in flight, on a unique experimental helicopter: the Bell 205 variable stability helicopter. Designing and flight testing such prototype compensators is instrumental in demonstrating the applicability of H_∞ control theory to flight control.

A three-tonne helicopter, aggressively manoeuvring in turbulent atmosphere is more than a simple application - it is a very challenging problem, due to its complexity and its multivariable nature. The fact that H_∞ was successfully used on a helicopter enforces our belief that this design methodology is fairly generic and can be applied to other industrial problems. In the process of designing and flight testing the H_∞ control laws, many useful issues relating to the design and implementation have been highlighted. This work has given some answers, closing the gap between theory and practice, and has advanced the application of active control technology to real engineering problems.

7.1.1 The main contributions

- **H_∞ Loop shaping and the helicopter control problem:** It has been shown that the robust stability guarantees of H_∞ loop shaping make the method very useful for the helicopter control problem. The design example, which demonstrates these robust stability properties, is also utilised to introduce a multivariable control law structure that can be used over the whole rotorcraft flight envelope.
- **Analysis of the stabiliser effects bar on the rotorcraft behaviour:** Comparisons between experimental data and quasi-static mathematical models, confirm the analytical predictions about the effects of the Bell stabiliser bar on the helicopter responses. The outcome of these comparisons is very helpful in designing a flight control law and interpreting its performance on the real aircraft.

- **Design and piloted simulation of an H_∞ loop shaping compensator for the Bell 205 airborne simulator:** A two degrees-of-freedom H_∞ loop shaping compensator has been designed for the experimental Bell 205 helicopter. The controller was synthesised using quasi-static linearisations and tested in piloted simulation using high order nonlinear models developed independently. Good performance and robustness were achieved.
- **Real time implementation issues of multivariable controllers:** Implementing multivariable controllers in state space form is not common in the aerospace industry. The designed controllers were updated in real time using Euler-type integration techniques as well as difference equations. It was shown that the popular Shannon's sampling rule does not guarantee satisfactory real time operation of a control law, when Euler integration is used to update the compensator's equations. The designer must also ensure that the ratio of the largest and smallest eigenvalues of the compensator is "reasonably small".
- **In-flight evaluation of H_∞ loop shaping controllers:** Three H_∞ controllers were tested in flight. The first was designed using quasi-static linearisations and two DOF H_∞ loop shaping. The second and the third compensators were synthesised using one and two DOF H_∞ loop shaping; for both these controllers we used high order models, which included high order rotor dynamics. Extensive experimental evaluations were carried, to highlight their differences and obtain handling quality ratings by the test pilots. This was the world's first in-flight investigation of an H_∞ controller on a rotary wing aircraft.
- **Analysis of the effects of the aircraft configuration on the assessment of flight control laws:** The effects of other aircraft systems and environmental conditions on the perceived handling qualities were analysed in detail.
- **Quantitative analysis of an H_∞ loop shaping compensator:** The qualitative opinions of the test pilots were verified using flight test data analysis. This analysis enabled us to compare the predicted and achieved helicopter performance and to propose several modifications for the enhancement of the control law performance.
- **Agreement between piloted simulations and flight tests:** Very good agreement between the ground based piloted simulations and the in-flight investigations has been achieved. This highlights the usefulness of ground based piloted assessments as well as demonstrates the effectiveness of a carefully planned flight test.
- **Effects of high order rotor dynamics to H_∞ -like control law design:** It was shown that the performance of the H_∞ compensator was improved when high order rotor dynamics are included in the controller design process. This compensator is

more sensitive to gain variations than a controller designed only with rigid body measurements.

- **Robustness improvements from using high order rotor dynamics and H_∞ optimisation:** In-flight investigations showed that mixed rate predictor-type feedback, which filters out a significant amount of noise from the measurements can be eliminated if an H_∞ -like controller is designed with models which include high order rotor states.
- **Optimal design of multivariable, observer-based, gain-scheduled compensators:** A new *systematic* methodology H_∞ loop shaping compensator, which not only stabilises the linearised plants in the scheduling region, but also achieves H_∞ performance control objectives.

7.2 Suggestions for future research

During the course of this work, a number of issues arose, which could be fruitfully investigated in the future.

- The high order nonlinear model used in chapter 5 was shown to have significant deficiencies in predicting the Bell 205 cross axis responses. Further work needs to be undertaken to arrive to a more representative model of the Bell 205 aircraft. Including a dynamic inflow model (e.g. Pitt and Peters [55]), wake distortion effects, and engine parameters in the nonlinear model would be a good start in the this direction. The dynamic inflow is largely responsible for the pitch-roll cross couplings and engine information would improve greatly the heave-yaw interaction.
- The gain scheduling procedure developed in chapter 6 was demonstrated using nonlinear simulations. It would be very beneficial if a gain scheduled controller was designed and tested in piloted simulation as well as in real flight.
- In chapter 6 we used only two scheduling variables for the control and filter Riccati gains H and F , respectively. This implies that each of the entries of these Riccati gains uses the same function to achieve the robustness and performance requirements in the scheduling region. For multivariable systems a greater number of scheduling functions would be desirable to meet the design requirements.
- Linear Parameter Varying theory has allowed us to address the gain scheduling problem in a more systematic way, since a global control law is synthesised in a single procedure, where stability and performance are guaranteed. We believe that for a successful application of the LPV method, the LPV model should take into account the inherent dynamics of the control problem. This is because of two reasons. Firstly,

if a pure LPV model is used for synthesis, the equations of motion must be transformed to a form which minimises the number of scheduling variables. Secondly, if interpolation of Jacobi linearisations is used to set up a quasi LPV model and the state space entries are used as scheduling variables, the designer must have a clear understanding which state space entry is more influential to the dynamical behaviour of the system. Then one can trade-off not only the number of scheduling variables, but also their range which is being used to calculate the gain scheduled controller. It is obvious here, that a shorter range of scheduling region greatly reduces the conservatism of the LPV solution to the problem.

- A useful tool to assist in the above point would be a qualitative notion of the distance between two LPV plants. A similar measure to the gap metric for linear systems is required.
- An important practical aspect of any gain scheduled system is the robustness properties of the synthesis algorithms to perturbations in the scheduling variable. In a realistic environment, parametric perturbations will always be present and the scheduling scheme must provide guarantees against these perturbations.
- Further development of the Bell 205 H_∞ controller would be beneficial.
- It would also be very interesting to test different control law design techniques on the Bell 205 variable stability helicopter e.g a sliding mode, μ synthesis or a dynamic inversion controller. This will allow to make comparisons between the different controller synthesis techniques as well as to find out which method is best applicable to the helicopter control problem.

List of Figures

1.1 Singular values of the model G	4
1.2 Condition number of the model G	4
1.3 One degree of freedom configuration	5
2.1 Feedback control configuration with disturbances	13
2.2 Design requirements in terms of the loop gain function GK	15
2.3 Two degrees-of-freedom configuration	21
2.4 General control configuration	21
2.5 Simplified pitch loop dynamics	24
2.6 Singular values of the model G_{sc}	26
2.7 $W_2G_{sc}W_1K_a$ (solid) and $GW_2K_\infty W_1$ (dashed)	26
2.8 Implementation of the two DOF H_∞ controller	30
2.9 Sensitivity function $(I - G_sK_2)^{-1}$	30
2.10 Complementary sensitivity function $(I - G_sK_2)^{-1}G_sK_2$	30
2.11 Specified vs achieved loop gains: two DOF formulation	31
2.12 Output step responses of roll angle (solid) and the ideal model (dashed)	31
3.1 The Bell 205 stabiliser bar	35
3.2 Stabiliser bar block diagram	36
3.3 Time history of doublet input in lateral axis	37
3.4 Comparison of flight test data and NASA 6DOF model responses to a doublet input in lateral axis	37
3.5 Time history of doublet input in longitudinal axis	38
3.6 Comparison of flight test data and NASA 6DOF model responses to a doublet input in longitudinal axis	38
3.7 Time history of doublet input in yaw axis	38

3.8	Comparison of flight test data and NASA 6DOF model responses to a doublet input to directional axis	38
3.9	Comparison of flight test data and NASA 6DOF pitch axis responses to a doublet input in the lateral axis	39
3.10	Comparison of flight test data and NASA 6DOF yaw axis responses to a doublet input in the lateral axis	39
3.11	Comparison of flight test data and NASA 6DOF roll axis responses to a doublet input in the longitudinal axis	39
3.12	Comparison of flight test data and NASA 6DOF yaw axis responses to a doublet input in the longitudinal axis	39
3.13	Comparison of flight test data and NASA 6DOF pitch axis responses to a doublet input in the directional axis	40
3.14	Comparison of flight test data and NASA 6DOF roll axis responses to a doublet input in the directional axis	40
3.15	Comparison of open loop flight test data (solid) and NASA 6DOF model responses (dashed) to a frequency sweep input in lateral axis	40
3.16	Comparison of open loop flight test data (solid) and NASA 6DOF model responses (dashed) to a frequency sweep input in longitudinal axis	40
3.17	Comparison of open loop flight test data (solid) and NASA 6DOF model responses (dashed) to a frequency sweep input in yaw axis	41
3.18	The H_∞ controller architecture	44
3.19	Shaped helicopter model	48
3.20	Open loop singular values from all the inputs to each of the outputs.	48
3.21	Sensitivity function $S_o = (I - G_s K_2)^{-1}$ - Bell 205 control law	49
3.22	Complementary sensitivity function $T_o = (I - G_s K_2)^{-1} G_s K_2$ - Bell 205 control law	49
3.23	Time simulation, 5° heave demand	50
3.24	Time simulation, 5° heave demand	50
3.25	Time simulation, 5° heave demand - Actuator deflections	51
3.26	Time simulation, 5° pitch attitude demand	51
3.27	Time simulation, 5° pitch attitude demand	51
3.28	Time simulation, 5° pitch attitude demand - Actuator deflections	51
3.29	Time simulation, 5° roll attitude demand	52
3.30	Time simulation, 5° roll attitude demand	52
3.31	Time simulation, 5° roll attitude demand - Actuator deflections	52
3.32	Time simulation, 5° yaw rate demand	52
3.33	Time simulation, 5° yaw rate demand	53
3.34	Time simulation, 5° yaw rate demand - Actuator deflections	53

3.35 Handling Qualities Ratings: ground-based simulations for different aggression levels	56
3.36 Handling qualities ratings scale	58
4.1 The NRC Bell 205 Airborne Simulator	62
4.2 Handling Qualities Ratings: ground-based simulations vs flight test	68
4.3 Test data analysis procedure	68
4.4 Power spectral density function	68
4.5 Time histories of the pitch, bank, and heading angles during side-step task	69
4.6 Power spectral estimates of input signals during side-step task	70
4.7 Time histories of the pitch, bank, and heading angles during a quick-hop task	71
4.8 Power spectral estimates of input signals during a quick-hop task	72
4.9 Time histories of the bank angle, heading angle and indicated altitude during a precision hover manoeuvre.	73
4.10 Time histories of the pitch, bank, and heading angles during a 180° turn-to-target manoeuvre.	74
4.11 Power spectral estimates of input signals during a turn-to-target task	75
4.12 Roll axis frequency sweep: Input - Output time histories	76
4.13 Lateral cyclic to roll attitude estimated closed loop frequency response	76
4.14 Pitch axis frequency sweep: Input - Output time histories	77
4.15 Longitudinal cyclic to pitch attitude estimated closed loop frequency response	77
4.16 Yaw axis frequency sweep: Input - Output time histories	78
4.17 Pedal to heading estimated closed loop frequency response	78
5.1 Comparison between flight test data and high order model roll rate responses to a doublet input in lateral axis	84
5.2 Comparison between flight test data and high order model pitch rate responses to a doublet input in the lateral axis	84
5.3 Comparison between flight test data and high order model yaw rate responses to a doublet input in the lateral axis	84
5.4 Comparison between flight test data and high order model pitch rate responses to a doublet input in longitudinal axis	84
5.5 Comparison between flight test data and high order model roll rate responses to a doublet input in the longitudinal axis	85
5.6 Comparison between flight test data and high order model yaw rate responses to a doublet input in the longitudinal axis	85
5.7 Comparison between flight test data and high order model yaw rate responses to a doublet input in directional axis	86

5.8	Comparison between flight test data and high order model roll rate responses to a doublet input in the directional axis	86
5.9	Comparison between flight test data and high order model pitch rate responses to a doublet input in the directional axis	86
5.10	Comparison between open loop flight test data (solid) and nonlinear model responses (dashed) to a frequency sweep input in longitudinal axis	86
5.11	Comparison between open loop flight test data (solid) and nonlinear model responses (dashed) to a frequency sweep input in lateral axis	87
5.12	Comparison between open loop flight test data (solid) and nonlinear model responses (dashed) to a frequency sweep input in directional axis	87
5.13	Frequency responses of the high order model (solid), 15th order residualised (dashed) model and 13th order model (*).	90
5.14	Weighted frequency response of the Bell 205 helicopter	92
5.15	One degree-of-freedom compensator, -2° heave demand	93
5.16	One degree-of-freedom compensator, -2° heave demand	93
5.17	One degree-of-freedom compensator, -2° heave demand - Actuator deflections	93
5.18	One degree-of-freedom compensator, -20° pitch attitude demand	93
5.19	One degree-of-freedom compensator, -20° pitch attitude demand	94
5.20	One degree-of-freedom compensator, -20° pitch attitude demand - Actuator deflections	94
5.21	One degree-of-freedom compensator, 20° roll attitude demand	94
5.22	One degree-of-freedom compensator, 20° roll attitude demand	94
5.23	One degree-of-freedom compensator, 20° roll attitude demand - Actuator deflections	95
5.24	One degree-of-freedom compensator, $10^\circ/sec$ yaw rate pulse input	95
5.25	One degree-of-freedom compensator, $10^\circ/sec$ yaw rate pulse input	95
5.26	One degree-of-freedom compensator $10^\circ/sec$ yaw rate pulse input - Actuator deflections	95
5.27	Two degree-of-freedom compensator, output sensitivity function	97
5.28	Two degree-of-freedom compensator, complementary sensitivity function	97
5.29	Two degrees-of-freedom compensator, 2° heave demand	98
5.30	Two degrees-of-freedom compensator, 2° heave demand	98
5.31	Two degrees-of-freedom compensator, 2° heave demand - Actuator deflections	98
5.32	Two degrees-of-freedom compensator, -20° pitch attitude demand	98
5.33	Two degrees-of-freedom compensator, -20° pitch attitude demand	99
5.34	Two degrees-of-freedom compensator, -20° pitch attitude demand - Actuator deflections	99

5.35	Two degrees-of-freedom compensator, 20° roll attitude demand	99
5.36	Two degrees-of-freedom compensator, 20° roll attitude demand	99
5.37	Two degrees-of-freedom compensator, 20° roll attitude demand - Actuator deflections	100
5.38	Two degrees-of-freedom compensator, 10°/sec yaw rate pulse input	100
5.39	Two degrees-of-freedom compensator, 10°/sec yaw rate pulse input	100
5.40	Two degrees-of-freedom compensator, 10°/sec yaw rate pulse input - Actuator deflections	100
5.41	The three-inceptor configuration	102
5.42	The central console	102
5.43	Handling Qualities Ratings - two degrees-of-freedom compensator	105
5.44	Convergence of $\alpha e^{-M\Delta T}$	108
6.1	Gain-scheduling control: general case	111
6.2	Right coprime configuration	115
6.3	Generalised uncertainty model with feedback controller	116
6.4	H_∞ controller in observer form	120
6.5	Optimal values for $\lambda(U_i)$, $\mu(U_i)$	124
6.6	Comparison of ideal ($G_{20}^s K_{20}^{id}$) and optimised ($G_{20}^s K_{20}$) loop gains	125
6.7	Comparison of ideal G_{20}^s and interpolated G_{20}^{in} shaped plants	126
6.8	Roll manoeuvre: roll rate p , pitch rate q , yaw rate r , and roll angle ϕ	128
6.9	Roll manoeuvre: pitch angle θ , yaw angle ψ , heave velocity \dot{h} , forward speed U	128
6.10	Roll manoeuvre: lateral cyclic δ_{lat} , longitudinal cyclic δ_{long} , pedal δ_{pedal} , and collective δ_{coll} inputs	128
6.11	Pitch manoeuvre: roll rate p , pitch rate q , yaw rate r , and roll angle ϕ	128
6.12	Pitch manoeuvre: pitch angle θ , yaw angle ψ , heave velocity \dot{h} , forward speed U	129
6.13	Pitch manoeuvre: lateral cyclic δ_{lat} , longitudinal cyclic δ_{long} , pedal δ_{pedal} , and collective δ_{coll} inputs	129
6.14	Yaw manoeuvre: roll rate p , pitch rate q , yaw rate r , and roll angle ϕ	129
6.15	Yaw manoeuvre: pitch angle θ , yaw angle ψ , heave velocity \dot{h} , forward speed U	129
6.16	Yaw manoeuvre: later cyclic δ_{lat} , longitudinal cyclic δ_{long} , pedal δ_{pedal} , and collective δ_{coll} inputs	130
B.1	Sidestep task	145
B.2	Quick-hop task	146
B.3	Precision hover task	146

7.2 Suggestions for future research

140

B.4 Pirouette circle

147

A

Controller Code

```
/*  INITIALIZATION          */
r [0] = -DENET/5;
r [1] = DANET/5;
r [2] = -DRNET/5;

state [0] = (THETA - th0)*DEG2RAD;
state [1] = (PHI - ph0)*DEG2RAD;
state [2] = (R - r0)*DEG2RAD;
state [3] = (Q - q0)*DEG2RAD;
state [4] = (P - p0)*DEG2RAD;

if (FSW_REG & BIT_8){
state [2] = (R_MIX - r0)*DEG2RAD;
state [3] = (Q_MIX - q0)*DEG2RAD;
state [4] = (P_MIX - p0)*DEG2RAD;
}

/*  FORWARD CONTROLLER    */

for ( i=0; i<6; i++ ) {
BRM1 [i] = 0.0;
for ( j=0; j<3; j++ ) {
BRM1 [i] += BoSF[i][j] * r[j];
}
}
for ( i=0; i<6; i++ ) {
```

```

AoXo [i] = 0.0;
for ( j=0; j<6; j++ ) {
AoXo [i] += Ao[i][j] * Xo[j];
}
}
for ( i=0; i<6; i++ ) {
XoDOT [i] = AoXo [i] + BRM1 [i];
}
for ( i=0; i<6; i++ ) {
Xo [i] += XoDOT [i] * DELT;
}
for ( i=0; i<5; i++ ) {
RM2 [i] = 0.0;
for ( j=0; j<6; j++ ) {
RM2 [i] += F2[i][j] * Xo[j];
}
}
/* FEEDBACK CONTROLLER */

for ( i=0; i<14; i++ ) {
HCS [i] = 0.0;
for ( j=0; j<5; j++ ) {
HCS [i] += HF[i][j] * state[j];
}
}
for ( i=0; i<14; i++ ) {
BSX [i] = 0.0;
for ( j=0; j<5; j++ ) {
BSX [i] += BS[i][j] * RM3[j];
}
}
for ( i=0; i<14; i++ ) {
ASX [i] = 0.0;
for ( j=0; j<14; j++ ) {
ASX [i] += A11K[i][j] * XHAT[j];
}
}
for ( i=0; i<14; i++ ) {
XHATDOT [i] = HCS [i] + BSX [i] + ASX [i];
}

```

```

}
for ( i=0; i<14; i++ ) {
XHAT [i] += XHATDOT [i] * DELT;
}
for ( i=0; i<5; i++ ) {
RM4 [i] = 0.0;
for ( j=0; j<14; j++ ) {
RM4 [i] += F1[i][j] * XHAT[j];
}
}
for ( i=0; i<5; i++ ) {
RM3 [i] = RM2 [i] + RM4 [i];
}

/* PRE COMPENSATOR                                     */

for ( i=0; i<3; i++ ) {
BRM3 [i] = 0.0;
for ( j=0; j<5; j++ ) {
BRM3 [i] += BW[i][j] * RM3[j];
}
}
for ( i=0; i<3; i++ ) {
DRM3 [i] = 0.0;
for ( j=0; j<5; j++ ) {
DRM3 [i] += DW[i][j] * RM3[j];
}
}
for ( i=0; i<3; i++ ) {
AWXW [i] = 0.0;
for ( j=0; j<3; j++ ) {
AWXW [i] += AW[i][j] * XW[j];
}
}
for ( i=0; i<3; i++ ) {
XWDOT [i] = AWXW [i] + BRM3 [i];
}
for ( i=0; i<3; i++ ) {
XW [i] += XWDOT [i] * DELT;
}

```

```
}  
for ( i=0; i<3; i++ ) {  
  CWXW [i] = 0.0;  
  for ( j=0; j<3; j++ ) {  
    CWXW [i] += CW[i][j] * XW[j];  
  }  
}  
for ( i=0; i<3; i++ ) {  
  drive [i] = CWXW [i] + DRM3 [i];  
}  
  
* fda = drive [1]/2.54;  
* fde = drive [0]/2.54;  
* fdr = drive [2]/2.54;
```

B

Flight test manoeuvres - ADS-33 tasks

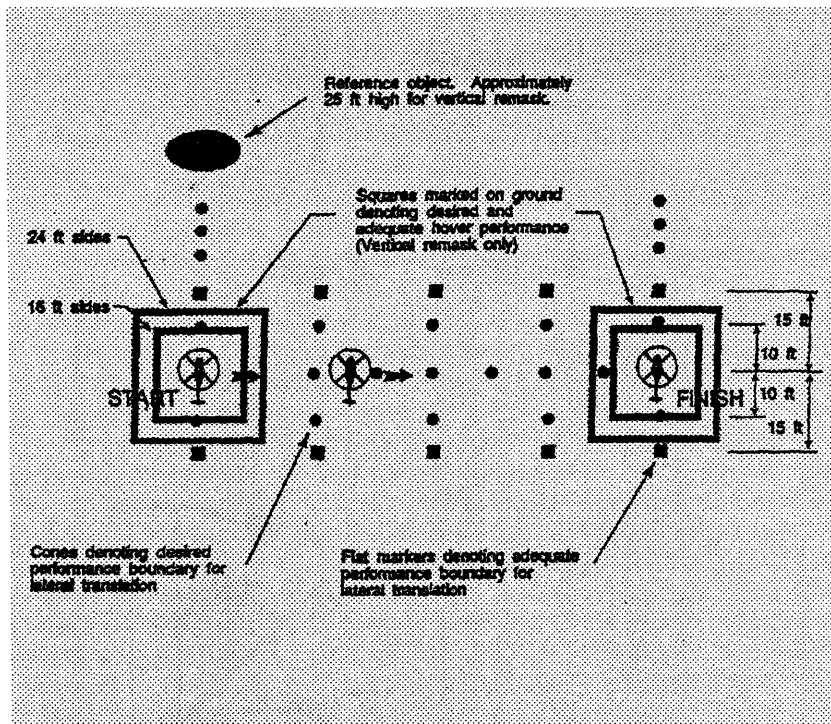


Figure B.1 *Sidestep task*

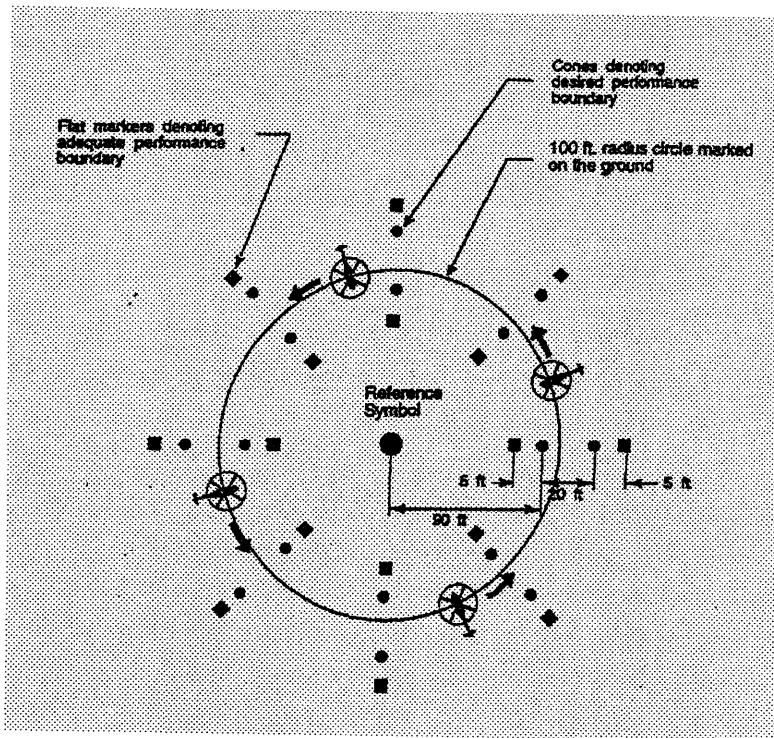
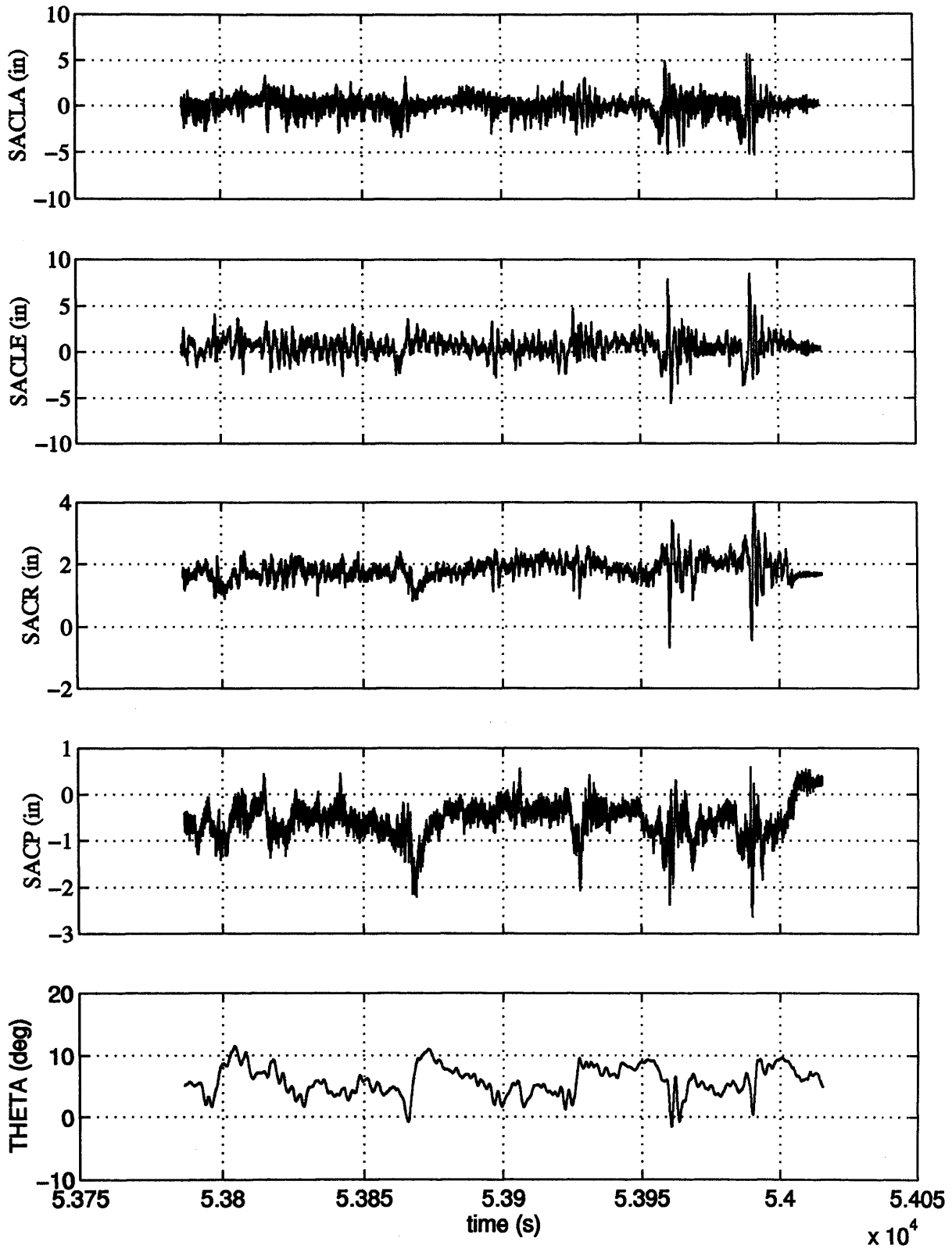
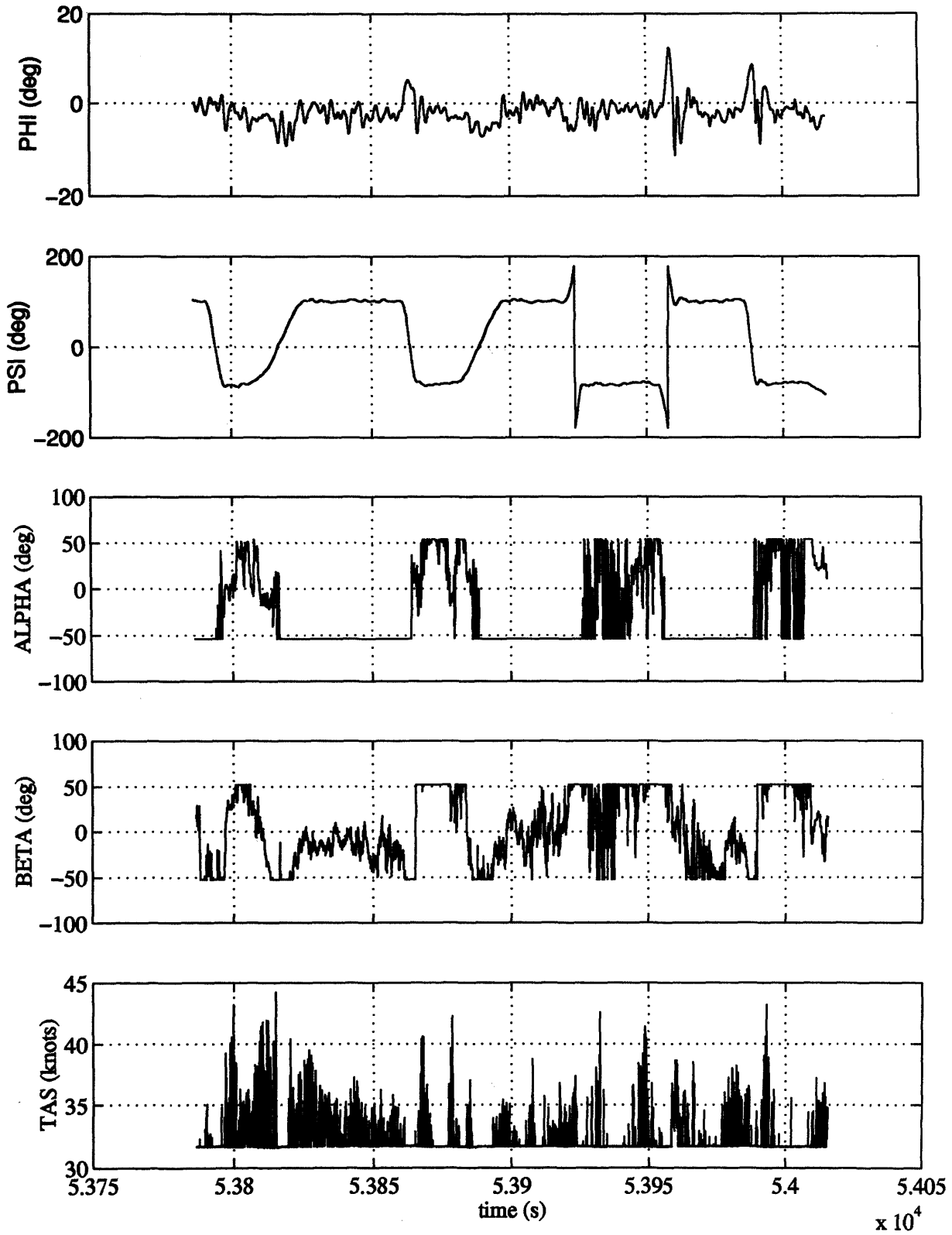


Figure B.4 *Pirouette circle*

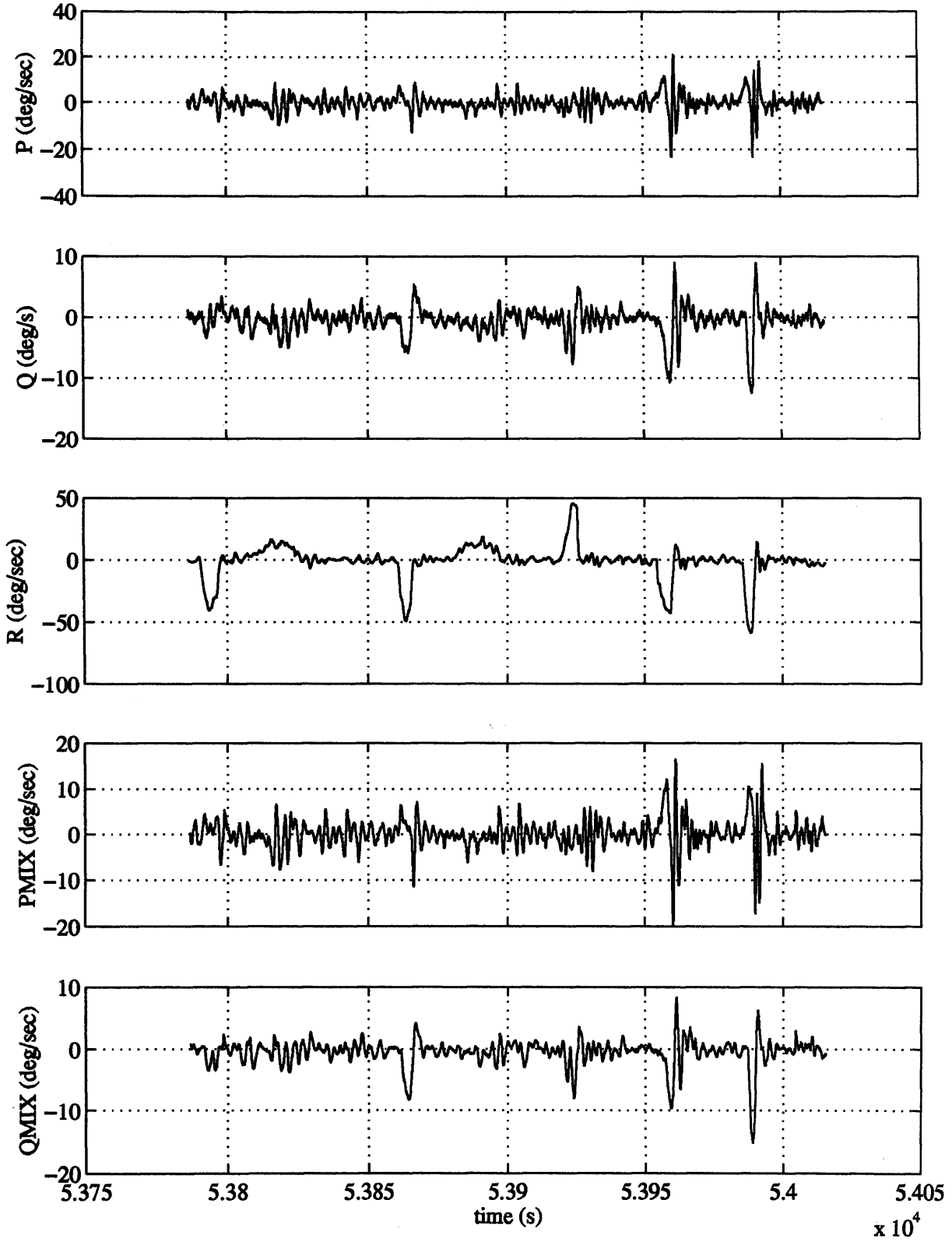
C

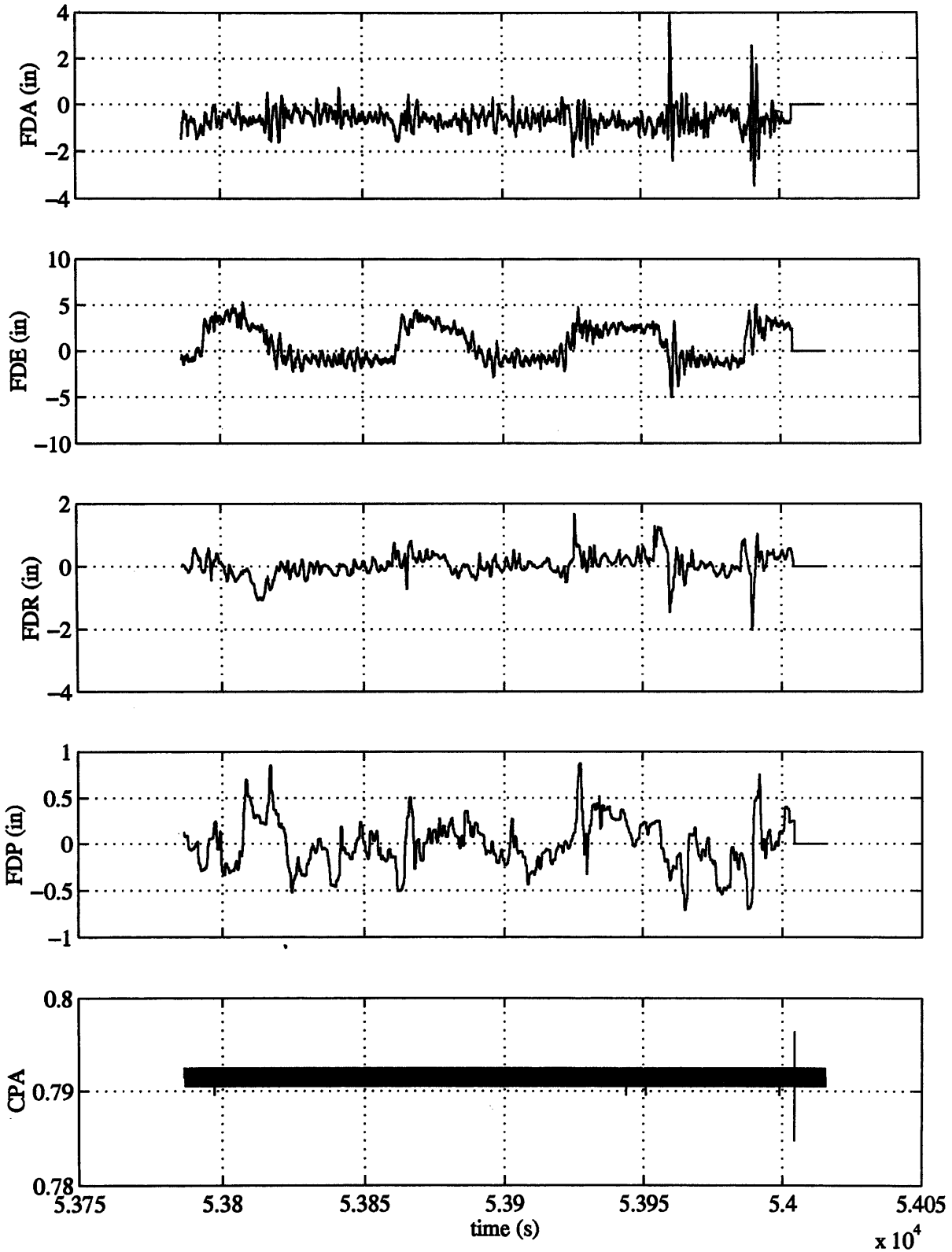
Recorded Flight Test Data - Time Histories of spot turn manoeuvre

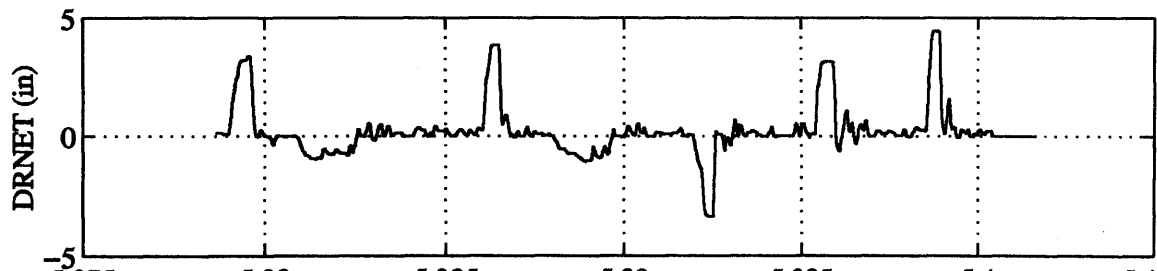
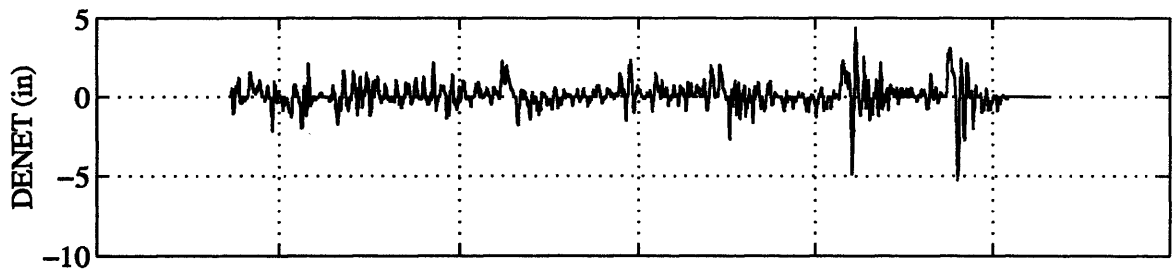
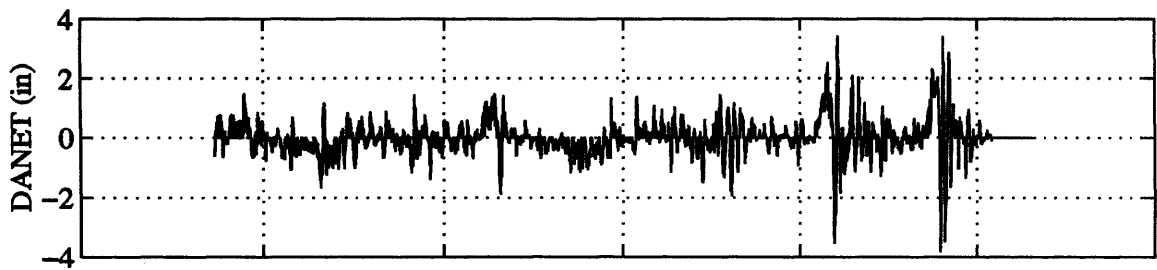
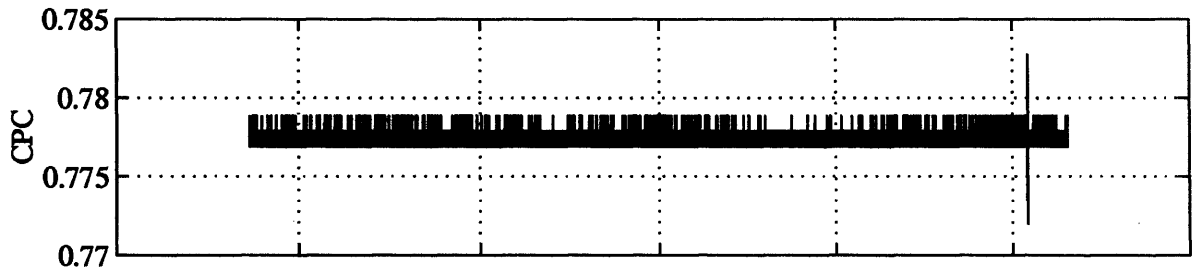
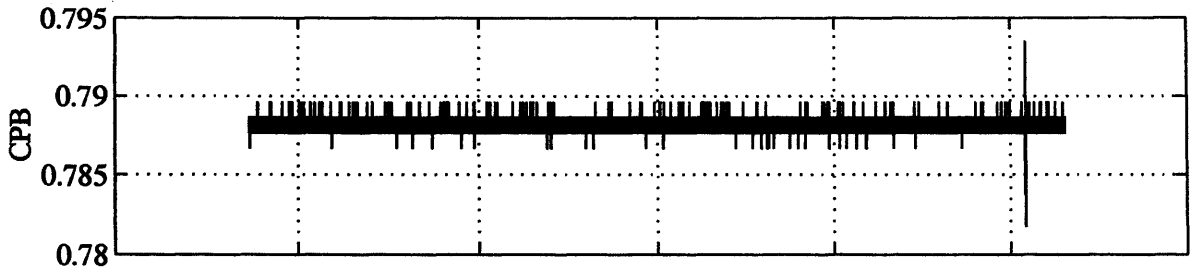




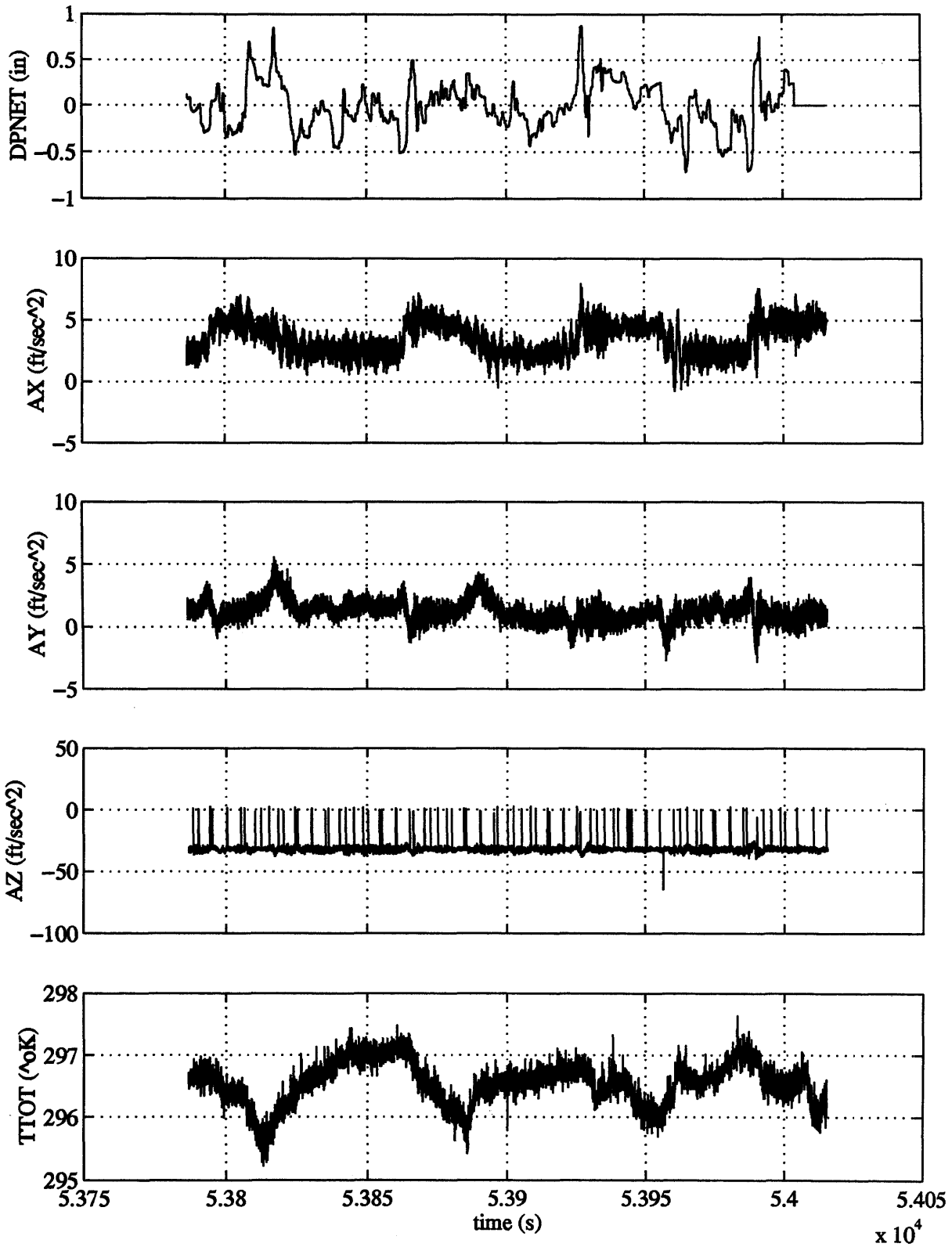
Data: /control13/ajs15/jul97tests/y97043/y97043.e22

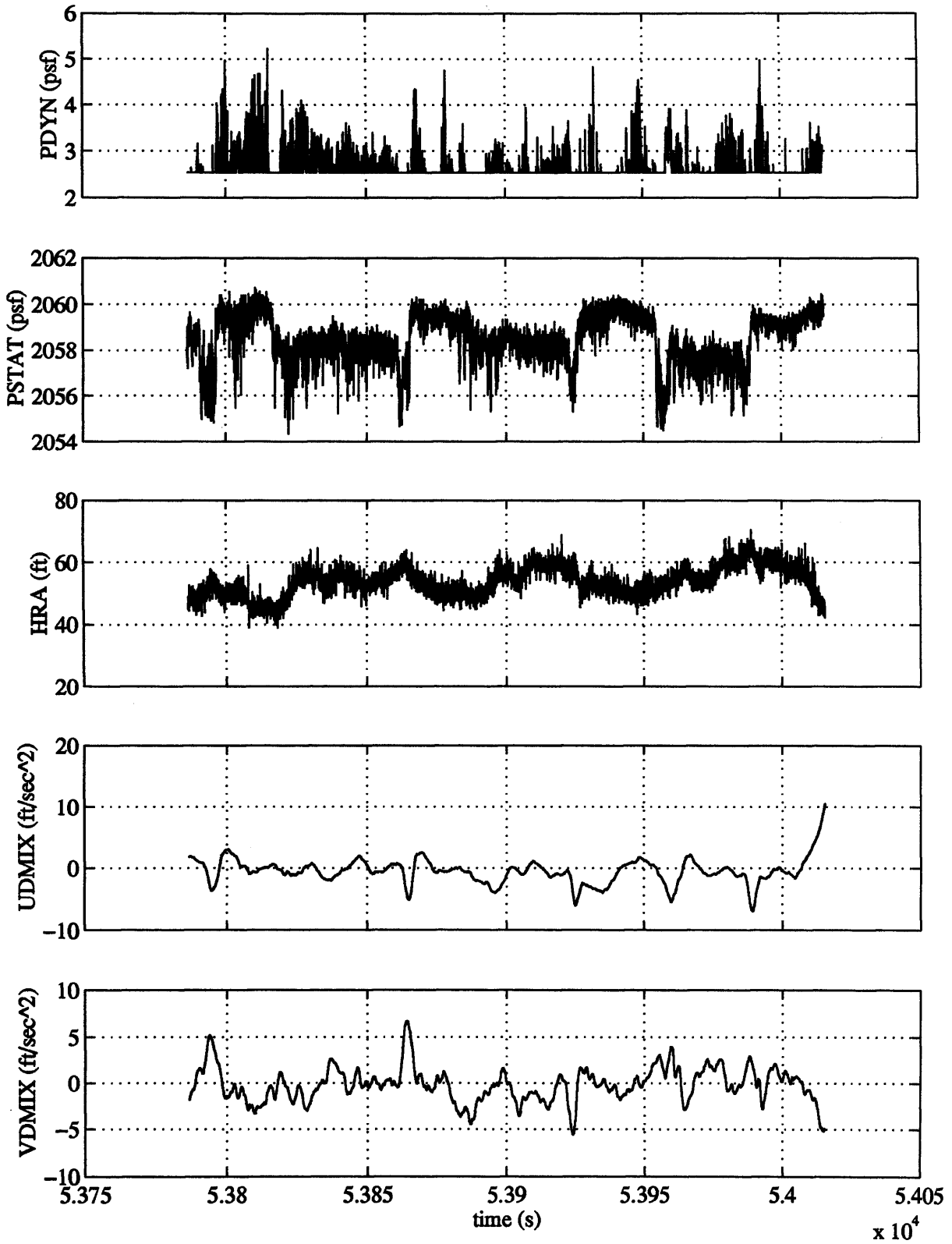


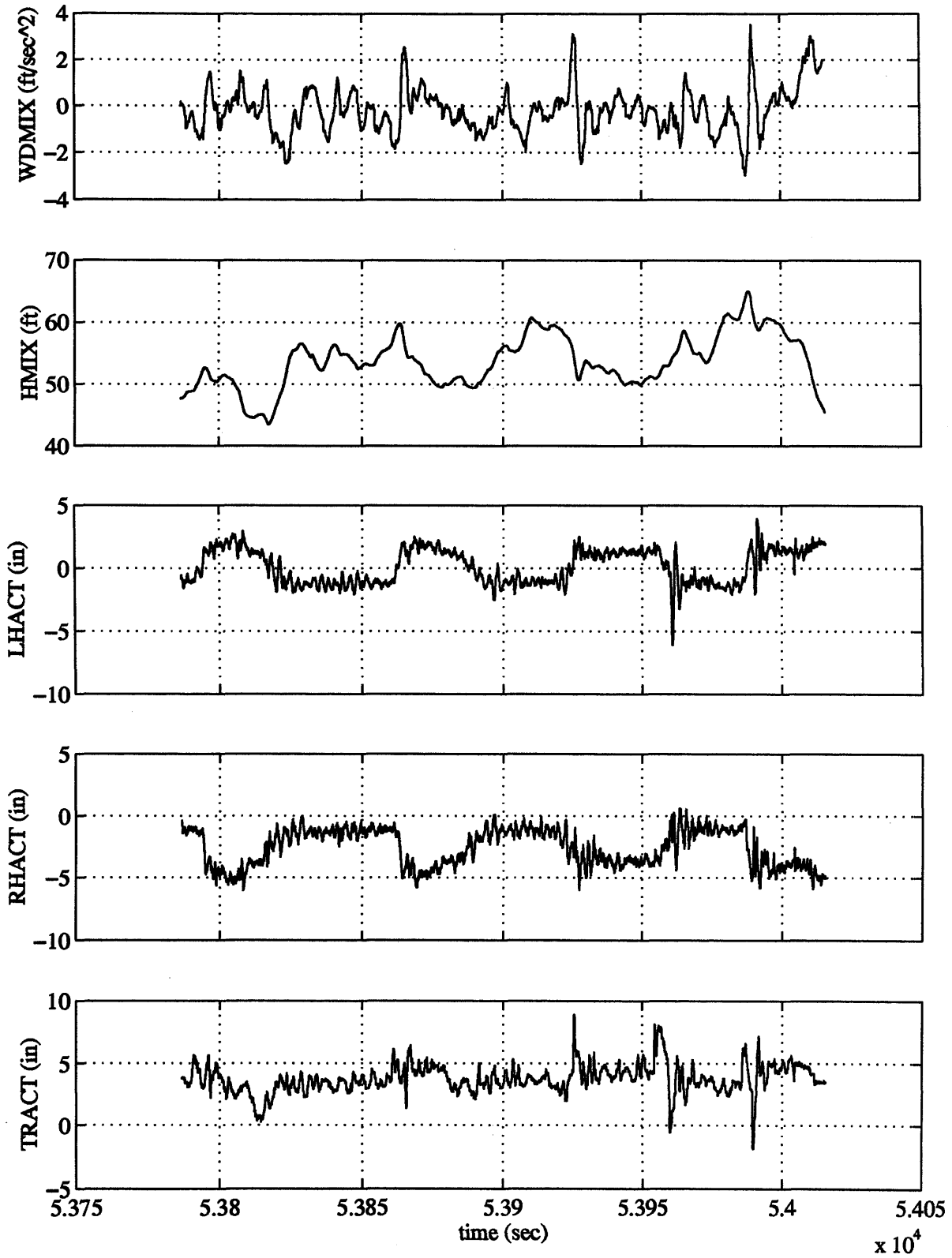


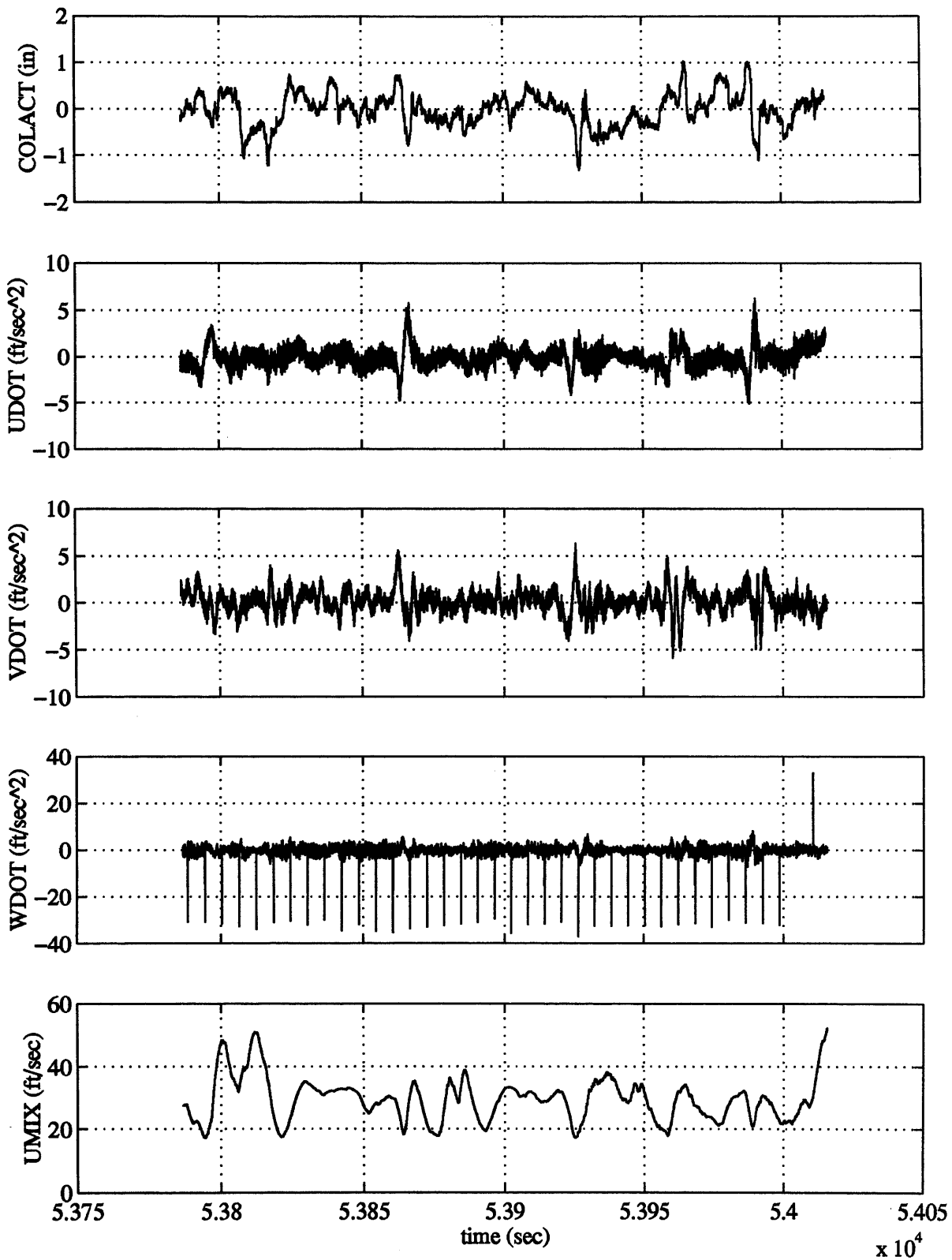


5.375 5.38 5.385 5.39 5.395 5.4 5.405
time (s) $\times 10^4$









Bibliography

- [1] Moran W. A. Operational and Developmental Experience With the F/A-18A Digital Flight Control System. Review Evaluation and Projections. Technical Report CP-384, AGARD, 1984.
- [2] Anonymous. Handling Qualities Requirements for Military Rotorcraft, Aeronautical Design Standard ADS-33C. Technical report, US Army AVSCOM, St. Louis, Missouri, 1989.
- [3] Anonymous. Handling Qualities Requirements for Military Rotorcraft, Aeronautical Design Standard ADS-33D. Technical report, United States Army ATCOM, St. Louis, MO, July 1994.
- [4] P. Apkarian and R. J. Adams. Advanced Gain-Scheduling Techniques for Uncertain Systems. *IEEE Transactions on Control Systems Technology*, 6(1):21–32, 1998.
- [5] P. Apkarian and J-M. Biannic. Self-Scheduled h_∞ Control of Missile via Linear Matrix Inequalities. *Journal of Guidance, Control and Dynamics*, 18(3):532–538, May-June 1995.
- [6] P. Apkarian and P. Gahinet. A Convex Characterization of Gain-Scheduled h_∞ Controllers. *Transactions in Automatic Control*, 40(5):853–864, May 1995.
- [7] P. Apkarian, P. Gahinet, and G. Becker. Self-Scheduled H_∞ Control of Linear Parameter-Varying Systems: A Design Example. *Automatica*, 31(9):1251–1261, May 1995.
- [8] S. W. Baillie, J. M. Morgan, and K. R. Goheen. Practical Experiences in Control Systems Design using the NRC Bell 205 Airborne Simulator. *Flight Mechanics Panel Symposium*, pages 27.1–27.12, January 1994.

- [9] G. J. Balas, J. C. Doyle, K. Glover, A. Packard, and R. Smith. *μ -Analysis and Synthesis Toolbox: User's Guide*. MUSYN Inc. and The Mathworks, Inc., 1993.
- [10] G. Becker, A. Packard, D. Philbrick, and G. Balas. Control of Parametrically-Dependent Linear Systems: A Single Quadratic Lyapunov Approach. *American Control Conference*, pages 2795–2799, 1993.
- [11] G. T. Black and D. J. Moorhouse. Flying Qualities Design Requirements for Sidestick Controllers. Technical Report AFFDL TR-79-3126, U.S. Air Force Flight Dynamics Laboratory, 1979.
- [12] H. W. Bode. *Network Analysis and Feedback Amplifier Design*. Van Nostrand, Princeton, 1945.
- [13] A.R. Bramwell. *Helicopter Dynamics*. Arnold, 1976.
- [14] M. A. Branch and A. Grace. *Optimization Toolbox*. Natick, MA: The MathWorks, Inc., 1996.
- [15] R. Chen. Effects of Primary Rotor Parameters on Flapping Dynamics. Technical Report TP-1431, NASA, 1980.
- [16] R. Y. Chiang. *Modern Robust Control Theory*. PhD thesis, University of Southern California, 1988.
- [17] D. Cooper. YUH-60A Stability and Control. *33rd Annual Forum of the American Helicopter Society*, May 1977.
- [18] E.M. Kasenally D.J.N. Limebeer and J.D. Perkins. On the design of robust two degree of freedom controllers. *Automatica*, 29(1):157–168, 1993.
- [19] D.J.Walker and I. Postlethwaite. A Full-Flight Envelope High-Bandwidth Rotorcraft Flight Control System. In *Proceedings of the 30th IEEE Conference on Decision and Control, Brighton*, December 1991.
- [20] J. C. Doyle, K. Glover, P. P. Khargonekar, and B. A. Francis. State-Space Solutions to Standard \mathcal{H}_2 and H_∞ control problems. *IEEE Transactions on Automatic Control*, 34:831–847, August 1989.
- [21] J. C. Doyle and G. Stein. Multivariable Feedback Design: Concepts for a Classical/Modern Synthesis. *IEEE Transactions on Automatic Control*, 26:4–16, February 1981.
- [22] J.C. Doyle, B. Francis, and A. Tannenbaum. *Feedback Control Theory*. Macmillan Publishing Co., 1992.

- [23] G. S. Bushgens (Eds). *Aerodynamics, Stability and Controllability of Supersonic Aircraft (in Russian)*. Zhukovsky Central Aerohydrodynamic Institute, Moscow, Nauka, Fizmatlit, 1998.
- [24] Charles W. Ellis. Effects of Articulated Rotor Dynamics on Helicopter Automatic Control System Requirements. *Aeronautical Engineering Review*, 12(7), 1953.
- [25] C. Yu. Esaulov, O. P. Bakhov, and I. C. Dmitriev. *The Helicopter as Control Object*. Machinostroyeniye (in Russian), 1977.
- [26] J. Howitt et. al. Experimental evaluation of high bandwidth helicopter flight control system designs exploiting rotor state feedback. *Proceedings of the 23rd European Rotorcraft Forum, Treff Hotel, Dresden, Germany*, pages 105.1 –105.13, September 1997.
- [27] N. Foster. *Advanced Multivariable Control Law Design for Future ACT Rotorcraft*. PhD thesis, University of Leicester, UK, 1995.
- [28] J.S. Freudenberg. Plant Directionality, Coupling and Multivariable Loop Shaping. *International Journal of Control*, 51(2):365–390, 1990.
- [29] Powers B. G. Active Control Technology Experience With the Space Shuttle in the Landing Regime. Technical Report TM-85910, NASA, 1984.
- [30] T.T. Georgiou. On the Computation of the Gap Metric. *Systems and Control Letters*, 11:253–257, 1988.
- [31] T.T. Georgiou and M.C. Smith. Optimal Robustness in the Gap Metric. *IEEE Transactions on Automatic Control*, 35(6):673–686, June 1990.
- [32] J. C. Gibson and R. A. Hess. Stick and Feel System Design,. Technical report, AGARD-AG-332, Advisory Group for Aerospace Research and Development, NATO, May 1997.
- [33] K. Glover. All Optimal Hankel-norm Approximations of Linear Multivariable Systems and their L^∞ -error Bounds. *International Journal of Control*, 39(6):1115–1193, 1984.
- [34] R. K. Heffley, W. F. Jewell, J. M. Lehman, and R. A. Van Winkle. A Compilation and Analysis of Helicopter Handling Qualities Data. Contractor Report 3144, NASA, 1979.
- [35] R. L. Heimbold and C. D. Griffith. Synthesis of an Electromechanical Control System for a Compound Hingeless Rotor Helicopter. *American Helicopter Society Journal*, 17(2), April 1972.

- [36] A. Helmersson. *Methods for Robust Gain Scheduling*. PhD thesis, Linköping University, Sweden, 1995.
- [37] R. D. Holdridge, Hindson W. S., and Bryson A. E. LQG-Design and Flight Test of a Velocity Command System for a Helicopter. *Proceedings of AIAA Guidance, Navigation and Control Conference, Snowmass, CO*, August 1985.
- [38] D. Hoyle, R. Hyde, and D. J. N. Limebeer. An H_∞ Approach to Two-Degree-Of-Freedom Design. *Proceedings of the IEEE CDC*, pages 1581–1585, December 1991.
- [39] R. A. Hyde. A Robust Multivariable Control Law for the DRA VAAC Programme. Internal Report, Cambridge University Engineering Department, UK, December 1993.
- [40] R. A. Hyde. *H_∞ Aerospace Control Design - A VSTOL Flight Application*. Advances in Industrial Control. Springer-Verlag, 1995.
- [41] R. A. Hyde and K. Glover. The Application of Scheduled H_∞ Controllers to a VSTOL Aircraft. *IEEE Transactions in Automatic Control*, 38(7):1021–1039, 1993.
- [42] R. A. Hyde, K. Glover, and G. T. Shanks. VSTOL First Flight of an H_∞ Control Law. *IEE Computing and Control Engineering Journal*, 6(1):11–16, February 1995.
- [43] Glusman S. I., Landis K. H., and Dabundo C. Handling Qualities Evaluation of the ADOCS Primary Flight Control System. *42nd Annual Forum of the American Helicopter Society, Washington DC*, June 1986.
- [44] A. Kenneth. Handling Qualities of the Army/Hughes YAH-64 Advanced Attack Helicopter. *34th Annual Forum of the American Helicopter Society*, May 1978.
- [45] D. McFarlane and K. Glover. An H_∞ Design Procedure Using Robust Stabilization of Normalized Coprime Factors. *Proceedings of the 27th Conference on Decision and Control*, pages 1343–1348, December 1988.
- [46] D. McFarlane and K. Glover. *Robust Controller Design Using Normalized Coprime Factor Plant Descriptions*. Information and Control Sciences. Springer-Verlag, 1990.
- [47] T. Meressi and B. Paden. Gain Scheduled H_∞ Controllers for a Two-Link Flexible Manipulator. *Journal of Guidance Control and Dynamics*, 17(3):537–543, 1994.
- [48] V. Mukhopadyay. Stability Robustness Improvement Using Constrained Optimisation Techniques. *Guidance Control and Dynamics*, 10(2):172–177, 1987.
- [49] Resa Neshat. *A High Order Simulation Model for the Bell 205 Helicopter*. PhD thesis, Ottawa-Carleton Institute for Mechanical and Aerospace Engineering, August 1995.

- [50] R. A. Nichols, R. T. Reichert, and W. J. Rugh. Gain Scheduling of H_∞ Controllers; A Flight Control Example. *IEEE Transactions on Control Systems Technology*, 1(2):69–79, 1993.
- [51] A. Packard. Gain Scheduling via Linear Fractional Transformation. *Systems & Control Letters*, 22:79–92, 1994.
- [52] G. D. Padfield. Theoretical Model of Helicopter Flight Mechanics for Application to Piloted Simulation. Technical Report TR 81048, Royal Aircraft Establishment, 1981.
- [53] Gareth Padfield. *Helicopter Flight Dynamics*. Addison-Wesley, 1996.
- [54] G. Papageorgiou, K. Glover, A. Smerlas, and I. Postlethwaite. *A Tutorial in H_∞ Loop-Shaping*. Number 224 in Robust Flight Control by J.F.Magni, S.Bennani, J.Terlouw, Lecture Notes and Information Sciences. Springer-Verlag, January 1997.
- [55] D. Pitt and D. Peters. Theoretical Foundation of Dynamic Inflow Derivatives. *Verica*, 5:21–34, 1981.
- [56] R.A.Hyde. *The application of Robust Control to VSTOL Aircraft*. PhD thesis, Department of Engineering, Cambridge University, UK, 1991.
- [57] M.Kinnaerti R.Hanus and J.L.Hemotte. Conditioning technique, a general anti-windup and bumpless transfer method. *Automatica*, 23:729–739, 1987.
- [58] R. Samar. *Robust Multi-Mode Control of High Performance Aero-Engines*. Phd dissertation, University of Leicester, 1995.
- [59] D. E. Sattler. The National Aeronautical Establishment Airborne Simulator Facility. Technical report, Canadian National Research Council, 1984.
- [60] J. Sefton and K. Glover. Pole-Zero Cancellations in the General H_∞ Problem with Reference to a Two Block Design. *Systems & Control Letters*, 14:295–306, 1990.
- [61] S. M. Shinnars. *Modern Control Systems Theory*. John Wiley and Sons Inc., 1992.
- [62] S.J.Garg. A Simplified Scheme for Scheduling Multivariable Controllers. *Control Systems Magazine*, 17(14), August 1997.
- [63] S. Skogestad and I. Postlethwaite. *Multivariable Feedback Control*. John Wiley and Sons, 1996.
- [64] A. J. Smerlas, I.Postlethwaite, and D.J.Walker. Robust Gain Scheduling in Helicopter Control. *Proceedings of the 23rd European Rotorcraft Forum, Treff Hotel, Dresden, Germany*, pages 84.1–84.5, September 1997.

- [65] A. J. Smerlas, I. Postlethwaite, and D. J. Walker. Full Envelope Robust Control Law for the Bell-205 Helicopter. *Proceedings of the 22nd European Rotorcraft Forum., Brighton, UK*, pages 105.1–105.6, September 1996.
- [66] D. J. Stilwell and W. J. Rugh. Interpolation of Observer State Feedback Controllers for Gain Scheduling, technical report jhu/ece-97-09. Technical report, The Johns Hopkins University, August 1997.
- [67] M.D. Takahashi. H_∞ Helicopter Flight Control Law Design With and Without Rotor State Feedback. *Journal of Guidance, Control and Dynamics*, 17(6):1245–1251, 1994.
- [68] M. B. Tischler. *Advances in Aircraft Flight Control*. Taylor and Francis, London, 1996.
- [69] M. Tombs. *Robust Control System Design With Application to High Performance Helicopters*. PhD thesis, University of Leicester, U.K., 1987.
- [70] M. Vidyasagar. *Control System Synthesis: A Coprime Factorization Approach*. MIT Press, 1985.
- [71] G. Vinnicombe. *Measuring Robustness of Feedback systems*. PhD thesis, University of Cambridge, 1993.
- [72] D. J. Walker. On the Structure of a 2-Degrees-Of-Freedom Controller. *International Journal of Control*, vol. 63, No 6, pages 1105–1127, 1996.
- [73] D. J. Walker, I. Postlethwaite, J. Howitt, and N. P. Foster. Rotorcraft Flying Qualities Improvement Using Advanced Control. *American Helicopter Society/NASA Conference on Flying Qualities and Human Factors*, page No.2.3.1, 1993.
- [74] D.J. Walker and I. Postlethwaite. Full Authority Active Control Design for a High Performance Helicopter. *European Rotorcraft Forum*, page Paper No. 3.3.2, 1990.
- [75] K.Zhou with J.C.Doyle and K.Glover. *Robust and Optimal Control*. Prentice Hall, 1996.
- [76] F. Wu, X. H. Yang, A. Packard, and G. Becker. Induced l_2 -norm Control for LPV Systems With Bounded Parameter Variation Rates. *International Journal of Robust and Nonlinear Control*, 6(9/10):983–998, 1996.
- [77] A. Yue. H_∞ Design and The Improvement of Helicopter Handling Qualities. PhD thesis, University of Oxford, UK, 1988.
- [78] A. Yue and I. Postlethwaite. Improvement of Helicopter Handling Qualities Using H_∞ Optimisation. *IEE Proceedings*, D:115–129, 1990.

- [79] G. Zames and A. K. El-Sakkary. Unstable Systems and Feedback: The Gap Metric. *Proc. Allerton Conference*, pages 380–385, October 1980.
- [80] Kemin Zhou and John Doyle. *Essentials of Robust Control*. Prentice-Hall Inc., 1998.